UNIVERSITY OF CAPE TOWN

DOCTORAL THESIS

Dark matter searches with cosmic-ray detectors and the Square Kilometre Array

Author:
Miguel Méndez Isla

Supervisor:
Dr. Álvaro de la Cruz Dombriz
Co-supervisor:
Prof. Peter K. S. Dunsby

A thesis submitted in fulfillment of the requirements for the degree of Doctor of Philosophy

in the

Cosmology and Gravity Group
Department of Mathematics and Applied Mathematics

April 18, 2020

Declaration of Authorship

I, Miguel MÉNDEZ ISLA, declare that this thesis titled, "Dark matter searches with cosmic-ray detectors and the Square Kilometre Array" and the work presented in it are my own. I confirm that:

- This work was done wholly or mainly while in candidature for a research degree at this University.
- Where any part of this thesis has previously been submitted for a degree or any other qualification at this University or any other institution, this has been clearly stated.
- Where I have consulted the published work of others, this is always clearly attributed.
- Where I have quoted from the work of others, the source is always given. With the exception of such quotations, this thesis is entirely my own work.
- I have acknowledged all main sources of help.
- Where the thesis is based on work done by myself jointly with others, I have made clear exactly what was done by others and what I have contributed myself.

Signed: Signed by candidate

Date:

DECLARATION ON INCLUSION OF PUBLICATIONS IN A PhD THESIS

Note: PhD students who have been granted approval by the DDB to include publications in their thesis, must add the following separate signed statement, listing the publications that they were given permission to include (this statement must be included in your thesis, after the declaration that it is your own work):

"I confirm that I have been granted permission by the University of Cape Town's Doctoral Degrees Board to include the following publication(s) in my PhD thesis, and where co-authorships are involved, my co-authors have agreed that I may include the publication(s)"

1- J. A. Cembranos, A. de la Cruz-Dombriz, P. K. Dunsby, and M. Méndez-Isla. ***Analysis of branon dark matter and extra-dimensional models with AMS-02.*** Physics Letters B, vol. 790, **(2019).**

2- P. Bull et al. ***Fundamental Physics with the Square Kilometer Array*** **(2018)**. arXiv: 1810.02680 [astro-ph.CO]

3-J. A. R. Cembranos, A. de la Cruz-Dombriz, V. Gammaldi, and M. Mendez-Isla. ***SKA-Phase 1 sensitivity for synchrotron radio emission from multi-TeV Dark Matter candidates.*** (**2019**). arXiv: 1905.11154 [hep-ph].

SIGNATURE: Signed by candidate DATE: 11-11-2019

STUDENT NAME: Miguel Méndez Isla STUDENT NUMBER: MNDMIG001

"Gira el haz de luz para que se vea desde alta mar.
Yo buscaba el rumbo de regreso sin quererlo encontrar.
Pie detrás de pie, iba tras el pulso de claridad.
La noche cerrada apenas se abría, se volvía a cerrar.

Un faro quieto nada sería,
guía mientras no deje de girar,
no es la luz lo que importa en verdad,
son los doce segundos de oscuridad.

Para que se vea desde alta mar,
de poco le sirve al navegante que no sepa esperar.
Pie detrás de pie, no hay otra manera de caminar.
La noche del cabo revelada en un inmenso radar.

Un faro para solo de día,
guía mientras no deje de girar,
no es la luz lo que importa en verdad,
son los doce segundos de oscuridad."

12 segundos de oscuridad, Jorge Drexler.

To my parents, Salud and Martín,
and
my siblings, Salud, Martín, Pilar and Magdalena,
for writing with me the story that brought me to this precise moment

Acknowledgements

Firstly, I would like to thank my supervisors Dr. Álvaro de la Cruz Dombriz and Prof. Peter K.S. Dunsby, for giving me the opportunity to work in the Cosmology and Gravity Group. This thesis has been possible thanks to their trust and support. I am also thankful to them for encouraging me to present this work at different international conferences in Spain, Norway, the Netherlands, China and South Africa.

I would like to thank the University of Cape Town that has been my home during these years. Working side by side with its workers, learning side by side with its students, has been very inspirational for me. I would like to express my profound gratitude to my collaborators Dr. Viviana Gammaldi and Prof. José Alberto Ruiz Cembranos, from whom I have learnt so much. It has been really a great pleasure to work with you. I am also deeply indebted to institutions as IFT-UAM, UCM (Spain), the Institute of Theoretical Astrophysics (Norway) and the people working there, that have facilitated the development of this work in different ways. I would like to thank also the financial support of the University of Cape Town - Faculty of Science Doctoral Fellowships and the National Astrophysics and Space Science Programme (NASSP) and I would like to acknowledge financial support from Project No. FPA2014-53375-C2-1-P from the Spanish Ministry of Economy and Science, Project No. FIS2016- 78859-P from the European Regional Development Fund and Spanish Research Agency (AEI), Project No. CANTATA CA-15117 from COST Action EU Framework Programme Horizon 2020, University of Cape Town Launching Grants Programme and National Research Foundation Grants No. 99077 2016-2018, Ref. No. CSUR150628121624 and 110966 Ref. No. BS170509230233, the NRF Incentive Funding for Rated Researchers (IPRR), Ref. No. IFR170131220846, and Project UTF-2016-long-term/10067 "Cosmology and Gravity Education - University of Cape Town (UCT) and University of Oslo (UiO)", Norwegian Centre for International Cooperation in Education. Also, I would like to express my sincere thanks to the examiners of this thesis, for their work, interest and also for comments and suggestions, which significantly improved the original thesis.

I would especially like to thank two colleagues, and friends, who I admire both professionally and personally, Francisco José Maldonado Torralba, Pepe, and Dr. Sulona Kandhai. Pepe, you have always been there, from my first to my last step, from the *branons with AMS* to the *model-independent with SKA*, in Duiker Island and Hovedøya, from the *Aces* to the *Let it be*. Thanks for every moment, for the laughter and for your advice. I am eternally grateful to you. Sulona, you taught me how to be courageous and strong, how to be patient and meticulous in my work. I have become a better person thanks to you and that is invaluable.

Also, I would like to express my appreciation to my colleagues and friends of the Cosmology and Gravity Group. Mariam Campbell and Jack Morrice, for your support and friendship, and for motivating me throughout this research. I am also grateful to Avishek Dusoye, Louis Perenon, Sim Dlamini, Lestinah Mthombeni, Idrees Khan, Anthony Walters, Juhi Hurgobin and Ira Georg. I also wish to thank Raúl Carballo and Héctor Villarubia Rojo.

Quiero agradecer también a mi familia y amigos. A mis padres, Salud y Martín, por su apoyo emocional y económico. Quiero agradecerles porque esta tesis doctoral ha sido también fruto de su esfuerzo y de su trabajo durante muchos más años de los que yo tengo. Quiero agradecer a mis hermanos, Salud, Martín, Pilar y Magdalena, por ofrecerme cada uno de ellos las palabras precisas en el momento en que más las necesitaba. A Alberto y a Carmen. A Alberto por compartir conmigo esta feliz estancia en el Cabo y vivir la mayor parte de los momentos que

me han marcado para siempre. A Carmen, por hablar conmigo cada uno de los días de esta travesía, lloviendo o nevando. A José Miguel, por acompañarme en este viaje, que no solo ha sido científico sino también personal. Y a Clara, que siempre ha estado allí.

Por último, pero no por ello menos importante, quiero agradecer a Bea, por animarme y apoyarme en la última etapa y versión final de este manuscrito.

1

UNIVERSITY OF CAPE TOWN

Abstract

Science
Department of Mathematics and Applied Mathematics

Doctor of Philosophy

Dark matter searches with cosmic-ray detectors and the Square Kilometre Array

by Miguel MÉNDEZ ISLA

Beyond gravitational evidence for dark matter, a set of search techniques are employed in the present thesis within the particle dark matter paradigm. Under the possibility of dark matter annihilating into particles of the Standard Model of Particle Physics, we study the products of annihilation with cosmic-ray detectors, such as AMS, Fermi-LAT and PAMELA, and radio telescopes, such as the SKA. In this work, we focus on the positron fraction measured in the Solar System due to dark matter annihilating in the dark matter galactic halo, but also on radio signals from the Milky Way and dwarf spheroidal galaxies. Our main purpose is to constrain the dark matter parameter space under the light of the latest experimental data for cosmic-rays and the new sensitivities reached in radio astronomy. Furthermore, we discuss some of the most promising locations and synchrotron frequencies to search for dark matter with masses around the TeV scale. The analysis presented in this thesis lies in setting constraints on model-independent dark matter. However, some specific dark matter candidates in the context of extra-dimensional theories are considered as well. Indeed, brane fluctuations, dubbed branons, are new degrees of freedom appearing in flexible brane-world models. These new fields behave as standard weakly interacting massive particles with a significant associated thermal relic density and would explain dark matter observational features.

Contents

List of Abbreviations

ACC	**A**nti**C**oincidence **C**ounter
ACD	**A**nti**C**oincidence **D**etector
AGN	**A**ctive **G**alactic **N**uclei
BBN	**B**ig **B**ang **N**ucleosynthesis
BH	**B**lack **H**ole
BSM	**B**eyond **S**tandard **M**odel
CAL	**CAL**orimeter
CDM	**C**old **D**ark **M**atter
CMB	**C**osmic **M**icrowave **B**ackground
CP	**C**harge-**P**arity
DM	**D**ark **M**atter
dSph	**d**warf **Sph**eroidal
ECAL	**E**lectric **CAL**orimeter
EFT	**E**ffective **F**ield **T**heories
FoV	**F**ield **o**f **V**iew
GAC	**G**alactic **A**nti**C**entre
GC	**G**alactic **C**entre
GR	**G**eneral **R**elativity
ICS	**I**nverse **C**ompton **S**cattering
ISM	**I**nter**S**tellar **M**edium
IMBH	**I**nter**m**ediate-**M**ass **B**lack **H**ole
IRF	**I**nterstellar **R**adiation **F**ield
LKP	**L**ightest **K**aluza-Klein **P**article
l.o.s.	**l**ine **o**f **s**ight
MSSM	**M**inimal **S**upersymmetric **S**tandard **M**odel
NM	**N**on-**M**odulated
NFW	**N**avarro **F**renk **W**hite profile
PWN	**P**ulsar **W**ind **N**ebula
QCD	**Q**uantum **C**hromo**D**ynamics
QED	**Q**uantum **E**lectro**D**ynamics
rms	**r**oot **m**ean **s**quare
SEFD	**S**ystem **E**quivalent **F**lux **D**ensity
SM	**S**tandard **M**odel
SHM	**S**tandard **H**alo **M**odel
SNR	**S**uper**N**ova **R**emnant
SUSY	**SU**per**SY**mmetry
TOF	**T**ime **O**f **F**light detector
TRD	**T**ransition **R**adiation **D**etector
UED	**U**niversal **E**xtra **D**imensions
WIMP	**W**eakly **I**nteractive **M**assive **P**article

Physical Constants

Boltzmann constant	k_b
Electron mass	m_e
Electron charge	e
Gravitational constant	G
Hubble constant	H_0
Reduced Hubble Constant	h
Planck mass	M_p
Proton mass	m_p
Reduced Planck constant	$\hbar$
Rydberg constant	R_∞
Speed of Light	c
Solar mass	$M_\odot$
Thomson cross section	σ_T
Vacuum permittivity	ϵ_0

Preface

The *missing mass problem* enunciated by Fritz Zwicky in 1933 and addressed by many other authors throughout the twentieth and twenty-first centuries, still represents one of the biggest challenges for contemporary physics. Many of the challenges in Astrophysics and Cosmology converge toward the same idea: either there exists a component of non-luminous matter in the Universe or some of the most successful theoretical models in Modern Physics should be revised. Such a non-luminous matter, the so-called *dark matter*, would accommodate within the cosmological ΛCDM Concordance model. In fact, under the ΛCDM paradigm and according to measurements by COBE, WMAP and PLANCK, dark matter accounts for the 86% of the matter in the Universe. Also, even though the Standard Model of elementary particles is the most successful framework in particle physics, its incompleteness has been revealed in some aspects. The neutrino mass, the not-inclusion of gravity, the CP violation or the hierarchy problem constitute some of the open questions that require the existence of physics beyond the Standard Model. In an effort to complete the conundrum both in Cosmology and Particle Physics -the former includes unknown novel elements while the latter is an unfinished theory- a common study framework based on particle dark matter is established in this work. Beyond dark matter gravitational evidence, a set of different techniques founded on particle features fixes a point of departure for collider, direct and indirect dark matter searches. This latter strategy, followed in the present thesis, comprises processes of decay and annihilation of dark matter, opening the possibility to pass from the dark matter sector to the Standard Model of particles. Indeed, under the prediction of dark matter constituting halos in which galaxies are immersed, dark matter may either annihilate or decay into stable particles contributing to a significant component for cosmic rays.

Conversely, from an astroparticle physics point of view, intensive research on cosmic rays allowed to develop solid statements about particle propagation, chemical abundances of the interstellar medium, and global properties of our Galaxy. Models such as the Leaky Box and Nested-Leaky Box together with sophisticated numerical codes (GALPROP or DRAGON) have successfully reproduced cosmic-ray abundances under the assumptions from Fermi acceleration theory. However, combining the same approach for distinct cosmic-ray abundances confirms some anomalies. One of them is the unexpected rise of the positron fraction for $E > 10$ GeV reported by PAMELA, confirmed by Fermi-LAT and measured very precisely by AMS. Without modifying the main foundations of cosmic-ray propagation, alternative sources for positrons have been proposed, such as supernova remnants or pulsar wind nebulae. In addition, among the most exotic sources, annihilating dark matter has been widely considered to explain the positron excess. In the next years, novel results above 500 GeV may be able to determine the reason for the rise in the positron fraction as well as the positron spectrum.

Furthermore, electrons and positrons propagating along the Galaxy suffer from radiative losses in the interaction with the interstellar medium generating photons in a large range of frequencies. Interactions of such particles with the galactic magnetic field are responsible for synchrotron emission mainly centred on radio frequencies, although other processes such as Inverse Compton scattering result in signals ranging typically from X-ray to gamma-ray emission. In the present research, an original study of indirect searches for dark matter has been done with the

purpose of either constraining or prospecting annihilating dark matter models. This work is mainly focused on particle dark matter with masses in the TeV scale. Firstly, we have focused on model-independent dark matter that would be in agreement with the positron fraction measured by cosmic-ray detectors such as PAMELA, Femi-LAT and AMS. This study allowed us to provide general statements in the broad outlook of indirect searches. Indeed, the main goal is clarifying those annihilation channels that are more suitable to explain the positron excess and comparing them with previous works. Consequently, the same strategy is considered to study extra-dimensional dark matter in Brane-World scenarios. In fact, such theories predict particles that accommodate as natural dark matter candidates, dubbed branons. In this context, we set constraints on the branon parameter space determined by the mass and the tension of the brane for different astrophysical scenarios. In addition, we provide the best fit for the positron fraction in the case of such candidates were considered. Furthermore, we also study the synchrotron emission in the Milky Way from electrons and positrons with a view in the crucial steps achieved lately in observational radio astronomy. Radio signals from dark matter annihilation are expected to be large toward the Galactic Centre, however, disentangling them from the radio background could be a difficult task in which high sensitivity radio telescopes such as MeerKAT and the SKA would play an essential role. In this study, we provide the synchrotron signals in different regions of the Milky Way with the aim of determining which coordinates of the sky would be promising areas for future radio detectors. Finally, in order to avoid the radio background, we also study the synchrotron signals due to the annihilation of dark matter in dwarf spheroidals. In the first place, we discuss those astrophysical features that would affect dark matter constraints in order to establish the reliability of current researches for this kind of target. After that, we analyse the SKA sensitivity for the detection of model-independent dark matter. Then, particular candidates are considered for the same study. Firstly those candidates that may fit the cut-off in the gamma-ray spectra observed by HESS from the J1745 - 290 Galactic Centre, but also branon dark matter previously studied. Further discussions about alternative astrophysical scenarios, including either dark matter substructures or central intermediate massive black holes, are also taken into account.

Finally, these studies allow us to delineate some conclusions about the best locations and frequencies to be considered in dark matter searches, depending on the mass and the thermally averaged cross section. Some of these conclusions will be related to other search strategies that have emerged over the last years.

Chapter 1

Dark Matter: concept, evidence and characteristics

1.1 Overview and leitmotiv

This Chapter intends to provide an introduction to the main pillars constituting the present dark matter paradigm. Our intention is not only to address the most relevant aspects but also to show how the ideas in this area were formed. Therefore, in the beginning, we follow a historic perspective to achieve a more complete picture of the current situation. To be able to do this, we have followed some authors and works that guided us through this Chapter outlining its structure.

For the historical sections 1.2.1 and 1.2.2, we followed [1–3] and references therein. Regarding the dark matter astrophysical evidence, for X-ray emission in galaxy clusters (Section 1.2.2), we recommend [1, 4, 5] while for gravitational lensing (Section 1.2.2) we consulted [6–8]. Concerning the cosmological description of dark matter (Section 1.3.1), we followed primarily [9], but also [10, 11]. Furthermore, for the Thermal history of the Universe and the Big Bang Nucleosynthesis (Section 1.3.2), references [9, 12] became our pathway. For the Cosmic Microwave Background (Section 1.3.2) we considered [13, 14] while for the Section of thermal relics (Section 1.3.3), [15–17] were consulted. Finally, the particle description for dark matter (Section 1.4) is supported by [9, 18, 19].

Chapter 1 constitutes, therefore, a brief overview to provide the foundations for dark matter detection. Hence, for further details, the reader may also refer to the above references. Throughout this Chapter, we will explicitly use the words *dark matter* because the concept changes historically (both the *dark* and *matter* meanings). From Chapter 2 onwards, the abbreviation DM will be used.

1.2 Dark matter in Astrophysics

1.2.1 Before dark matter

Most of the work on the dark matter field usually relates the beginning of the concept to the astronomical discoveries in the mid-twentieth century. The work on galaxy clusters by Fritz Zwicky in 1930s [20, 21] or the work on galactic rotation curves by Vera Rubin in 1970s [22] set a precedent in the dark matter history, however, the concept has been building for a very long time.

Indeed, ancient philosophers speculated about the nature of matter and its qualities. The first noticed rational justification of matter dates back to the Atomists in ancient Greece in the fifth century BC. For the Atomists, all the matter was made by eternal, infinite in number and indivisible blocks, dubbed atoms. Some of the Atomist trends alleged that the wholeness

of the Universe was made by atoms, while others maintained that matter only included the corporeal reality. Many of these ideas went beyond other old classic schools, as in the case of the Epicureans. However, with the Aristotelian philosophy, these thoughts were abandoned. It was not until 1804 when the concept of the atom was retrieved by John Dalton, entailing the first brick of our modern particle paradigm.

Throughout the Middle Ages, the Aristotelian cosmology was the prevailing worldview, characterised by strong opposition to unknown or invisible forms of matter that could be controversial with the immutable, stable and static established Universe. With the invention of the first telescopes, at the beginning of the seventeenth century, Galileo Galilei not only questioned the Aristotelian paradigm but also opened the door to a way of thinking which would continue to the present day: the Universe contains objects that may not be noticed with our current techniques.

By the end of the seventeenth century, Isaac Newton provided, through his universal theory of gravity, what would be one of the triggers for Astrophysics and also for future dark matter evidence: the possibility of predicting the gravitational mass of an object by observing its dynamical aspects. This fact would promote the discovery of unobservable bodies in the sky extending the idea of undetected matter. However, it would still take several centuries to pass from that idea of unobservable matter to our current understanding of dark matter. Nevertheless, at the end of the eighteenth century, steps towards that direction began. Indeed, the prediction of objects so massive that light would not escape from their gravitational influence, proposed by John Michell in 1783 and discussed later by Pierre Simon Laplace starting the history of black holes.

In 1844, Friedrich Bessel conducted the first prediction of an undiscovered astronomical object studying the stars Procyon and Sirius. Bessel observed anomalies of their proper motion and assigned these irregularities to unseen massive companions. It should be kept in mind that binary stars were well known at that time. In view of this prediction, Bessel argued that considering that light is not a real property of mass, then there should be many of these dark stars. This was the driving reasoning in the Neptune discovery predicted by Urbain Jean Joseph Leverrier from the Uranus motion and observed by Johann Gottfried Galle in 1846. On the other hand, in 1862, Alvan Graham Clark and his father Alvan Clark accidentally discovered a weak massive companion predicted by Bessel almost 20 years before, Sirius B.

In the late nineteenth century, with the invention of the astrophotography, scientists were able to observe obscure clouds darkening the light of the objects behind them (what later on became known as stellar nebulae). The idea of dark stars was then extended also to other astronomical objects. At that time, scientists began to be aware of different alternatives of non-detectable matter in our Galaxy. At the end of the nineteenth century, it was proposed what is likely the main step in some of the present methods for dark matter detection. William Thomson, aka Lord Kelvin, suggested the idea of treating the stars of the Milky Way as a gas of particles under the influence of gravity [23]. This method allowed to apply the theory of gases to stars and calculate by a kinematic study the total number of stars, including the dark ones. The approach was well received by Henri Poincaré [24] who verified this argument and confirmed that the theoretical predictions were in agreement with telescope observations. In his own words,

> "*...then there is no dark matter or at least no so much as there is of shining matter.*" [24]

Even though Henri Poincaré wrote *dark matter* in his publication, the term was not referred to as the current meaning but the bulk of non-visible stars. Indeed, the concept of *dark matter* as non-visible matter inferred by its gravity was first used by Jacobus Kapteyn some years later. Kapteyn studied the velocity dispersion of stars in the Milky Way and in 1922 presented a

general theory of motion of our galaxy [25]. As the Milky Way motion model improved, some authors began to determine the dynamical density of matter in the Solar vicinity through the vertical motion of stars. First, Ernst Öpik concluded that such an oscillatory motion could be explained satisfactorily in terms of only the already known stellar population [26], and second Kapteyn estimated that the unseen mass could not be excessive. In 1932, using more-realistic kinematic models, Jan Oort studied the local matter density observing that the total density from dynamical data exceeded the density of visible stellar populations in a small proportion [27]. From these last works, astronomers started to apply the concept of non-visible matter not only to undetectable stars, as Kelvin and Poincaré conceived, but also to nebulous and meteoric matter: the notion of dark matter had begun to transform into its current meaning.

1.2.2 Evidence

a) First evidence for dark matter: from the virial theorem to the 21 cm line

The thermodynamic treatment of celestial bodies by Lord Kelvin and Poincaré together with the kinematic studies by Öpik, Kapteyn, Oort and others defined a strong line of thought that would continue along the twentieth century and, in some extent, remains until now.

In 1933, Fritz Zwicky used for the first time the virial theorem to estimate indirectly* the mass of a galaxy cluster [20]. Zwicky had observed the redshift of eight galaxies belonging to the nearly spherical Coma cluster that displayed a large velocity dispersion as was previously reported by Edwin Hubble and Milton Humason [28]. Assuming that the cluster had reached a mechanically stationary state, the application of the virial theorem

$$\langle E_{\rm kin} \rangle = -\frac{1}{2} \langle E_{\rm grav} \rangle \,, \tag{1.1}$$

where $\langle\rangle$ indicates time averaging, was straightforward. Since only line-of-sight (l.o.s.) velocities can be measured, Zwicky assumed that the galaxies were evenly distributed in a sphere of radius $R_{\rm Cl}$, then the total kinetic energy was three times the kinetic energy in one direction. The radius $R_{\rm Cl}$ was taken as $\sim 10^6$ light-years. Under these assumptions, Zwicky calculated the total potential energy of the system, $E_{\rm grav} = -(3/5)GM_{\rm Cl}^2/R_{\rm Cl}$, first estimating the mass of the Coma Cluster as a product of the number of observed galaxies and the averaged mass of each galaxy, assumed as $10^9 M_\odot$. After that, by using Eq. (1.1), Zwicky determined a velocity dispersion σ of 80 km/s, while the observed velocity dispersion over the l.o.s. was $\sim$ 1000 km/s. In order to satisfy the equilibrium, the Coma cluster needed much more mass than expected only by luminous matter. In Zwicky's own words:

"If this should be verified, it would lead to the surprising result that dark matter exists in much greater density than luminous matter." [20] †

As already indicated, this was not the first time that the word *dark matter* was used. However, it is usually taken as the starting point of the concept, setting one of the most important precedents.

Three years later, Sinclair Smith replicated the analysis for the Virgo Cluster, increasing the sample [30]. Smith assumed that galaxies were moving in a circular motion and calculated the l.o.s. projection measured for the radial velocity of 30 galaxies. By applying $M_{\rm Cl} = v_c^2 r/2G$ and dividing by the number of observed galaxies, 500, Smith obtained an average mass of $2 \cdot 10^{11} M_\odot$, much higher than that estimated by Hubble ($\sim 10^9 M_\odot$) [31].

*In reality, in this work specifically, Zwicky estimated the velocity dispersion and then drew conclusions about the mass in later works.

†Translated in [29].

In 1937, Zwicky extended the virial theorem analysis of the Coma cluster to determine the average mass of the galaxies [21]. Assuming 1000 galaxies evenly distributed in a sphere of radius $\sim 2 \cdot 10^6$ light-years, Zwicky calculated the cluster mass through

$$M_{\mathrm{Cl}} = \frac{5R_{\mathrm{Cl}} \left\langle \left\langle \sigma^2 \right\rangle \right\rangle}{3G}, \tag{1.2}$$

being $\left\langle \left\langle \sigma^2 \right\rangle \right\rangle$ the velocity averaged over mass and over time. Excluding outliers and applying the above expression, a lower limit for the average mass per galaxy was estimated in $\bar{M} > 4.5 \cdot 10^{10} M_{\odot}$. The result was unexpected when he considered an averaged luminosity for cluster galaxies equal to $8.5 \cdot 10^7 L_{\odot}$, since the obtained mass-to-light ratio, $M/L \sim 500$, was several hundred times larger than the mass-to-light ratio measured by Kapteyn in the solar neighbourhood of the Milky Way, as discussed in Zwicky's work [21]. As a consequence of these results, Zwicky considered that the Coma cluster may not have been in virial equilibrium contemplating two possibilities: either the cluster is governed by the kinetic energy and will ultimately fly apart or it is dominated by the gravitational potential, in which case there should be more unseen mass. According to Zwicky, this unseen mass would correspond either to intergalactic matter or to more massive galaxies than what is inferred by luminosity studies.

With the increase of studies on galaxy clusters, the dark matter problem extended, becoming a general issue in which different explanations were proposed. The dark matter hypothesis was neither accepted nor excluded [32]. Meanwhile, astronomers started to consider alternative possibilities about the nature of dark matter. Studies on dynamical processes in galaxy clusters concluded that the missing mass should be in the intergalactic medium and not inside the galaxy itself [33, 34]. In this regard, X-ray of the intracluster medium concluded that the dark matter problem could not be explained in terms of intergalactic gas and novel exotic possibilities started to be contemplated (see, for example, [35]).

In parallel, the history of the galactic rotation curves, which were crucial in the evolution of the concept of dark matter, was also developing. From the beginning of the twentieth century, galactic rotation curves were used to infer the mass of galaxies. In this method, the circular velocity of a galaxy is obtained, through spectroscopic observations, as a function of the distance to the Galactic Centre (GC), $v_{\mathrm{c}}(r)$. According to Newton's Second Law, such a circular velocity is expected to decrease with distance, as seen in the simplest case of a spherically symmetric potential, whose $v_{\mathrm{c}}^2(r)$ is proportional to $1/r$. Even though the first mass estimations (M31 by Hubble [39] and Oort [27]) presented the expected values, as novel studies came up, discrepancies with the Newtonian behaviour appeared. Indeed, the studies of the mass-to-light ratio of M81 and M33 by Knut Lundmark in 1931 [40] or the discovery of high values in the velocity at outer regions of M31, by Horace Babcock [41] became the departure point for unconventional explanations. Such facts were associated with extinguished stars, clouds, meteors or absorption effects in outer regions of the galaxies.

After World War II ended, some of the military radars begun to be used for scientific purposes promoting the development of radio astronomy, and consequently, significant discoveries in this field were made. The most crucial for the dark matter paradigm was the discovery of the 21 cm line of neutral hydrogen, anticipated by Hendrik van de Hulst and confirmed by Harold Ewen and Edward Purcell in 1951. Indeed, two striking events changed the history of dark matter from this fact. First of all, the estimation of the Milky Way-M31 reduced mass by Franz Daniel Kahn and Lodewijk Woltjer who knew from 21 cm observation that both galaxies were approaching each other at 125 km/s [42]. In order to estimate a lower bound for the reduced mass, Kahn and Woltjer assumed that the orbital period of the system was smaller than the age of the Universe. The value they obtained was about six times the reduced mass calculated theoretically. This fact

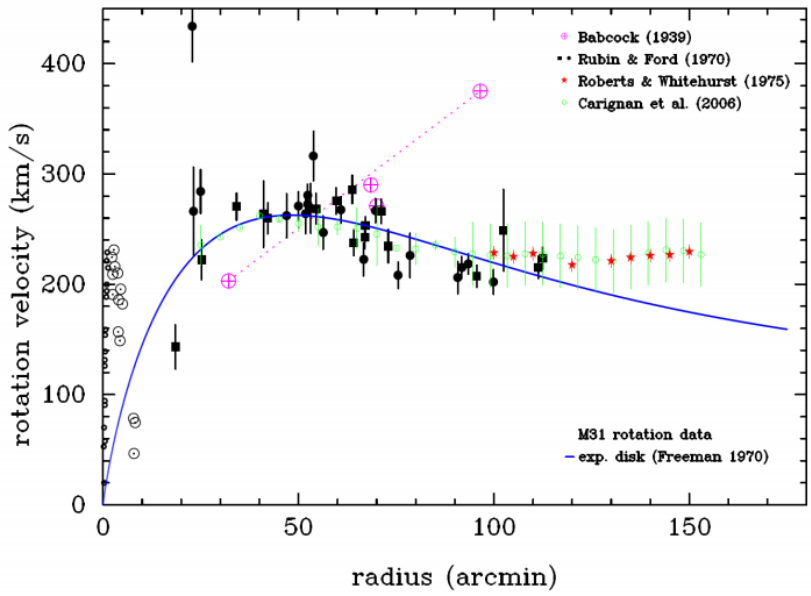

FIGURE 1.1: From Bertone and Hooper 2016 [1]. Galactic rotation curve of M31 according to different authors. In blue, the galactic rotation curve for an exponential disk alone. The data in black correspond to the optical measurement by Rubin and Ford in 1970 as a function of radius [36], while red and green points correspond to 21-cm data from Roberts and Whitehurst [37]; and Carignan respectively [38]. Points in purple correspond to the emission line data from Babcock. The image not only shows the unexpected flatness of the rotation velocity but also the great advance after the discovery of the 21 cm line.

represented one of the first forecasts of the amount of dark matter in the Local Group. Second, the 21 cm line allowed to extend the rotation curves to radii larger than the luminous disk of stars. This fact represented a significant step since the observed rotation curves at that time did not reach large enough radii to prove the presence of dark matter convincingly. With the 21 cm line discovery, many authors began to use this technique concluding that galactic rotation curves at outer regions were flat. In 1972 [37] and 1973 [43], Morton Roberts confirmed this fact observing the 21 cm line for M31, M81 and M101, and in 1978, Albert Bosma who performed an analysis of 25 galaxies [44]. Also in 1978, the infrared analysis by Vera Rubin, Kent Ford and Norbert Thonnard confirmed the flatness in the galactic rotation curve for M31 [22]. In Fig. 1.1, taken from [1], the M31 rotation curve is shown, from different authors and methods.

Under these pieces of evidence, the only direct way to skip the conflict of velocities at larger radii is assuming the presence of an unknown almost spherical population of matter. Indeed, a very simplistic but illustrative calculation of the distribution of matter along the galaxy would be by imposing the condition $v_c(r) = \text{constant}$ to

$$v_c^2(R) = \frac{GM(r < R)}{R}. \tag{1.3}$$

Considering $M(< R) \equiv 4\pi \int_0^R r^2 \rho(r) \mathrm{d}r$, the density distribution then yields

$$\rho(r) \propto \frac{1}{r^2} \tag{1.4}$$

that corresponds to what is usually dubbed an isothermal and spherical density profile. This assumption conveys a gross simplification. In fact, the question about how dark matter is

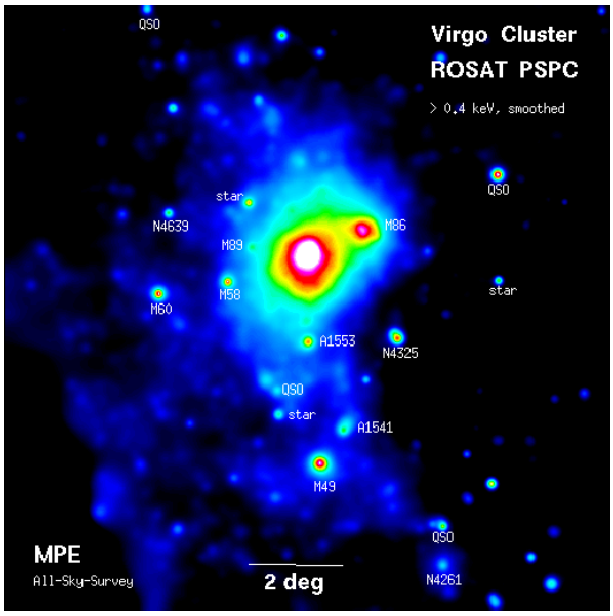

FIGURE 1.2: From Bohringer et al. 1994 [48]. Virgo cluster in X-ray observed by ROSAT. The cluster consists of a compact core region centred on M87 (white) and an expanded region in blue that reveals the irregularities and dynamics of a young cluster. It has been widely considered that the core is in hydrostatic equilibrium, enabling to trace the mass distribution and fit the dark matter density profile.

distributed constitutes an extensive investigation field, based largely, on the study of galactic rotation curves but also on the results of N-body simulations. Accordingly, elaborate models have been suggested, among them, profiles motivated by the observations of galactic rotation curves, such as Isothermal or Burkert [45], but also those coming from numerical N-body simulations, as the Navarro-Frank-White (NFW) [46] or the Einasto profile [47], became at hand.

b) Dark matter with X-ray

As commented in the previous section, with the well-established missing mass problem in the Virgo and Coma clusters, in the late 1960s, astronomers started to set limits for dark matter in the intracluster medium by the use of radio, visible and X-ray observations. X-ray observations of the hot intracluster gas become specifically important [49] since galaxy clusters appear as well resolved extended emission, with the luminosity proportional to the square of the gas density (for a review, consult [4]). The gas is not usually associated with individual galaxies but with the whole cluster, except the case in which a dominant galaxy is at the centre of the cluster [50]. Furthermore, the total mass of gas usually exceeds the mass of stars in several orders of magnitude. Thus, through X-ray observations [51–54] and under the assumption of hydrostatic equilibrium, both the gas density, the temperature and the mass of the cluster can be estimated.

With the launch of the satellites Uhuru (1970) and HEAO-1 (1977), the analysis of galaxy clusters through X-ray was consolidated. Until today, these techniques have been used to determine the mass required to bind the gas in the medium as well as the dark matter density distribution (see [53] and references therein). In general, they are applied in symmetric X-ray morphology systems with a single-phase intracluster medium to ensure hydrostatic equilibrium. The hot intracluster gas would emit X-ray photons due to the loss of energy of particles through *bremsstrahlung* (for more information consult Section 2.4.2 e)). The observations of the spectrum of the gas would allow us to determine the gas temperature $T_g(\mathbf{x})$ and the gas density $\rho_g(\mathbf{x})$ as functions of the

position. Indeed, assuming hydrostatic equilibrium one gets

$$\nabla\Phi_{\rm grav} = -\nabla P_g/\rho_{\rm g}. \tag{1.5}$$

In the previous expression, the pressure of the gas can be determined as $P_g(\mathbf{x}) \propto \rho_g T_g(\mathbf{x})$, and therefore, the gravitational potential $\nabla\Phi_{\rm grav}$ can be reconstructed. Once the gravitational potential is obtained, the enclosed mass $M_{\rm Cl}$ can be specified. In the spherical case, such a mass can be directly calculated by

$$M_{\rm Cl}(<r) = -\frac{rk_B T_g}{G\mu m_p}\left[\frac{{\rm d}\log\rho_g}{{\rm d}\log r} + \frac{{\rm d}\log T_g}{{\rm d}\log r}\right], \tag{1.6}$$

where m_p is the proton mass and μ is the effective mass of the gas constituents. Assuming a generic density profile for dark matter, it is possible to determine how accurate the fit is, under the assumption of dark matter, and reconstruct the distribution. In general, the determination of $T_g(\mathbf{x})$ and $\rho_g(\mathbf{x})$ is usually complicated and an isothermal cluster is assumed, with its gas radially distributed according to the β-profile,

$$\rho_{\rm g} = \rho_{g0}\left[1 + \left(r/r_{gc}\right)^2\right]^{-3\beta_p/2}. \tag{1.7}$$

The spatial and spectral resolution capabilities of X-ray observations have improved throughout the years, from the first generation as Einstein, EXOSAT or ROSAT to the latest one, as XMM-Newton or Chandra. The discovery of X-ray emitting gas particularly bright in Coma, Virgo and Perseus cluster gave rise to a major interest in dark matter searches around these particular systems [55]. However, X-ray studies are usually conditioned to some particular regions where the hydrostatic equilibrium can be ensured. In other words, the hydrostatic equilibrium holds locally (see discussion in [4]). For example, Virgo possesses irregularities that limit the studies to focus the X-ray study on specific locations. Originally, these studies were referred to surroundings of the predominant galaxies, as the case of M87 (see Fig. 1.2), however, it is not still clear whether some of these regions are in hydrostatic equilibrium [56, 57]. A similar debate also emerges in the case of Coma and Perseus, in which cluster masses cannot be well-determined under this assumption even when the X-ray data is highly accurate [58].

Even though the challenges to carry out the X-ray studies persist, it is well known that typical galaxy cluster masses lie between $\sim 10^{14} - 10^{15} M_\odot$, and also their luminosities around $\sim 10^{12} L_\odot$. Such orders of magnitude provide a conservative quotient between the total mass and its luminosity, a mass-to-light ratio, $M/L = 200 - 500 M_\odot/L_\odot$ implying that dark matter would be the predominant component [5].

c) Dark matter with gravitational lensing

According to General Relativity (GR), the curvature of space provoked by a massive object deflects rays of light travelling in its vicinity. In 1919, Eddington measured the light bending around the Sun for the first time, being one of the first confirmation of Einstein's theory. During the 1920s, astronomers began to consider how light moving in a curved space-time surrounding a massive object could produce multiple images of the source. However, it was not until 1937 that Fritz Zwicky suggested that galaxies would also act as gravitational lenses, distorting and amplifying background objects. Gravitational lenses have been also proposed to probe the dark matter sector, particularly at galaxy clusters scales (often as a complementary analysis of the X-ray studies mentioned above).

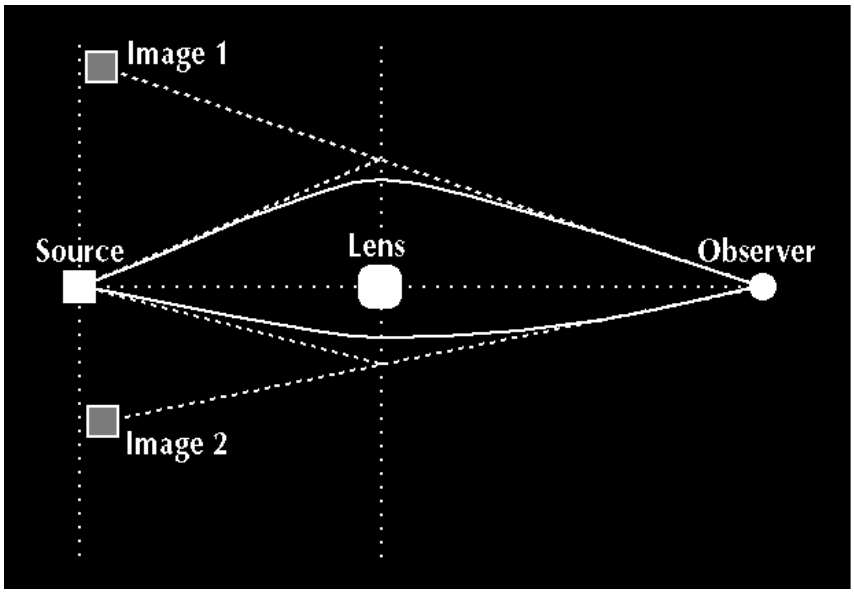

FIGURE 1.3: Image taken from [59]. Schematic representation of a gravitational lens. Light from distant objects is bound by a massive object (lens) forming images that would allow to reconstruct both its gravitational potential and thus, also, its mass distribution.

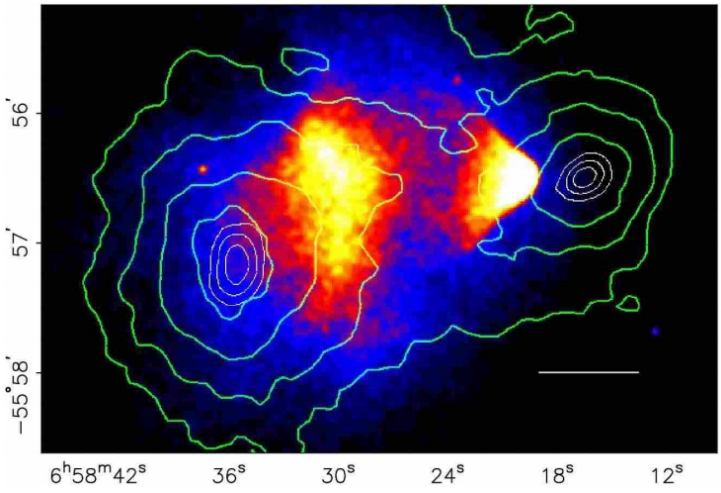

FIGURE 1.4: From Clowe *et al.* 2006 [60]. Image of the Bullet Cluster in X-ray by Chandra with the gravitational lens reconstruction. The plasma of the Bullet Cluster emits in the X-ray due to bremsstrahlung, showing that most of the content of the gas is spread at the centre of the region. However, the weak lensing reconstruction (green and white contours) allows to observe that most of the mass is separated in two regions non-detectable in the optical or infrared (typical from stars) and whose centres do not coincide with the X-rays emission. One of the most well-received explanations invokes the collision of two clusters whose gas clouds remain at the centre interacting, while dark matter, weakly interacting, would pass through without colliding. This would induce a delay between the luminous gas and dark matter that can be observed in this figure.

In Fig. 1.3, we show a simplified scheme of a gravitational lens: light coming from distant objects is affected by the gravitational potential of a massive object (lens) forming images that could be used to measure the mass of the lens and eventually to reconstruct its gravitational potential. Indeed, in the limit of the thin lens, the source position $\boldsymbol{\theta}_S$ and the observed position $\boldsymbol{\theta}_I$ are related by

$$\boldsymbol{\theta}_S = \boldsymbol{\theta}_I - \frac{D_{LS}}{D_{OS}}\boldsymbol{\alpha}(\boldsymbol{\xi}) \tag{1.8}$$

with $\boldsymbol{\xi} = D_{OL}\boldsymbol{\theta}_I$ and D_{OL}, D_{LS} and D_{OS} hold for the observer-lens, lens-source and observer-source distances respectively. Furthermore, the deflection angle $\boldsymbol{\alpha}$ is related to the gravitational potential $\Phi_{\text{grav}}(\boldsymbol{r})$ projected along the l.o.s.:

$$\boldsymbol{\alpha}(\boldsymbol{\xi}) = \frac{2}{c^2}\int \nabla_\perp \Phi_{\text{grav}}(\boldsymbol{r})\mathrm{d}z, \tag{1.9}$$

$\nabla_\perp$, being the perpendicular component of the gradient operator.

Furthermore, the mass determines the bending, and therefore, the amplification and distortion of light. It is therefore customary to distinguish between two regimes. First, in the strong lensing regime, space-time is extremely warped and light can travel along multiple paths around the mass and still be deflected back towards the observer. In addition, it is possible to see more than one image of the source formed. In fact, in this regime, constructing the model of the mass distribution turns into a great challenge. Some lenses with non-regular shapes can magnify or demagnify in different ways the multiple images of the source, or some distant galaxies can also appear as arcs. Moreover, if the bright source lies exactly along the l.o.s. of the lens, then the resultant image is an Einstein ring around the lens. Second, in the weak lensing regime, the light does not pass close to the strong gravitational lens and thus, the deflection is slight. Indeed, in such a weak approximation the distortion of resolved sources can be approximated as a locally linear transformation of the sky that includes the effects of shear, magnification and rotation.

Gravitational lensing is an independent method to calculate not only the total mass of galaxy clusters (and its distribution) but also to constrain the dark matter density profile. The estimation for the mass-to-light ratio in galaxy clusters generally satisfies $M/L > 100 M_\odot/L_\odot$ [9], which implies clusters are dominated by dark matter. Concerning the X-ray emission method, discrepancies in the mass may appear when the gravitational lens method is used instead. These are usually attributed to cluster substructures in X-ray emission or triaxiality of the three-dimensional potential.

To conclude, let us mention that one of the most claimed evidence for dark matter emerges from the study of strong and weak lensing for the Bullet Cluster [60, 61]. There (see Fig. 1.4), the gravitational lensing analysis reveals what seems to be two gravitational potentials corresponding to two galaxy clusters colliding, not detectable as luminous matter. However, the X-ray emission from the hot gas is concentrated at the centre. The explanation in terms of weakly interactive dark matter has become popular in the scientific community. In this, the image represents two galaxies colliding in which dark matter, weakly interacting, would pass through without interacting and not slowed by the impact. Instead, the interacting hot gas remains at the centre and separated from dark matter. If hot gas were the most massive component of the clusters, such a separation would not have been seen.

1.3 Dark matter in Cosmology

1.3.1 Cosmological description of dark matter

Besides the astrophysical evidence, discrepancies between matter and luminous matter have been also found in Cosmology. Based on Einstein's GR, Cosmology tries to find solutions of Einstein's equation

$$R_{\mu\nu} - \frac{1}{2} g_{\mu\nu} R = 8\pi G T_{\mu\nu} + \Lambda g_{\mu\nu} \tag{1.10}$$

to geometrically describe the Universe. In Eq. (1.10), the left- hand side accounts for the space-time geometry, described by the metric tensor $g_{\mu\nu}$, the curvature given by the Ricci tensor $R_{\mu\nu}$ and the Ricci scalar, $R \equiv g^{\mu\nu} R_{\mu\nu}$. The right-hand side corresponds to the energy-momentum tensor $T_{\mu\nu}$ and the speed of light is taken as $c = 1$. The constant Λ has been widely debated in Cosmology, introduced to obtain Einstein's static solution. When the expansion of the Universe was discovered, Λ was removed from the equation. However, it was later re-introduced to account for the explanation of the present acceleration of the Universe [62, 63].

The point of departure for the Universe description is finding a metric tensor $g_{\mu\nu}$ with the smallest number of assumptions based on data and modelling. For this, a set of principles constituting the Standard, also dubbed Concordance, Model of Cosmology has been proposed. Probably the most fundamental one is that the Universe is isotropic and homogeneous at large scales (from ~ 10 Mpc), also known as the *cosmological principle*. The condition of homogeneity comes from a large scale extension of the Copernican principle that, in general words, states that we do not lie in a special place of the Universe. This assumption combined with the isotropic hypothesis implies the cosmological principle. With respect to this latter assumption, strong indications of the isotropy of the Universe have been observed on the Cosmic Microwave Background (CMB) radiation (Section 1.3.2), although the debate still remains [64].

The cosmological principle together with the expansion of the Universe discovered by E. Hubble and V. Slipher are some of the pillars for the theoretical Cosmology formalism. Indeed, such conditions are very strong and allow us to characterise the space-time interval resulting in the Friedman-Lemaître-Robertson-Walker (FLRW) description

$$\mathrm{d}s^2 = \mathrm{d}t^2 - a^2(t) \left\{ \frac{\mathrm{d}r^2}{1 - kr^2} + r^2 \mathrm{d}\theta^2 + r^2 \sin^2\theta \mathrm{d}\phi^2 \right\}, \tag{1.11}$$

where $a(t)$ is the scale factor, $c = 1$ and k is the spatial scalar curvature in which the Universe is open if $k = -1$, spatially flat if $k = 0$ and close if $k = 1$. The reference system in such an expression lies with a comoving observer with the expansion. Once the space-time interval is explicitly set, the left-hand side of Eq. (1.10) can be fully determined. In addition, the energy-momentum $T_{\mu\nu}$ tensor is set by the space-time symmetries imposed by the cosmological principle, that correspond to the description of a perfect fluid:

$$T_{\mu\nu} = (\epsilon + P) u_\mu u_\nu - P g_{\mu\nu}. \tag{1.12}$$

In Eq. (1.12), ϵ and P are the energy density and the pressure respectively while u_μ is the 4-velocity of the fluid. Here we should remark that the content of the Universe comprises three components; radiation (or ultra-relativistic plasma), cold (or non relativistic) matter and dark energy, each of them associated to one energy density (ϵ_R, ϵ_M, ϵ_Λ) and pressure (P_R, P_M, P_Λ). In

such a way, from Eq. 1.10, it is possible to obtain the cosmological equations

$$\left(\frac{\dot{a}}{a}\right)^2 + \frac{k}{a^2} - \frac{\Lambda}{3} = \frac{8\pi}{3} G\epsilon \tag{1.13}$$

$$\frac{\ddot{a}}{a} = \frac{\Lambda}{3} - \frac{4\pi \mathrm{G}}{3}\left(\epsilon + 3P\right), \tag{1.14}$$

and from the condition $\nabla_\nu T^{\mu\nu} = 0$, the continuity equation

$$\frac{\mathrm{d}\epsilon}{\mathrm{d}t} + 3H(\epsilon + P) = 0, \tag{1.15}$$

where $H \equiv \dot{a}/a$ holds for the Hubble parameter. The form of these expressions is completely determined by the cosmological principle. The only remaining freedom is the election of the equation of state that relates the pressure P and the energy density ϵ. For all the species is usually assumed a linear relation and the equations of state yields $P_i = w_i \epsilon_i$. In the case of the radiation component $w_R = 1/3$, while for matter and the cosmological constant is $w_M = 0$ and $w_\Lambda = -1$ respectively.
Furthermore, Eq. (1.13) is usually written in the dimensionless form

$$\Omega_M + \Omega_R + \Omega_\Lambda + \Omega_k = 1, \tag{1.16}$$

where $\Omega_i = 8\pi G\epsilon_i/3H^2$ is the density parameter for radiation or matter, while $\Omega_\Lambda = \Lambda/3H^2$ and $\Omega_k = -k/(aH)^2$ are the density parameters for the cosmological constant and the curvature respectively. All the densities can be also described in terms of the quantity $\epsilon_{\mathrm{cr}} \equiv 3H^2/8\pi G$ that is the so-called critical density and represents the value of the total ρ such that the spatial curvature is null.

Eq. (1.16) allows us to concentrate all the content of the Universe in one expression written in terms of densities. For decades, cosmologists tried to calculate their values by different methods. Constraints for the density parameters have been obtained by observation of the CMB from experiments such as WMAP and PLANCK [65, 66]. With respect to the dark matter question, the main challenge from the cosmological point of view lies in measuring Ω_M and probing whether the luminous matter, usually referred to as baryonic matter, can fully explain such a value. For this, the baryonic density Ω_b has to coincide with the value Ω_M. This requires the knowledge of the baryonic abundances and understanding nuclei formation mechanisms throughout the thermal history of the Universe.

1.3.2 Cosmological evidence

a) Thermal history of the Universe and Big Bang Nucleosynthesis

According to the above discussion, in this section we will comment the generalities to obtain Ω_b. Indeed, in the previous section we presented expressions for an expanding Universe, including the continuity equation

$$\frac{\mathrm{d}\epsilon}{\mathrm{d}t} + 3H(\epsilon + P) = 0. \tag{1.17}$$

A thermodynamic treatment of Eq. (1.17) provides significant information when the energy $U \equiv \epsilon V$ and the volume (proportional to the expansion rate), $V \propto a^3$, are defined. Comparing Eq. (1.17) with the first and second law of thermodynamics $T\mathrm{d}S = p\mathrm{d}V + \mathrm{d}U$, it is immediate to obtain $\mathrm{d}S = 0$, implying that the Universe is expanding adiabatically and, therefore, in

equilibrium state at each instant. In general, this only occurs when either there is no interaction between different species (particles) in the Universe or when the rate of interactions between them is high, reaching the thermal equilibrium. The latter case can be expressed as

$$\Gamma \gg H, \tag{1.18}$$

indicating that the interaction rate Γ is larger than the expansion rate H, being $\Gamma \equiv \langle n\sigma v_{\rm rel}\rangle$, v_{rel} the relative velocity of interaction, n the particle number density and σ its cross section. This provides an intuitive idea of how different species behaved in the early Universe. At the very beginning, when $\Gamma \gg H$, all the particles were in thermal equilibrium in a primordial plasma. As the Universe expanded, the condition $\Gamma \sim H$ was reached for one of the species and then it decoupled from the rest, fixing its cosmological density at that time (freeze out). Indeed, when $\Gamma \sim H$, there is a break of the chemical equilibrium and, therefore, of the thermodynamic equilibrium, thus, Eq. (1.17) would not take place. Instead, the limit of disequilibrium requires to be described by the Boltzmann equation, such that for the interaction of particles $1+2 \leftrightarrow 3+4$ can be written as follows

$$\frac{1}{a^3}\frac{\mathrm{d}\left(n_1 a^3\right)}{\mathrm{d}t} = n_1^{(0)} n_2^{(0)} \langle\sigma v\rangle \left(\frac{n_3 n_4}{n_3^{(0)} n_4^{(0)}} - \frac{n_1 n_2}{n_1^{(0)} n_2^{(0)}}\right), \tag{1.19}$$

where n_i and $n_i^{(0)}$ are, respectively, the particle number density and the value at equilibrium for the species i. Eq. (1.19) is valid both for bosons and fermions. The term $\frac{1}{a^3}\frac{d\left(n_1 a^3\right)}{dt}$ can be easily related with the left side of Eq. (1.17) and $\langle\sigma v\rangle$ is the thermally averaged cross section defined by

$$\langle\sigma v\rangle \equiv \frac{1}{n_1^{(0)} n_2^{(0)}} \int \frac{\mathrm{d}^3\mathbf{p}_1}{(2\pi\hbar)^3 2E_1} \int \frac{\mathrm{d}^3\mathbf{p}_2}{(2\pi\hbar)^3 2E_2} \int \frac{\mathrm{d}^3\mathbf{p}_3}{(2\pi\hbar)^3 2E_3} \int \frac{\mathrm{d}^3\mathbf{p}_4}{(2\pi\hbar)^3 2E_4} \cdot$$
$$(2\pi)^4 \delta^{(3)}\left(\mathbf{p}_1 + \mathbf{p}_2 - \mathbf{p}_3 - \mathbf{p}_4\right) |\mathcal{M}|^2 \mathrm{e}^{-(E_1+E_2)/(k_{\rm B}T)} \tag{1.20}$$

with $\mathcal{M}$ the amplitude for such an interaction.

Eq. (1.19) is equally applicable to the case of non-thermal equilibrium, but also recovers the case of thermal equilibrium in which either particles do not interact at all ($\langle\sigma v\rangle \to 0$) or they highly interact under the condition

$$\frac{n_3 n_4}{n_3^{(0)} n_4^{(0)}} = \frac{n_1 n_2}{n_1^{(0)} n_2^{(0)}}, \tag{1.21}$$

which is usually called the Saha equation.

As stated above, the species abundances throughout the history of the Universe can be estimated through the particle number density n_i by solving Eq. (1.21) for thermal equilibrium and Eq. (1.19) for non-thermal equilibrium. Both equations allow us to calculate the relative abundances of the primordial plasma species. In the computation of abundances two limits are usually considered [‡]. That one in which particles are non-relativistic ($m_i >> T$) so that the number density in equilibrium is exponentially suppressed by $n_i = n_i^{(0)} \sim (m_i T)^{3/2}\, \mathrm{e}^{-m_i/T}$ and the relativistic case ($m_i << T$) with $n_i = n_i^{(0)} \sim T^3$. The former expression indicates that non-relativistic particles that remain for a long time in thermal equilibrium would decrease their number density until zero. Instead, if their interaction freezes-out at a temperature close to their mass, the species can have a significant abundance today.

[‡]There also exists the semi-relativistic case, in which the thermally averaged cross section $\langle\sigma v\rangle$ is interpolated from the relativistic to the non-relativistic regime.

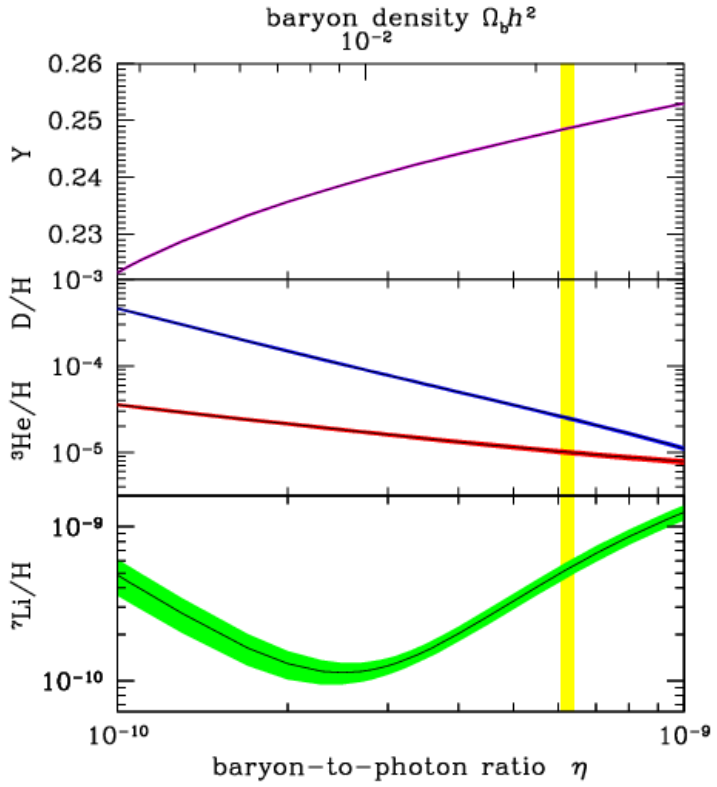

FIGURE 1.5: Taken from Cyburt 2008 [67]. Abundances of the lightest elements, D, ^{3}He, ^{7}Li with respect to H, and the mass fraction of ^{4}He as a function of the baryon-to-photon ratio. The yellow band corresponds to the WMAP measurements that coincide with the predicted abundance elements. In the plot is possible to see that such coincidence provides an $\Omega_b h^2$ close to 0.02.

Going back in time, when the temperature was extremely high, massive species such as atomic nuclei could not form. Indeed, when $T >> 1\,\text{MeV}$ the primordial plasma was constituted by photons, electrons, positrons, neutrinos, antineutrinos, protons and neutrons. All of them were in thermal equilibrium and radiation dominated. At $T \sim 1 - 0.7\,\text{MeV}$, neutrinos decoupled from the thermal plasma since weak interactions cannot sustain the thermal equilibrium. Therefore, protons and neutrons also deviate from such an equilibrium through the β-decay reaction, in which the number of neutrons started to decrease. In this epoch, also another fraction of those neutrons could be captured by protons forming deuterium at $T \sim 0.7 - 0.05\,\text{MeV}$. This process had to occur when the radiation density of the medium was low and the photodissociation avoided. Deuterium nuclei interacted themselves forming ^{3}He, that subsequently interacted with deuterium to form ^{4}He. The increase of the Coulomb barrier for nuclei of atomic mass larger than ^{4}He together with the drop in the temperature and density indicates why there are no significant nuclei beyond He in a large proportion (for example, ^{3}Li). Finally, the remaining free neutrons decayed being the end of the Big Bang Nucleosynthesis (BBN). As the temperature of the Universe remains large in comparison to the hydrogen ionization energy, matter is ionised and photons are coupled to electrons through Compton scattering. When the temperature is close to 13.6 eV, radiation decouples from matter and photons propagating free by constituting fossil radiation called the CMB.

The complete description of how baryons formed widely exceeds the objective of this thesis. However, let us remind that the procedure is focused on the chain of reactions of each nucleus and the computation of the Saha or the full Boltzmann equation, considering the effective

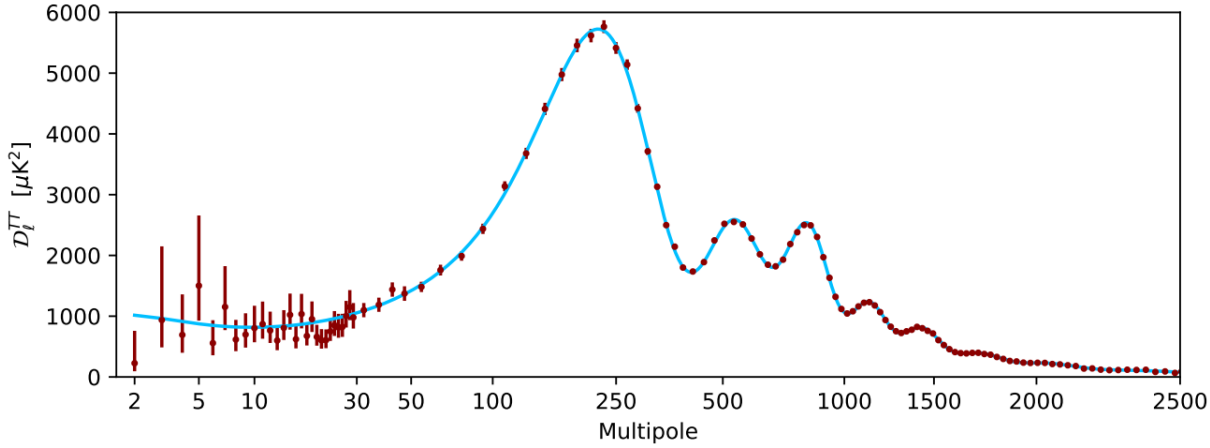

FIGURE 1.6: The angular power spectra of the CMB measured by Planck in 2018 [69].

number of degrees of freedom of species, dubbed g_*. We would like to conclude this discussion by remarking two significant facts with regard to the BBN. The first one is that it is possible to calculate the baryon-to-photon ratio n_b/n_γ, showing that there are a billion photons for each proton and electron, producing the so-called deuterium bottleneck, in which photons with energy higher than 2.2 MeV are able to destroy newly formed deuterium nuclei. The second is that, according to BBN data baryonic matter reveals an $\Omega_b h^2 \simeq 0.02205 \pm 0.00028$ as measured with high precision by WMAP [68] (Fig. 1.5), a value that only corresponds to $\sim$ 5% of the total content of the Universe.

b) The Cosmic Microwave Background

As already mentioned in Section 1.3.2, thermal photons at temperatures close to the hydrogen ionization decouple from matter propagating along the expanding Universe and constituting fossil radiation called CMB. CMB radiation is the smoking gun of the last scattering surface in the primordial Universe. Predicted by Ralph Asher Alpher and Robert Herman in 1948, the CMB was confirmed by Arno Penzias and Robert Wilson who detected an unexpected signal in all directions. The temperature of the CMB is defined as the averaged temperature of the whole sky

$$T_{\gamma 0} = \frac{1}{4\pi} \int T(\theta, \varphi) \sin\theta \mathrm{d}\theta \mathrm{d}\varphi. \tag{1.22}$$

Years later, the COBE/FIRAS experiment measured the isotropic signal with accuracy $T_{\gamma 0} = 2.725 \pm 0.001$ K, revealing that the spectrum is close to that of a black-body one. This is an evidence that photons could have been thermalised before decoupling due to the interactions with electrons. However, at the redshift of decoupling, radiation would not have had time to be thermalised, and energy injection due to the interaction of matter and photons would deviate the CMB spectrum from the expected black-body spectrum. Therefore, anisotropies from the background were expected, revealing information about that energy injection.

New estimations of the CMB by COBE (1992) [71], WMAP (2003) [72] and Planck (2013) [73] showed such fluctuations. The most visible one appeared around the order to mK scale, where a dipole is observed. This effect is compatible with the motion of the Solar System and the Milky Way with respect to the CMB rest frame, and therefore, is removed. As the observations improved, CMB anisotropies showed at the scale of the μK. To explain such anisotropies in the

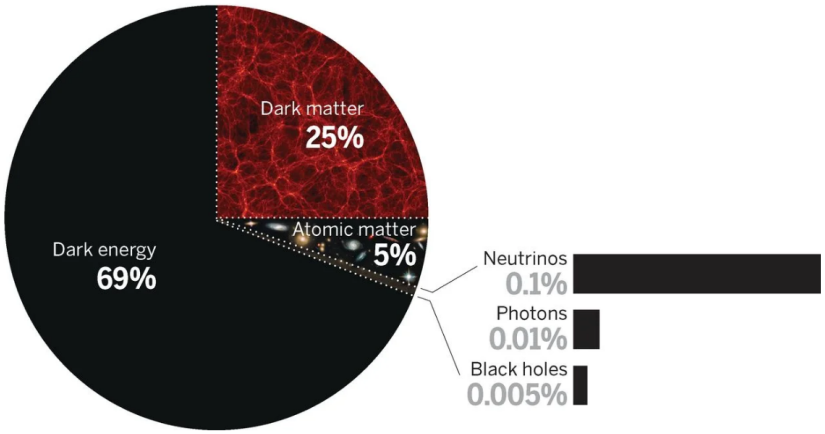

FIGURE 1.7: From Spergel 2015 [70]. Schematic representation of the energy densities of Eq. 1.16 with the methods discussed in sections 1.3.2 and 1.3.2. In this figure, Ω_M has been split into Ω_b (atomic matter in the figure) and Ω_χ (dark matter in the figure). According to the cosmological perspective, the amount of dark matter not only would not coincide with the amount of luminous matter but also is much larger.

sky, some observables were studied in terms of spherical harmonics such as

$$\frac{\delta T(\theta,\phi)}{T_{\gamma 0}} = \sum_{lm} a_{lm} Y_{lm}(\theta,\phi). \tag{1.23}$$

By subtracting foreground effects such as dust, galactic emission, synchrotron or free-free scattering (very different from the Planck spectrum), it is possible to do a study of the remaining anisotropies through power spectrum analysis.

In Fig. 1.6, we present an image of the CMB power spectrum measured by Planck [69] with three well-distinguished regions. First, the Sachs-Wolfe plateau in the almost horizontal region of $l \lesssim 100$ (where l corresponds to the l^{th} multipole), where photons decoupled from a non-zero gravitational potential, would experience an additional redshift and a delay in the release of the radiation. Second, the acoustic peaks, in the range of $100 \lesssim l \lesssim 1000$. Indeed, when the proton-electron plasma was tightly coupled to the photons, these components behaved as a single photon-baryon fluid, with the photons providing most of the pressure. Baryons collapse due to gravity onto regions where the density is higher than average while radiation pressure from photons resists collapse producing oscillating cycles on all scales. The cools in the expansion and heats in the compression creating fluctuations in the temperature of the CMB. Once photons and baryons decouple, oscillations stop and such temperature fluctuations remain imprinted. Third, the damping tail for $l \gtrsim 1000$, which takes into account the effects of non-instantaneous recombination.

The power spectrum, particularly the shape and location of each peak, highly depends on the combination of the cosmological density parameters Ω_b, Ω_M and Ω_Λ. Indeed, it is possible to determine the proportion of each energy density through measurements of the CMB. Fig. 1.7 is a scheme with the proportions of the different contents of the Universe. Among them, Ω_M from PLANCK [69] estimated in $\Omega_M = 0.315 \pm 0.017$, constituting 31% of matter contents of the Universe while the baryonic content estimated by BBN is 5%. With the idea that not all the matter content is baryonic, clues about a cosmological description of dark matter are opened. Furthermore, according to this result, baryons would not be sufficient to explain the dark matter component. That means that unseen massive objects, as the dark stars proposed from the end of

the eighteenth centuries would not be suitable to explain the dark matter content.

1.3.3 The WIMP miracle

In Section 1.3.2, we showed the discrepancies between the values for Ω_M and Ω_b. Thus, the remaining dark matter content in Ω_M requires to be investigated as a new species coupled to the primordial plasma in the early Universe. The decoupling of dark matter is then explored by assuming a stable massive particle χ that is initially in thermodynamic equilibrium. The main interaction undertaken for dark matter *relics* would be the annihilation into lighter particles (l) represented as

$$\chi + \overline{\chi} \longmapsto l + \bar{l}, \tag{1.24}$$

where bar means antiparticle. A relic is usually referred to as the residual abundance of certain species once the interaction abandons the thermodynamic equilibrium. The reason to consider non-relativistic massive particles as dark matter candidates lie in the fact that relativistic ones would not produce the pattern of galaxies observed in the Universe. Indeed, relativistic species would erase matter density perturbations through free-streaming, smoothing out any fluctuations and precluding the formation of clumps that becomes the seed of small galaxies. While the predictions of relativistic dark matter particles, like neutrinos, disagree with observations of structures, the non-relativistic cold dark matter scenario seems to reproduce the observations [§]. Under the non-relativistic dark matter assumption, it would be possible then to observe whether dark matter can explain the present Ω_M. In order to do that, the Boltzmann equation

$$\frac{1}{a^3}\frac{\mathrm{d}\left(n_\chi a^3\right)}{\mathrm{d}t} = \langle\sigma v\rangle\left(n_\chi^{(0)2} - n_\chi^2\right) \tag{1.25}$$

is solved under the assumption $n_l^{(0)} = n_l$ (light particles are still coupled to the primordial plasma at the temperature of the dark matter decoupling). Eq. (1.25) can be rewritten in terms of the variable $Y_\chi = n_x/s$ and $x = M/T$, where s is the entropy per unit of volume, then

$$\frac{\mathrm{d}Y_\chi}{\mathrm{d}x} = \frac{1}{3H}\frac{\mathrm{d}s}{\mathrm{d}x}\langle\sigma_A v\rangle\left(Y_\chi^2 - Y_{\chi,eq}^2\right), \tag{1.26}$$

which is solved numerically.

In Fig. 1.8, we show a scheme with the solutions of Eq. (1.26), where the generic picture for dark matter decoupling can be appreciated. The solutions qualitatively follow the already mentioned behaviour: cold dark matter particles would be initially in thermal equilibrium in a process of annihilation, coupled with photons and matter with which $Y_\chi(x) = Y_{\chi,eq}(x)$. Since the interaction rate Γ decreases with the temperature, at some point it matches the expansion rate at $x = x_f$, at which time the particle decouples from the rest of species and the abundance remains frozen. This is the case of solid lines in Fig. 1.8. The initial abundance is not relevant for the final relic density. The latter only depends on dark matter abundances at the moment of freeze-out, or in other words, on the thermally averaged cross section defined in Eq. (1.20). The relic density measured by Planck is shown in the figure with a grey line and correspond to a thermally averaged cross section equal to $(2-3)\cdot 10^{-26}\mathrm{cm}^3/\mathrm{s}$ [¶]. Provided the annihilation is smaller than that value, then dark matter freezes out earlier and the relic density observed today would be larger (red line). Instead, in the case in which the thermally averaged cross section is larger, the decoupling from the plasma happens later in time (so temperature decreases) and then, according to $n_i = n_i^{(0)} \sim (m_i T)^{3/2} e^{-m_i/T}$, the present abundance is smaller. For illustrative

[§] Even though observations cannot rule out the whole dark matter being semi-relativistic, there exist strong constraints from observations from Lyman-α data [74, 75].

[¶] Hereafter, we will assume such limit in $3\cdot 10^{-26}\mathrm{cm}^3/\mathrm{s}$.

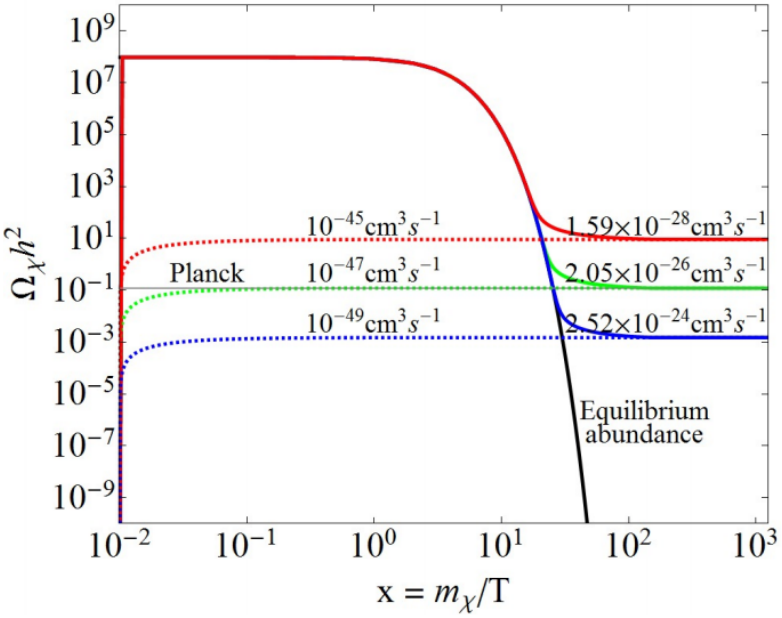

FIGURE 1.8: From PS Dev 2013 [16]. Evolution of the cosmological dark matter density for non-relativistic dark matter, with a mass 100 GeV, according to two scenarios. The first scenario, represented by solid lines in colors, accounts for the freeze-out mechanism in which dark matter is in thermal equilibrium with the primordial plasma until decoupling with a specific thermally averaged cross section. Second, represented by dotted lines, the freeze in mechanism in which there exists a dependency between the primordial dark matter density (no thermal equilibrium with the plasma) and the dark matter density today. The black solid line represents the expected density for a non-relativistic particle that would continue in thermal equilibrium with the plasma.

purposes, Fig. 1.8 shows the case of a thermal relic equal to $M = 100\,\text{GeV}$. Therefore, taking the asymptotic value Y_χ when x tends to infinity, it is possible to calculate the value of the dark matter relic density today. Indeed, the density is approximately

$$\frac{\Omega_\chi h^2}{0.12} \simeq \frac{0.1c\,\text{pb}}{\langle\sigma v\rangle}. \tag{1.27}$$

As already mentioned, the value of the thermally averaged cross section times velocity able to fit the present Ω_M related to Ω_χ is $3 \cdot 10^{-26}\,\text{cm}^{-3}/\text{s}$. According to the Fermi's theory, the mass of a particle for such a cross section, proportional to $\sim G_F^2 M_\chi^2$, is $\sim 100\,\text{GeV}$ can be accommodated in the range of weak interactions. This fact, that allows us to interpret a Weakly Interactive Massive Particle (WIMP) as dark matter. This is the so-called WIMP miracle.

Besides, as we mentioned above, in Fig. 1.8 there is another situation also to be contemplated. If the annihilation rate is not sufficiently large to keep the full thermodynamic equilibrium but dark matter still couples weakly with the plasma, then such a plasma still populates the dark matter until $\Gamma \ll H$ and the dark matter freezes in. In this case, the final density not only depends on the annihilation rate but also on the initial abundance at the beginning.
Both cases of Fig. 1.8 are referred to as thermal dark matter [16], i.e., dark matter either highly coupled (in thermal equilibrium) or weakly coupled (non-thermal case) with the primordial plasma. This fact implies a maximum limit on the thermally averaged cross section for thermal relics of $3 \cdot 10^{-26}\text{cm}^3/\text{s}$.

1.4 Dark matter in Particle Physics

Throughout this chapter, we analysed the dark matter concept from different points of view. Specifically, in Section 1.3.3, we commented about the possibility of connecting a cosmological dark matter description with a Particle Physics counterpart that is able to fit the Ω_M today. However, none of the Standard Model (SM) particles provides a dark matter candidate with these characteristics. Extensions of the SM have been proposed with the aim of considering such a kind of particles but also, in most of the cases, to solve some of the issues found in an incomplete SM of Particle Physics.

In the previous section, the main motivation to focus on non-relativistic dark matter lied in the fact that the structures in the Universe, mainly simulated on N-body numerical codes, can be well explained. However, other possibilities for dark matter can be also contemplated. In this Section, we will mainly focus on non-baryonic dark matter since both BBN (Section 1.3.2), gravitational lensing (Section 1.2.2) or also the large scale structure presents strong arguments against baryonic dark matter. According to [9, 19], there are three possible general ways of classifying non-baryonic dark matter.

- First, a classification performed on the basis of the dark matter mass comparable to the temperature when galaxy forms ($T \sim 1\,\mathrm{keV}$). If particles have a mass, $M << 1\,\mathrm{keV}$, then they are called *hot dark matter* (e.g., light neutrinos), for masses $M \sim 1\,\mathrm{keV}$ are *warm dark matter* (e.g., sterile neutrinos or gravitinos) and particles with $M >> 1\,\mathrm{keV}$ are *cold dark matter* (e.g., neutralinos, axions, WIMPZILLAs and solitons). Hot dark matter was relativistic at the time of galaxy formation and consequently escaped from the formed structures preventing the formation of small structures. Cold dark matter was non-relativistic when galaxies formed, and due to its negligible pressure, it was able to collapse effectively under gravity influence. Warm dark matter is an intermediate case.

- Second, a classification based on the production mechanism distinguishing between *thermal relics*, i.e. particles which were coupled with the primordial plasma in the Early Universe (e.g., neutrinos or neutralinos) or *non-thermal* relics that never had the possibility of thermal equilibrium (e.g., axions or WIMPZILLAs).

- Third, a classification that depends on how the candidate is included or not within the Particle Physics framework. Among them, we have the *existing candidates* (e.g., neutrinos), *candidates that are motivated* but not observed (e.g., axion and light supersymmetric particles), i.e. candidates that would solve a Particle Physics problem not related with dark matter, and also *exotic candidates* (e.g., WIMPZILLAs).

1.4.1 Dark matter candidates

In this Section, we will focus on some of the most notorious candidates mentioned above and describe them from a general point of view.

a) Active neutrinos

SM neutrinos would be the lead example for dark matter that has already been discovered [76]. Indeed, they are electrically neutral and stable particles, but also weak interacting. By observing indirectly the neutrino flavour oscillations, we know that at least two neutrinos have non-vanishing mass. Indeed, the estimation of their total relic density is

$$\Omega_\nu = \frac{\epsilon_\nu}{\epsilon_c^0} = \frac{\sum_i m_i}{93.14 h^2 \mathrm{eV}}, \tag{1.28}$$

where m_i is the mass of a particular neutrino (ν_e, ν_μ, ν_τ). The tightest constraints come from the Planck collaboration setting $\sum m_\nu < 0.194\,\text{eV}$ [66], that implies an upper bound of $\Omega_\nu h^2 \lesssim 0.004$, showing that neutrinos are not abundant enough to constitute the dark matter dominant component. This fact also has been indicated by N-body simulations. In fact, neutrinos are one hot dark matter candidate and, as already mentioned, they would not accommodate an explanation of the observed structures in the Universe. Neutrinos are able to erase fluctuations due to their free-streaming length slowing down the growth of gravitational potential wells. Furthermore, neutrinos would lead to an alternative formation history where big structures form first from a huge gas cloud larger than the resulting galaxy. The main difficulty of this particular hierarchy formation is that galaxies would take a long time to form, which would contradict high redshift observations showing early onset of galaxy formation. Second, these theories predict a significant galaxy formation going on today, which is in contradiction to observations. Therefore, even though neutrinos may be dark matter candidates, they are not able to explain the whole dark matter composition.

b) Heavy neutrinos

In the SM, the fermion masses are generated by the Higgs field through the coupling of their right and left chiral states. Since experimental evidence indicates that neutrinos (antineutrinos) only come in left-handed (right-handed), theoretically they should be massless. However, as already mentioned, observations of Sun, atmosphere, reactors and accelerators show that their flavours change in their propagation corresponds to three different neutrino masses. With the exception of neutrinos, the rest of the fermions have both left- and right-handed chiral states. Therefore, one of the possible approaches to explain the neutrino masses is extending the SM by adding right-handed neutrinos and assuming they are Dirac fermions. Indeed, the Lagrangian would include the term

$$\overline{\nu_L} m_D \nu_R + h.c. \tag{1.29}$$

This right-handed neutrino would not have colour or electromagnetic charge like left-handed neutrinos, but also they would not have weak interactions either, since only left-handed chiral fermions couple to the W and Z bosons. Those are the so-called sterile neutrinos (for a review, consult [77]), that would act as dark matter candidates. Conversely, unlike charged leptons and quarks, neutrinos, without a charge, may be also a Majorana fermion whose mass term yields

$$\frac{1}{2}\overline{\nu_L} m_L \nu_L^c + \frac{1}{2}\overline{\nu_R} m_R \nu_R^c + h.c. \tag{1.30}$$

and would violate the lepton number conservation. The general treatment consists of including in the Lagrangian both Majorana and Dirac terms for different neutrino generations. Such a neutrino model would not only explain why the neutrino is massive but also the "mass puzzle", i.e., the fact that the neutrino mass is many orders of magnitude smaller than other SM fermion. This would enable us to understand the low mass in SM neutrinos via the seesaw mechanism: heavier masses for the sterile neutrinos lead to lighter masses for the active ones. This fact would open the possibility with different dark matter candidates and different masses.

c) Axions

Suggested by Peccei and Quinn (1977) [78, 79], axions have been proposed to solve the strong CP problem in QCD in which the term

$$\mathcal{L}_\theta = -\frac{\overline{\theta} g^2}{64\pi^2} \epsilon^{\mu\nu\rho\sigma} G^a_{\mu\nu} G^a_{\rho\sigma} \tag{1.31}$$

violates parity and time reversal (for review, consult [80, 81]). Instead, CP experiments have not been observed CP violation in QCD. In particular, the term in Eq. (1.31) violates the CP symmetry inducing a neutron electric dipole moment with a magnitude $|d_{\rm n}| \sim 10^{-16}\overline{\theta}\, e$cm, when the experimental limit is $|d_{\rm n}| < 6.3 \times 10^{-26}\, e$cm, being e the electron charge. In principle, there is no reason to expect such a small value of $\overline{\theta}$. The question of why the angle $\overline{\theta}$ should be nearly zero despite the CP violation is the so-called strong CP problem. Peccei and Quinn introduced a dynamical quantity, the axion field, assuming that there is a global symmetry $U(1)_{PQ}$. Such an axion field would mimic the $\overline{\theta}$ parameter making it zero in the low energy Lagrangian. At some levels of energy, the $U(1)_{PQ}$ symmetry would be spontaneously broken resulting in a light pseudo-Nambu-Goldstone boson called axion. Axions are expected to be spin-zero whose mass is determined by one parameter, $f_{\rm a}$,

$$m_{\rm a} \simeq 6 \times 10^{-6}\text{eV} \left(\frac{10^{12}\text{GeV}}{f_{\rm a}}\right) \tag{1.32}$$

that characterises the scale of the symmetry breaking. Even though they are light, i.e, masses generally around 0.01-1 meV, axions are postulated as cold dark matter, produced out of thermal equilibrium [82]. Three production mechanisms have been proposed for cold axions: vacuum realignment [83], string decay [84] and domain wall decay [85].

The original Peccei-Quinn axion prototype was ruled out [86]. However, models with a higher symmetry breaking scale have been proposed. Some particularities in the axion phenomenology usually make them suitable in their searches. Indeed, axions present different ways of couplings. Among them, on the one hand, axion couple to two photons allowing their decay through an effective coupling $g_{a\gamma\gamma}$. Furthermore, axions can oscillate into photons in the presence of a magnetic field, which is usually called the axion conversion. Axions phenomenology opens a wide variety of strategies enabling us to constrain their parameter space. Some of the experiments to detect Axions are ADMX, CAST or PVLAS.

d) Supersymmetric particles

Supersymmetric particles, from the supersymmetry theories (SUSY), are one of the best motivated dark matter candidates. SUSY emerges as the only possible generalisation of the Poincaré group in quantum field theories through a symmetry that associates fermions with bosons and vice versa (for more details, see for example [9, 88, 89]). The generator of the symmetry would be a fermionic operator Q that increases 1/2 the spin of a particle such as

$$Q|\text{ boson }\rangle = |\text{ fermion }\rangle \qquad \text{and} \qquad Q|\text{ fermion }\rangle = |\text{ boson }\rangle, \tag{1.33}$$

implying that each particle state has at least a superpartner.

SUSY has been claimed to solve three open questions in Fundamental Physics. First, the unification of fundamental forces. Indeed, the coupling constants of electromagnetic, weak and strong interactions are close to joining at high energies (Fig.1.9). Increasing the number of particles that contributes to interactions, it is possible to join the coupling constants with the energy beyond the SUSY-breaking scale. Second, SUSY also helps to protect the masses of fundamental scalar particles from divergences, contributing with opposite sign to the loop corrections and cancelling them, as in the case of the Higgs boson. Third, it provides a set of heavy particles that could be accommodated as dark matter candidates whose coupling would occur at very high scales.

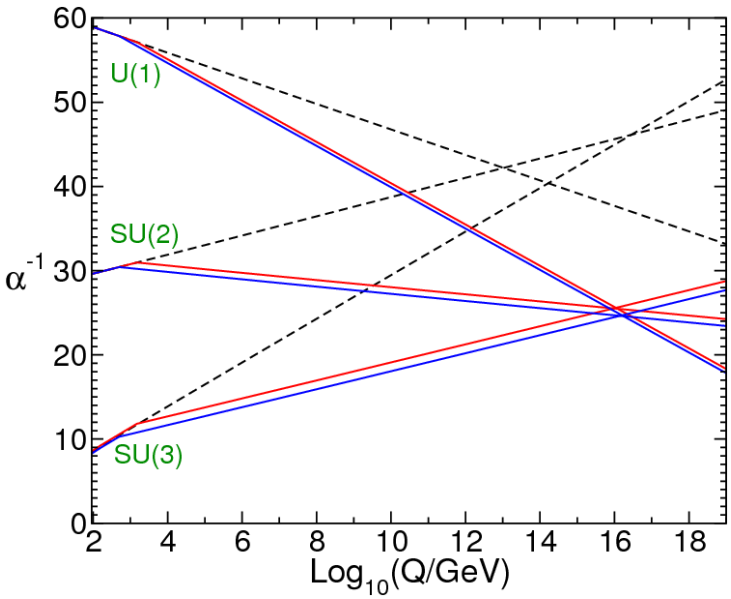

FIGURE 1.9: From [87] Coupling constants of electromagnetism ($U(1)$), weak ($SU(2)$) and strong ($SU(3)$) almost join at high energies but not exactly, as seen in the black dashed lines. SUSY allows us to join them by the addition of the number of particles that contribute to that interaction. In particular, the solid lines in red and blue represents the MSSM framework with different opening thresholds of supersymmetry

Among these candidates, probably the most well-known is the neutralino described within Minimal Supersymmetric Standard Model (MSSM). The MSSM introduces only one supersymmetry, (N=1 SUSY) assigning a vector multiplet to each gauge field and a chiral multiplet to each matter field present in the SM. In the MSSM, the baryon and lepton numbers are not conserved by all of the renormalisable couplings in the theory. In particular, this implies a fast proton decay by many orders of magnitude with respect to the current limits ($\sim 10^{34}$ yrs). The R-parity symmetry

$$R = (-1)^{3B+L+2s} \tag{1.34}$$

was proposed to forbid this fact. In Eq. (1.34), B is the baryon number, L is the lepton number and s is the spin, which implies that all the SM particles have $R = +1$ and their superpartners have $R = -1$. A consequence of the R-parity preservation is that the lightest SUSY particle has to be stable since it cannot pass from a state with $R = -1$ to the state $R = +1$. The name of this particle, is a natural candidate for WIMP called neutralino.

Even though we only focused on the case of neutralino, there also exist other dark matter candidates in SUSY as the sneutrinos (with masses between 500 GeV and 2 TeV), gravitinos (masses from eV to GeV) or axinos (masses $\sim$ keV).

e) Extra-dimensional candidates

With the aim of solving some of the open questions in Physics (grand unification without SUSY, hierarchy problem, novel sources of CP violation or dark matter candidates among others) some authors propose theories with extra dimensions. In many of these scenarios, our Universe would be a $(3+1)$-dimensional hypersurface called a brane that is embedded in a higher $D = 1 + (3 + \delta_D)$ dimensional space, the bulk. Depending on the specific theory some of the SM fields would be either only confined in the $(3+1)$-dimensional brane or they would propagate in all the dimensions [90–92].

Extra-dimensional theories emerged in the context of the unification of electromagnetism and gravity. At beginning of the twentieth century, Kaluza (1921) and Klein (1926) proposed the addition of one extra dimension to the usual (1+3) space-time and obtained, under some specific assumptions on the geometry, the Einstein and Maxwell equations together with one unidentified component that could be associated to a gauge scalar field. The answer to the question as to why we are not able to observe such an extra dimension was implicit in its assumed geometry: the extra dimension is unobservable because it is compactified (Kaluza and Klein proposed circles for that compactification) and its longitude is around the Planck scale $(1/M_P)$. Due to such a compactification, all the fields propagating in the extra dimensions can be expanded in Fourier modes, the Kaluza-Klein states, with respect to the periodic dimension. Indeed, the field can be decomposed into an infinite tower of 4-dimensional modes with masses $m_n^2 = n^2/R_5^2$. Since R is small, the masses associated with each mode are very large ($\sim M_P$) and thus it would not be accessible to experiments with the present precision.

Over time, different extensions of Kaluza-Klein theory emerged [93, 94]. We briefly show two lines of reasoning. First, those in which the branes do not exist and all the SM fields propagate in the whole extra dimensions. This is the case of universal extra dimensions (UED) [95]. In this model, the K-parity $(-1)^{|n_{KK}|}$ is conserved (here n_{KK} is the Kaluza-Klein quantum number), making at least one of the Kaluza-Klein first field excitations stable if the K-parity is conserved, similar to the R-parity in SUSY. The lightest one is the LKP (from Lightest Kaluza-Klein particle) whose range of masses from few GeV to few TeV and it is postulated as a possible dark matter candidate.

Second, the Brane-World scenarios in which the SM fields would only propagate in (3+1)-dimensional brane while the gravity interaction is extended to higher dimensions, the bulk space. Such formalisms would be able to explain the hierarchy problem in physics. Here we will focus on Large extra dimension models (for Randall-Sundrum ones see Ref. [96, 97]). In the original idea by Arkani-Hamed Dimopoulos Dvali model (ADD model) [90–92], as mentioned, the SM fields would be confined in a brane maintaining their usual behavior, while gravity propagates in a bulk usually compactified in toroids (although other topologies are possible) of radius R_B. In such a framework, the fundamental scale of gravity would not correspond to the Planck scale M_P but another scale M_D given by

$$M_P^2 = V_{\delta_D} M_D^{2+\delta_D} \tag{1.35}$$

where V_{δ_D} is the volume of compactified extra dimensions and defined as $V_{\delta_D} = 2\pi R_B$ in the toroidal case (see, e.g., [98]). The volume produces a dilution in the strength of gravity. In the original ADD models, the fundamental mass of gravitation in D dimensions, M_D is fixed around the electroweak scale $\sim$ TeV, in order to lower the fundamental Planck scale to an energy near the electroweak scale, and then the radius of the compactified volume would be around 1 mm and 10 Fermi (much larger than the original Kaluza-Klein longitudes) for $\delta_D = 2$ and $\delta_D = 7$ respectively. However, in other brane cosmology models, M_D can be much larger than the TeV scales (see discussion in [99] and references therein).

Besides gravitons propagating through bulk causing a Kaluza-Klein tower of massive gravitons on the brane, as previously indicated, a remarkable phenomenology is associated with the existence of the brane fluctuating in the bulk [100]. Indeed, rigid objects are not consistent with relativistic theories, thus the brane oscillates with a finite tension f[‖] breaking spontaneously the translational invariance along the extra-dimensions. This fact gives rise to a pseudo-Goldstone boson, dubbed a branon, that is a natural dark matter candidate. Branons will be specifically

[‖] The tension is also referred to as $\tau = f^4$.

studied in the next section since it is the dark matter model we will constrain in the following chapters.

1.4.2 Branon dark matter

As mentioned, the fact that rigid objects are not congruent with relativistic theories implies necessarily the fluctuation of the brane. Such a fluctuation breaks spontaneously the translational symmetry along the extra-dimensions, resulting in a pseudo-Goldstone boson, dubbed a branon. Brane-World senarios can be described through the manifold $\mathcal{M}_D$=$\mathcal{M}_{1+3} \times B$, with the $\mathcal{M}_{1+3}$ brane four-dimensional space-time embedded in a $D-$dimensional bulk, both of them defined by their metric tensors, $\widetilde{g}_{\mu\nu}$ and g'_{mn}. In fact, the global space-time of such a manifold can be represented by the line element

$$\mathrm{d}s^2 = \widetilde{g}_{\mu\nu}\,(x)\,W\,(y)\,\mathrm{d}x^\mu \mathrm{d}x^\nu - g'_{mn}\,(y)\,\mathrm{d}y^m \mathrm{d}y^n, \tag{1.36}$$

where x^ν and y^m, with $\mu, \nu = 0, 1, 2, 3$ and $m, n = 4, 5, 6..., D-1$, indicate the coordinates for the four-dimensional brane and the compact extra-dimensional space respectively. Also, $W(y)$ depicts the warp factor in the extra-dimensions. In the case where $W(y) \neq 1$, the most general one, the warp factor would generate a curvature that explicitly breaks the translational symmetry and the brane oscillation can be parametrised by a massive pseudo-Goldstone field, π^α (being $\alpha = 1, ..., N$ the subindices for the N branon fields), dubbed branon of mass M. In the limit of low tension ($f \gtrsim M$), where Kaluza-Klein modes decouple from SM, the branon description is given by the Nambu-Goto action included to the usual SM action, represented with the following Lagrangian [101–106];

$$\mathcal{L}_{Br} \;=\; \frac{1}{2} g^{\mu\nu} \partial_\mu \pi^\alpha \partial_\nu \pi^\alpha - \frac{1}{2} M^2 \pi^\alpha \pi^\alpha + \frac{1}{8 f^4} (4 \partial_\mu \pi^\alpha \partial_\nu \pi^\alpha - M^2 \pi^\alpha \pi^\alpha g_{\mu\nu}) T^{\mu\nu}_{\mathrm{SM}}. \tag{1.37}$$

As seen in Eq. (1.37), the coupling between branons and SM particles is highly suppressed by the tension of the brane by a factor f^{-4}. Also, the brane Lagrangian Eq. (1.37) conserves parity and terms with odd number of branons are not allowed, hence, branons are stable. Branons being weakly interacting, massive and stable, they are natural candidates for dark matter [99, 107–110].

Branons have the possibility of annihilating into SM particles, whose probability of annihilation is expressed by the thermally averaged cross section $\langle \sigma v \rangle$, that depends on the branon mass M and the tension of the brane f. Once the number of extra dimensions is fixed, the pair $\{M, f\}$ sets the parameter space describing both the field and the probability of annihilation. Branons may annihilate into Dirac fermions ψ with mass m_ψ. In this case, the cross section yields [111]

$$\langle \sigma_\psi v \rangle \;=\; \frac{M^2 m_\psi^2}{16 \pi^2 f^8} (M^2 - m_\psi^2) \sqrt{1 - \frac{m_\psi^2}{M^2}}\,, \tag{1.38}$$

whereas for a massive gauge fields (Z), of mass m_Z, it reads [111]

$$\langle \sigma_Z v \rangle \;=\; \frac{M^2}{64 \pi^2 f^8} \left(4\, M^4 - 4\, M^2\, {m_Z}^2 + 3 {m_Z}^4\right) \sqrt{1 - \frac{{m_Z}^2}{M^2}} \tag{1.39}$$

However, for W bosons, the expression (1.39) has to be multiplied by a factor 2. Finally, let us remark that a monochromatic gamma-ray line is also expected at the energy equal to the branon mass as a consequence of direct annihilation into photons since branons couple directly to them. However, this annihilation takes place in d-wave channel and consequently it is highly

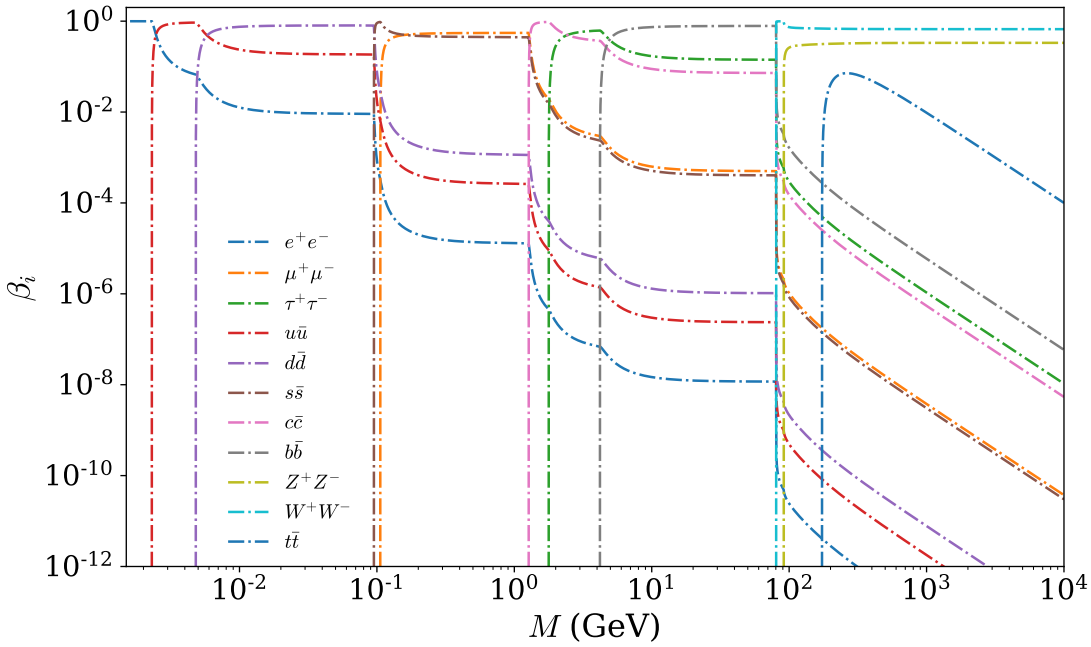

FIGURE 1.10: Branching ratios of annihilation for branons. These branching ratios, indicated with β_i, represent the probability of annihilation of branons into different channels. For example, for a mass $M = 100$ GeV, branons would mainly annihilation via W and Z channels.

suppressed [111]. In Fig. 1.10, we represent the branching ratios β_i for branons, defined as $\beta_i = \langle \sigma_i v \rangle / \langle \sigma v \rangle$, where i is a specific channel of annihilation.

In Eqs. 1.38 and 1.39, we presented the thermally averaged cross section for branons assuming M and f being independent parameters. However, for branons compatible with thermal relic dark matter with a thermally averaged cross section $\sim 3 \cdot 10^{-26} \mathrm{cm}^3/\mathrm{s}$, some expressions $f(M)$ can be obtained. Indeed, for one extra dimension, we will use in the following chapters the expression $f(M) = 7.91\, M^{0.75}$ from the limits obtained in Ref. [112].

1.5 Chapter conclusions

Throughout this Chapter, we have sought simply to address the development of the concept *dark matter* from the very beginning to more recent advances. The approach we followed was not with the intention of explaining what dark matter may be, but more what dark matter seems to not be. Indeed, first descriptions were in terms of dark stars while the most recent ones are from a particle perspective. Such an evolution has been accompanied, as far as we understand, by three significant changes of paradigm throughout the history:

- First, Kelvin's idea of applying the theory of gases to a stellar system. That represented an unprecedented connection between celestial bodies and thermodynamics. This is probably the most relevant precursor of present astrophysical techniques since it allowed us to determined the dynamical mass of an astrophysical system globally. In this paradigm, dark matter appears as an explanation for the dynamical anomalies in different astrophysical systems. Indeed, in its fundamental description, this problem is completely Newtonian being, nevertheless, the dynamical mass not that expected from Newton's laws.

- Second, the cosmological approach of a homogeneous and isotropic Universe, in which dark matter is described (as the rest of components) as a fluid governed by an equation of state. The need for dark matter can be fundamentally reflected in the discrepancies between Ω_b able to fit the abundances of the lightest elements in the Big Bang Nucleosynthesis and Ω_M able to explain the power spectrum in the study of the Cosmic Microwave Background.

- Third, the link between the cosmological perspective and the thermodynamic description of thermal relics through the Boltzmann equation. This connection becomes much narrower when it is recognised that the Standard Model of Particle Physics is not complete and new degrees of freedom, some of them postulated as dark matter candidates, are necessary.

The second and third points above seem more related. Indeed, we specifically presented their connection in Section 1.3.3. The first point seems to be a different definition of the problem, however, it is the contrary. As a matter of fact, the growth of cosmological structures through the linear perturbation theory and N-body simulations seem to be the joint of the three paradigms, for example, the structure at cosmological scales with dark matter halos predicted in astrophysics. Proper treatment of this subject would require an extension that would lie out of the purpose of this thesis. However, we would like to remark the importance of this field in the global description of dark matter.

From the three different points of view we presented in this Section, it was suggested from X-ray observations that dark matter is not constituted by undetected gas. Also, in a stronger constraint than that one from X-ray data, we also discussed that dark matter is not consistent to be baryonic (at least in a large proportion), according to the Big Bang Nucleosynthesis and the Cosmic Microwave Background measurements. Furthermore, thanks to the decoupling of relics from the primordial plasma, we have concluded that cold dark matter would be sufficient to address the explanation of the present content of dark matter today. However, it should be kept in mind that even though hot dark matter would not be in agreement with the structure formations, warm dark matter still would be valid.

Finally, we would like to finish the section by mentioning the existence of alternative theories to dark matter. In the first place, MOND, proposed by Milgrom in 1983 [113], emerges as a phenomenological modification of Newtonian gravity and is able to explain the flatness of galaxy rotation curves. It is usually pointed out that MOND should be consistent with a limit of a more complete modified General Relativity. In Ref. [114] the MOND framework is revised according to the three main challenges that such general models are exposed to: theoretical (the model has to be stable and derived from an action principle admitting a well-posed Cauchy problem), experimental (i.e., whether the model passes the predicted light deflection of weak lensing and also solar-system and binary-pulsar tests) and aesthetical (that tests whether the proposed model is natural or becomes a fit of experimental data).

In the modification of General Relativity, besides the graviton and the Standard Model matter fields, new degrees of freedom are introduced into the theory, having in mind that the effect of gravity on the matter fields can only be through interactions with a rank-2 tensor. This defines a gravitational theory with a set of field equations. In the case such field equations are different from those ones obtained from the Einstein-Hilbert action, then the theory is called modified. In addition, the inclusion of new degrees of freedom has to be within the paradigm of currently accepted physical theories, in order to avoid pathologies. There are quite a lot of modified gravity theories in the market, depending on how one chooses to extend the Einstein-Hilbert Lagrangian. Some examples include Horndeski [115] and beyond-Horndeski theories [116], torsion [117] and non-metric [118] theories or non-local gravity [119, 120]. We refer the reader to Ref. [121] for an extensive review, in which modified gravity theories are grouped into Extra Field theories, Higher Derivative and Non-Local theories of Gravity, Higher Dimensional Theories of Gravity or the Parameterised Post-Friedmannian Approaches.

Chapter 2

Dark matter detection: an Astroparticle Physics perspective

2.1 Overview and leitmotiv

In Chapter 1, we discussed the main motivations to incorporate dark matter (DM) to the present paradigm in Physics. Among these motivations, the most remarkable ones are; the presence of DM in galaxy clusters, the flatness of galactic rotation curves at outer radii, the abundances in BBN, the explanation for the CMB anisotropies and the growth of cosmological structures. Also, according to Section 1.3.3, DM could be accommodated to behave as a Weakly Interacting Massive Particle (WIMPs). All these aspects are supplemented with observations that allow us to disentangle some of the most relevant DM properties: non-relativistic at the moment of decoupling [122], sufficiently heavy [123], stable or long-lived [124], effectively non-photon-interacting [125], collisionless [126–129] and smoothly distributed at cosmological scales [130–132]. Hereafter, we will assume DM to be a WIMP. This assumption will affect the strategies followed in its detection. In this Chapter, we shall introduce different pathways in DM searches, generally grouped into three branches:

- *Collider searches*, in which SM particles after colliding would produce DM particles as product of that collision [133]. This case will be described in Section 2.2.

- *Direct searches*, in which DM particles would be detected through the signals left from their collisions with a detector [134, 135]. This detection strategy will be treated in Section 2.3.

- *Indirect detection*, in which DM particles interact themselves to produce SM particles [136]. We shall present such a DM search in Section 2.4.

In this Chapter, we will specifically focus on indirect searches since it will be our main methodology to set constraints on DM (Chapters 3, 4 and 5). Our reasoning line will be centred in the analysis of e^+/e^- cosmic rays and the radio signals originated from the e^+/e^- interaction with the galactic magnetic field. Also, in Section 2.5.3, we will present the principal detectors able to measure DM signals indirectly: PAMELA (whose mission was completed in 2016) [137], Fermi-LAT [138] and AMS for cosmic rays, and the SKA [139] for radio emission.

2.2 Collider searches

Even though astrophysical and cosmological observations are one of the strongest experimental evidence for the possible existence of DM, Particle Physics Beyond the Standard Model (BSM), also provides itself solid reasons. Indeed, as mentioned in Section 1.4, some of the SM open questions, as the CP-violation or the hierarchy problem can be partially solved with formalisms in which BSM particles would be involved. Some of these particles are proposed as

DM candidates. Considering this, one of the most immediate strategies to find such candidates is through the use of colliders.

In general words, collider searches for DM consist of producing DM particles as a result of the collision of SM particles, assuming that there exists a coupling between them. This powerful tool would allow to disentangle the particle nature of DM directly. However, it is usually claimed that such searches would not be able to strictly determine whether what is detected is a DM particle. Indeed, DM produced at colliders would often pass without leaving any signature in the detector due to their weak interaction. These weak particles are commonly referred as *invisible particles* and their characteristics are usually reconstructed through the remaining products of the collision (jets, photons, heavy bosons) and the imbalance of different quantities in the transverse plane of the beams, such as the transverse missing momentum $\not{\mathbf{p}}_{\mathbf{T}}$. Indeed, particles colliding and their subsequent products would not have a significant momentum contribution in the transverse direction and the vectorial sum of the transverse components must vanish resulting

$$\not{\mathbf{p}}_{\mathbf{T}} = -\sum_j \mathbf{p}_{\mathbf{T}} \tag{2.1}$$

In order to reconstruct $\not{\mathbf{p}}_{\mathbf{T}}$, it is necessary to include contributions from all particles in the event, and thus, precise measurements have to be done in all detector systems. In the case of the LHC, in the reconstruction of the transverse missing momentum, it is usually considered specific testable DM models, grouping them in: either highly specified models (as SUSY) whose collider searches are optimal, or simplified models whose main parameters can be captured by colliders but are more difficult to constrain. Among these testable DM models, let us mention:

- First, the portal models, in which only one type of DM particle would account for the SM extension and whose interaction with SM particles would be mediated by either the Higgs or the Z boson. Within this framework, the main drawback of these searches is the large neutrino background that is also part of the invisible component. Z portal models have been strongly constrained by LEP through the inference of the invisible Z width [140]. Most of the Dirac fermion DM candidates in the Z portal with masses smaller than m_Z are constrained to values in which the thermally averaged cross section is smaller than the limit for thermal relics. Also, the allowed scenarios are those in which DM is a fermion with either an axial coupling and whose mass is $\sim m_Z/2$ or with a vector coupling and a mass greater than 6 TeV.

Furthermore, in the Higgs portal, the Higgs decays into a Z pair that contributes in a small proportion to the total width of the Higgs. With present observations, if the Higgs is coupled to an additional invisible particle then it could be observable. However, it is necessary to do additional assumptions in the coupling with the Higgs to obtain the total width, and consequently, these predictions are not model-independent. From [140], the allowed scenarios are those in which DM has a mass of around $m_H/2$ and masses greater than 400 GeV for scalar DM and 1.16 TeV for vector DM.

- Second, Effective Field Theories (EFT) and Simplified Models, where the mediator for DM-SM interaction is a new BSM particle. In the case of EFT, if the mediator is heavy in comparison with the beam particles in the collision, then the DM-SM interaction can be seen as a contact interaction and all the observables are completely determined by one parameter (aside from the DM mass and the Lorentz structure): the contact interaction scale (or cut-off scale). The validity of such an approximation depends on both the range of DM mass and the range of the coupling [141].

Furthermore, provided the collision energy near or higher than the mediator mass, the EFT

approximation is not valid anymore and then it is necessary to, at least, developing a simple description of the particle phenomenology. Those are the Simplified Models, where the coupling between incident particles with the mediator g_i and the coupling DM-mediator $g_{\rm DM}$ have to be considered, together with the mediator mass $m_{\rm med}$ and the DM mass, M. More complications appear when Simplified Models improve towards the so-called Less-Simplified Models.

Furthermore, the complexity of the processes involved in EFT and Simplified Models influences the composition of the detected transverse momentum, and therefore, different signatures are expected (see discussion in Ref. [142]). Under this framework, colliders follow minimal assumption strategies of solely detecting an excess of the missing transverse energy over the SM background. Among these strategies, the mono-X searches, in which hadrons collide producing DM as a final state together with an X product (jet, photon, Higgs, Z) is one of the most powerful strategies. The mono-X searches can be also combined with the mediator searches, in which the BSM is produced from the collision of two hadrons that subsequently decay to a pair of leptons or quarks, producing an excess of events either in the mass spectrum or in the angular distributions.

• Leaving aside general models, SUSY stabilises the gauge hierarchy problem and propose at least a yet-undiscovered partner for every SM particle: with the same quantum numbers and gauge interactions, but differing in spin by 1/2. The most well-studied type of DM in this paradigm is the neutralino, χ, although other possibilities, such as the gravitino DM, have been also contemplated. In general, searches in this sector have been based on simplified model approaches, exploring the range of energies in which the involved particles would decouple to simplify the phenomenology, avoiding effects from heavier particles (see discussion in Ref. [133]). In this regard, the lightest candidates from MSSM have been widely considered.

SUSY has received much attention from ATLAS and CMS, however, no SUSY search has produced a conclusive signal due to the large variety of expected signatures. One of the most solid statements is the study of gluino and squark masses decaying via neutralino to photons. Indeed, it provides a limit of exclusion of around 2 TeV for both gluino and squark for different neutralino masses [143]. Although no LHC searches have so far probed SUSY, searches for more rare processes are now entering their prime, as the study of the electroweakino parameter space.

• Fourth, long-lived particles, compared to SM particles, at the weak scale. Long-lived particles travel a macroscopic length within the detector before decaying. LHC detectors are not optimised for this purpose, and additional work is required for searches to be sensitive.

As already mentioned, although collider searches offer a sophisticated method to study of DM features, it may not be conclusive, and thus, it has to be complemented by other kinds of searches, among them, direct searches that will be described in the following Section.

2.3 Direct searches

Direct detection is based on signatures left by DM particles (of the DM halo) when they are scattered by the nuclei of a detector. Detectors usually operate in deep underground laboratories to reduce the background from cosmic rays (γ-ray, neutrons and solar/atmospheric neutrinos) and natural radioactivity in the rock. After scattering, part of the DM energy fraction is deposited in the detector, leaving (potentially) three kinds of signatures: heat (phonons), scintillations (light) and ionization (e^-) that has to be discriminated from background events. For this, the selection of the detector is crucial since its visible signal strongly depends on the interaction mechanism. Some of the most important requirements are high radiopurity of the detector material, good response to nuclear recoils, long term stability, spatial information on the

interaction, particle discrimination or low energy threshold. According to these characteristics, the most used detectors are

- for heat, cryogenic detectors (CRESST I [144]),
- for scintillation, NaI, CsI and Xe/Ar detectors (DAMA/LIBRA [145], ANAIS [146], COSINE [147], SABRE [148], KIMS [149], DEAP [150] and XMASS [151]),
- and for ionization, semiconductors or superheated liquids (CoGeNT [152], DAMIC [153], NEW-G [154], DRIFT [155], NEWSdm [156], PICO [157]).

On the other hand, some of them combine signatures as

- scintillation-heat using $CaWO_4$ or NaI (CRESST II/III [158, 159] and Cosinus [160]),
- heat-ionization based on Ge, Si detectors (CDMS [161] and EDELWEISS [162]),
- and scintillation-ionization with liquid Xe/Ar (XENON [163], LUX [164], PandaX [165], LuX-Zeplin [166], ArDM [167], WArP [168] or DarkSide [169]).

Unlike collider searches, the DM-SM scattering rate lies in astrophysical assumptions. First of all, it depends on the local DM density, estimated in $\rho_\odot = 0.39 \pm 0.03\,\mathrm{GeVcm}^{-3}$ [170]*, assuming a halo locally smooth and virialised. Second, it also depends on the local dark-matter velocity distribution $f(\mathbf{v})$ at the solar system frame. Indeed, the velocity dispersion of particles is usually taken as a Maxwell-Boltzman distribution, taking into account the velocity of the Sun around the GC and also the Earth around the Sun. The assumption of the smoothness of the halo in an isothermal sphere with an isotropic Maxwellian velocity is usually called the Standard Halo Model (SHM) [172]. Under these assumptions, one of the usual quantities used to set constraints on DM particles is the total recoil energy spectrum, that for a detector composed of N nuclei would be

$$\frac{\mathrm{d}R}{\mathrm{d}E_R} = \sum_N N_N \frac{\rho_\odot}{M} \int_{v_{\min}}^{v_{\mathrm{esc}}} \frac{\mathrm{d}\sigma_{(\mathrm{DM}-N)}}{\mathrm{d}E_R} v f(\mathbf{v}) \mathrm{d}^3 v, \tag{2.2}$$

where M is the DM candidate mass and $\frac{\mathrm{d}\sigma_{(\mathrm{DM}-N)}}{\mathrm{d}E_R}$ is the DM-nuclei differential scattering cross section. Also, the recoil energy is defined as $E_R = \frac{m_r^2 v^2}{m_N}(1-\cos\theta^*)$ with m_r the reduced mass of DM-nuclei system and θ^* the scattering angle in the centre-of-mass system. Depending on the coupling on DM-nuclei, the cross section scattering $\sigma_{\mathrm{DM}-N}(E_r)$ can be divided into two contributions, one spin-independent σ_{SI} and other spin-dependent σ_{SD}. The differential cross-section for the DM-nuclei scattering can be written as follows

$$\frac{\mathrm{d}\sigma_{(\mathrm{DM}-N)}}{\mathrm{d}E_R} = \frac{m_N}{2\mu_N^2 v^2}\left(F_{SI}^2(E_R)\,\sigma_0^{SI,N} + F_{SD}^2(E_R)\,\sigma_0^{SI,N}\right) \tag{2.3}$$

where $\sigma_0^{SI,N}$ and $\sigma_0^{SD,N}$ are the spin-independent and the spin-dependent components of the cross sections at momentum transfer equal to zero, and $F_{SI,SD}$ the form factors (see Ref. [134] for a complete description). In addition, the quantities involved are DM model-dependent. Thus, comparing $\frac{\mathrm{d}R}{\mathrm{d}E_R}$ with the experimental data enables to set constraints on the DM parameter space.

Besides the total recoil energy spectrum $\frac{\mathrm{d}R}{\mathrm{d}E_R}$, two more quantities are also measured: the annual modulation and the directionality of the signal. The former comes from the DM particle flux

*Although the value can vary between 0.2 and 0.4 [171].

that varies periodically due to the movement of the Earth with respect to the DM particle rest frame. Indeed, the annually modulating recoil rate yields

$$\frac{\mathrm{d}R}{\mathrm{d}E}(E,t) \approx S_0(E) + S_m(E)\cos\left(2\pi\frac{(t-t_0)}{T}\right), \tag{2.4}$$

in the case in which the DM distribution is isotropic in the particle DM rest frame. In Eq. (2.4), S_0 is the time-averaged rate, S_m is the modulation amplitude and t_0 the phase of the modulation in years. The latter (directionality) accounts for the spatial distribution of the detected signal,

$$\frac{\mathrm{d}R}{\mathrm{d}E\mathrm{d}\cos\gamma_D} \propto \exp\left[\frac{-\left[(v_E+v_\odot)\cos\gamma_D - v_{\min}\right]^2}{v_c^2}\right], \tag{2.5}$$

being γ_D the direction relative to the mean direction of the solar motion, v_E the Earth velocity, $v_\odot$ the sun motion, $v_c \equiv \sqrt{3/2}v_\odot$ and $v_{\min}$ is the minimum DM velocity necessary to excite a nuclear recoil.

The modulation detected by the NAI(Tl) detector DAMA/LIBRA would be the potential most significant signal from DM, reaching $12.9\,\sigma$. From the results, the spin-independent case is disfavoured by the data, being the best candidates a particle with a mass of ~ 8 GeV, disfavoured by $5.2\,\sigma$, and a candidate with a mass of ~ 54 GeV, disfavoured by $2.5\,\sigma$. The case of isospin violating spin-independent interactions is favoured by a DM mass around ~ 10 GeV. On the other hand, spin-dependent DM-nucleon interactions are favoured as well. In this case, the best candidates would be DM masses of ~ 10 GeV or ~ 45 GeV [145]. Nevertheless, experiments as XENON100 and XMASS disfavour the particles proposed by DAMA/LIBRA to explain such a modulation [173, 174]. The possibility of the existence of an exotic DM particle needs those experiments to be repeated with detectors of the same material. In this regard, NAI(Tl) detectors as COSINE [147] or ANAIS [146] would be determinant. Indeed, COSINE has measured in the last years different signatures, and for the moment the data can be well adjusted with the absence of DM candidates [147].

2.4 Indirect searches

2.4.1 Generalities

Indirect DM searches constitute a series of strategies, that unlike collider and direct searches, enable us to disentangle the main features of DM, in addition to the Milky Way, in extragalactic sources. The studies based on indirect detection lie in the fact that DM may annihilate or decay into different channels of the SM in the predicted DM halos. Indeed, after the annihilation, these products would decay or hadronise resulting in stable particles such as γ-rays, neutrinos, electrons-positrons or protons-antiprotons [175] that would be discriminated from the background through distinctive signatures. In fact, in the context of interstellar, intergalactic or intracluster environments, the injection of SM particles due to the DM annihilation can be seen as a new cosmic-ray component. DM may be an exotic source to be considered apart from those astrophysical ones that also would be responsible for cosmic-ray production. After the injection, the annihilation products then propagate from the annihilation point through the transport process.

Due to the propagation some signals may be directly detected at the Earth in the form of annihilation products or in the secondary processes of these stable particles with the environment, such as radio signals from synchrotron emission [176–180] or γ-rays in the case of Inverse Compton Scattering (ICS). Then, as stated above, the phenomenology for indirect searches can be simply

referred to as a particle propagation process whose source is DM. The amount of cosmic rays injected in the DM halo can be describe by a source term

$$q(\mathbf{r}, E) = \frac{1}{2} \langle \sigma v \rangle \left(\frac{\rho_{\rm DM}(\mathbf{r})}{M} \right)^2 \sum_j \beta_j \frac{{\rm d}N_i^j}{{\rm d}E}\,, \tag{2.6}$$

for annihilating DM, where $\langle \sigma v \rangle$ is the thermally averaged cross section, and

$$q(\mathbf{r}, E) = \Gamma_{\rm dec} \frac{\rho_{\rm DM}(\mathbf{r})}{M} \sum_j \beta_j \frac{{\rm d}N_i^j}{{\rm d}E}\,, \tag{2.7}$$

for decaying DM, being $\Gamma_{\rm dec}$ the decay rate. In both expressions, Eq. (2.6) and (2.7), the proportion $\rho_{\rm DM}(\mathbf{r})/M$ corresponds to the DM number density, the DM mass M and the DM density profile $\rho_{\rm DM}(\mathbf{r})$ for the halo. Both for the annihilating and decaying case, ${\rm d}N_i^j/{\rm d}E$ is the injection spectrum and provides the number of cosmic-ray per unit of energy and annihilation. Each spectrum ${\rm d}N_i^j/{\rm d}E$ is referred only to one channel of annihilation/decay j, i.e., DM annihilating/decaying into the j channel with a branching ratio β_j, which subsequently decays or hadronises into the cosmic-ray i. The sum over j is, therefore, the contribution from different channels of decay/annihilation to the total contribution of cosmic rays. Therefore, $\sum_j \beta_j {\rm d}N_i^j/{\rm d}E$ allows us to set the channels that will determine the DM candidate specifically. The injection spectra ${\rm d}N_i^j/{\rm d}E$ have been computed using the functions provided by the software PPC4DMID [175], based on Monte Carlo event generators such as PYTHIA and HERWING. For example, according to Fig. 1.10, for a branon with a mass of 100 GeV producing e^+/e^- as final state we would have $\beta_W \left({\rm d}N_e^W/{\rm d}E\right) + \beta_Z \left({\rm d}N_e^Z/{\rm d}E\right)$ since the annihilation is mainly into those two channels.

Once the source term is determined, the propagation of products depends on the cosmic-ray species to be studied.

• Neutrinos and γ-rays have the advantage of maintaining their original direction due to their null electric charges. The associated brightness or specific intensity I_ν, usually measured by telescopes, is given by the l.o.s. integral of the emissivity that for neutrinos and γ-rays is $j_\nu^i(\mathbf{x}) = (1/4\pi) q(r, E) E$. However, for example in γ-ray detections, in order to not propagate the systematic uncertainties of the photons energy E also measured in real time, the quantity calculated is usually

$$\left(\frac{{\rm d}\Phi}{{\rm d}E}\right)_i = \frac{1}{2M^2} \langle \sigma v \rangle \sum_j \beta_j \frac{{\rm d}N_i^j}{{\rm d}E} \frac{1}{4\pi} \int_{\Delta\Omega} {\rm d}\Omega \int_{\rm l.o.s.} {\rm d}s\, \rho_{\rm DM}(s), \tag{2.8}$$

in which

$$\langle J \rangle_{\Delta\Omega} \equiv \frac{1}{4\pi} \int_{\Delta\Omega} {\rm d}\Omega \int_{\rm l.o.s.} {\rm d}s\, \rho_{\rm DM}(s), \tag{2.9}$$

is usually defined as the astrophysical factor, with the second integral performed along the l.o.s. In this regard, Eq. (2.8) can be divided in one factor that is Particle Physics dependent and the astrophysical factor[†]. This is an indication that the energy dependence of neutrinos and γ-rays signals at the Earth is the same dependence as the spectrum in the point of injection.

[†]Note, though, that these two factors are not totally independent, as the precise properties of the DM particle will affect the minimum scale of the formed structures, and thus the value of the astrophysical factor for a given target will formally differ for different DM particle models.

In a similar way, it is straightforward to derive the flux from decaying DM by replacing the $\frac{1}{2M^2}\langle\sigma v\rangle\sum_j \beta_j \frac{dN_i^j}{dE}$ factor by $(\Gamma_{\rm dec}/M)\sum_j \beta_j \frac{dN_i^j}{dE}$.

- The case of charged particles, as electrons/positrons, protons/antiprotons and also charged antimatter is completely different. After the injection, those particles would travel governed by a transport equation, that in its general version (see [181]) yields

$$\begin{aligned}\frac{\partial\psi}{\partial t} &= \nabla\cdot(D_{xx}\nabla\psi - \mathbf{V}\psi) + \frac{\partial}{\partial p}D_{pp}\frac{\partial}{\partial p}\frac{1}{p^2}\psi \\ &-\frac{\partial}{\partial p}\left[b(p)\psi - (p/3)(\nabla\cdot\mathbf{V})\right] - \frac{1}{\tau_f}\psi - \frac{1}{\tau_r}\psi + q(\mathbf{r},p,t),\end{aligned} \tag{2.10}$$

usually referred to as both the Parker and the Ginzburg-Syrovatsky equation. In this case, we will see that the Particle Physics counterpart is mixed with the astrophysical parameters of the transport. So, at first glance, the charged-cosmic-ray problem may seem more complicated than the neutrinos and γ-rays case, since in the former, the injection spectrum $\beta_j\frac{dN_i^j}{dE}$ is not fully equal to that one after the propagation[‡]. However, the fact that charged particles interact with their environment (either galactic environment or intracluster medium) would induce eventual losses of energy that produce photons to be detected in a large range of frequencies. This would allow us to compare multiple signatures coming from one solely process. The study of these signals sets the basis of DM indirect searches through multi-wavelength astronomy; depending on the energy loss mechanism distinctive signals could be detected at different frequencies, either via synchrotron emission, ICS, *bremsstrahlung* or Coulombian interactions. In this case, indirect searches with charged particles allow studying different signatures in the process of annihilation. On the other hand, the important improvements implemented in radio astronomy in the last decades, make the radio telescopes one of the most competitive in terms of sensitivity and resolution, ideal to detect possible synchrotron signals from e^+/e^- after DM annihilation.

In the following sections, we will focus on e^+/e^- as the final state of the annihilation. First, we will take a phenomenological approach to understand each term of Eq. (2.10) for cosmic rays and then we will focus on the e^+/e^- case with the assumptions that this implies. After that, we will set constraints on DM through the positron fraction and the synchrotron emission from the interaction of e^+/e^- with the magnetic field.

2.4.2 Cosmic-ray transport

There are two ways to derive Eq. (2.10). The first one, which we shall follow in this Section, is a phenomenological construction derived from the continuity equation while the second one is a generalisation of the Fokker-Planck equation. In the former, the point of departure is the continuity equation for the cosmic-ray species i,

$$\frac{\partial N_i(\mathbf{r},t)}{\partial t} = -\oint \mathbf{j}\cdot d\mathbf{A} + Q_i(\mathbf{r},t), \tag{2.11}$$

characterised by the source term $Q_i(\mathbf{r},t)$. According to the divergence theorem $\oint \mathbf{j}\cdot d\mathbf{A} = \int \nabla\cdot\mathbf{j} dV$, where dV is the volume element within the closed surface dA and also considering

[‡]It should be emphasised that the observed γ-ray spectrum may also be distorted and different from the one at the emitting source for the case of sufficiently distant extragalactic objects due to Extragalactic Background Light attenuation or also due to the redshifted energies in the Universe expansion.

$N = n\mathrm{d}V$, the differential form of the continuity equation yields

$$\frac{\partial n_i(\mathbf{r},t)}{\partial t} = -\nabla\cdot\mathbf{j} + q_i(\mathbf{r},t), \tag{2.12}$$

being $q_i(\mathbf{r},t)$ the abovementioned source term per unit of volume. Assuming the Fick's law in which particles flow from a region of higher concentration to another of lower concentration, with a magnitude proportional to the density gradient $\mathbf{j} = -\hat{\mathbf{D}}\nabla n_i(\mathbf{r},t)$, Eq. (2.12) becomes

$$\frac{\partial n_i(\mathbf{r},t)}{\partial t} - \nabla\cdot\left(\hat{\mathbf{D}}\nabla n_i(\mathbf{r},t)\right) = q_i(\mathbf{r},t)\,. \tag{2.13}$$

or also alternatively

$$\frac{\partial \psi_i(\mathbf{r},p,t)}{\partial t} - \nabla\cdot\left(\hat{\mathbf{D}}\nabla \psi_i(\mathbf{r},p,t)\right) = q_i(\mathbf{r},p,t)\,. \tag{2.14}$$

where ψ holds for the cosmic-ray number density per unit of energy. As a relevant historic example, one the most considered assumptions lies on

$$\nabla\cdot\left(\hat{\mathbf{D}}\nabla \psi_i(\mathbf{r},p,t)\right) = -\psi_i(\mathbf{r},p,t)/\tau_{esc}, \tag{2.15}$$

representing the basis for the well-known *Leaky Box models*. Such models assume cosmic rays within a confinement volume with an escape probability per unit of time τ_{esc}. This scenario, presented here in its most simplistic version, has been used to describe some average values of cosmic rays and still is being used and relevant under some modifications. In the following, we shall present the remaining terms of Eq. (2.10).

a) Cosmic-ray production: spallation, decay and injection

Cosmic rays are subjected to collisions with particles in the interstellar medium (ISM). In such collisions, fragmentation of nuclei and decay of radioactive products would either destroy through the terms $-\frac{1}{\tau_f}\psi$ and $-\frac{1}{\tau_r}\psi$ or inject particles of a particular species through the term $q_i(\mathbf{r},p,t)$. In Eq. (2.10) τ_f is the time scale for loss by fragmentation, and τ_r for radioactive decay. In $q_i(\mathbf{r},p,t)$ all the processes of injection are considered, not only those of production through spallation and decay, but also the injection of particles from supernova remnants (SNR) and other astrophysical sources. In other words,

$$q_i(\mathbf{r},p,t) = q_i^{\mathrm{prim}}(\mathbf{r},p,t) + \sum_{k>i}\frac{1}{\tau_{ik}^f}\psi_i + \sum_{k>i}\frac{1}{\tau_{ik}^r}\psi_i, \tag{2.16}$$

Indeed, such terms, once included in the transport equation (Eq. 2.10), allow us to treat cosmic rays according to their origin:

- Primary cosmic rays, $q_i^{\mathrm{prim}}(\mathbf{r},p,t)$, are those produced in astrophysical sources as SNR, pulsars or other exotic sources. Their injection spectrum is usually taken as $\sim E^{-\delta}$, according to the well-known First-order Fermi acceleration mechanism proposed in 1949 (together with a Leaky box description as in Eq. (2.15)). Under such a mechanism, cosmic rays experiment acceleration scatters from the upstream to downstream in the wavefront of a shockwave and vice versa (for example, in SNR): cosmic rays gain energy during each crossing, increasing their probability of escaping from the ISM. The boundary conditions for an ideal shockwave upstream and downstream (Rankine-Hugoniot conditions) impose both the conservation of mass flux, momentum conservation and energy conservation predicting an injection spectra to the ISM (escape from the shockwave) proportional to $E^{-\delta}$. This is one of the main pillars in the

construction of a cosmic-ray propagation theory. Due to the propagation, those primary cosmic rays usually change their spectra in $E^{-\delta-\beta}$.

- Secondary cosmic rays of the species i, given by $\sum_{k>i} \frac{1}{\tau_{ik}^f}\psi_i + \sum_{k>i} \frac{1}{\tau_{ik}^r}\psi_i$, are those produced due to either spallation or radioactive decay of the nuclei k in the ISM. The energy dependence for these secondary species is usually taken as $E^{-\delta-\beta}$, i.e., the spectra of the primary cosmic rays in equilibrium when they propagate. On the other hand, τ_{ik}^f and τ_{ik}^r, the time scale for spallation and decay respectively, are closely related with the particle reactions process.

From now on, in order to simplify the notation, we will omit the subindex i introduced in Eq. (2.14), that we used to refer to as the cosmic-ray species i. The reader should have in mind, unless otherwise specified, that the expressions we will describe in the following sections would apply to many different cosmic-ray species.

b) Cosmic-ray diffusion

The cosmic-ray diffusion is the result of the particles scattering on random magnetohydrodynamic waves in the ISM. There, particles are predominantly scattered by the irregularities of the galactic magnetic field $\mathbf{B}$, usually modelled by a large-scale uniform component $\mathbf{B}_0$ and a small-scale fluctuating irregular component $\delta\mathbf{B}$. In general, the diffusion tensor, D_{xx} in Eq. (2.10), can be written in terms of the magnetic field vector components B_i and the diffusion coefficients that can be parallel or perpendicular to the mean field, together with an antisymmetric counterpart, yielding [182]

$$D_{ij} = D_\perp \delta_{ij} - \frac{\left(D_\perp - D_\parallel\right) B_i B_j}{B^2} - \varepsilon_{ijk} D_A \frac{B_k}{B}. \tag{2.17}$$

where D_A considers particle drifts due to the variations of the large-scale-magnetic field and ε_{ijk} is the Levi-Civita symbol. In Eq. (2.17), the symmetric part corresponds to the diffusion associated to the fluctuating irregular component, while the antisymmetric is associated to the large-scale magnetic field and it is usually neglected.

The D_{ij} coefficient can be analytically determined under the so-called quasi-linear approximation, in which magnetic fluctuations are weaker than the uniform component ($|\delta\mathbf{B}| << \mathbf{B}_0$) and the only prevailing term would be $D_\parallel$ (see [181–183] and references therein). Sophisticated numerical codes able to fit most of the cosmic-ray species in our galaxy usually rely on this approximation. Despite this assumption, there is still a wide debate about whether the linear regime is accurate to describe plasmas in astrophysical environments [184, 185]. One of the main questions is the role played by the perpendicular component of the diffusion tensor, classically related to the parallel component as $D_\perp/D_\parallel = 1/[1+(\lambda_\parallel/r_g)^2]$, being $\lambda_\parallel$ the mean free path of cosmic-rays in the parallel direction and r_g the particle Larmor radius. Several studies coincide in the importance of the perpendicular component, extending the expression for $D_\perp/D_\parallel$. For example, the escape of cosmic rays from the Milky Way probably occurs via transport normal to the Galactic Plane. From this fact, numerical simulations, such as Particle-in-Cell schemes or Test-Particle simulations have been widely considered to determine the diffusion tensor. The main challenges of these methods are, in fact, the lack of precise information about plasma parameters and the need to specify initial and boundary conditions.

Specifically, the quasi-linear approximation, followed by a wide variety of authors and usually assumed for indirect searches studies, allows us to write the diffusion tensor as a scalar function that depends on cosmic-ray kinetic energy. Indeed, in this framework, the interaction between particles and irregularities is of resonant character and maximal when the wave vector of

the turbulence, **k**, is parallel to the regular magnetic field, being $k_{\parallel} = \pm s/(r_g \mu)$. In such an expression μ is the particle pitch angle[§], and the integers $s = 0, 1, 2...$ correspond to cyclotron resonances of different orders. The predicted function for the diffusion coefficient then yields $D = D_{\parallel} \simeq (\delta B_{\rm res}/B)^{-2} \, v r_g/3$, being $\delta B_{\rm res}$ the amplitude of resonant fluctuations, when $k = k_{\parallel} \sim 1/r_g$, that corresponds to the first-order resonance s = 1, the most relevant for the isotropic diffusion (for further details, follow [186]). By performing a Fourier analysis for the fluctuations, that can be characterised by $\left\langle B^2(k) \right\rangle \propto k^{-2+\delta}$, the diffusion coefficient in the quasi-linear regime renders

$$D(E) = D_0 E^{\delta}. \tag{2.18}$$

Depending on the formalism chosen to describe how the kinetic energy is distributed in the turbulences dynamic of the galactic plasma, two theoretical values are usually considered, 1/3 for the well-known Kolmogorov type spectrum [187] and $\delta = 1/2$ typical for the Kraichnan diffusion [188], although such coefficients are also fitted by numerical codes using the ratios between different cosmic-ray species measured by cosmic-ray detectors.

c) Cosmic-ray reacceleration

In 1949, Fermi proposed a mechanism in which cosmic rays would gain energy by bouncing off moving magnetic clouds in the interstellar plasma medium: the so-called Second-order Fermi acceleration [189]. The magnetic irregularities that scatter cosmic rays are not merely static but also in random motion with characteristic velocities of order the Alfvén speed, according to the alfvenic plasma waves motion. It may happen that a magnetic cloud with high field intensity moves toward the cosmic-ray particle and collide against it, and thus, such a particle would gain energy in the collision. However, it is also possible that such a cloud moves away from the cosmic-ray particle and, since the latter moves faster than the cloud, it would reach the irregularity being reflected backwards and losing energy in the process. The estimated net result is an averaged gain since head-on collisions are more frequent than tail-in scatters and the relative velocity is larger in the former case. The reacceleration mechanism can be treated as diffusion in momentum space characterised by the coefficient D_{pp}.

Considering that both diffusion and reacceleration are produced due to magnetic field irregularities in interstellar plasma, both processes should be linked. Indeed, following the heuristic analysis in [190], it is possible to relate both as $D_{xx} D_{pp} = \frac{1}{9} p^2 V_A^2$, where V_A is the Alfvén speed estimated as $V_A = B/\sqrt{\mu_0 \rho_{\rm pl}}$, μ_0 is the permeability of the vacuum and $\rho_{\rm pl}$ is the total mass density of plasma particles. In a more general description, the diffusion and reacceleration term would be related to the diffusion coefficient [191]

$$D_{xx} D_{pp} = \frac{p^2 \, V_A^2}{\delta \, (4 - \delta) \, (4 - \delta^2)}, \tag{2.19}$$

The relation lies in the following interpretation. If the scattering is very strong, cosmic rays would suffer from a large change in momentum and a small in space. Therefore, particles whose diffusion is dominant have a negligible probability of having a momentum change when they get through plasma irregularities.

Reacceleration parameters can be usually measured by energy tracers in cosmic-ray abundances left by K-capture from isotopes, in which a 1s electron is captured by a parent nuclei in ${}^{A}_{Z}\mathrm{X} + e^- \rightarrow {}^{A}_{Z-1}\mathrm{Y} + \nu_e$. K-capture is strongly suppressed in high diffusion environments because high-energy nuclei are generally fully stripped of their electrons. Such a process is highly

[§]defined as the angle between the magnetic field and the particle velocity.

energy-dependent being low-energy nuclei more likely to suffer it. Some of those nuclei in environments with high reacceleration would spend more time at low energies. The nuclei ${}^{A}_{Z}X$ would show an abrupt decrease in their abundances, while on the contrary, ${}^{A}_{Z-1}Y$ should show a rise. Among the most used elements for these probes are the isotopes ^{37}Ar, ^{44}Ti, ^{49}V, ^{51}Cr.

d) Cosmic-ray drift and the Galactic wind

The stellar activity in galaxies may drive powerful galactic winds which can push a significant fraction of the gas and the magnetic field out from the galactic plane. Spatially resolved high-redshift observations indicate that these winds are launched directly from the sites of typically strongly-clustered star formation [192–194]. Indeed, a large cosmic-ray flux travelling through a magnetised plasma with a mean velocity greater than the Alfvén speed leads to the growth of magnetic fluctuations. Such fluctuations, subsequently, extract momentum and energy from the cosmic rays and transfer it to the interstellar thermal gas. The thermal gas is heated and accelerated and the net effect is a galactic wind that globally pushes cosmic rays perpendicularly outwards from the galactic plane. Indeed, analysis of the γ-ray emission measured by EGRET in the Galactic disk, reveals that cosmic rays are approximately uniform distributed in the radial direction of the disk. However, in Ref. [195] a wind model applied to the Milky Way, driven by both cosmic-ray and thermal gas pressure, shows that the observed Galactic diffuse soft X-ray emission can be better understood by wind than by static gas models.

The mathematical treatment is generally by adding an advection term $\mathbf{j_C}$ to the continuity Eq. (2.14) with

$$\mathbf{j_C} = \mathbf{V} n(\mathbf{r}, t), \tag{2.20}$$

although the galactic wind effect would result in a more complicated spatial framework to work. In fact, 1-zone and 2-zone models have been proposed. In the one 1-zone model convection and diffusion is everywhere, while a 2-zone model has diffusion only up to some distance from the plane, and diffusion plus convection beyond. In general, $\mathbf{V}$ is a function of $\mathbf{r}$. Both models are consistent with different signatures such as the energy dependence of the cosmic-ray abundances and radioactive isotopes (see discussion in [181]), constraining velocity for galactic wind values of around 10 km/s for the 1-zone model at inner regions of the galactic disk and 100 km/s for the outer regions in the 2-zone model.

Furthermore, the Galactic wind not only corresponds to transport of cosmic rays away of the galactic plane but also adiabatic energy losses, due to expanding plasma, since the convection velocity increases with the distance from the plane. Considering the equation of state of an ultra-relativistic gas in a non-relativistic velocity field $\mathbf{V}$ is possible to write the adiabatic energy losses as

$$\left(\frac{\mathrm{d}E}{\mathrm{d}t}\right)_{\mathrm{adb}} = -\frac{1}{3}\left(\nabla \cdot \mathbf{V}\right) E \tag{2.21}$$

e) Radiative losses

The term $b(p)$, usually defined in terms of energy as $b(E) = -\left(\mathrm{d}E/\mathrm{d}t\right)_{\mathrm{rad}}$, corresponds to the energy losses or cooling, that provides the rate of change in the energy of a single cosmic-ray particle due to radiative processes suffered in the ISM. Depending on the particle to be studied some losses prevail over others. Among them, synchrotron emission, cyclotron radiation, ICS, *bremsstrahlung*, ionization and Coulombian losses.

• Charged particles could be deflected by galactic magnetic fields resulting in the emission of electromagnetic radiation. Depending on the velocity regime of such charged particles, two different emissions could be distinguished. On the one hand, namely *cyclotron radiation* in the case of non-relativistic particles, emission lines are associated to this kind of radiation. The frequency of emission is merely the frequency of gyration. Cyclotron signals would not be detected from extragalactic sources with magnetic fields $B \sim \mu$G since its frequency ($\nu \sim$ Hz) is lower than the plasma frequency limit ($\nu_{\rm p} \sim 2$ kHz) of the ISM. In this regard, only some targets with extremely high magnetic fields, such as neutron stars, would provide detectable signatures. On the other hand, ultra-relativistic particles interacting with magnetic fields would emit in a continuous range of frequencies, yielding the *synchrotron emission* expected typically in radio frequencies.

• In the *ICS*, particles scatter background photons from the interstellar radiation field (IRF). If the moving particle has sufficient kinetic energy compared to the photon, some energy may be transferred from the particle to the photon. Therefore, photons results more energetic after colliding in the reaction $e^- + \gamma(E) \rightarrow e^- + \gamma(E')$ with $E' > E$, where the expected signal is typically from X-ray to γ-ray.

In the ICS, two energy regimes can be usually distinguished. A first one corresponds to the Thomson regime, in which the mass of the particle is much lower than the energy of the incident photon. The scattering is almost elastic and well determined with the Thomson cross section. The result is a small transfer of energy to the photon, thus, the frequency is practically equal ($E \sim E'$). A second one is the highly-inelastic Klein-Nishina regime with E larger than the rest energy of particles. The Thomson cross section does not provide a full description of the process and a treatment in QED is necessary.

Furthermore, the IRF has to be determined for a proper description of ICS losses. Three main contributions are expected to the IRF. Firstly, the predominant stellar contribution of late spectral classes with its peak of emission in the near-infrared and an energy density of $0.5\,\mathrm{cm}^3/\mathrm{s}$ [196]¶. Second, the dust component heated by absorption of starlight and emitting in far-infrared. The energy density of this emission is estimated in $0.05\,\mathrm{cm}^3/\mathrm{s}$ and $0.3\,\mathrm{cm}^3/\mathrm{s}$ [196–198]. Third, photons from the CMB with an energy density of $0.25\,\mathrm{cm}^3/\mathrm{s}$.

• The *bremsstrahlung*, sometimes called free-free radiation in plasma physics, holds the deceleration of particles when it is deflected thermal ions and e^-. Even though *bremsstrahlung* would also include cyclotron and synchrotron radiation also, the name is usually used for charged particles accelerated in matter. *Bremsstrahlung* is unlikely dominant unless the density is higher than the typical in the bulk of the ISM. In this regard, their effects could be important for the γ-ray spectrum, mostly from directions close to the Galactic Plane.

In their classical description ($E << Z^2 2\pi\hbar c R_\infty$) a charged particle pass close to the surroundings of an ion of charge Ze with an impact parameter b_c. However, in order to understand the process completely, it is required a quantum treatment since photons with energies comparable to the incident particle can be produced in the atom. The usual treatment consists of developing a classical description of the process and treat the quantum effects as corrections by using the Kramers-Gaunt factors. In addition, the relativistic case can be addressed with the virtual quanta, which allows to describe the *bremsstrahlung* as an ICS in a reference frame where the particles are initially at rest and the ion is moving towards the particle. In such a reference frame, the electrostatic field of the ion can be seen as a transversal electromagnetic pulse.

¶Also, a stellar component with stars of class OB is expected in UV but the energy density is very low with respect to the late ones.

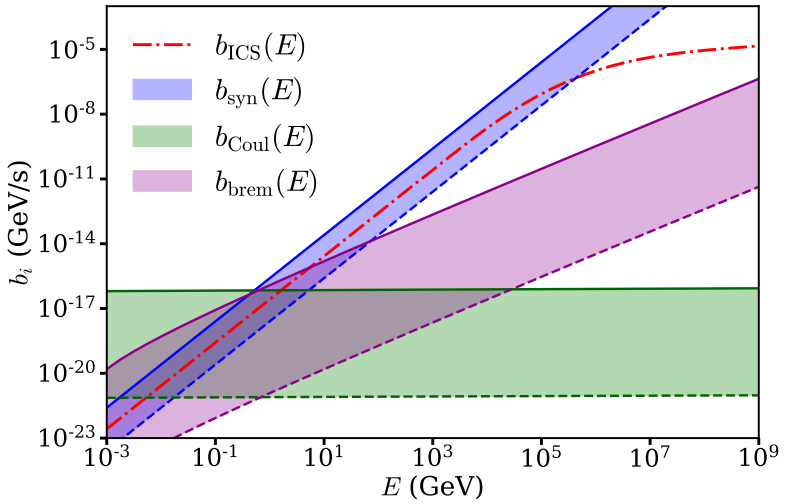

FIGURE 2.1: Radiative losses b_i dependence on the e^+/e^- kinetic energy E [199]. The blue band corresponding to synchrotron emission has been computed for a magnetic field between $B = 1$ μG (dashed line) and $B = 10$ μG (solid line). The bands for *bremsstrahlung* and Coulombian losses take into account the electron number density of the medium, n_e, between 10^{-6} cm^{-3} (dashed) for dwarf spheroidals (dSphs) and 0.1 cm^{-3} (solid) for galaxies. The analytical expressions for all the radiative losses in terms of n_e and B can be found following [179, 200, 201]. While Coulombian losses dominate at low energies, synchrotron emission and ICS lead the e^+/e^- emission signals at higher energies. For ICS losses both the Thomson and Klein-Nishina regimes have been considered in the interaction of e^+/e^- with the CMB photons with a temperature $T_0 = T_{\gamma 0} = 2.73$ K [202].

• Finally, *ionization* and *Coulomb losses* are referred to the interaction with neutral matter or with ionised plasma respectively. Indeed, high energy cosmic rays traversing atoms would lose energy due to the ionization and excitation of atomic levels, while in Coulomb losses it is produced mainly by the inelastic collisions of individual plasma particles together with the excitations of collective motions of the plasma. Indeed, in Coulomb losses, collision and plasma oscillation effects are considered, whose minimum excitation corresponds to the energy $h\nu_p$.

Sychrotron emission, ICS, Coulombian losses and *bremsstrahlung* would be relevant for e^+/e^- at different range of energies. Conversely, heavier particles as nuclei would see suppressed their loss emission inversely proportional to the powers of their masses (i.e., for protons, $m_e/m_p \sim 5 \cdot 10^{-4}$). The only mechanism significant for nuclei are Coulombian losses and ionization in the galactic disk, although negligible when it is compared to the e^+/e^- energy losses. Focusing on the e^+/e^- case, we present the expressions for the energy losses [179, 200–202]. Firstly, the synchrotron losses yields

$$b_{\rm synch}(\mathbf{r}, E) = \frac{4}{3}\frac{\sigma_T}{m_e^3 c^5} E^2 U_B(\mathbf{r}), \tag{2.22}$$

where σ_T is the Thomson cross section for e^- and U_B is the magnetic energy density in cgs, defined as $U_B(\mathbf{r}) = B^2(\mathbf{r})/8\pi$. Second, *bremsstrahlung* and Coulomb losses, whose main effect considered in this work is due to the interaction with thermal e^- of the ISM, with a number density n_e. For both energy losses, the expressions are

$$b_{\rm brem}(E) = 1.51 \cdot 10^{-16} n_e E \left[\log(E/m_e) + 0.36\right], \tag{2.23}$$

and

$$b_{Coul}(E) = 6.13 \cdot 10^{-16} n_e \left[1 + \log(E/n_e m_e)/75\right]. \tag{2.24}$$

Indeed, n_e, the electron number density, would vary according to the environment. For our galaxy, the estimation is $n_e \sim 0.1\,\mathrm{cm}^{-3}$, while for dSphs or a cluster of galaxies would be $n_e \sim 10^{-6}\,\mathrm{cm}^{-3}$ and $n_e \sim 10^{-3}\,\mathrm{cm}^{-3}$ respectively. Third, three different regimes are differentiated for ICS, according to what it was mentioned above in this section. The Thomson regime (for $\frac{\gamma k_b T_0}{m_e c^2} < 3.8 \cdot 10^{-4}$) and the Klein-Nishina ($1.8 \cdot 10^3 < \frac{\gamma k_b T_0}{m_e c^2}$) have been considered in the following expression:

$$b_{\mathrm{ICS}}(E) = \begin{cases} \frac{4}{3}\frac{\sigma_T}{m_e c}\gamma^2 U_{\mathrm{rad}} & \text{if } \frac{\gamma k_b T_0}{m_e c^2} < 3.8 \cdot 10^{-4} \\ \frac{E^2 m_e c^2 (k_b T_0)^3}{\gamma} \exp\left[\sum_{i=0}^{5} c_i \left(\ln \frac{\gamma k_b T_0}{m_e c^2}\right)^i\right] & \text{if } 3.8 \cdot 10^{-4} < \frac{\gamma k_b T_0}{m_e c^2} < 1.8 \cdot 10^3 \\ \frac{\sigma_T}{16}\frac{(m_e k_b T_0)^2}{\hbar^3}\left(\ln \frac{4\gamma k_b T_0}{m_e c^2} - 1.9805\right) & \text{if } 1.8 \cdot 10^3 < \frac{\gamma k_b T_0}{m_e c^2}, \end{cases} \tag{2.25}$$

with an intermediate region linking both behaviours. For the intermediate region, $c_i = \left\{74.44, -0.1953, -9.97 \cdot 10^{-2}, 4.352 \cdot 10^{-3}, 3.546 \cdot 10^{-4}, -3.01 \cdot 10^{-5}\right\}$ [202]. On the other hand, σ_T, k_b and T_0 are the Thomson cross section, the Boltzmann constant and the temperature of the gas of photons respectively. In our case, we considered the contribution of the CMB, thus, $T_0 = T_{\gamma 0} = 2.73$ K.

In Fig. 2.1, the most relevant energy losses for e^+/e^- are plotted. There, colour bands show the dependence of the energy losses the electron density n_e (0.1 cm^{-3} for galaxies [203] and 10^{-6} cm^{-3} for dSphs [204]) and with the magnetic field (taken as constant $B(\mathrm{r}) = B$, with B between 1 μG and 10 μG). Synchrotron and ICS are dominant at high energies beyond GeV whereas *bremsstrahlung* and Coulombian losses predominate the sub-GeV range. Some of the above mechanisms prevail over others at different energies in different targets, as shown in Fig. 2.1, where energy losses due to *bremsstrahlung*, Coulombian, ICS and synchrotron emission have been depicted. The most significant loss mechanisms for e^+/e^- constitute the energy loss function

$$b(\mathbf{r}, E) = b_{\mathrm{syn}}(\mathbf{r}, E) + b_{\mathrm{ICS}}(E) + b_{\mathrm{brem}}(E) + b_{\mathrm{Coul}}(E). \tag{2.26}$$

2.5 Indirect dark matter searches with e^+/e^-

In the following, we will focus on the assumptions on the transport equation (Eq. 2.10) for e^+/e^- and the solution in this specific case.

2.5.1 Assumptions and solution for cosmic-ray transport

In Section 2.4.1, we referred the general expression for the transport of cosmic rays injected by a source term $q(\mathbf{r}, p, t)$. Now, let us focus on the specific cases of DM annihilating into SM particles producing e^+/e^- as a final state. This fact will allow us to do some considerations on the general transport equation (Eq. 2.10) presented previously.

First of all, we shall remark that in our calculations we are only interested on the component of cosmic rays injected by annihilating DM. The rest will be consider as a part of the astrophysical background as we will discuss in the next Chapter. This means that we consider a primary component for e^+/e^- since it is directly injected from the source and not due to collisions of

particles in the ISM, thus,

$$q_e(\mathbf{r},p,t) = q_e^{\rm prim}(\mathbf{r},p,t) = q_e^{\rm DM}(\mathbf{r},p,t) = \frac{1}{2}\langle\sigma v\rangle\left(\frac{\rho_{\rm DM}(\mathbf{r})}{M}\right)^2\sum_j \beta_j \frac{{\rm d}N_e^j}{{\rm d}E}. \tag{2.27}$$

Moreover, the diffusion in e^+/e^- travelling ultra relativistically along the ISM is expected to be dominant, however convection and reacceleration may have an important role at some range of energies E. In general, convection, solar wind modulation and reacceleration are negligible in two cases considered in upcoming sections. First, for e^+/e^- reaching the Solar System with energies above a few GeV [205]. This is the case we will see in Chapter 3. Second, for targets with low baryonic content and low ISM, it is generally assumed that diffusion is the predominant way of transport. This is the case we will see in Chapter 5. Under these conditions and assuming the quasi-stationary regime, i.e., $\partial\psi(E,\mathbf{r},t)/\partial t \simeq 0$, the transport equation (Eq. 2.10) can be rewritten as a purely diffusion expression that, for annihilating DM, it renders

$$-D_0 E^\delta \nabla^2\psi - \frac{\partial}{\partial E}\left[b(\mathbf{r},E)\psi\right] = \frac{1}{2}\langle\sigma v\rangle\left(\frac{\rho_{\rm DM}(\mathbf{r})}{M}\right)^2\sum_j \beta_j \frac{{\rm d}N_e^j}{{\rm d}E}\,. \tag{2.28}$$

This equation can be solved by the Green's method. The coordinates in the Laplacian together with the boundary conditions define the symmetry of the problem and also the kind of solution. This forces us to specify the target under consideration in our studies. In fact, two targets have been considered along this investigation: the Milky Way and dSphs. The Green's solutions for both targets is only valid under the condition $b(\mathbf{r},E) \simeq b(E)$ in the Green function. Indeed, we approximate $b_{\rm syn}(\mathbf{r},E) \sim b_{\rm syn}(E)$, with an averaged magnetic field $B_{\rm avg}$. This approximation is solely considered in the determination of the quantity λ_D that we will see here below, being the spatial dependence in $b_{\rm syn}(\mathbf{r},E)$ fully considered for the rest of functions. This is the usual approach followed in [179, 204]. Therefore, the targets under discussion in our work together with their solutions of Eq. (2.28) are

- The Milky Way, in which e^+/e^- are assumed to be confined inside a propagation region described by a cylinder of radius R and thickness $2L_z$ centred at the centre of the galaxy. The radius of the diffusion disk is taken as $R = 20\,{\rm kpc}$ (close to the galactic disk value) and the vertical half-thickness L_z depends on the diffusion model. Outside the propagation zone, e^+/e^- are no longer confined by the magnetic field so their density is expected to rapidly drop and it would be negligible with respect to the rest of the density within the disk. Therefore, the boundary conditions to solve the Eq. (2.28) are $\psi(R,z) = 0$ and $\psi(r,\pm L_z) = 0$. For this specific problem, we will consider the solution in [206], where the e^+/e^- density ψ is expanded as the Bessel series. Indeed, the Green's method presents a problem at imposing $r = R$ so the Bessel approach has been proposed as an improvement of the usual Green formalism.

$$\psi(\mathbf{r},E) = \sum_{i=1}^{\infty}\sum_{n=0}^{\infty} J_0\left(\frac{\alpha_{0,i}}{R}r\right)\varphi_b(z)\,P_{i,n}(\mathbf{r},E), \tag{2.29}$$

where J_0 are Bessel functions of the first kind with $\alpha_{0,i}$ zeros and $\varphi_b(z) = \sin\left(\frac{n\pi}{2L}(z+L_z)\right)$. On the other hand, $P_{i,n}(\mathbf{r},E)$ renders

$$P_{i,n}(\mathbf{r},E) \;=\; \frac{1}{b(\mathbf{r},E)}\int_E^M {\rm d}E_s\, Q_{i,n}(E_s)\exp\left\{-\frac{\lambda_D^2(E,E_s)}{4}\left[\left(\frac{n\pi}{2L_z}\right)^2 + \left(\frac{\alpha_i^2}{R^2}\right)\right]\right\}.$$

In this method, e^+/e^- are injected at x_s and time t_s with an energy E_s. Once a particle is injected at the source point, it reaches the coordinate (x,t) with an energy E. The distance between these

two points is called the diffusion length λ_D such as

$$\lambda_D^2(E, E_s) = 4 \int_E^{Es} \mathrm{d}\varepsilon \, \frac{D_0 \, \varepsilon^\delta}{b(\varepsilon)}. \tag{2.30}$$

On the other hand, the factor $Q_{i,n}(E_s)$ in expression (2.30) corresponds to the Bessel and Fourier transforms of the source term yielding

$$Q_{i,n}(E_s) \quad = \quad \frac{2}{L_z \, R^2 \, J_1^2(\alpha_i)} \int_0^R \int_{-L_z}^{L_z} r \, \mathrm{d}r \, \mathrm{d}z \; J_0\left(\frac{\alpha_i}{R} r\right) \varphi_b(z) \, q(\mathbf{r}, E_s), \tag{2.31}$$

where α_i are the zeros of the Bessel function J_0.

- dSphs, whose diffusion is usually assumed spherically symmetric. The radius of the diffusion region is r_h at which a free escape boundary condition is imposed. After a suitable change of variables, the diffusion equation Eq. (2.28) can be rewritten as a heat-like equation [207] obtaining

$$\psi(\mathbf{r}, E) = \frac{1}{b(\mathbf{r}, E)} \int_E^M \mathrm{d}E_s \, G(r, E, E_s) \, q(\mathbf{r}, E_s), \tag{2.32}$$

in terms of Green's function $G(r, E, E_s)$. The spherical symmetry of the problem suggests the image charge method over the Green's function, as explained in [207, 208] in which charges are positioned at $r_n = (-1)^n r + 2nr_h$. Thus $G(r, E, E_s)$ turns into

$$\begin{aligned} G(r, E, E_s) = & \frac{1}{\sqrt{\pi \lambda_D^2(E, E_s)}} \sum_{n=-\infty}^{\infty} (-1)^n \int_0^{r_h} \mathrm{d}r' \frac{r'}{r_n} \\ & \times \left(\frac{\rho_{\mathrm{DM}}(r')}{\rho_{\mathrm{DM}}(r)}\right)^2 \left[\exp(-g_n^-) - \exp(-g_n^+)\right], \end{aligned} \tag{2.33}$$

with $g_n^\pm(r', E, E_s) = \frac{(r' \pm r_n r)^2}{\lambda_D^2(E, E_s)}$ and a radius of diffusion r_h. In the above expression, $\lambda_D(E, E_s)$ is the mean free path of e^+/e^- described above.

2.5.2 Signals from dark matter annihilation

In this section we will focus on the signatures used to set constraints on DM in the next chapters:

- On the one hand, once we solve the diffusion equation, Eq. (2.28), we obtain the number density of e^+/e^- per unit of energy after the process of diffusion. The first signature one could detect is the e^+/e^- flux reaching the Earth by cosmic-ray detectors, such as PAMELA, Fermi-LAT or AMS. In this regard, the description we have to use for this calculation is that for the Milky Way in cylindrical coordinates. The only requirement is imposing the coordinates of the Earth from the GC, considering that the origin of the coordinates has been established at the centre of the cylinder, and thus, the centre of the Milky Way. After that, the e^+/e^- flux would be a function of the e^+/e^- kinetic energy, E. Indeed the e^+/e^- flux can be expressed as follows

$$\Phi_{e^+/e^-}^{\mathrm{DM}}(\mathbf{r}_\odot, E) = \frac{v_e(E)}{4\pi c} \psi(\mathbf{r}_\odot, E), \tag{2.34}$$

with the condition $r = \mathbf{r}_\odot$ and taking as $\mathbf{r}_\odot \sim 8$ kpc. Furthermore, considering a high diffusion and low reacceleration for energies $E > 10\,\mathrm{GeV}$ ultra-relativistic e^-/e^+ would reach the limit

$v_e(E) \simeq c$. The e^+/e^- flux, $\Phi^{\rm DM}_{e^\pm}(\mathbf{r}_\odot, E)$ would only give information about one coordinate in the Galaxy, and therefore, this detectable signal would not count with spatial information. In our work, we shall compute the e^+/e^- flux at the Earth, $\Phi^{\rm DM}_{e^+/e^-}(\mathbf{r}_\odot, E)$ and compare it with the current data.

- Furthermore, as already mentioned in the previous section, $b(\mathrm{r}, E)$ leads the emission of photons in a long range of frequencies due to the loss of energy of e^+/e^-. In fact, solving the diffusion equation, Eq. (2.28), we obtain the number density per unit of energy $\psi(\mathbf{r}, E)$ of e^+/e^- at each galactic coordinate. In other words, we calculate the number density per unit of energy of the emitters responsible for the photons emission at the coordinate $\mathbf{r}$. Associating a radiative power to each emitter $\psi(\mathbf{r}, E)$, it is immediate calculating the emissivity for such processes through

$$j_\nu(\mathbf{r}, z) \;=\; \int_E^M \mathrm{d}E\,(\psi_{e^+} + \psi_{e^-})\,P(\nu, \mathbf{r}, E, z) = 2\int_E^M \mathrm{d}E\,\psi(\mathbf{r}, E)P(\nu, \mathbf{r}, E, z), \tag{2.35}$$

where $j_\nu(\mathbf{r}, z)$ accounts for the emissivity both for e^- and e^+. In addition, $P(\nu, \mathbf{r}, E, z)$ is the power associated with the emission process. In this work, we will focus on the synchrotron emission as a result of the interaction of e^+/e^- with the magnetic field. The predominant emission is expected to happen in radio frequencies. Other signals from either ICS or *bremsstrahlung* would be expected in the range of γ-ray. The steps for their calculation would be the same as that we will present for synchrotron emission but with another power corresponding to the emission process. As already mentioned, each e^+/e^- is responsible for the synchrotron power of emission, $P_{\rm syn}(\nu, \mathrm{r}, E, z)$ that relates the e^+/e^- kinetic energy E with the frequency of emission. The emitted power of a single e^+/e^- at redshift $z \approx 0$ is

$$P(\nu, \mathbf{r}, E, z) = P_{\rm syn}(\nu, \mathbf{r}, E, z) = \int_0^\pi \mathrm{d}\alpha \frac{\sin^2\alpha}{4\pi\epsilon_0}\frac{\sqrt{3}e^3 B(\mathbf{r})}{m_e c} F_i\left(\frac{\nu(1+z)}{\nu_c(\mathbf{r}, E)\sin\alpha}\right) \tag{2.36}$$

with

$$F_i(u) \;=\; u\int_u^\infty \mathrm{d}\xi\, K_{\frac{5}{3}}(\xi) \simeq \frac{5}{4}u^{\frac{1}{3}}\exp(-u)\left(648 + u^2\right)^{1/12}, \tag{2.37}$$

being $K_{\frac{5}{3}}(\xi)$ a modified Bessel function, ϵ_0 the vacuum permittivity and α the angle formed by the perpendicular component of the magnetic field with respect to the e^+/e^- momentum. Moreover, $\nu_c(\mathbf{r}, E)$ holds for the critical frequency

$$\nu_c(\mathbf{r}, E) = \frac{3eB(\mathbf{r})}{4\pi m_e}\gamma^2(E). \tag{2.38}$$

Close to this frequency, e^+/e^- emit the most part of their energy. Once ψ is obtained from Eq. (2.32), the specific intensity I_ν (i.e, the magnitude usually measured by radio telescopes) can be computed by integrating $j_\nu(\mathbf{r}, z)$, Eq. (2.35), over the l.o.s. Here, it is important to remark that a change of coordinates would be necessary to calculate the specific intensity $I_\nu(\theta, z)$. Indeed, the diffusion problem for Eq. (2.28) is being defined at the centre of the galaxy, both for the Milky Way and dSphs, while the detection is at the Earth coordinates. This does not imply an issue for the computation of the positron fraction since $\Phi^{\rm DM}_{e^+/e^-}(\mathbf{r}_\odot, E)$ is related to one point of coordinates $\mathbf{r}_\odot$ from the GC, as mentioned. However, the synchrotron emission received at the Earth from different directions of the Universe requires a change of coordinates, locating the radio telescope at the origin. In this work, we considered two changes of coordinates:

- For the Milky Way, we follow $r = \sqrt{r_\odot^2 + s^2\cos(b)^2 - 2r_\odot s\cos l\cos b}$ and $z = s\sin b$, where b

is the galactic latitude, l is the galactic longitude in the galactic coordinate system and $r_\odot = 8$ kpc.

- For dSphs, the limits of integration are $s_{\max/\min} = d_t \cos\theta \pm \sqrt{r_h^2 - d_t^2 \sin^2\theta}$ and $r = \sqrt{d_t^2 - 2 d_t s \cos(\theta) + s^2}$, being θ the angle subtended from the centre to any point of the target, r_h the radius of diffusion and d_t the distance to the target [209].

In both expressions above, s accounts for the line joining the telescope and the centre of the target. As mentioned, integrating over the l.o.s. would give us the contribution of the emission rate over an entire column along the l.o.s. of the detector, obtaining the specific intensity

$$I_\nu(l, b, z) = \int_{\text{l.o.s.}} \mathrm{d}s \, \frac{j_\nu(s, l, b, z)}{4\pi}, \tag{2.39}$$

where l and b represents the galactic coordinates (l, b) from the Earth. In the case of dSphs, the specific intensity has spherical symmetry and then

$$I_\nu(\theta, z) = \int_{\text{l.o.s.}} \mathrm{d}s \, \frac{j_\nu(s, \theta, z)}{4\pi}, \tag{2.40}$$

where θ is the angle subtended from the centre of the dSphs. Furthermore, the emission from a volume, is determined by the flux density $S_\nu(z)$ over the solid angle Ω is given by

$$S_\nu(z) = \int_\Omega \mathrm{d}\Omega \, I_\nu(\theta, z) \, . \tag{2.41}$$

In our work, we shall compute the specific intensity $I_\nu(\theta, z)$ and the flux density $S_\nu(z)$, solving Eq. (2.28) in order to set constraints on DM. The specific intensity, $I_\nu(\theta, z)$, provides a differential distribution of the emission along the angular size of the source; and the flux density, which takes into account the integrated flux over either the angular size of the source or the beam selected for the analysis. Whereas the specific intensity I_ν rather focuses on the spatial distribution of the target, the advantage of working with the flux density is that such a quantity allows us to determine the best frequency range - and therefore suitable detectors - to detect specific DM candidates. Furthermore, we will use $I_\nu(\theta, z)$ to extract spatial information of the synchrotron signals from annihilating DM and we also compare $S_\nu(z)$ with the sensitivity from radio telescopes such as the Square Kilometre Array (SKA).

2.5.3 Detectors

In the following, we shall describe the characteristics of the detectors relevant for our analysis

a) Cosmic-ray detectors

- **AMS**

At 400 km altitude, the Alpha Magnetic Spectrometer, AMS (*c.f.* [210–212] for a thorough insight on AMS technicalities), is an external module installed on the International Space Station designed to detect cosmic rays in the range of energies of GeV-TeV. The main goals of the project are studying the abundances and propagation of cosmic rays (heavy species) but also the direct detection of antimatter and DM through positrons and antiprotons production. The design is prepared to operate until $\sim$ 2030 and the whole detector counts on 7.5 tons in a volume of $5\,\text{m} \times 4\,\text{m} \times 3\,\text{m}$ whose acceptance is $\sim 0.5\,\text{m}^2\text{sr}$. AMS is composed of different elements,

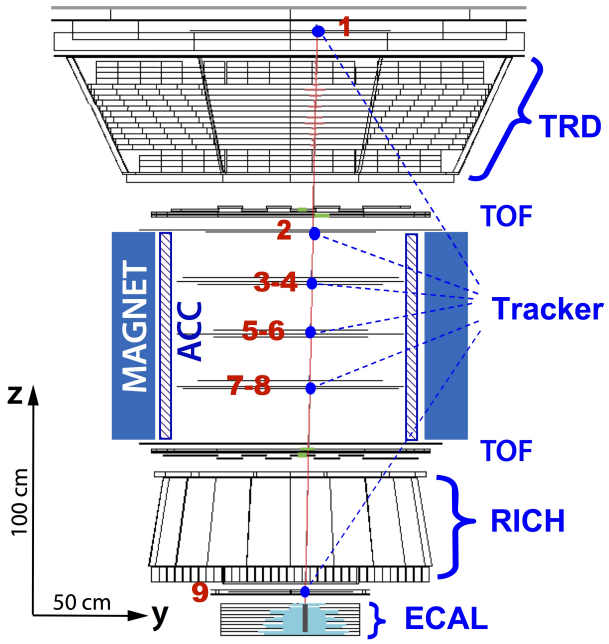

FIGURE 2.2: From Aguilar *et al.* 2013 [210]. Schematic representation of the bending (y-z) plane of AMS detector and its components

presented in Fig. 2.2, consisting of nine silicon trackers in different parts of the detector, a transition radiation detector (TRD), the time of flight detector (TOF), a magnet, anticoincidence counters (ACC) in the inner tracker surroundings, a ring imaging Cherenkov detector (RICH) and an electromagnetic calorimeter (ECAL).

First, silicon trackers can determine the trajectory and the absolute charge measuring the coordinates and the energy loss of the incident particles. In total, there are 9 trackers, one at the entrance of the module, on the top of TRD, the second below the TOF with other six constituting the inner tracker and the ninth tracker between RICH and ECAL.

Second, the TRD that allows to distinguish between e^+/e^- from protons through the transition radiation (TR), and also different nuclei through the particle energy deposition $\mathrm{d}E/\mathrm{d}x$. Indeed, e^+/e^- can be distinguished from protons by measuring its TR-Xray. High energy charged particles crossing the interface among different dielectrics produce photons at small angles with energies $\sim 5-30\,\mathrm{keV}$. In order to carry out this radiative detection, AMS accounts for 20 layers of 5248 tubes filled with Xe/CO_2 arranged in 16-tube modules and alternating with layer of fibre fleece radiator of $0.006\,\mathrm{g/cm^3}$. The tubes are able to measure X-ray and the particle energy deposition $\mathrm{d}E/\mathrm{d}x$, while the fleece maximises the number of points in which a TR X-ray can be generated.

Third, two planes with TOF, above the magnet (below the TRD), and two planes below the magnet allowing to measure the time of particles with a precision of 160 ps, and therefore, both Z and $\beta = v/c$ with a resolution of $\delta Z = 0.05$ (at $Z = 1$) and a resolution of 4% (at $Z = 1, \beta \sim 1$) respectively. Each plane includes scintillating paddles with photomultiplier tubes indicating when the clock is activated and stopped. The magnet produces a magnetic field of 1.4 kG in the x direction (see Fig. 2.2), allowing to separate charges $\pm Z$. Furthermore, the ACC, composed of sixteen scintillators, surrounds the inner tracker to determined events of particles that leave or enter the inner tracker, being unwanted for the experiment. In addition, RICH is a high precision detector for the velocity $\Delta\beta/\beta \sim 10^{-3}$ and magnitude charge, Z through the

Cherenkov radiation of particles impacting two dielectric radiators with refractive indices of $n = 1.33$ and $n = 1.05$. Placed at the base of RICH, 10880 photosensors detect the Cherenkov radiation.

Finally, ECAL is the electromagnetic calorimeter that provides a 3D image of the cosmic-ray shower allowing to determine not only the energy but also the direction of γ-rays and e^-/e^+. In order to do this, ECAL is constituted by a multilayer sandwich of 98 lead foils and around $5 \cdot 10^5$ scintillating fibres.

- **Fermi-LAT**

Even though it was designed for the study of γ-ray photons, the Fermi Large Area Telescope, Fermi-LAT (*c.f.* [213, 214] for a thorough insight on Fermi-LAT technicalities), is a satellite prepared to detect and identify charged particles at an altitude around 500 km. Indeed, the LAT is a pair-conversion detector conceived to reconstruct electromagnetic showers. Considering that electromagnetic showers produced from an e^+/e^- or a γ are similar, the measurement techniques are the same. Therefore, Fermi-LAT also can report a measure of the e^+/e^- flux.

Fermi-LAT combines measurements from different modules. First, an anticoincidence detector (ACD)[‖], constructed from tiles of plastic scintillators, is placed surrounding all the upper panel of the LAT. The ACD produces flashes of light when it is reached by charged cosmic rays, allowing to separate them from γ-rays that would pass without interacting. Second, below the ACD, the tracker/converter, composed by silicon micro-strip planes interleaved with tungsten. The tracker facilitates the pair creation from photons interacting with the tungsten but also measures the e^+/e^- direction in their interaction with the silicon. Third, an electromagnetic calorimeter (CAL) with 8 layers of CsI(Tl) crystals that enable us to measure the energy of the particles and reconstruct the shower.

Should the purpose rely on detecting charged particles, then the events considered are required to not pass the ACD criteria to select photon events. Even though the Fermi-LAT filters (due to the ACD but also the software of the data acquisition system) are designed to reject charged particles, all events with deposition energy in the CAL larger than 20 GeV are accepted. However, studying energies beyond 1 TeV implies a big challenge since at those energies only $\sim 35\,\%$ of the shower is inside the CAL and also a significant fraction of the CAL crystals can be saturated. In this case, alternative methods improving the track and shower reconstruction have to be considered together with strategies to remove the background [215].

- **PAMELA**

The Payload for Antimatter Matter Exploration and Light-nuclei Astrophysics (PAMELA) (*c.f.* [137] for a thorough insight on PAMELA technicalities) was a module incorporated in the Russian Resurs-DK1 satellite launched from the years 2006 to 2016. With a weight of 470 kg and an acceptance of $21.5\,\mathrm{cm^2 sr}$, PAMELA was mainly devoted to detect cosmic-ray antimatter, mainly, antiprotons and positrons (and also searches of antinuclei) but also electrons, protons, He and nuclei from Li to O. PAMELA consisted of a TOF, an anticoincidence system (ACS), a permanent magnet spectrometer, an electromagnetic calorimeter, a shower tail catcher scintillator and a neutron detector.

The TOF was constituted by 6 layers of plastic scintillators assembled in three planes and where each pair of layers was placed orthogonally. The TOF was combined with the track length information from the magnetic spectrometer to determine particle velocities and reject albedo

[‖] Although the anticoincidence detector was referred to as ACC in AMS, we have sought to maintain the original names used in each detector.

particles. The scintillator layers allowed to measure the $\mathrm{d}E/\mathrm{d}x$ from ionization up to $Z = 8$. In addition, two ACS were included. One of them consisted of 4 plastic scintillators surrounding the magnet and covering the top. The second ACS consisted of 4 plastic scintillators surrounding two of the TOF planes. The magnetic spectrometer was formed by the permanent magnet and a silicon tracker that allowed to determine the charge of the particle (through ionization losses) up to Z=6 and its sign together with the momentum. The electromagnetic calorimeter was constituted by 44 single-sided silicon sensor planes interleaved with 22 plates of tungsten, allowing to identify among electromagnetic and hadronic showers and also to reconstruct them.

b) Radio telescopes

- **SKA telescope**

The Square Kilometre Array (SKA) program (*c.f.* [139, 216] for a thorough insight on SKA technicalities) is an international endeavour to develop one of the largest radio telescopes. Its interferometric settings have been configured as an improvement of the angular resolution of single-dish detectors. In this respect, a long baseline would reduce the hard diffraction limit of radio waves guaranteeing a high resolution. In addition, a competitive sensitivity is ensured as the result of combining the baseline length with a large effective area of collection A_e. Specifically, SKA is constituted by a low-frequency aperture array situated in Australia (SKA-LOW) and a mid-frequency array of reflector antennas, placed in South Africa (SKA-MID). Currently, the SKA precursors such as ASKAP [217], KAT-7 [218] and MeerKAT [219] are operating and being prepared towards a definite phase, the SKA-Phase 1 (SKA1).

The SKA1-LOW will be constituted by around $131,000$ log-periodic dual polarised antennas. Some of these are grouped in a 1 km compact core while the rest constitutes approximately 512 stations allocated along 40-km. Each station would reach 10s meters of diameter. The frequency range of SKA1-LOW lies between 50 MHz and 350 MHz according to the lengths of the shortest and longest dipole antenna elements. After antennas collect the radio waves, the signal is built in a particular direction introducing a time delay. This allows to synthesize a signal beam, where the signals of different antenna pairs are cross-correlated through the correlator. The combination of different sets of timing delays enables to construct independent signal beams covering a large Field of View (FoV) and increasing the survey speed. The limitations for such FoV is given by the signal processing. After this signal processing, a visibility map is obtained together with the details of the specific intensity of the source.

Conversely, SKA1-MID frequency range is separated into five different frequency bands ranging from 350 MHz to $\sim$ 14 GHz**. The SKA1-LOW includes 64 dishes (13.5-m diameter per dish) from the MeerKAT and 190 15-m built especially for the SKA1. The antennas will be allocated in a $\sim$ 1 km compact core, a 2-dimensional array of randomly distributed dishes until to $\sim$ 3 km radius and three spiral arms out to a radius of $\sim$ 80 km. Once the signal is measured and cross-correlated with each other, a processing analysis is performed.

Both high resolution and sensitivity are critical in the detection of radio faint sources, goals that SKA1 is able to attain. For the former, the spatial configuration of the SKA1 allows to develop antenna configuration strategies to achieve a high angular resolution. Although radio-astronomy presents more limitations than higher frequency astronomy, the SKA1 baseline lengths ensure one of the highest angular resolutions according to the Rayleigh standard, $\theta_{\mathrm{res}} = 58.61\lambda/D_{\mathrm{base}}$ (in deg) where λ is the wavelength of the inward signal and D_{base} is the baseline length. At 350 MHz, i.e., the frequency that separate SKA1-LOW and SKA1-MID, $\theta_{\mathrm{res}} \sim 0.001$ deg provided a baseline $D_{\mathrm{base}} = 50$ km (SKA1-LOW) while it lies in $\theta_{\mathrm{res}} \sim 2.5 \cdot 10^{-4}$ deg for a baseline of

**In principle, the dishes would be able to measure until 20 GHz.

$D_{\rm base} = 200$ km (SKA1-MID). Besides the higher resolutions ensured by long baselines, it is also necessary to optimise the interferometric strategies (the spatial configuration and the effective area A_e) to not compromise the sensitivity in the measurement. This sensitivity would indicate us the minimal detectable flux $S_{\rm min}$ through the radiometer equation

$$S_{\rm min} = \frac{2k_b T_{\rm sys}}{\eta_s A_e (\eta_{\rm pol} \tau \Delta\nu)^{1/2}}\,, \tag{2.42}$$

for a bandwidth $\Delta\nu$ in an interval of time τ, where k_b is the Boltzmann constant, η_{pol} is the number of polarisation states, and $\eta_s \sim 0.9$ the efficiency of the system. The effective area A_e is taken in this expression as the result of combining a set of antennas. Indeed, A_e accounts for the efficiency when the electromagnetic wave is collected and depends on the frequency and the gain of the receptor. For SKA1-LOW, there exist two different behaviours for frequencies lower and greater than 110 MHz, according to the sparse-dense transition of the detector. The sparse transition takes place when the antenna elements are more distant than around one wavelength acting independently and making the A_e to be proportional to λ^2. In the dense transition, i.e., when the separation is smaller than ~ 0.5 times the incoming wavelength, the interaction between the antenna elements force the A_e to be constant. With regard to the system noise temperature in Eq. (2.42),

$$T_{\rm sys} = T_{\rm sky} + T_{\rm rcvr}\,, \tag{2.43}$$

it can be separated into two contributions, the sky noise $T_{\rm sky}$, i.e., all the sky emission different of the target we would like to measure, and the receiver noise or instrument noise, $T_{\rm rcvr}$. $T_{\rm rcvr}$ only dominates in frequencies smaller than 250 MHz and it is considered as a constant temperature (~ 40 K) plus a 10% of $T_{\rm sky}$. Conversely, the SKA FoV is tied with diameter of the dish $D_{\rm dish}$ [139]

$$\Omega_{\rm FoV} = \frac{\pi}{4}\left(\frac{66\lambda}{D_{\rm dish}}\right)^2. \tag{2.44}$$

For SKA1-LOW, 35 m circular stations are formed by a group of related dipole antennas and, in principle, it is possible to take $D_{\rm dish} = 35$ m, being the FoV 20.8 deg^2 at 110 MHz. Also for SKA1-MID, the diameter of each dish is $D_{\rm dish} = 15$ m, and thus the FoV becomes 0.25 deg^2 for $\nu = 1$ GHz. In our calculus, instead, we consider a similar magnitude, the largest angular scale determined by the minimal baseline, $D_{\rm min}$ through

$$\theta_{\rm max}(\lambda) = 58.61\lambda / D_{\rm min}, \tag{2.45}$$

expressed in deg.

Finally, as referred in [139], SKA would be prepared to test integration times of order 1000 hours and therefore, this becomes the longest integration time τ we consider in our work to determine the minimal detectable flux. Also, the bandwidth $\Delta\nu$ is taken as 300 MHz.

2.6 Code and numerical treatment of dark matter indirect signals

The code for the study of the e^+/e^- and synchrotron signals from DM annihilation was developed on *Python* 2.7.4 and the package Anaconda in a laptop with a multiprocessor Intel(R) Core (TM) i7-4500U CPU @ 1.80GHz and 2.40 GHz (CPM). Our code is prepared to compute both e^+/e^- fluxes and synchrotron emission both for the Milky Way and extragalactic sources,

such as dSphs. Also, it is being incorporated a module to calculate γ-rays derived from ICS. Our code is sufficiently flexible to extend the multi-wavelength studies to different targets, DM candidates and other cosmic-ray species. The main objetive for such a code is solving the highly oscillatory integrand involved in the computation of dark matter signals through a Monte Carlo Adaptive method. This latter strategy would allow us to study the tension between time computing and the expected dark matter signature without a significant noise. In addition, we wanted to create a flexible code to add some specific conditions to, for instance, the DM halo by including the presence of a black hole.

In our code, we solve the numerical integration of Eq. (2.29) for the Milky Way and Eq. (2.32) for dSphs ensuring the convergence of both series, depending on the target to consider. For this, we have used a Monte Carlo Adaptive Method through the package *Vegas.Integrator*[††] that allowed us to evaluate both arbitrary multidimensional integrals and long term series through the *Vegas* algorithm [220, 221]. In the *Vegas* algorithm there is, first, a transformation of the integration variables to flatten the integrand, and then a Monte Carlo estimate of the integral. In each iteration, it is collected information to improve the transformation to use in the next step.

Vegas.Integrator relies on an adaptation process in which it is possible to specify the number of iterations in the resolution of the integral/series by the *Vegas* algorithm (called *nitn* in the *Vegas* specifications) and also the maximum number of integrand evaluation made per iteration (*neval*). From this method, it is obtained a weighted average value that depends on the latter two parameters. In general, in our code *nitn* is a value around between 10 and 30, while *neval* can be from $1 \cdot 10^5$ to $1 \cdot 10^7$.

Furthermore, the code is prepared to be parallelised and run in multiple cores. Indeed, in our case, some of the computations we performed were using a number of cores ranging between 8 and 50 both in the *Zeus* cluster (UCT) and the *Sciama HPC* (ICG Portsmouth).

Our code has been tested by reproducing the results in Refs. [176, 179, 206]. In future works, we will compare the performances of our particular code with different ones. Once the benefits of our code have been secured in terms of time and flexibility, we will make it public.

2.7 Chapter conclusions

In this Chapter, we summarised the main techniques for particle dark matter detection. Indeed, all of them present advantages and inconveniences. Collider searches only depends on particle aspects cancelling all the astrophysical parameters found in direct and indirect searches. However, as mentioned, reconstructing the transverse missing momentum $\not{\mathbf{p}}_T$ of an invisible particle, as dark matter, would be turned into a difficult task and requires either very specific searches of dark matter or setting weaker constraints in a more general approach. Indeed, there is still the possibility that dark matter particles do not couple with Standard Model particles at the range of energies that can be reached by present colliders or even do not couple at all.

Direct searches may be an alternative to the latter possibility since the observed signatures would be basically the result of inelastic collisions. Indeed, direct searches offer a model-independent dark matter approach. However, they depend significantly on the local astrophysical environment, particularly on the halo properties. In Section 2.3, we briefly mentioned the Standard Halo Model, which describes the smooth component of dark matter halo in the local neighbourhood with a Maxwellian velocity distribution. This is a first approximation to the problem. Indeed, the presence of unvirialised components of the halo can generate a structure in the spatial and velocity distribution, affecting the signal in the detector and its interpretation: from effects

[††] `https://pypi.org/project/vegas/`.

in the count rates of the measured spectra to the change of the phase and amplitude in the annual modulation measurements. Dark matter cosmological simulations of Milky Way-size halos (Via Lactea [222, 223], Aquarius [224] and also more modern simulations at this same mass scales such as ELVIS [225], CATERPILLAR [226], APOSTLE [227] or AURIGA [228]) find residual substructure from the merging processes, such as clumps, cold streams and debris flows but also streams of material stripped from infalling satellites, as the Sagittarius stream. Also, the detector material limits the parameter space for the detection, i.e., not all the WIMP phase space is accessible. Indeed, for sub-GeV dark matter, the maximum energy in an elastic collision lies below the detectors' energy threshold (and also there are high uncertainties due to the background) while heavy dark matter is subjected to the exposure time and the target nuclei.

Finally, indirect searches offer a wide variety of targets and signals to detect. In fact, this pathway would be the only of the three methods able to detect dark matter signatures in a non-local environment. The main inconvenience lies in the need for a highly accurate description of the astrophysical background together with the specification of the parameters that describe its subtle dynamic. Furthermore, this strategy lies in the assumption that dark matter particles would either annihilate or decay into Standard Model particles.

Under this overview, it is obvious that the best strategy is a combination of the three kinds of searches. However, the parameter space that can be excluded from different experiments is different and a general model-independent study grouping the three methods is not possible. Instead, given a specific kind of search, model-independent studies can be performed. In the next Chapter, we shall specifically focus on dark matter indirect searches.

Chapter 3

Dark matter indirect searches with cosmic rays

3.1 Overview and leitmotiv

In Chapter 2, we exposed the mathematical formalism to model the propagation of products resulting from DM annihilation. According to this, if DM annihilates we would be able to detect some signatures in the sky as a consequence of this annihilation. In this Chapter, we will focus on the e^-/e^+ final state coming from DM annihilation into SM particles, which subsequently would decay or hadronise into such e^-/e^+ component. We shall present a quantity dubbed positron fraction, $\mathcal{F}_{e^+}$ that can be directly measured by the cosmic-ray detectors at the Earth ($r = 8\,\text{kpc}$ from the GC) or sometimes derived from the e^-/e^+ fluxes. The main goal of this Chapter will consist of setting constraints on general DM frameworks, i.e., model-independent DM, but also in more specific scenarios as it is the case of the Brane-World parameter space $\{M, f\}$. Also, we will propose DM candidates that would be in agreement with the data from cosmic-ray detectors.

The order in which this Chapter has been written exactly coincides with the order of our investigation [229]. This will allow the reader to understand the steps followed in the inclusion of the latest data updates at the end of the Chapter. The work has been organised as follows:

■ In Section 3.2, we will provide the main picture of cosmic rays from an astrophysical point of view. We will present their production mechanisms together with their standard propagation scenario used to fit the relative abundances of different cosmic-ray species. This analysis will be highly relevant for the discussion in the upcoming sections since it will allow us to understand the emergence of the excess in the positron fraction together with the concept of what will be called the astrophysical background.

■ In Section 3.3, we shall briefly summarise the three principal reasoning lines able to explain the positron fraction excess:

- In the first place, we shall briefly provide an idea of some of the non-conventional models of propagation that would accommodate to the data: from modifications on propagation coefficients to alternative astrophysical scenarios as the proposed Nested Leaky-Box model.
- Second, we will discuss some of the most suitable astrophysical sources to account for an injection of secondary e^+ able to explain the rise of the positron fraction.
- Lastly, we will provide our calculations of the positron flux at the Earth due to DM annihilating into different channels.

■ In Section 3.4, we will set some constraints on the $\{M, f\}$ parameter space for DM in Brane-World scenarios. Here, two astrophysical possibilities will be considered. A first model,

in which the positron fraction can be fitted by the contribution of a pulsar, and a second scenario, in which the only responsible for the excess is DM.

■ In Section 3.5, we shall obtain the best fit of the positron fraction with branons by performing a χ^2 analysis over the $\{M, f\}$ parameter space.

■ In Section 3.6, we will present a generalisation of the study of the previous sections. Here, we shall propose a set of χ^2 minima able to explain the positron fraction in the case of model-independent DM. Also, we will discuss the influence of the background on such fits.

■ In Section 3.7, we will present the role of the astrophysical background at the time of fitting the positron fraction.

■ In Section 3.8, we shall analyse the most recent data measured by AMS at the beginning of 2019, together with new implications for our previous results.

■ Finally, Section 3.9 shall be devoted to our main conclusions for this Chapter.

3.2 Astrophysical considerations for cosmic rays

The most striking aspect of the study of cosmic rays lies in the fact that they provide the only sample available of the interstellar and intergalactic medium. Their energy, ranging from 10^6 to 10^{20} eV when reaching the Earth, reveals a set of phenomenology elements not only influenced by particle interactions but also by both global galactic mechanisms and details about the sources where such cosmic rays are generated. Some of the most important features of cosmic-ray spectrum, such as the knee ($E \sim 10^{15}$ eV) and the ankle ($E \sim 10^{19}$ eV), see Fig. 3.1, have been well determined by observing the so-called cosmic-ray shower in the atmosphere by the use of ground-based detectors (CASA-MIA [230], KASCADE [231], HEGRA [232], AGASA [233], Hires [234], Auger [235]). However, only space telescopes can provide information about comic rays at relatively low energies ($E < 10\,\text{GeV}$). Indeed, this last range provides relevant information about cosmic-ray composition such as their isotopic abundances and the spectra of individual species. The importance of the latter aspects lies in the fact that such quantities are tightly correlated with global properties of galaxies usually related to cosmic-ray propagation, such as parametrisation coefficients or the scope of cosmic rays within the propagation region.

The main inconvenience is that cosmic rays are extremely correlated with their production mechanism, and thus, both abundances and spectrum present a high dependence with those parameters from the sources they were injected*. This fact turns the study of cosmic-ray propagation into a difficult task. The usual method to deal with such a source-dependence problem is through the study of secondary cosmic rays, generated in the collision of primary cosmic rays with the ISM. Indeed, injected primary cosmic rays impact on matter of the ISM, fragmenting heavy nuclei and producing secondary cosmic rays. The ratio between such secondary particles and the parent nuclei is independent of the source information, leaving almost exclusively propagation effects and not the information related to their production in the sources where injected. Therefore, assuming a theoretical framework to derive secondary cosmic-ray abundances, their fraction concerning primary nuclei can be adjusted by fitting experimental fractions measured in detectors. Usual nuclei for such purposes are Li, Be, B or sub-Fe nuclei (Sc+Ti+V). The main reason can be seen in Fig. 3.2. Comparing the cosmic-ray abundances both in the Solar System and in the Galaxy, we observe a difference between both of them. Such a difference is optimal in the case of Li, Be, B or also Sc, Ti and V. The key lies in the fact that none of these nuclei

*Those cosmic rays that are directly injected from astrophysical sources, as SNR, are referred as primary cosmic rays.

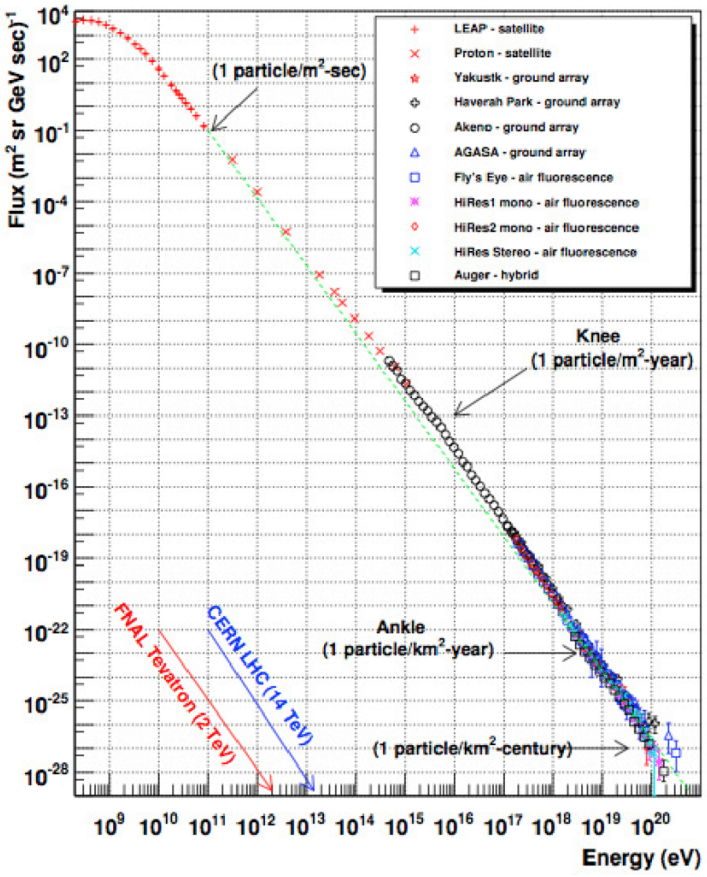

FIGURE 3.1: From Lopez-Oramas (2014) [236]. Measurements of the cosmic-ray spectrum by different experiments. In this figure, the knee and the ankle are represented. Those Cosmic rays reaching the Earth with energies below the knee would be originated in the galaxy, while for greater energies than the ankle would be extragalactic.

(excepting ^{7}Li) would survive under violent processes of either stellar or primordial Nucleosynthesis, and thus, they should have been created out of such a conventional scenario. Indeed, the BBN stops at A $= 7$, consequently primordial thermonuclear fusion has been unable to create heavier elements than ^{7}Li. Conversely, elements from C to U have been formed in stellar Nucleosynthesis, however, Li, Be, B are destroyed by proton capture in the interior of stars at temperatures ranging $0.5 - 5 \cdot 10^6$ K. Then, another mechanism is necessary to generate such species. The most accepted scenario to explain their production is that in which cosmic rays are injected by spallation. Thus, a conventional way to determine global propagation parameters is mainly by considering the Boron-to-Carbon (B/C), which can be easily experimentally measured and its theoretical production is better understood than other species. Nevertheless, describing such ratios relies on models with many parameters and usually model-dependent. Hence, other ratios, ^{9}Be/^{10}Be and the sub-Iron/Iron (sub-Fe/Fe), are usually considered to break the degeneracy. Moreover, some elements are relatively more sensitive to different propagation mechanisms and its selection depends on the type of study.

Furthermore, the number of parameters necessary to describe such a cosmic-ray transport depends on the selected theoretical formalism. The first semi-phenomenological approach for cosmic-ray propagation is the Leaky-Box model, presented in Section 2.4.2. In its simplest version, it states that cosmic rays diffuse within a confinement volume with a constant escape

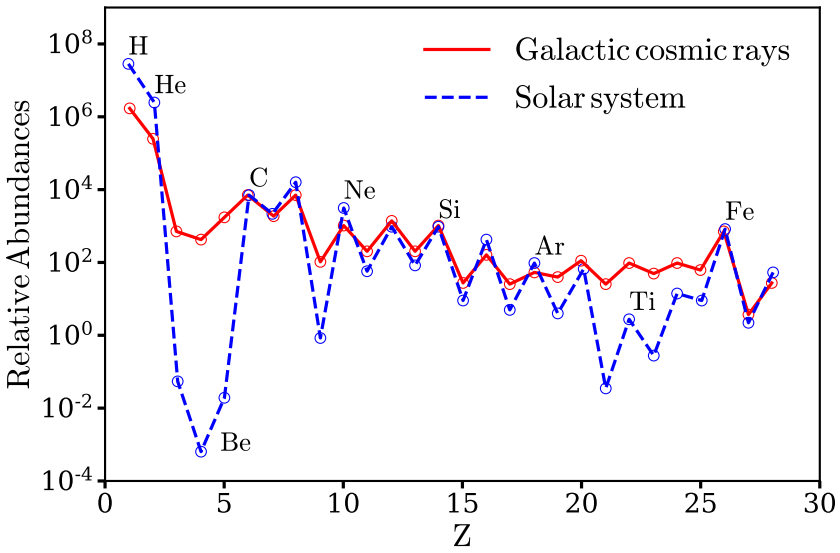

FIGURE 3.2: Relative abundances against the atomic number for Galactic cosmic rays (solid red line) and cosmic rays in the Solar System (dashed blue line). Galactic cosmic rays are usually detected through spectrometers situated in spacecrafts or satellites (HEAO-3 [238], ACE [239]) while solar system abundances are measured mostly in the solar photosphere (since the sun is the 99% of the solar system) through absorption lines, but also the meteorites composition [240]. The abundances difference in Li, Be, B or Sc, Ti, V reveals the existence of a mechanism of cosmic rays out of the BBN and star Nucleosynthesis paradigm: the cosmic-ray spallation. The creation of nuclei due to cosmic-ray spallation depends on the propagation models and their parameters, and therefore, their abundances play an important role in understanding cosmic-ray transport.

probability per unit of time, $\tau_{\rm esc}$, although more complicated mechanisms as cosmic-ray fragmentation or energy losses can be included, evolving in more sophisticated formalisms. The advantage of Leaky-Box models lies in the fact that it is possible to obtain averaged values of different observables in a semi-analytical scenario. However, by improving the experimental information, incoming ideas about cosmic rays revealed the need for solving the transport equation (Eq. 2.10) through numerical codes. Among them, GALPROP, whose first version was released in 1990s[†].

Within the study of cosmic rays, one of the first numerical challenges accounted by such codes is that related to the explanation of the cosmic-ray positron fraction

$$\mathcal{F}_{e^+} = \frac{\Phi_{e^+}}{\Phi_{e^+} + \Phi_{e^-}} \tag{3.1}$$

measured by MASS2, TS93 and HEAT (for earlier experiments consult Ref. [237] and therein). Indeed, the positron fraction was computed by solving the transport equation, Eq. (2.10), without convection [198] over a cylinder of radius R and height L_z. There, boundary conditions established that $\psi(r, L_z, p) = 0$ and $\psi(R, z, p) = 0$, in which ψ is the number density per unit of energy of one particular cosmic-ray species.

The pathway for computing the positron fraction $\mathcal{F}_{e^+}$ was, first, obtaining the diffusion parameters to fit the B/C ratio the following two scenarios. The first one was without considering

[†]https://galprop.stanford.edu/.

reacceleration, with $D = \beta D_0$ if the rigidity[‡] $\mathcal{R} < \mathcal{R}_0$ or $D = \beta D_0 \left(\frac{\mathcal{R}}{\mathcal{R}_0}\right)^{\delta}$ if $\mathcal{R} > \mathcal{R}_0$ (no specification at $\mathcal{R} = \mathcal{R}_0$) in Eq. (2.10). The second one, with reacceleration, takes a diffusion coefficient $D = \beta D_0 \left(\frac{\mathcal{R}}{\mathcal{R}_0}\right)^{\delta}$ and assumes the Kolmogorov description with $\delta = 1/3$. In this case, the reacceleration term considered was derived in Ref. [241] and described in Eq. (2.19). There the Alfven velocity, v_A, acts as a free parameter. The injection of B and C, collected in the function $q(\mathbf{r}, E, t)$ of Eq. (2.10), is assumed to follow a power law $\propto E^{-\gamma}$ according to the Fermi propagation theory.

Once propagation parameters were obtained by fitting the B/C ratio, the proton and He spectra could be computed. The reason lies in the fact that they are the main responsible in the generation of secondary e^+ and e^- (proton corresponds to 90% of the total cosmic rays while Helium is 9%). Fitting the proton and Helium data based on LEAP, IMP8 and, HEAO-A3, the source injection term for these species can be obtained.

The next step is computing secondary e^+ and e^-, having in mind the particle processes in which they are created ($q(\mathbf{r}, E, t)$ accounts for that information). In this regard, the main mechanism to be considered for e^+ and e^- production is the proton-proton collision (but also, in a lower proportion, $p + \text{He}$, $\alpha + \text{H}$, and $\alpha + \text{He}$) resulting in pions that, subsequently, decay into two ways:

- π^0 decaying into γ-ray[§].
- charged pions producing charged muons through

$pp \to X\pi^{+}_{-}$, that subsequently produce e^+/e^- through the process $\mu^- \to e^- \nu_\mu \overline{\nu_e}$ and $\mu^+ \to e^+ \overline{\nu_\mu} \nu_e$.

Another process to consider in the generation of secondary e^+ and e^- is that in which kaons are involved, but in a lower proportion. Indeed, kaons are generated through:

- proton-proton collision through $pp \to XK^{+}_{-}$. Such kaons, subsequently, produce muons through $K^{+}_{-} \to \mu\nu_\mu$[‡], $K^{+}_{-} \to \pi^0\pi^{+}_{-}$ and $\pi^{+}_{-} \to \mu\nu_\mu$ mediated by the exchange of the W^{+}_{-} bosons. As shown above, muons decay into e^+/e^-.

Considering the processes above, the injection of secondary e^+/e^- can be computed. The remaining step in the computation of the positron fraction $\mathcal{F}_{e^+}$ is determining the injection of primary e^- from sources to the environment. The standard paradigm is that the bulk of Galactic electrons, as well as the rest of cosmic rays, are produced in SNR and injected to the ISM [243]. The main argument lies in the fact that SNR provide an efficient way to accelerate cosmic-ray along the Galaxy, even if the efficiency of the process is low. In this regard, the luminosity of cosmic rays required to fit the observed cosmic-ray energy density ($\rho_{\text{CR}} = 1\,\text{eV/cm}^3$) is around $\sim 5 \cdot 10^{40}\,\text{erg/s}$, while the average output in kinetic energy of Galactic supernovae remnants is $3 \cdot 10^{42}\text{erg/s}$ [244, 245]. The fact that cosmic rays, together with primary electrons, are produced in the supernova process, results in the injection of them with a power law γ in $\propto E^{-\gamma}$, according to first Fermi shock acceleration theory in supernova shock waves.

[‡]The rigidity is defined as $\mathcal{R} = pc/Ze$, where p is the particle momentum and Ze accounts for the cosmic-ray charge.

[§]Fitting the proton and Helium data directly as mentioned above, ensures the abundances of these species locally, however, the γ-ray flux bump from 100 to 1000 MeV (see, for example, EGRET measurements [242]) in π^0 processes allows to either confirm or adjust the theoretical predictions of proton and Helium spectra along the whole Galaxy.

[‡]For the muon and muon neutrino term none of their charges are specified. Conjugated charges should be (or not) conveniently considered to satisfy necessary symmetries in the whole reaction.

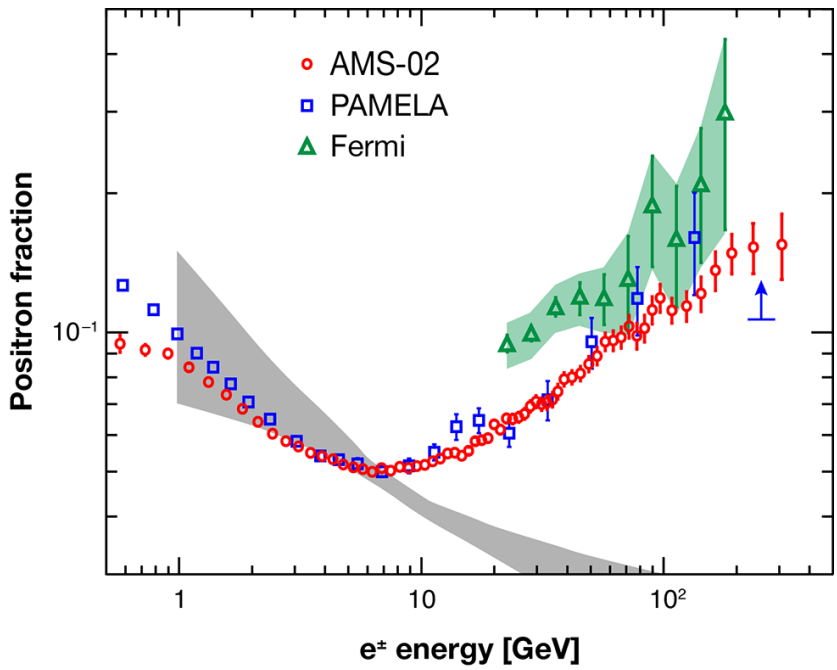

FIGURE 3.3: From Coutou (2013) [251]. Positron fraction, $\mathcal{F}_{e^+}$, as measured by PAMELA after 1229 days [252], by Fermi after 34 months [253] and by AMS after 18 months [210]. The positron fraction presented in this plot is not the latest version of the data, however, it has been selected for illustrative purposes. The grey band corresponds to the range of the positron fraction expected theoretically and proposed in Ref. [198, 208]. Indeed, theoretical predictions indicate that $\mathcal{F}_{e^+}$ decreases with energy beyond $\sim$ 10 GeV according to the Fermi mechanism. Nevertheless, PAMELA, Fermi-LAT and AMS detect an unexpected rise in the positron fraction $\mathcal{F}_{e^+}$ from 10 GeV that would be in agreement with primary sources of e^+, such as PWN or DM. Also, alternative propagation mechanisms are also suggested to explain this anomaly called positron excess.

The method to constrain the injection index, γ in $\propto E^{-\gamma}$ consists of comparing the predicted synchrotron-emission and gamma-ray signals from primary electrons (in the interaction with the environment mainly through synchrotron emission or ICS) with the distribution of signals measured experimentally. In Ref. [198], the study concludes that $\gamma \sim -2.1$ (no reacceleration) in order to reproduce the synchrotron signals from 38 to 1420 MHz at high galactic latitudes, but also the COMPTEL and EGRET data between 1 MeV and 1 GeV [246, 247]. Regarding to the electron injection, whose spectrum is usually described by a power law, it is necessary to emphasize that some works also include a power law with an exponential cut-off at a maximum energy in which the energy gain rate for shock acceleration is comparable with the loss due to interactions with the environment, and thus, $q(E) = Q_0 E^{-\gamma} \exp(-E/E_{\rm cut})$ [248–250].

From the moment when first numerical descriptions of cosmic rays started, the understanding of cosmic-ray production and propagation improved and alternative mechanisms that were not included in the transport equation at the beginning, such as the influence of the galactic wind, have been added in subsequent versions for more than 20 years. The incorporation of additional terms in the transport equation allowed a better description by including new parameters whose degeneration is broken by fitting primary-to-secondary ratios of alternative species. The last version of GALPROP, version 56, allows calculating the cosmic-ray distribution for all cosmic-ray species ($Z \leq 28$) taking into consideration energy losses, diffusion, stochastic reacceleration, convection, fragmentation, radiative decay, and including parameter constraints from multi-wavelength observations [254].

In addition, at the time of comparing the numerical predictions with the data, all the parameters considered in the computation of cosmic-ray spectra have to be compatible with the abundances of all the cosmic-ray species. However, the positron fraction $\mathcal{F}_{e^+}$ cannot be accommodated within the measurements by PAMELA [252], Fermi-LAT [253] and AMS [210]. This fact presents a challenge that is not yet well understood. In Fig. 3.3, we illustrate the outlook. Therein the blue, green and red points represent the positron fraction $\mathcal{F}_{e^+}$ measured by PAMELA, Fermi and, AMS respectively, while the grey band represents the theoretical prediction based on GALPROP analysis [198, 208]. Such a prediction is performed by computing Eq. (3.1) assuming primary e^-, injected in SNR, and secondary e^+/e^- generated due to cosmic-ray interaction, mainly, in proton-proton collisions. Although the positron fraction fits well for $E < 10$ GeV (the variation of the grey band is due to the solar modulation effect), there is an unexpected rise at larger energies that cannot be explained with conventional propagation models described above. Even more, such transport mechanisms predict a positron fraction $\mathcal{F}_{e^+}$ decreasing with energy [198]. In other words, the positron fraction presents an excess from 10 GeV onwards, when positrons contribution is only given in terms of cosmic-ray spallation (secondary products).

The positron fraction excess has opened a wide discussion about alternative sources injecting high energy positrons while other authors question the accuracy of cosmic-ray propagation models. Two aspects should be mentioned to provide a more general framework in this discussion. First, for the case where new sources inject positrons, one remarkable feature visible in the positron fraction $\mathcal{F}_{e^+}$, Fig. 3.3, has to be considered. Its rise starts to flatten at energies $\sim$ 200 GeV, opening the possibility of finding a cut-off in the data that will be measured in the following years. If cosmic-ray detectors confirm the existence of such cut-off, the new sources must be able to explain it. From this fact, two kinds of sources injecting positrons are usually taken into account (besides the SNR scenario). Pulsar Wind Nebula (PWN), immersed in the shock wave of SNRs, whose spectrum presents a break that can be seen between radio and X-ray emission which is believed to be the result of synchrotron cooling [255]. The case we will focus on in our work, i.e., annihilating (decaying) DM, is also considered to explain such an excess. In this case, the energy cut-off comes from the conservation of 4-momentum when DM annihilates into SM particles. Second, the second aspect would be to confirm if there exists another cosmic-ray excess supporting the positron fraction anomalies. Indeed, there is a debate about a possible antiproton-to-proton $\overline{p}/p$ excess announced in the *AMS Days at CERN* (2015) [256]. However, in Ref. [257] such a $\overline{p}/p$ value is explained in a conventional way. Even though that $\overline{p}/p$ can be fitted by DM (and it cannot by PWN), such a rate could be also described only by secondary processes [258] in the standard scenario, without making extra assumptions.

3.3 Explanations for the positron excess

As mentioned in the previous section there are at least three conventional ways to explain the excess in the positron fraction. First, alternative cosmic-ray propagation models where primary e^- and secondary e^-/e^+ would still explain the rise. Second, new astrophysical sources accelerating secondary or injecting primary e^+ at high energies. Third, by invoking an alternative paradigm in physics, namely the need for DM. Let us discuss each of them below.

3.3.1 Alternative propagation models

Among the most significant modifications, the inclusion of inhomogeneities and anisotropies in the diffusion models has been widely discussed in the literature. In general words, the usual approach relies on changing the diffusion coefficient by adding spatial dependence. Indeed, the spatial distribution is different depending on the element responsible for such a change,

as for example, spatial sources distribution [259, 260], position-dependent galactic magnetic field [261] or alternative models for the galactic wind [262]. To illustrate this, in Ref. [261], authors introduce the change $D \rightarrow D_0 E^{\delta} f(z)$, with both $f(z) = |z|^{\mu}$ and $f(z) = \exp(az)$. This modification motivated by the spatial distribution of the galactic magnetic field (also responsible for the diffusion process) can reproduce the high energy part of the measured positron fraction $\mathcal{F}_{e^+}$ only with secondary e^+ [261].

Another alternative description is the Nested Leaky-Box model [263–265]. In GALPROP, primary sources are smoothly distributed and temporarily constant. In this different framework, particles are accelerated in a large number of sources sprinkled along the Galaxy that are surrounded by a cocoon-like region (regions with larger grammage[¶]) where spallation of nuclei takes place without reacceleration. The storage in the cocoon-like region depends on cosmic-ray energy. Therefore, secondary-to-primary cosmic-ray ratios generated by spallation in the source are also energy-dependent. This could explain why the energy index β in the spectrum of positrons propagating, $E^{-\beta}$, is similar to the energy index of their parental protons, $E^{-\beta}$, when a difference $E^{-\beta-\delta}$ due to, at least, either escape or radiative losses is expected [265] (see also the discussion in Sections 11.5 and 11.6 of [266]). This scenario, that also predicts an energy dependence in the B/C ratio, is compatible with the rise in the positron fraction $\mathcal{F}_{e^+}$ reaching an asymptotic value of ~ 0.7 beyond 1000 GeV. Even though the model gives a good fit for $\mathcal{F}_{e^+}$, such predictions do not seem to be following the B/C ratio measured by AMS [267].

Furthermore, the model-independent approach by [268] emerges as an attempt of setting general features in the positron fraction, by reducing the number of parameters used in numerical models. The idea lies in the fact of not considering energy losses for secondary e^+, showing that a similar saturation behaviour to that measured experimentally in the $\mathcal{F}_{e^+}$ is obtained. The rise in the positron fraction $\mathcal{F}_{e^+}$ cannot be fitted, although an upper limit is set only in terms of secondary positrons, indicating that there is no need for e^+ primary sources.

In Ref. [269], the usual cosmic-ray scenario is revisited by considering mainly the $^{10}\mathrm{Be}/^{9}\mathrm{Be}$ ratio from SMILI [269]. In such a scenario, the authors present a galactic confinement time of $1-2$ Myr for light secondary cosmic rays, showing that energy losses for positrons cannot be large for energies below a few hundred GeV. Also, it is shown that positrons have a spectral index similar to that of the parental protons at the energies at which they are produced, suggesting that e^+ are predominantly secondary. Finally, the asymmetry between the electron and positron energy losses, responsible for the rise in the positron fraction, can be explained since secondary positrons are produced due to its continuous distribution in time, unlike the electron arrival time which would be determined by the distance to the nearest source. One aspect to remark is that this explanation is in agreement with the positron fraction and also would be allowed within the GALPROP restrictions for cosmic-ray abundances.

3.3.2 Alternative astrophysical sources

In the previous subsection, we presented a set of different approaches that reformulate the assumptions considered for the calculation of the positron fraction. All those scenarios, as already mentioned, were based on the flux of primary e^- and secondary e^+/e^- modifying characteristics of the propagation environment. Other alternatives, related to astrophysical sources have been studied in the literature. The usual astrophysical sources [255, 270] to interpret the positron excess would be both SNRs [271] and nearby pulsars [272]. Taking into account the contributions from averaged distant sources, fluxes from both local supernovae (Green Catalog [273]) and pulsars from the ATNF database [274], measurements of AMS can be well-fitted

[¶]grammage is defined as the amount of matter traversed by cosmic rays during their propagation, measured in $\mathrm{g/cm^2}$.

[255]. Between SNRs and pulsars, an important subtlety has to be kept in mind. In the former secondary e^+ may be produced in proton-proton collisions *inside* SNRs and then accelerated before escaping into the ISM. Therefore, e^+ are not strictly injected as a primary component. Conversely, in pulsars, e^+ are directly injected by the source constituting a primary component of positrons.

Concerning the SNRs, it is claimed that the production of secondary particles in the SNRs environment could have been underestimated. It seems that the grammage that particles have to get through around such sources is smaller compared to the grammage of the ISM. However, secondary particles produced in such an environment may have an important contribution to the total positron fraction [275–277]. For example, in Ref. [277], the strategy consists in solving the transport equation for the phase space density of different species $f_i(\vec{x}, p)$ with GALPROP. The model includes the spallation of cosmic rays inside the source by imposing boundary conditions up-stream and down-stream the shock wave of the Fermi acceleration scenario. Such considerations enable us to fit the whole positron fraction $\mathcal{F}_{e^+}$ just by providing a sole old population of SNRs as an effective strengthening of the positron-fraction [276]. In some of these models, the only undetermined parameter is the maximum rigidity at which cosmic rays are accelerated in the SNRs environment, being able to reproduce either a cut-off or a positron fraction increasing with energies [277]. The major challenge for the SNRs acceleration lies in the fact that provided a larger amount of positrons is expected from such sources, also a bump should be observed in other cosmic-ray species, such as the case of the B/C ratio. In this regard, there has no been evidence for any rise up to the B/C highest measured energies (see the discussion in [278] and references therein). Indeed, only a 25% of the rise in the positron fraction could be attributed to this mechanism [278], although the model would still be valid for those species if the diffusive parameters are changed to higher values, expected in diffusion-convection models. Following the same line of reasoning, some authors proposed a scenario where, besides the old population of SNRs, a distant younger population on average with strong shock and amplified magnetic fields are also included allowing to reproduce also the decreasing in the B/C ratio [279].

In the case of pulsars, as mentioned, e^+ are directly injected, constituting a primary component. The most accepted framework is the injection due to the combination of high magnetic fields ($B \sim 10^{12}$ G for young pulsars) with fast-spinning, producing strong electric ($\Delta V = 10^{18}$ V) fields and pulling particles away from the neutron star surface. Such charged particles accelerate following the intense magnetic field lines yielding photons (radio, optical, X-ray and γ-ray) through curvature radiation and synchrotron emission. Such photons, in the high electromagnetic field environment, generate pairs (e^+e^-) that subsequently produce again photons, setting cascades of photons and charged particles [280]. The whole environment of photons, charged particles and magnetic field constitute the pulsar magnetosphere, where particles, mainly e^+e^-, constitute a plasma subjected to a strong magnetic field and high rotations. The pulsar magnetic field forces the plasma to co-rotate with the neutron star. As far as particles increase their velocities, following the magnetic field lines, they start to occupy the outer radius and the co-rotating velocity approximates to the speed of light, the limit where the light cylinder $\Omega R_{\rm LC} = c$ is defined. Thus, the light cylinder radius defines the location where the co-rotation velocity is equal to the speed of light. This clearly gives rise to two different behaviours.

- First, provided the magnetic field lines lie close without reaching the light cylinder then particles remain trapped by the neutron-star magnetic field. This behaviour is characteristic in the pulsar equator where the magnetic intensity lines are more separated.

- Second, particles (mainly e^+e^- and possibly a small fraction of ions) that follows magnetic lines crossing the light cylinder, essentially in the cup poles, stop the co-rotation due to the

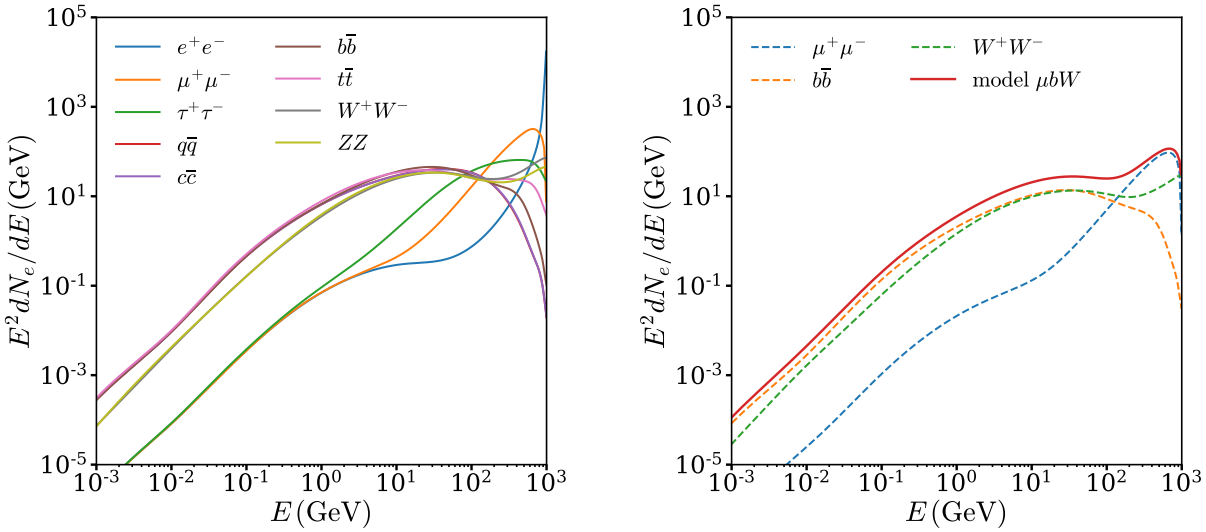

FIGURE 3.4: *Left panel:* e^+/e^- prompt spectra from $M = 1$ TeV DM annihilating into different final states that subsequently decay or hadronise into e^+/e^-. All the spectra (the e^+ channel as well although it is not possible to see it in the plot) show a cut-off according limited by the WIMP mass. *Right panel:* e^+/e^- prompt spectrum from $M = 1$ TeV DM annihilating into $\mu^-\mu^+$ (30%), $b\bar{b}$ (30%), W^-W^+ (40%) (model μbW). Both channels have been computed with the PPPC4DMID with electroweak corrections [175].

limit imposed by the speed of light, escaping from the pulsar surroundings and constituting the pulsar wind.

Ultimately, the wind is confined by hosting SNR surrounded by the ISM. The impact of the pulsar wind on the much slower ejecta of the supernova creates a reverse shock (the termination shock) that propagates backwards. The region bounded by the wind termination shock on one side and the ejecta on the other side, a bubble of relativistically hot magnetised plasma, is the so-called PWN or plerion [281]. How many pairs from the pulsar magnetosphere set the PWN is not well understood. Besides, the e^+/e^- spectrum trapped inside the PWN can be measured by observing photons from synchrotron and ICS revealing a break between the radio and X-ray regimes. However, the time evolution of such an emission is unknown, thus, it is not clear if it represents the spectrum at the Earth, providing large uncertainties in the parametrisation of its source function [282] given by

$$q(E) = Q_0 (E/E_0)^{-\gamma} \exp(-E/E_{\mathrm{cut}}) \tag{3.2}$$

3.3.3 Dark matter

Further explanations, such as DM in the DM Galactic halo, have also been considered in the literature [283–286]. In this regard, there exists a wide variety of astrophysical and cosmological phenomena whose explanation requires to resort to DM. In Chapter 1, we presented the most remarkable pieces of evidence: the presence of DM in galaxy clusters and the flat galactic rotation curves (Section 1.2.2), gravitational lensing (also in Section 1.2.2), BBN abundances (Section 1.3.2) and the CMB anisotropies (also in Section1.3.2). From these pieces of evidence and the study of thermal relics it is derived one of the accepted frameworks for DM, the WIMPs. Several DM models have been proposed (*c.f.* [287, 288] and references therein) to explain the WIMPs features which cannot be accommodated within the SM of elementary particles.

TABLE 3.1: Astrophysical parameters for Fig. 3.5.

Profile	$B(r)$	$B_0\,(\mu\mathrm{G})$	$L_z\,(\mathrm{kpc})$	$D_0\,(\mathrm{kpc}^2/\mathrm{Myr})$	δ	$n_e\,(\mathrm{cm}^{-3})$
NFW	Constant	6	15	0.0765	0.46	0.1

WIMPs may annihilate or decay into SM particles that are kinematically accessible. Many of these SM particles are unstable, and also decay and hadronise into stable particles: e^+, e^-, $p, \overline{p}$, γ, ν, and heavy nuclei, setting the prompt emission spectra. Such emission may only not come from one channel, being the differential total spectrum:

$$\frac{\mathrm{d}N_i}{\mathrm{d}E} = \sum_j \beta_j \frac{\mathrm{d}N_i^j}{\mathrm{d}E}. \tag{3.3}$$

In this expression, there are j different channels contributing to the prompt emission spectra of the stable particle i. Such a spectrum can be calculated using the PPPC4DMID package[‖] that includes electroweak corrections, important for multi-TeV candidates [289].

In Fig. 3.4 left panel, we provide an example of such spectra coming from the annihilation of DM into one channel whose final state is e^+/e^-. The plot suggests that the leptonic channels provide more e^+/e^- in the range of energies close to the DM candidate mass, while quark and boson channels dominate at lower energies. In this regard, the leptonic spectrum is harder than the rest, concentrating most of the emission in a specific energy band. In the right panel we also consider the electron spectra $\frac{\mathrm{d}N_e}{\mathrm{d}E}$ as coming from three contributions: 30% from the channel $\mu^+\mu^-$, 30% from the channel $b\overline{b}$ and 40% from W^+W^-. The spectrum $\frac{\mathrm{d}N_e}{\mathrm{d}E}$, either coming from one or several channels, is what it is referred as the injection spectrum and it provides the number of e^+ or e^- per unit of energy at the point of annihilation/decay. After the injection, e^+/e^- propagate along the Galaxy, according to the Eq. (2.28) until reaching the Earth. The flux of e^+/e^- at the Earth, can be written in terms of a Bessel Fourier series according to Eq. (2.29) and computed by Eq. (2.34).

In Fig. 3.5, e^-/e^+ spectra $E^2\Phi^{\mathrm{DM}}_{e^-/e^+}$ after diffusion have been represented for 1 TeV DM candidates with the aim to compare them with those in Fig. 3.4. The details about the astrophysical parameters chosen to compute Fig. 3.5 have been collected in Table 3.1. Such parameters remain fixed during the whole computation for DM fluxes. In addition, the number of terms in the Bessel-Fourier series is $(n, i) = (399, 399)$. The calculations have been performed in our code, based on *Python* with the package *Vegas*, an improved version of the adaptive Monte Carlo. The number of samples *neval* (Section 2.6) for each value $\Phi_{e^+}(E)$ calculated with this algorithm is $5 \cdot 10^6$. Some features in Fig. 3.5 are:

- As observed in both panels, the spectra of positrons after the propagation change with respect to the injection counterpart in Fig. 3.4. In the left panel, for DM annihilating into one single channel, the plot suggests that the biggest differences are located in regions at higher energies close to the mass of the candidate. One of the main reasons for such a change is the cooling of e^+/e^- due to radiative losses playing an important role in the propagation dynamic. In this regard, such a cooling increases fundamentally as $\propto E^2$, for high energies, where synchrotron emission is predominant (see Fig. 2.1).

[‖] http://www.marcocirelli.net/PPPC4DMID.html

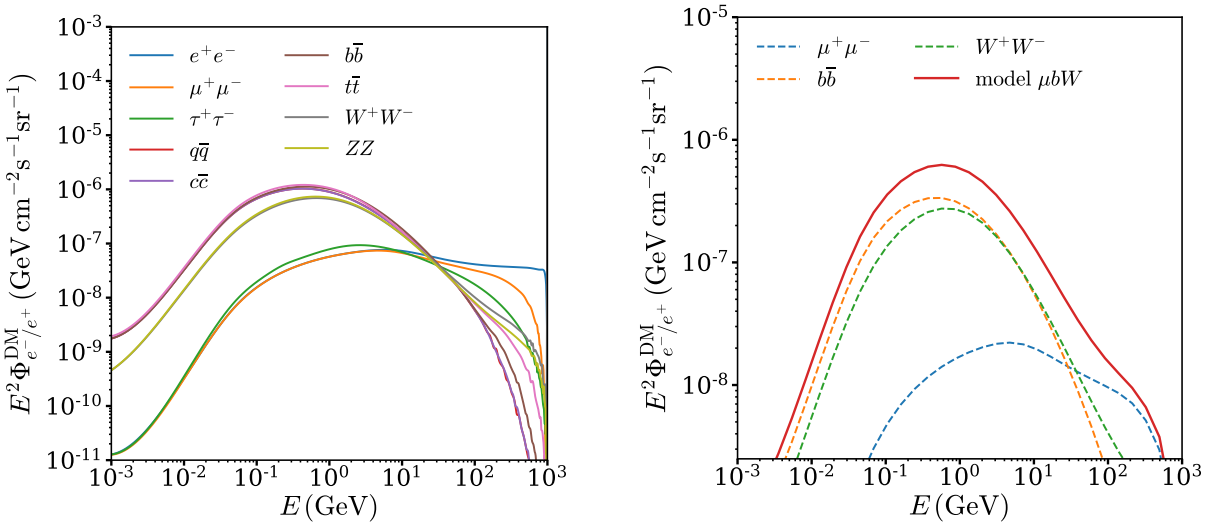

FIGURE 3.5: *Left panel*: Flux of positrons at the Earth after the propagation, for $\left\{D_0\,[\mathrm{kpc}^2/\mathrm{Myr}], \delta, L_z\,[\mathrm{kpc}]\right\} = \{0.0765, 0.46, 15\}$ and an NFW profile. The magnetic field is constant and equal to 6 μG for different masses. *Right panel*: Flux of positrons at the Earth after the propagation for the model of 1 TeV DM candidate annihilating into $\mu^-\mu^+$ (30%), $b\bar{b}$ (30%), W^-W^+ (40%) (model μbW).

• Conversely, the e^+/e^- flux in Fig. 3.5 presents a slight noise for energies close to $M = 1$ TeV. This fact derives from the sharp drop in e^+/e^- flux in several orders of magnitude. Hence, the adaptive Monte Carlo *Vegas* algorithm used to integrate the e^+/e^- flux would need more sample points when energies lie close to the limit imposed by the DM mass.

Eq. (3.1) allows us to calculate the positron fraction through the already calculated e^+ flux from DM annihilation, $\Phi^{\rm DM}_{e^+}$. However, first, it is necessary to set also the flux from both the primary e^- and secondary e^+/e^-, what from now we will call *background*. In this regard, we use a simple background based on the discussions of the previous sections, whose chosen parametrisation is that from [290]. Such a background will be also used in the next sections of the present Chapter.

In view of the above discussion, DM could either partially or completely explain the aforementioned excess [206, 290–292]. Although some studies fit the positron fraction excess with either astrophysical sources or DM separately, the large parameter space accounting for both astrophysical sources and DM contributions, enables us to describe the positron excess with a combination of them (*c.f.* [282, 293, 294] for recent attempts) bearing in mind that no source model can produce more e^+/e^- than those observed by experimental data. In order to describe the astrophysical scenarios where DM can be involved, and according to the model in [210, 212], we divide the non-modulated (NM) positron flux $\Phi^{\rm NM}_{e^+}$ as follows

$$\Phi^{\rm NM}_{e^+}(E) = \Phi^{\rm prim}_{e^+}(E) + \Phi^{\rm sec}_{e^+}(E) + \Phi^{\rm DM}(E) \tag{3.4}$$

with

$$\begin{aligned} \Phi^{\rm prim}_{e^+}(E) &= C_s E^{-\gamma_s} \exp\left(-\frac{E}{E_s}\right), \\ \Phi^{\rm sec}_{e^+}(E) &= C_{e^+} E^{-\gamma_{e^+}}, \end{aligned} \tag{3.5}$$

where the energy E is expressed in GeV. The NM e^+ flux is that referred to the flux that does

not consider solar modulation effects at low energies and primary means positrons that would be produced in a pulsar environment under strong magnetic fields through the decay of high-energy photons into positron-electron pairs (Section 3.3.2). On the other hand, secondary ones are produced in the primary component collisions with the ISM in the process of spallation. In the expression (3.4), besides secondary e^+ and $\Phi^{\rm DM}(E)$ corresponding to DM, we also include $\Phi^{\rm prim}_{e^+}(E)$ as a possible contribution from PWN because we will consider two possible scenarios in our study:

- **Model A** in which the e^+ flux, $\Phi^{\rm NM}_{e^+}(E)$, is due to a contribution of DM and pulsars only.
- **Model B** in which the e^+ flux, $\Phi^{\rm NM}_{e^+}(E)$ is only due to the contribution of DM ($\Phi^{\rm prim}_{e^+} = 0$).

Consequently, although not relevant in the range of energies of the excess, a correction for the solar modulation through the parameter ϕ_{e^+}/ϕ_{e^-} can also be considered at low energies. Following the force field approximation [295, 296] for the solar modulation, Eq. (3.4) would change as follows

$$\Phi_{e^+}(E) = \frac{E^2}{(E+\phi_{e^+})^2}\Phi^{\rm NM}_{e^+}(E+\phi_{e^+})\,. \tag{3.6}$$

Regarding to the e^-, flux $\Phi_{e^-}(E)$, Fermi acceleration mechanism predicts a power law in their injection spectra through E^{γ_1}, while secondaries would follow also a power law E^{γ_2} modified by energy losses and escape. Then, the expression for e^- yields

$$\Phi_{e^-}(E) = \frac{E^2}{(E+\phi_{e^-})^2}\left[C_1(E+\phi_{e^-})^{\gamma_1} + C_2(E+\phi_{e^-})^{\gamma_2}\right]. \tag{3.7}$$

The used parameters in Eqs. (3.4), (3.5), (3.6), (3.7), according to [290] are $C^+_e = 61\,{\rm s}^{-1}{\rm sr}^{-1}{\rm m}^{-2}{\rm GeV}^{-1}$, $\gamma_{e^+} = 3.70$, $C_s = 2.4\,{\rm s}^{-1}{\rm sr}^{-1}{\rm m}^{-2}{\rm GeV}^{-1}$, $\gamma_s = 2.60$, $E_s = 1.4\,{\rm TeV}$ and $\phi_{e^+} = 0.83\,{\rm GV}$ for e^+, bearing in mind that **Model B** considers $\Phi^{\rm prim}_{e^+} = 0$, and parameters corresponding to that term are not used in such a case. For e^-, the parametrisation accounts for $C_1 = 2.6\cdot 10^3\,{\rm s}^{-1}{\rm sr}^{-1}{\rm m}^{-2}{\rm GeV}^{-1}$, $\gamma_1 = 3.83$, $C_2 = 35{\rm s}^{-1}\,{\rm sr}^{-1}{\rm m}^{-2}{\rm GeV}^{-1}$, $\gamma_2 = 2.83$ and $\phi_{e^-} = 1.3\,{\rm GV}$. Where not otherwise specified in the following section, we will use this specified model of background and it will be represented in plots as a green band when PWNs do not contribute and with a dashed line when their contribution is taken into account (refer, for example, to Fig. 3.7 of the next section). Finally, in order to help the reader to have a better understanding of our research, we present our results in chronological order in the following sections of this Chapter.

3.4 Brane-World dark matter with AMS: constraints

In this section, we present the analysis performed to set constraints on extra-dimensional DM in the Brane-World theories framework, previously introduced in Section 1.4.2. For illustrative purposes, we have considered one extra dimension in a range of masses $M = 200\,{\rm GeV} - 100\,{\rm TeV}$. In such a range, branons mainly annihilate via ZZ and W^+W^- according to the branching ratios presented in Fig. 1.10. The first step is fixing the parameters for the background described in the preceding section: both for primary e^+ and secondary e^+/e^- and possibly, it will be specified later, secondary astrophysical positrons in the case we assume a contribution from PWNs. With the astrophysical parameters set, the study is aimed at varying the parameter space corresponding to branon DM constituted by the branon mass, M, and the brane tension, f. In Section 1.4.2, we provided some expressions $f(M)$ for the thermal relics with $\langle\sigma v\rangle = 3\cdot 10^{-26}{\rm cm}^3/{\rm s}$, relating M and f. However, in view of Fig. 3.6, no remarkable positron signals

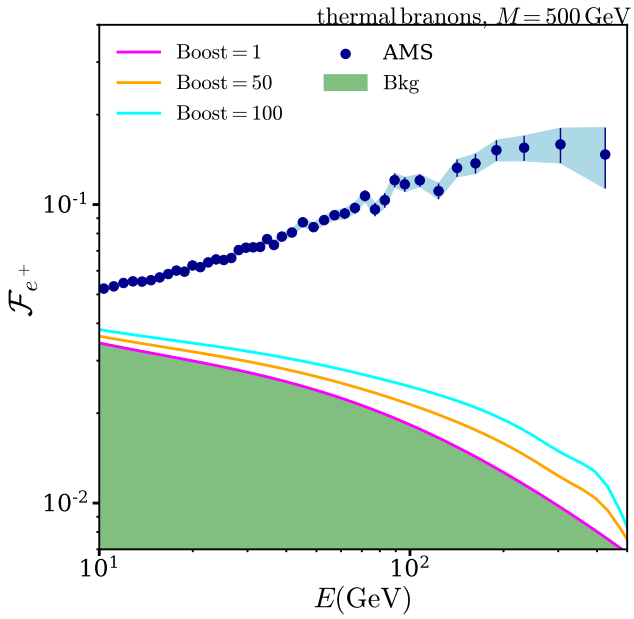

FIGURE 3.6: Positron fraction for branons with a thermally averaged cross section equal to $3 \cdot 10^{-26}\text{cm}^3/\text{s}$. The boost is taken as a multiplicative factor over the calculated signal $\Phi_{e^+}^{\text{DM}}$. In our work, we do not specify the mechanism of boosting, but the most common ones include the clumpines of DM halos [297, 298] and the Sommerfeld enhancement [299, 300]. The line in pink shows that there is no significant contribution over the background when only the e^+ signal is considered without any boost mechanism. On the other hand, even boost values of 50 or 100 do not contribute to the expected signal.

are expected and boost factors would be necessary. For this reason, we perform a study including values different from the thermal limit of $\langle \sigma v \rangle = 3 \cdot 10^{-26}\text{cm}^3/\text{s}$, treating M and f as independent parameters.

Conversely, being aware of the possible influence of the astrophysical context, the upcoming analysis has been performed for distinct diffusive models, in particular

TABLE 3.2: Diffusion values according to the conventional propagation models. In Ref. [301] MIN and MED were excluded. In this work we leave our first results on this two last scenarios for illustrative purposes.

	D_0 [kpc^2/Myr]	δ	L_z [kpc]
MIN	0.0016	0.85	1
MED	0.0112	0.70	4
MAX	0.076	0.46	15

and DM profiles (Isothermal and NFW) characterising their influence on the estimated results. In the following, we shall describe the methodology for branon constraints. In our analysis, we shall implement two lines of reasoning:

- In the first scenario (**Model A**), AMS excess from approximately 10 GeV onwards can be perfectly accommodated by the PWN contribution. Even if this is the case, the hypothesis of DM annihilating cannot be rejected. It should be emphasised, as mentioned above, that the cross section according to relic abundances would not produce a perceptive excess in the positron

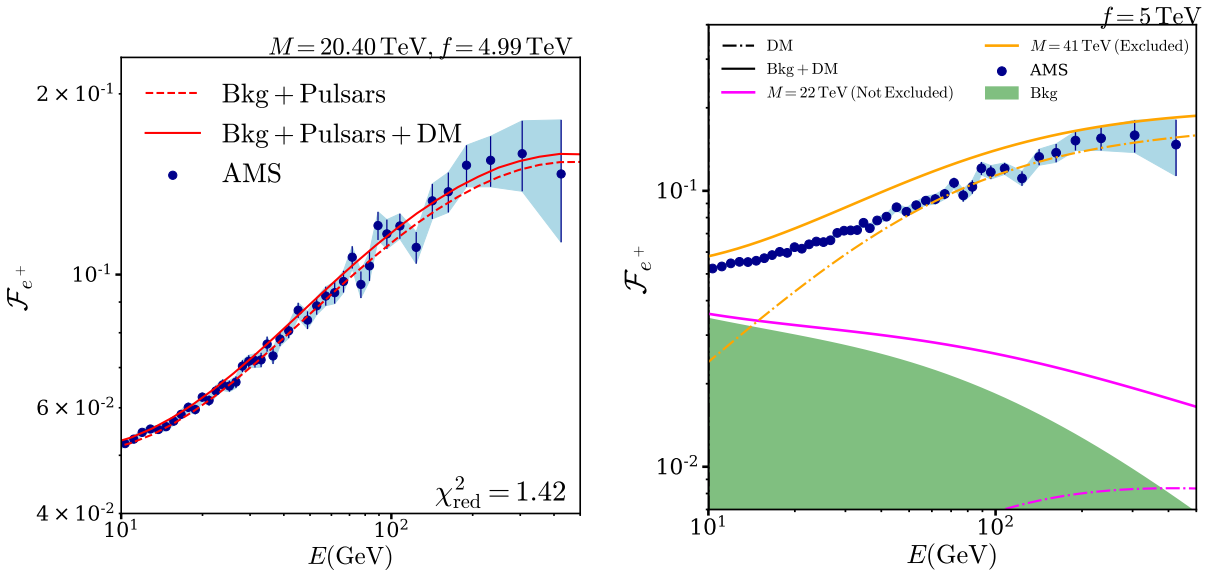

FIGURE 3.7: Methodology of exclusion for branons [229]. *Left panel*: The left panel represents the fit assuming background and pulsars to explain the AMS signal (**Model A**). As a paradigmatic example, we plot the branon with $\{f = 4.99\,\text{TeV}, M = 20.40\,\text{TeV}\}$ that shows a ($\chi^2 = 56.94$, $\chi^2_{red} = 1.42$). The method to set constraints on DM models consisted of excluding the branon masses for a tension of the brane unable to be in agreement, within their error bars, with the AMS experimental data. *Right panel*: In this panel, **Model B** is displayed. The method to set constraints on DM models has consisted of excluding the branon masses lying above the data. A χ^2 study has been also computed and subsequent exclusion maps obtained, as shown in Fig. 3.8.

fraction. Under this observation, we change $\{M, f\}$ to see the limits in which the fitting starts to not being in concordance with the data at 95% confidence level.

• Secondly (**Model B**) the supposition for the positron fraction is that the excess comes from branons together with a non-parametrised source injecting secondary positrons. The strategy would consist of excluding branon models that exceed the positron fraction $\mathcal{F}_{e^+}$, while those below the data are allowed. **Model B** opens the possibility of constraining values in the case in which the rise of secondary positrons is not only due to one source.

Both for **Model A** and **Model B**, we shall perform a χ^2 analysis, bearing in mind that the χ^2 test is not strictly correct since the AMS error bars do not follow a Gaussian distribution to a tee. Thus, rigorously speaking, it would be necessary to analyse variations in all the parameter space of both the astrophysical and the DM model to obtain the statistical significance of the predictions. Nevertheless, for the level of precision we are looking for, our approximation is sufficient to constrain branons characteristics. Indeed, we study masses from 200 GeV to 100 TeV. So that, in the following, we have used a likelihood analysis at the 95 % confidence level with 40 degrees of freedom (d.o.f.).

Furthermore, it is necessary to remark that the study is valid from the range of energies $E = 10\,\text{GeV}$, while for lower energies the analysis requires to study the influence of the galactic wind together with solar modulation [205] (see also, Section 2.5.1). In Fig. 3.7, we provide illustrative realisations for both cases.

• The **Model A** is plotted in the left panel, where the positron fraction $\mathcal{F}_{e^+}$ follows the expression (3.4) for e^+ with those parameters already specified in the previous section. Therefore,

we plot the total signal Bkg+Pulsars together with the contribution of branons with $M = 20.40\,\text{TeV}$ and $f = 4.99\,\text{TeV}$ with $\chi^2 = 56.94$, $\chi^2_{\text{red}} = 1.42$. The value for χ^2_{red} is not accepted within the 95% of confidence level.

- The right panel corresponds to the **Model B**. In such a panel, the candidate with $M = 22\,\text{TeV}$ and $f = 5\,\text{TeV}$ in pink is not since the remaining contribution may come from other sources injecting primary e^+. On the contrary, the line in orange representing a branon with $M = 41\,\text{TeV}$ and $f = 5\,\text{TeV}$ is ruled out. In this sense, all the models whose e^+ contribution exceeds the data are excluded. Also, in green, we plotted the background where primary e^- and secondary e^- and e^+ are considered.

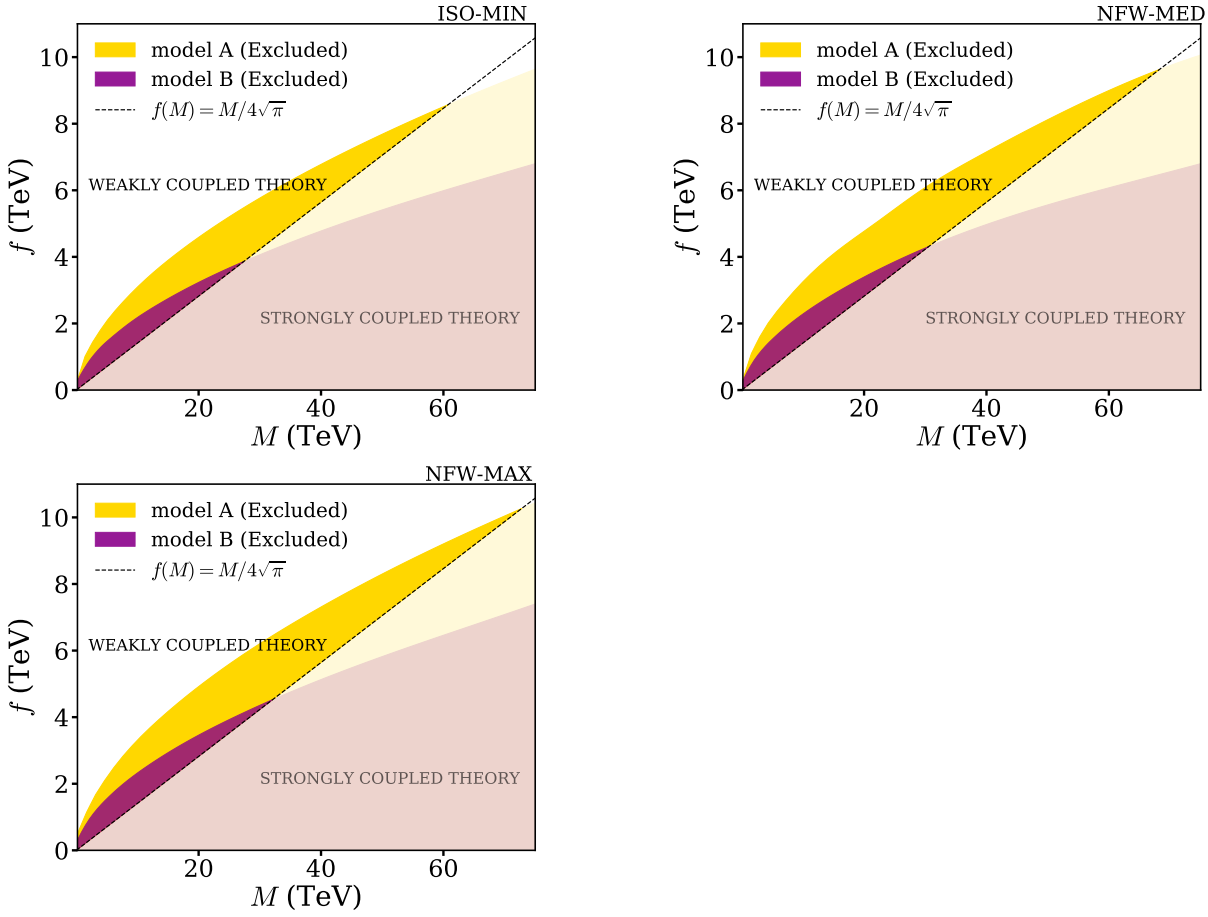

FIGURE 3.8: Exclusion diagrams for the **Model A** (purple) and **Model B** (yellow) [229]. Bright coloured areas indicate the excluded region in the parameter space (f, M) assuming the ISO-MIN (upper-left panel), NFW-MED (upper-right panel) and NFW-MAX (lower panel) DM profiles. The lowest mass in this study is 200 GeV, ensuring the annihilation into the channels W,Z. Dashed black line sets the limit of the perturbative theory for branons and the validity of tree-level versus loop branon effects [302]. The exclusion is only valid when the coloured area lies above the line (weakly coupled region).

Both **Model A** and **Model B** were computed under the assumption of MAX diffusion where $B = 6\,\mu\text{G}$ and the NFW profile. Model A is more restrictive than **Model B** since it starts with an injection of primary e^+ from PWN.

Furthermore, in this study, one has probably noticed that from Eq. (2.6), the injection of e^+ should be suppressed by $\propto 1/M^2$ and Fig. 3.7 shows the opposite. However, it is important to

TABLE 3.3: Intersection between the exclusion regions with the strongly coupled limit for branons. Model A refers to the study in which AMS rise can be perfectly accommodated by a PWN contribution. DM is also constrained in this last scenario. Model B relies on the standard scenario in which primary e^+ and secondary e^+/e^- are assumed as the total background. This study has been done both for the Isothermal and NFW density profile together with three different diffusion models usually labelled as MIN, MED and MAX

	Astro. scenario	M(TeV)	f(TeV)	$\langle\sigma v\rangle$(cm^3/s)
Model A	ISO - MIN	60.7	8.5	$3.9 \cdot 10^{-22}$
	NFW - MED	68	9.6	$3 \cdot 10^{-22}$
	NFW - MAX	77	10.3	$3.7 \cdot 10^{-22}$
Model B	ISO - MIN	27.3	3.8	$2.1 \cdot 10^{-21}$
	NFW - MED	30.5	4.3	$1.5 \cdot 10^{-21}$
	NFW - MAX	32	4.5	$1.4 \cdot 10^{-21}$

be aware of the parameters we select for our study, M and f. If we fix the thermally averaged cross section $\langle\sigma v\rangle$ to be constant, then the positron fraction is indirectly proportional to the mass. The latter applies also for branons, however, if we fix the tension f, following the expression (1.39), the thermally averaged cross section also depends on the mass, scaling as M^6. Thus, the signal, together with the thermally averaged cross section, rises with a mass increment.

The above analysis sets the basis to obtain Fig. 3.8. There, exclusion diagrams for branons according to **Model A** and **Model B** are represented. Exclusion areas correspond to the coloured area in yellow (**Model A**) and purple (**Model B**). In general lines, coloured regions in exclusion plots follow the branon particle behaviour that can be inferred from the Lagrangian in Eq. (1.37): heavier branons produce more e^+ but its production is suppressed by the tension, f. In this regard, three distinct panels show the influence of the astrophysical parameters in the exclusion plot, and, although some details differentiate them, qualitatively, all the panels show substantial similarities. From this fact, we suggest that different astrophysical scenarios for the Milky Way are not very significant as the particle counterpart on the branon constraints. This fact could be easily inferred considering that the coupling of branons with SM particles is suppressed by $1/f^4$ and their thermally averaged cross section $1/f^8$. In more detail, comparing the upper-right panel (NFW-MED) and the (NFW-MAX) lower panel in Fig. 3.8, we observe that differences in the propagation do not practically modify such constraints significantly. In fact, the largest deviations can be found for different DM density profiles, as comparing upper-left and upper-right panel.

Moreover, in Fig. 3.8, exclusion diagrams are separated by the dashed line $f = M/\sqrt{4\pi}$ providing the validity limit for the branon theories presented in this work. Branon description is constructed over a non-renormalisable effective Lagrangian formalism and its regularisation is made by considering an energy cut-off Λ for perturbative terms. From a phenomenological perspective, Λ/f parametrises how strongly (or weakly) coupled the quantum brane is, and thus controls the unknown relative importance of tree-level versus loop branon effects. In this sense, branon-loops effects on SM particles start to be relevant when $\Lambda \lesssim 4\sqrt{\pi} f N^{-1/4}$, being N the number of extra-dimensions [302]. In our work, the number of extra-dimensions considered, N, is 1 and Λ is taken in the range of energy of the branon mass M.

In Fig. 3.8, we observe that the intersection between the strongly coupled limit and the exclusion region for the NFW-MAX scenario lies at $\{M, f\} = \{77\,\text{TeV}, 10.3\,\text{TeV}\}$ for **Model A**

and {32 TeV, 4.5 TeV} for **Model B** corresponding this limits to thermally averaged cross section thermally averaged cross sections equal to $\langle\sigma v\rangle = 3.7 \cdot 10^{-22}\text{cm}^3/\text{s}$ and $\langle\sigma v\rangle = 1.4 \cdot 10^{-21}\text{cm}^3/\text{s}$ respectively. Likewise, in an NFW-MED framework maximum constraint values are reached at $\{M, f\} = \{68\,\text{TeV}, 9.6\,\text{TeV}\}$ for **Model A** and {30.5 TeV, 4.3 TeV} for **Model B** corresponding this limits to thermally averaged cross section thermally averaged cross sections equal to $\langle\sigma v\rangle = 3 \cdot 10^{-22}\text{cm}^3/\text{s}$ and $\langle\sigma v\rangle = 1.5 \cdot 10^{-21}\text{cm}^3/\text{s}$ respectively. Finally, for the ISO-MIN case, $\{M, f\} = \{60.7\,\text{TeV}, 8.5\,\text{TeV}\}$ for **Model A** and {27.3 TeV, 3.8 TeV} for **Model B** with $\langle\sigma v\rangle = 3.9 \cdot 10^{-22}\text{cm}^3/\text{s}$ and $\langle\sigma v\rangle = 2.1 \cdot 10^{-21}\text{cm}^3/\text{s}$ respectively. Beyond those values, the unitarity of the theory cannot be ensured. All these values have been summarised in Table 3.3 to provide a better understanding.

Finally, we shall remark that the contribution of branons to the positron fraction is independent of N, number of extra-dimensions and number of branon species. In fact, the contribution to positrons from each of the species is proportional to $1/N$ that is compensated by the higher abundance that a larger number of N species would provide.

3.5 Brane-World candidates

An alternative method not considered in the previous section would be fitting the positron fraction only with branons. For this, we do not consider PWNs contributions, so that, $\Phi_{e^+}^{\text{prim}} = 0$. The rest of expressions and parameters for the background are exactly those ones corresponding to primary e^- and secondary e^+/e^- as taken from Section 3.3.3.

In this analysis, we perform a χ^2 analysis for the whole branon TeV range of masses. As an illustrative example, in Fig. 3.9, we show the χ^2 map for branons in a range $M = [25, 40]$ TeV, $f = [4, 6]$ TeV for the NFW-MAX astrophysical scenario. Red regions correspond to the minima obtained for χ^2. Indeed, those regions where red is strongest the values of χ^2 are minimum while grey and black regions suppose an increment of such value. The parameter space study was performed thoroughly for $M = [0.2, 100]$ TeV, however, since the minima fall in a diagonal (red region in Fig. 3.9), we choose different intervals which included such a diagonal and not all the parameter space.

Concerning this scenario where there is no astrophysical injection of secondary positrons, in Fig. 3.9, we have computed such a χ^2-analysis in the $(M,\ f)$ parameter space. Herein we have found a global minimum at $M = 38.1 \pm 0.2$ TeV and $f = 4.99 \pm 0.04$ TeV ($\chi^2 = 37.15$, $\chi^2_{red} = 0.94$) **. The uncertainties both in M and f is taken as the separation between the next lower and upper values of M and f respectively in the χ^2 analysis. Furthermore, its thermally averaged cross section is equal to $1.76 \cdot 10^{-21}$ cm^3/s.

In order to plot Fig. 3.9, we compute pairs $\{M, f\}$ along the TeV branon space. Even though in such a plot we observe three minima, only the minimum corresponding to the candidate $M = 38.1$ TeV and $f = 4.99$ TeV would be in agreement with the positron fraction within the error bars. The main issue lies in the fact that even if the resolution in the tensions axis is 40 GeV, such a parameter suppresses the positron fraction with f^8, and thus, minor variations of f could change the positron fraction significantly. The analysis has not been precise enough to resolve 'the core' of those minima, however, although χ^2 would not be the appropriate approach, it could be a simple and useful strategy to determine the regions where minimum lie in an extensive region.

**The error for M and f is taken as the distance between two consecutive values both for M and f in the χ^2 analysis. In other words, the consecutive values for this χ^2 analysis were $M \pm \Delta M$ and $f \pm \Delta f$.

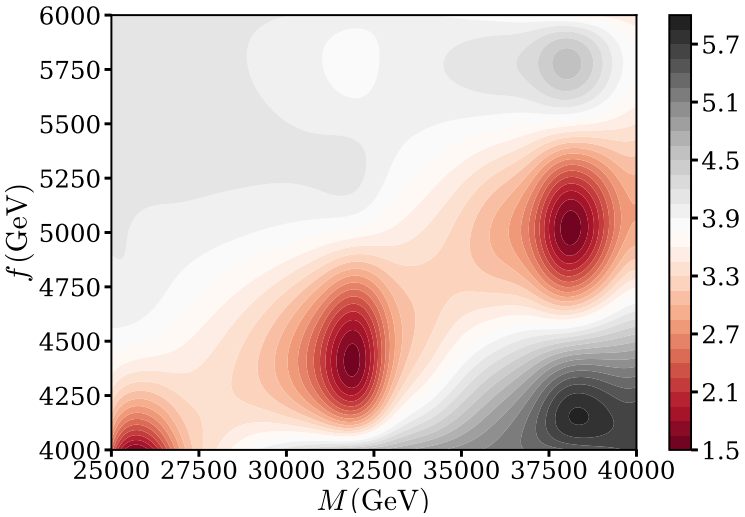

FIGURE 3.9: $\mathrm{Log}_{10}(\chi^2)$ map corresponding to the branon parameter space $\{M, f\}$. To carry out this process, we first computed the χ^2 for the range of masses 200 GeV − 100 TeV to detect those regions where the minima could be found. After that, we focused on the region presented in this plot whose range is $[25, 40]$ TeV in masses, while for tensions f is $[4, 6]$ TeV. Herein, a global minimum lies on $M = 38.1 \pm 0.2$ TeV and $f = 4.99 \pm 0.04$ TeV ($\chi^2 = 37.15$, $\chi^2_{\mathrm{red}} = 0.94$). Concerning the astrophysical considerations, the model is the NFW-MAX with a constant magnetic field equal to 6 μG.

Furthermore, in Fig. 3.10, we compute the positron fraction $\mathcal{F}_{e^+}$ for the branon $M = 38.1$ TeV and $f = 4.99$ TeV. Although for the sake of clarity the range of energies plotted is from 1 GeV to $\sim$ 500 GeV, we recall that the χ^2 analysis is from 10 GeV. In fact, the discrepancies from 2 GeV to 8 GeV in the positron fraction falls within the region in which the solar modulation influences the data changing with time, and thus such region would not allow to discard the candidate.

Conversely, for the branon with $M = 38.1$ TeV and $f = 4.99$ TeV, the thermally averaged cross section lies in $1.76 \cdot 10^{-21}\,\mathrm{cm}^3/\mathrm{s}$, much higher than that for cold thermal relics, $\langle \sigma v \rangle = 3 \cdot 10^{-26} \mathrm{cm}^3/\mathrm{s}$. The fact that the required boost to accommodate such a candidate within the cold thermal relic paradigm has to be 5 orders of magnitude bigger suggests that the pair $M = 38.1$ TeV and $f = 4.99$ would be hardly considered as a possible candidate. Also, such a candidate not only exceeds the limit for thermal relics, but also they would be within the strongly coupled theory region. As already mentioned, within this region, the Brane-World paradigm used here would not be applicable requiring radiative corrections to the tree level. In this regard, the ambiguity between cross section and enhancement mechanism would not allow us to disentangle whether those models are theoretically valid or not. Nevertheless, some boost mechanisms may be responsible for such high value in the thermally averaged cross section. Although unlikely, we do not completely exclude such a candidate, lying within the allowed region of Fig. 3.8.

3.6 Model-independent dark matter with AMS

The approach in this section consists in analysing model-independent DM in order to generalise the branon study of the previous section. To that end, we consider the e^+ injection due to DM annihilating into different channels to fit the positron fraction. Whereas some

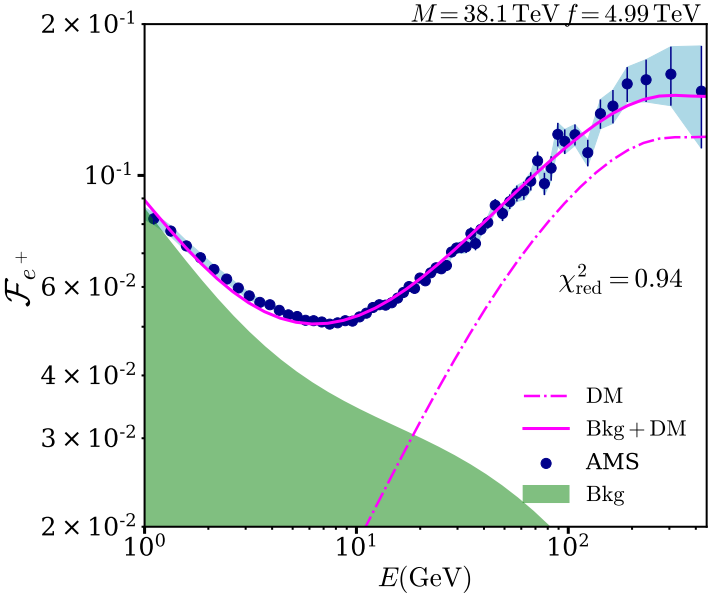

FIGURE 3.10: In this plot, the line in pink corresponds to the best fit of AMS with branons over a background in which pulsars are assumed to be completely absent. The branon mass lies at $M = 38.1\,\text{TeV}$ ($\chi^2 = 37.15$, $\chi^2_{\text{red}} = 0.94$) for the same tension $f = 4.99\,\text{TeV}$. Even though the study χ^2 has been computed for the range $[10, 350]$ GeV, for the sake of clarity the plot is extended until 500 GeV. The background for such a study has been taken without any other alternative source injecting primary e^+. The model is NFW-MAX with a constant magnetic field equal to $6\,\mu$G.

annihilation channels produce similar spectra at low energies (several tens GeV), according to Fig. 3.4 and Fig. 3.5, we restrict our study to some channels for the sake of simplicity. In fact, at that range of energies, channels W^+W^- and ZZ present some similarities themselves together with the quark channels, while the major differences are for leptonic channels. To accomplish the analysis, we perform the positron fraction $\mathcal{F}_{e^+}$ with a constant magnetic field equal to $6\,\mu$G for all the pairs $\{M, \langle\sigma v\rangle\}$ between 1 TeV and 100 TeV. The chosen astrophysical scenario is NFW-MAX.

Some authors provide fitting functions for the kind of analysis we compute in this section for the case of DM annihilating into SM model particles and whose final state are photons [303] (the case of non-charged particles). This was our first approach for the case of e^+. However, even though this can be a useful strategy for either photons or neutrinos, for e^+ it is not worthwhile. We should have in mind that photons and neutrinos conserve their injection spectra after their propagation. In other words, it is possible to factorise an astrophysical function from the energy dependence in the total flux. However, for e^+ the flux is written in terms of a Bessel-Fourier series (see Eqs. (2.29) and (2.34)), where the energy dependence only can be factorised from the astrophysical factor term by term in the series but not in the global function. Thus, any fitting function for the positron flux at the Earth would also depend on the propagation and the DM density profile.

In Fig. 3.11, we plot a map of the most promising parameter space intervals to find model-independent DM candidates. In order to do this, we undertook a χ^2_{red} study for W^+W^-, $b\bar{b}$ and $\tau^+\tau^-$ channels in a range of masses from 1 TeV to 100 TeV. Again, we remark that the χ^2_{red} analysis only suggests those regions on the parameter space where possible DM candidates lie, although it is not strictly correct since error bars do not follow a Gaussian distribution. Broadly,

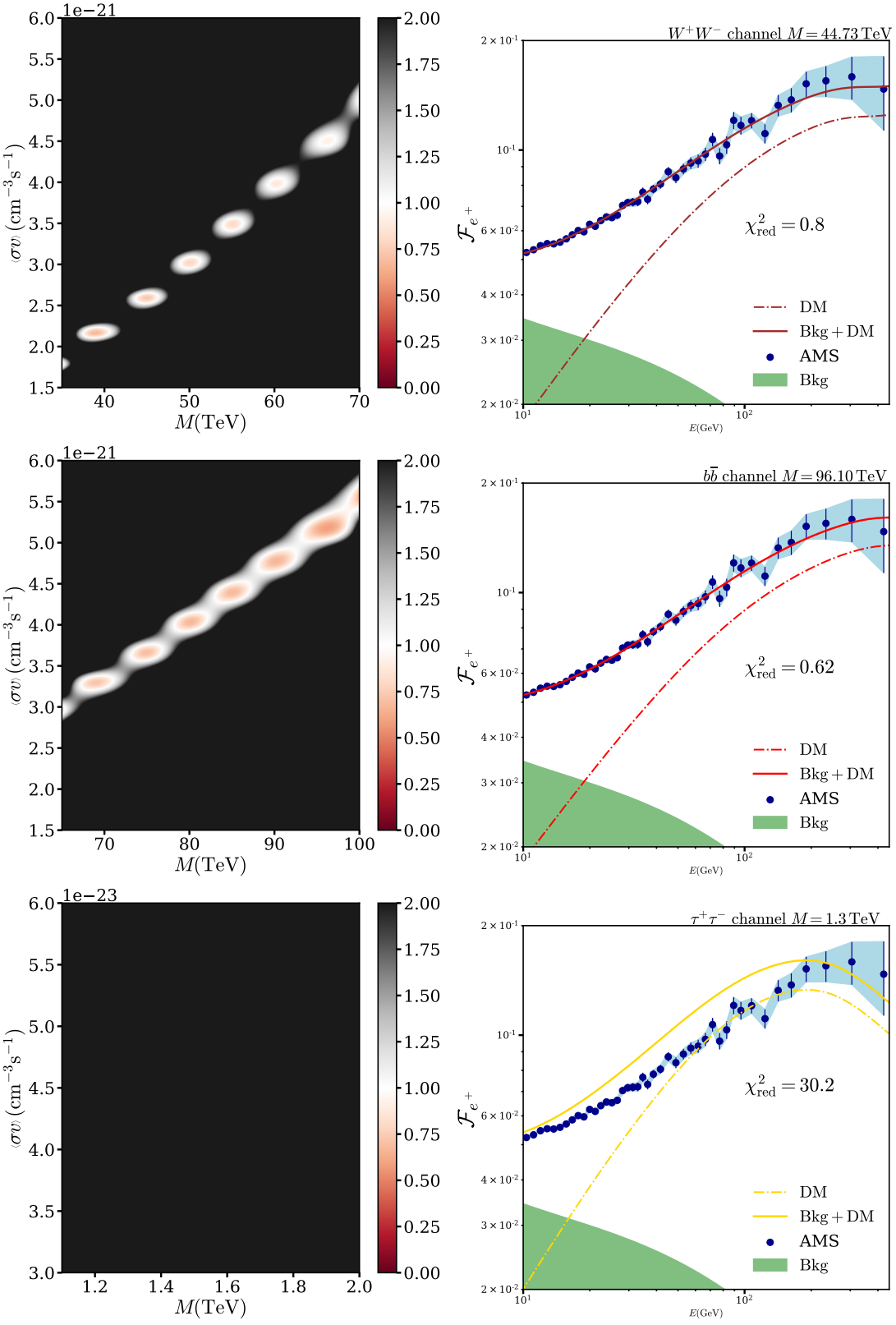

FIGURE 3.11: χ^2_{red} map for the positron fraction analysis. Unlike the study with branons, the parameter space considered is $\{M, \langle\sigma v\rangle\}$. In this study we examine the DM annihilation into three different channels, W^+W^-, $b\bar{b}$ and $\tau^+\tau^-$. For the channels W^+W^-, $b\bar{b}$, heavy DM seems to agree with AMS data. However, the thermally averaged cross section, $\langle\sigma v\rangle$, clearly exceeds the thermal relic density cross section, $3 \cdot 10^{-26}\,\mathrm{cm}^3/\mathrm{s}$, in five orders of magnitude.

as observed in Fig. 3.11, the smallest values for $\chi^2_{\rm red}$ lie on an increasing curve following:

$$\left.\frac{\langle\sigma v\rangle}{10^{-21}\,\mathrm{cm}^3/\mathrm{s}}\right|_{W^+W^-} = 4.86M^{1.01} - 5.18 \quad \text{for} \quad 35\,\mathrm{TeV} \leq M \leq 70\,\mathrm{TeV},$$
$$\left.\frac{\langle\sigma v\rangle}{10^{-21}\,\mathrm{cm}^3/\mathrm{s}}\right|_{b\bar{b}} = 7.15M^{1.00} - 7.66 \quad \text{for} \quad 65\,\mathrm{TeV} \leq M \leq 100\,\mathrm{TeV}, \tag{3.8}$$

with M in TeV, for the channels W^+W^- and $b\bar{b}$ respectively. Also, minima are discretised, possibly due to the separation of pairs we chose for the study $\chi^2_{\rm red}$ analysis. This might also suggest the existence of more minima over the curve.

The selected parameter space intervals, $\{M, \langle\sigma v\rangle\}$, for the model-independent DM case (Fig. 3.11) has been determined firstly studying qualitatively how the considered channels would be in agreement with the positron fraction. This allowed us to focus on specific regions of the parameter space that subsequently were plotted in Fig. 3.11. Outside the regions presented in this figure, we conclude that none of the DM candidates annihilating into W^+W^-, $b\bar{b}$ and $\tau^+\tau^-$ would fit the AMS data. Indeed, by doing an analysis of the concavity and convexity of the positron fraction (for an illustrative example, refer to the $\tau^+\tau^-$ channel in the right panel of Fig. 3.11), we observe that DM models annihilating predominantly in $\tau^+\tau^-$ channels only would explain AMS data provided the DM candidate had a mass of a few TeV. In Fig. 3.11, the $\chi^2_{\rm red}$ analysis reveals that $\tau^+\tau^-$ does not fit the AMS excess. For e^+ coming from the DM annihilating into either $b\bar{b}$ or W^+W^-, only heavy DM candidates may fit the positron fraction provided their masses are tens TeV. This fact may be important if either a cut-off is observed or not in the following years data. Theoretically, heavy DM candidates would have their cut-off at high energies according to the 4-momentum conservation, and thus, only such models would prevail if no cut-off is observed in the next data points of the positron fraction.

Moreover, in left panels of Fig. 3.11, we observe that $\tau^+\tau^-$ channel is only linked with DM whose thermally averaged cross section lies around $\sim 10^{-23}\,\mathrm{cm}^3/\mathrm{s}$. Although this value still exceeds the thermal relic cross section, it remains relatively close and a boost mechanism could be more easily justified than the case of either quarks or bosons for which $\langle\sigma v\rangle \sim 10^{-21}\,\mathrm{cm}^3/\mathrm{s}$. In right panels of Fig. 3.11, we plot the positron fraction for model-independent DM annihilating into W^+W^-, $b\bar{b}$ and $\tau^+\tau^-$ channels for specific minima of the $\chi^2_{\rm red}$ map (left panel). In the case of the W^+W^- channel we chose the mass $M = 44.93$ TeV in brown with $\langle\sigma v\rangle \sim 2.6 \cdot 10^{-21}\,\mathrm{cm}^3/\mathrm{s}$, while for $b\bar{b}$ the mass is $M = 96.1$ TeV with $\langle\sigma v\rangle \sim 5.1 \cdot 10^{-21}\,\mathrm{cm}^3/\mathrm{s}$, although other minima, as indicated in the left panels, can be found. On the other hand, for the case of $\tau^+\tau^-$, we considered several masses observing that none of them would be able to fit the AMS data. The right panel for $\tau^+\tau^-$ is an example of this fact.

3.7 The role of the background

Some works based on [304] has proposed a DM candidate whose mass is 1.2 TeV, yet in our analysis we have not found any candidates fitting the positron fraction which are close to that mass. Indeed such a candidate would annihilate in a significant proportion into leptons, obtaining a different result from the one we observed above. These facts have made us wonder those factors that may be determinant in the positron fraction explanation. Thus, we decided to study whether the role played by background is significant when fitting the positron excess. In the computation of previous fittings, we used the background expressions from [290] described in Section 3.3.3, that from now we will label as **BKG I**. In the following step, we have been inclined to observe the effect of considering another parametrisation slightly different from

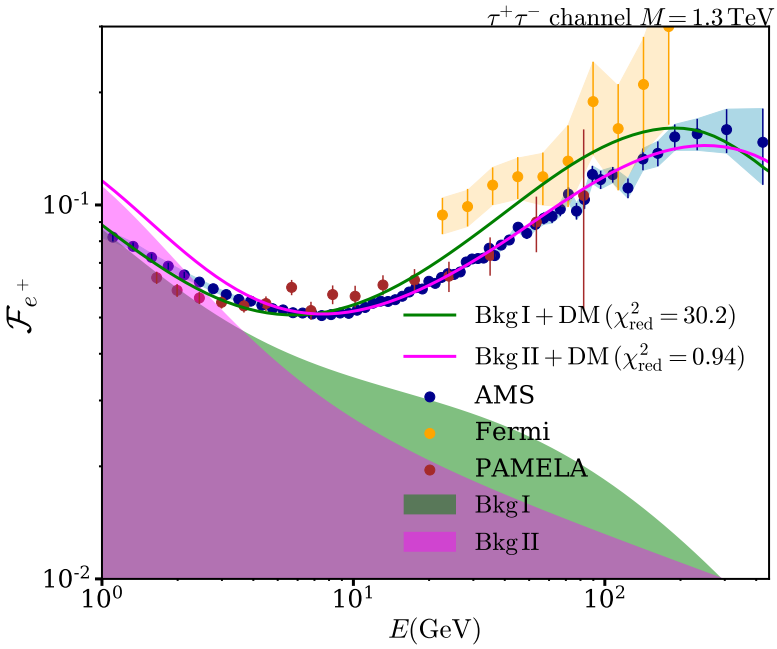

FIGURE 3.12: Positron fraction corresponding to a 1.3 TeV DM candidate annihilating in the single channel $\tau^+\tau^-$. The purpose of this plot is mainly comparing how the chosen background can highly influence the possible DM candidates. The green band is the **BKG I** used for our previous calculations (see Section 3.3.3 for more information). The fuchsia band **BKG II** is the background obtained in Ref. [208]. The green and fuchsia lines indicate the kind of background used for the 1.3 TeV DM candidate. As seen in this plot, the fuchsia line better fits the AMS data.

the background we have used. In order to do that, we followed the line of reasoning of some authors (see for example [206]) using the parametrisation of the results from GALPROP in 1998 from [208] (label as **BKG II**):

$$\Phi_{prim.\,e^-\,bkg} = \frac{0.16E^{-1.1}}{1+11E^{0.9}+3.2E^{2.15}}\ \text{GeV}^{-1}\text{cm}^{-2}\text{s}^{-1}\text{sr}^{-1} \tag{3.9}$$

$$\Phi_{sec.\,e^-\,bkg} = \frac{0.70E^{0.7}}{1+110E^{1.5}+600E^{2.9}+580E^{4.2}}\ \text{GeV}^{-1}\text{cm}^{-2}\text{s}^{-1}\text{sr}^{-1} \tag{3.10}$$

$$\Phi_{sec.\,e^+\,bkg} = \frac{4.5E^{0.7}}{1+650E^{2.3}+1500E^{4.2}}\ \text{GeV}^{-1}\text{cm}^{-2}\text{s}^{-1}\text{sr}^{-1} \tag{3.11}$$

$$\tag{3.12}$$

Therefore, the strategy followed in a large number of studies is computing the expected flux of positrons from DM annihilation and the background above and combine them with a multiplicative factor A_B, both that accounts for the normalisation of the background and the boost factor expected in the DM annihilations [206]. The used values in the bibliography for the background normalisation A_B is between 0.6 and 1.1. and has been used to fit the Heat 94+95 data. This normalisation accounts for additional sources at high energy.

In Fig. 3.12, we show two different models for the background; **BKG I** and **BKG II**, in fuchsia. Even though the study for DM has been performed for $E > 10$ GeV, we also show lower energies in order to understand better the background effect. In such a figure, we note that BKG I considers that there are more astrophysical sources injecting positrons at intermediate energies (10 GeV - 100 GeV) than in **BKG II**, while for the former **BKG I** the injection at low energies underestimates the positron fraction with respect to **BKG II** and the data. Moreover,

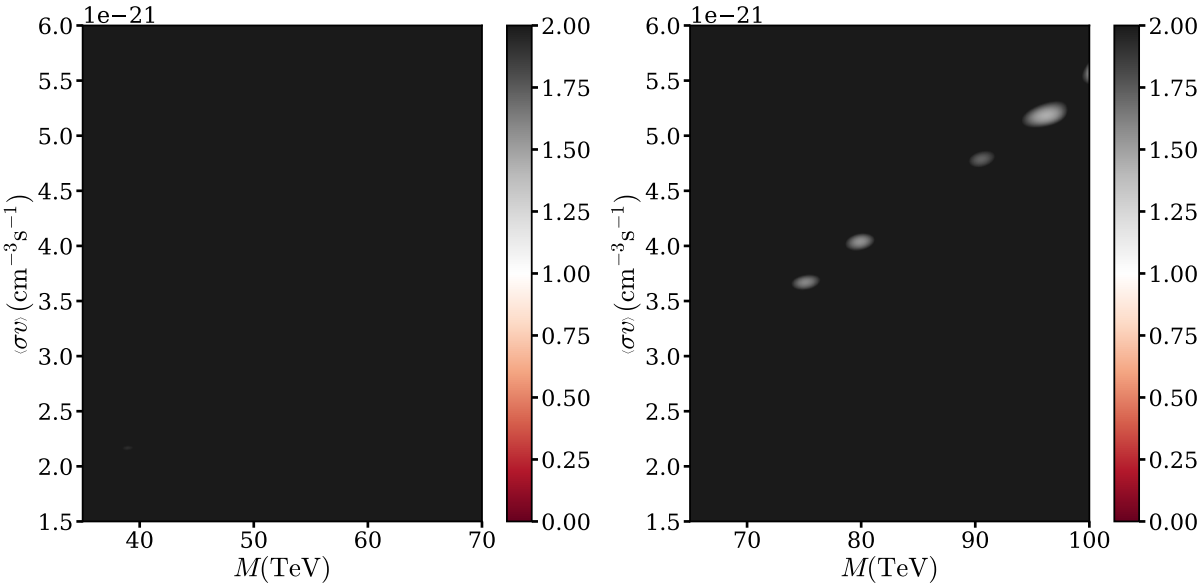

FIGURE 3.13: χ^2_{red} map for the positron fraction analysis with the AMS latest results. Only the relevant region of the χ^2 plot has been shown. In this study we examine the DM annihilation into two different channels, W^+W^-, $b\bar{b}$. Clearly, the new data leaves less room for the AMS excess interpretation in terms of heavy DM annihilating into these channels. The new values for the χ^2_{red} clearly exceeds the value equal to 1.

the fall around 10 GeV both background scenarios, will determine which models would fit better the positron fraction. On the one hand, **BKG I** decrease shows to be less sharp than in **BKG II**, thus, the best models to fit the positron fraction are those corresponding to signals with a smooth slope at those energies, as in the case of DM annihilating via either bosons or quarks. On the other hand, in order to compensate the significant decline in **BKG II**, the favoured DM candidates are those annihilating into leptons whose signal slope is more pronounced at those range of energies. Therefore, we conclude that the positron fraction is very sensitive to the model of background. Indeed, we conclude that background not only determines the preferred channel of annihilation but also the candidate mass.

In Fig. 3.12 we present an example of this. According to Fig. 3.11, a DM candidate annihilating into $\tau^+\tau^-$ is highly disfavoured when we consider **BKG I**. In the latter figure, the region with masses ranging from 1.225 GeV to 1.4 GeV presents a χ^2_{red} around 1.25, consequently, this model is not able to explain the positron excess. Nevertheless, for **BKG II**, the fuchsia line shows to be in agreement ($\chi^2_{red} = 0.94$) with the data when A=0.70 and with a boost of 1530. It is also important to remark that **BKG II** does not include the solar modulation effect, and that is the reason why this model exceeds the data around 1 GeV.

3.8 AMS latest results

In the course of this research, a set of new data from AMS has been released, changing some of the statements established in previous sections. Thus, the following results intend to serve as a pertinent update of some abovementioned statements in this Chapter.
Indeed, in January 2019, the AMS collaboration released a cosmic-ray positrons spectrum with energies up to 1 TeV, providing clearer pieces of evidence about the existence of a finite energy

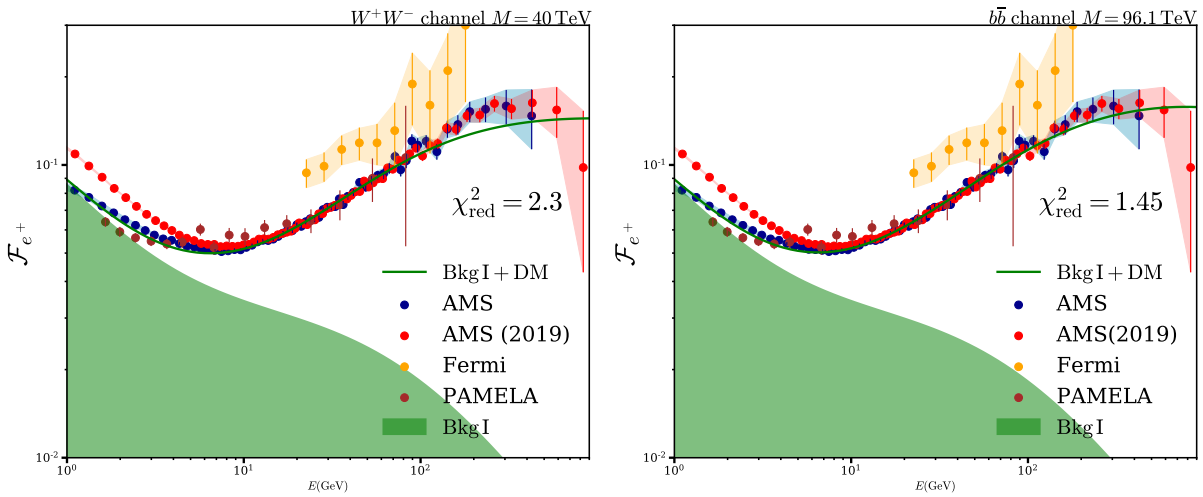

FIGURE 3.14: In this plot, the line in green corresponds to the fit of AMS provided the $\chi^2_{\rm red}$ of Fig. 3.13. Even though the study χ^2 has been computed for the range $[10, 810]$ GeV, for the sake of clarity the plot is extended from 1 to 900 GeV. The background for such a study has been taken without any other alternative source injecting primary e^+. The propagation model is the NFW-MAX with a constant magnetic field equal to 6 μG. *Left panel*: A DM model annihilating into W^+W^- has been represented. *Right panel*: We present the contribution from DM annihilating into $b\bar{b}$ channel. As seen in this figure, none of the models seem to follow the tendency of the latest data.

cut-off around 810 GeV [305]. The experimental results are consistent with the previous data considering that at low energies from 0.5 to 7.10 GeV there is a significant time variation of the spectrum due to solar modulation effects.

From such latest measurements, three regions for the positron fraction are well-defined, besides the already mentioned time variation, subjected to the solar modulation from 0.5 GeV to $\sim$ 7 GeV. Also, around 10 GeV, a flattening acting like an inflexion region between low energy positrons and the rise that starts around $\sim$ 20 GeV. This rise reaches a maximum at $\sim$ 290 GeV where a sharp fall starts. Such a complex behaviour of the positron fraction is consistent with the existence of an alternative source of high-energy e^+ with characteristic cut-off energy, either of DM or other astrophysical origin [305]. Moreover, such a convoluted behaviour in 2019 data is not consistent with the secondary production of positrons in collisions of cosmic rays exclusively.

In view of the most recent results, the channels corresponding to heavy DM proposed in previous sections would not able to reproduce the positron fraction anymore presenting a $\chi^2_{\rm red} > 1$, as is possible to see in Fig. 3.13 and Fig. 3.14. Within the DM explanation for the positron fraction, the confirmed fall at high energies would not be compatible either with specific heavy candidates as branons. This does not mean that most recent data rule out such candidates since in order to explain the positron fraction, the e^+ flux has to be multiplied by a boost factor. However, the new results would suggest that branons would neither fit such a positron fraction nor heavy DM, whose cut-off appears at larger energies. Finally, in Fig. 3.15, although qualitatively the candidate $\tau^+\tau^-$ with a mass around $M = 1.5$ TeV seems to accommodate to AMS 2019 measurements, in terms of $\chi^2_{\rm red}$, we observe that such a candidate would not fit the data. It is necessary to take this $\chi^2_{\rm red}$ value carefully since as we mentioned, the $\chi^2_{\rm red}$ is not strictly valid.

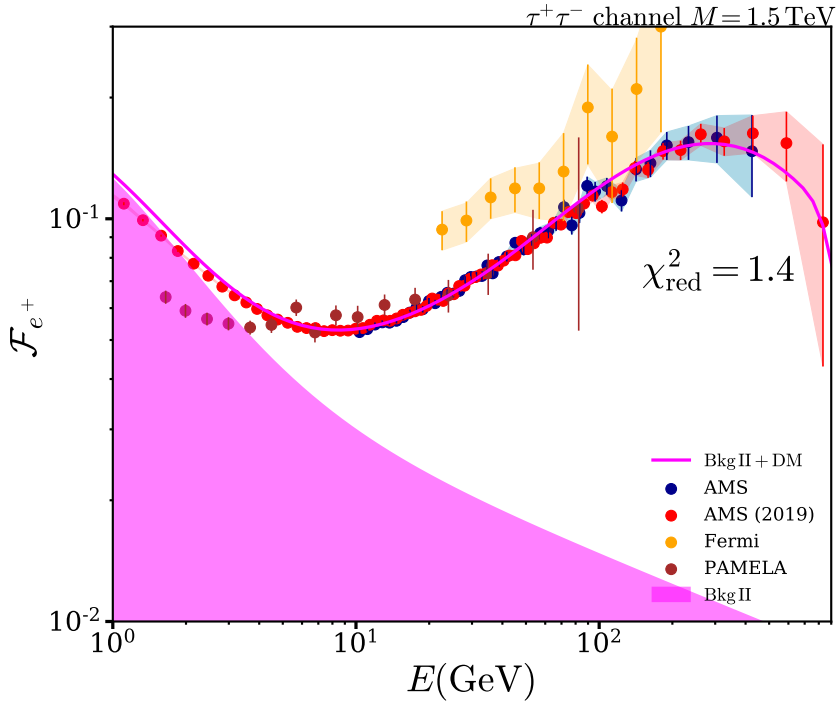

FIGURE 3.15: Best fit of the positron fraction with the latest AMS data. The background chosen for this fit is that we labelled as BKG II. The DM model corresponds to 1.5 TeV DM annihilating into the leptonic $\tau^+\tau^-$. The study χ^2 has been computed for the range $[10, 810]$ GeV. The astrophysical framework corresponds to an NFW-MAX model with a constant magnetic field equal to 6 μG.

3.9 Chapter conclusions

In Chapter 3, we presented the positron fraction excess which appears from 10 GeV onwards and was measured by PAMELA, then confirmed by Fermi-LAT and accurately observed by AMS. As mentioned, such excess cannot be explained, within the conventional propagation framework, by solely secondary positrons. Either the conventional propagation mechanisms need to be revised or alternative sources injecting positrons have to be added. The former seems to be disfavour, essentially on account of the difficulty of not spoiling the already well-explained abundances of other cosmic rays. Also, the positron fraction shows a cut-off at higher energies which would reinforce the idea of adding alternative sources injecting positrons. With regard to the latter, we divided the sources into astrophysical ones (supernovae or Pulsar Wind Nebula) or exotic ones (dark matter). The case we treated in our investigation is the case of annihilating dark matter within the WIMP paradigm discussed in Chapter 1 and Chapter 2.

In Section 3.2 and Section 3.3, we provided the main features to understand how the excess in the positron fraction can be interpreted from different points of view. Indeed, we focused on alternative propagation models to explain such an excess, but also on primary sources for positrons and electrons, such as pulsars and also dark matter. We presented specifically the latter case that was discussed in subsequent sections.

In Section 3.4, we focus on extra-dimensional dark matter, specifically on Brane-World theories in which the brane fluctuation would induce the production of branon dark matter. In our first approach, we set constraints on branons under two astrophysical possibilities: either the positron fraction is explained by pulsars (which is not a sufficient reason to rule out dark matter allowing to still set constraints) labelled as **Model A**, or it can be explained by a combination of non-parametrised sources and dark matter **Model B**. The tightest constraints obtained is for the

NFW-MAX profile excluding dark matter masses up to 77 TeV ($f = 10.3$ TeV) for **Model A** and 32 TeV ($f = 4.5$ TeV) for **Model B**. None of the exclusion regions belongs to thermal relic dark matter since we did not assume any boost factor. Indeed, the thermally averaged cross section lies around $\sim 10^{-21} - 10^{-22}\text{cm}^3/\text{s}$. Furthermore, in Section 3.5, we fitted the positron fraction with a branon candidate of mass $M = 38.1$ TeV and a tension of $f = 4.99$ TeV.

A similar study to that described in the above paragraph has been also applied to model-independent dark matter. In Section 3.6, we fitted the positron fraction with model-independent dark matter. Even though we aimed at the $b\bar{b}$, $\tau^+\tau^-$ and W^+W^- channels, during the computation we observed some similarities between channels that allowed us to set more general statements. In the first place, we observed that in order to explain the positron fraction, dark matter annihilating mainly into boson and quark channels are required to be heavy ($M > 40$ TeV) while leptonic channels seem to be lighter ($M \sim 0.5 - 2$ TeV), i.e., Fig. 3.11. This fact can be seen in the flux energy dependence of the different channels: leptonic channels present sharper spectra than the rest (Fig. 3.4). The mass difference between dark matter annihilating into leptons and dark matter annihilating into either bosons or quarks would suggest something else: to explain the positron fraction the heavier candidates ($M > 40$ TeV) would need a thermally averaged cross section of, at least, $\sim 10^{-21} - 10^{-22}\text{cm}^3/\text{s}$ that can only be explained in terms of a boost factor of $\sim 10^5$. Conversely, leptons would produce e^+ necessary to reach the order of magnitude of the data with a boost of 10^3. Therefore, dark matter annihilating into leptonic channels would be easier to accommodate within the usual astrophysical and cosmological framework. This fact is independent of what we will discuss in the following paragraphs.

Our model-independent analysis (see Fig. 3.11) initially revealed that the $\tau^+\tau^-$ channel would not be able to explain the positron fraction. However, this result was shown to be highly dependent on the chosen background, as seen in Fig. 3.12. In this regard, it is extremely important to understand the e^+/e^- propagation/injection mechanism at intermediate energies ($E \sim 10$ GeV). Indeed, the curvature of the fitting function in this range would determine not only the mass of the candidate but also the channel of annihilation according to the above discussion.

Finally, latest AMS results would suggest that heavy dark matter candidates would not be in agreement with the positron fraction. Indeed, the sharp fall at around ~ 290 GeV would strongly disfavour candidates with masses of tens TeV (see Fig. 3.13 and Fig. 3.14). Consequently, assuming that dark matter explains the positron fraction, then there would only be room left for dark matter annihilating into leptons. Nevertheless, our χ^2 analysis (in Fig. 3.15) shows that the channel $\tau^+\tau^-$ would not either explain such a positron fraction $\chi^2_{\text{red}} = 1.4$ giving more weight to an astrophysical justification. However, this analysis has to be taken very carefully due to the fact that the χ^2 analysis would not be strictly valid, as we already discussed. For this reason, we still consider that a dark matter candidate with a mass of 1-2 TeV annihilating into leptons would still be able to fit the positron fraction although the χ^2 analysis also disfavours it. It is also important to highlight that in the event that a particular dark matter model does not explain the positron fraction, this does not mean that it is discarded. It has to be kept in mind that in order to explain the positron fraction it is necessary a boost factor (Fig. 3.6) and thus the possibility of an annihilating dark matter candidate with a negligible contribution to the positron fraction is also possible.

In order to account for the positron fraction, some authors have proposed candidates with masses in the range of sub-TeV or a few TeV. Indeed, one of the most recent models would be a two-component dark matter candidate (with masses of 750 GeV and 2.3 TeV) decaying with a lifetime of 10^{26} s into a τ lepton pair [306]. In this regard, not-very-heavy (a few TeV) dark matter may be detected by other experiments with high sensitivity telescopes. In the next Chapter, we will focus on the dark matter radio signals coming from the Milky Way.

Chapter 4

Synchrotron emission from dark matter in the Milky Way

4.1 Overview and leitmotiv

In Chapter 3, we conducted a study on e^+/e^- cosmic rays by computing the e^+/e^- fluxes at the Earth. This study, in which we chose $r = r_\odot$, refers all the DM signatures to one coordinate in the Galaxy. Fortunately, the energy losses suffered by e^-/e^+ in their propagation (synchrotron emission, ICS, *bremsstrahlung* or Coulombian interactions), enable to measure signals from different regions of the sky. In Chapter 4, we will focus on the synchrotron emission as the result of the interaction of e^-/e^+ with the Milky Way magnetic field. This will allow us to focus on the diffuse emission, potentially observable, from the DM annihilation. Thus, the main objective of this chapter is to constrain DM features with radio signals in the Milky Way and studying the SKA1 capabilities to improve such constraints. The main results of this Chapter have been collected in Ref. [180]. The work has been organised as follows:

■ In Section 4.2, we will present the astrophysical scenario, relevant for upcoming sections. Firstly, we will summarise the main aspects relative to DM detection for the GC; in particular, the advantages and the challenges that this target presents. Secondly, we will also review DM searches outside the Galactic Plane. We will see that both the GC and other latitudes present excesses in signals at different ranges of frequencies. Also, we will briefly provide an idea of the Galactic Magnetic field together with the DM density profile expected in the Milky Way. Finally, we will discuss the numerical challenges that we found at the time of constraining DM with our codes.

■ In Section 4.3, we will compute temperature maps for the DM synchrotron emission in the Milky Way. Here, we will discuss how the spatial shape of the emission depends on the magnetic field. After this, we shall constrain DM models with the brightness temperature relative to the Galactic Plane at 45 MHz measured in Ref. [307]. Firstly, we will focus on the model-independent DM case and subsequently applied to DM in Brane-World theories.

■ In Section 4.4, assuming that DM signals can be disentangled from a well-known radio background, we will compute sensitivity constraints for SKA, both for the GC and Galactic AntiCentre (GAC). Again, we will first study the case of model-independent DM. After that, Brane-World DM will be also analysed.

■ Finally, based on our computational model (Section 2.6), in Section 4.5, we shall present regions of the sky in galactic coordinates (l, b) suitable to detect DM candidates with the SKA. These maps will intend to find alternative sky areas, out of the GC, in which even TeV DM would be detected.

4.2 Astrophysical considerations for the Milky Way

4.2.1 Generalities

The energy losses suffered by e^-/e^+ in their propagation (studied in Section 2.1) allows to measure signatures from different regions of the sky. As seen in such Section, depending on the energy loss mechanism, photons from the whole Galaxy reach the Earth with different frequencies. Indeed, DM particles would annihilate into SM particles that decay or hadronise into e^-/e^+, and subsequently, would produce diffuse emission from the interaction of those e^-/e^+ with the ISM. According to Fig. 2.1, synchrotron and ICS would dominate the emission when the e^-/e^+ kinetic energy is around hundreds of GeV. For synchrotron, the typical frequencies lie on radio although the emission could reach the X-ray band as well. For ICS the expected frequencies range from X-ray to γ-ray. From a more precise description, the dominant loss mechanisms in the whole Galaxy highly depends on the IRF (CMB+Dust+Stars) and the distribution of interstellar gas which would depend on spatial coordinates. Quantifying the flux of radiation that reaches the Earth from loss processes may provide relevant information about DM features as in the case of cosmic rays. Indeed, if charged particles were able to set constraints both in the mass M and its range of interaction (the latter being encoded in the thermally averaged cross section $\langle\sigma v\rangle$), one would also expect the same from radiative processes. The advantage, in this case, lies in the fact that those distinctive signatures would arise from different regions of the Milky Way. The strategy to follow for DM constraints is very similar to that applied for cosmic rays: first, the expected radiative background will be established and second, annihilating DM models will be constrained by comparing their theoretical expected emission with the current data.

Having presented the theory that is behind radiative fluxes from DM annihilation (Section 2.5), the immediate question is often related to determine the best location to focus on for DM detection. This question is closely connected with the knowledge of the spatial distribution of DM along the Galaxy. In this sense, in Section 1.2.2, we present the radial dependence in the DM density profile, generally, $\propto r^{-\gamma}$, indicating as suitable the region within a few degrees ($\sim 5^{\rm o}$) of the dynamical centre of the Galaxy, the GC. For example, in the conservative election of an Isothermal profile, the DM density at the GC presents a value 250% greater than in the Solar system. This is indeed one of the major reasons why DM indirect searches through multi-wavelength astronomy are widely considered in regions around the GC. The advantages are even more obvious considering that the GC is the brightest DM source in the sky. Its proximity provides significant advantages in measurements of the flux density, S_ν. For a point-like target at the distance of the GC ($\sim$ 8kpc), the flux density S_ν is proportional to $1/8^2$ (as follows an inverse-square law), while for the nearest galaxy M31 such a quantity would be suppressed by $1/780^2$. Thus, at first glance, the Milky Way, and specifically its GC, seems to be one of the most attractive targets to elucidate the elusive nature of DM. Moreover, a third aspect that makes the GC highly interesting is its extension, since it provides additional spatial information not accessible for far extragalactic sources.

Despite these advantages, the GC is also one of the most complicated regions of the sky since it is compounded by a wide variety of astrophysical sources emitting from radio to γ-ray frequencies. Indeed, SNRs, pulsars, colliding winds of massive stars, pulsars, transient radio, extragalactic sources, non-thermal filaments or HII regions are some of the elements to consider in the GC emission. In Fig. 4.1, we show the most relevant structures in the GC, based on the Very Large Array (VLA) radio frequency measurements ($\lambda = 90$cm) in a region $l \times b = 4^{\rm o} \times 2.5^{\rm o}$. A similar image with more resolution has been also taken by MeerKAT in a region of $2^{\rm o} \times 1^{\rm o}$*.

*https://www.ska.ac.za/media-releases/meerkat-radio-telescope-inaugurated-in-south-africa-reveals-clearest-view-yet-of-center-of-the-milky-way/

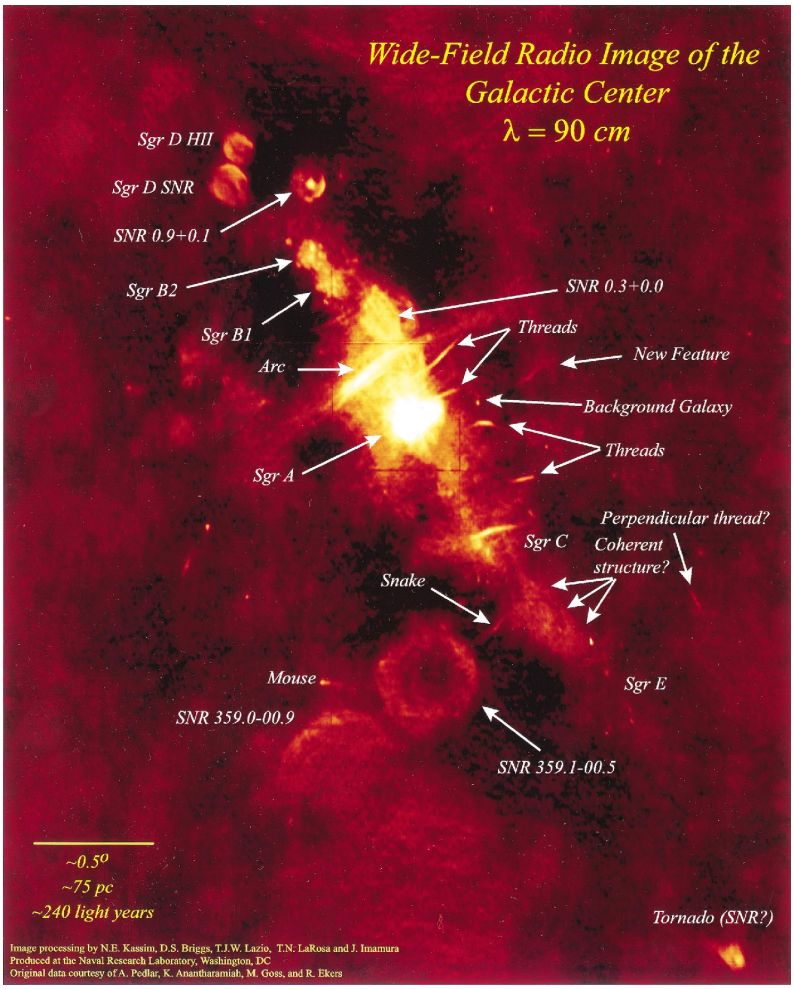

FIGURE 4.1: Taken from de la Rosa (2000) [308]. Map of the GC at 90 cm (radio) measured by VLA with a resolution of 43″. The Galactic Plane appears inclined, parallel to the pattern of emission. Coordinates are centred in Sgr A, divided in Sgr A East (SNR), Sgr A West (highly ionised gas emitting in thermal continuum) and the compact source Sgr A*. The estimated density flux S_{90} for the whole Sgr A is 361.50 Jy considering a size of $13.5' \times 13.5'$. Conversely, Sgr B1 and Sgr B2 are presented as HII regions whose $S_{90} = 17.42$ Jy and $S_{90} = 14.1$ Jy. Sgr C, however, is a non-thermal filament region with $S_{90} = 6.39$ Jy (size $11.1' \times 0.7'$) [308].

From the VLA image, hundreds of sources in the central region have been catalogued with a resolution of 43″ providing their flux density map ($\lambda = 90$ cm) from both thermal and non-thermal emission [308]. Even though there are some well-defined structures the main issue lies in disentangling the signals between some of the sources. For example, extended sources, such as Sgr A, Sgr B and Sgr C, can be partially resolved, thus some elements of their structure are hidden and may be confused with background elements. This situation is similar for the whole GC. There, unresolved populations, such as pulsars, may also provide an important contribution to the observed flux generating large uncertainties. The modelling emission of such unresolved sources is a big challenge since its analysis is based on extrapolations of detected members, which generally are a small fraction of the total population. In this aspect, high-precision radio interferometry could reveal crucial information. In fact, for $\lambda = 19$ cm the theoretical angular resolution for SKA1-MID lies around 0.19″ (baseline 200 km). Furthermore, another issue lies in the fact that some of these sources are surrounded by molecular clouds associated with past and current star formation. Such clouds constitute the Central Molecular Zone [309], a rich molecular

gas region in extreme conditions (high density, $10^4 \mathrm{cm}^{-3}$ [310], turbulent [311] and significantly hotter than the rest of the disk (50-100 K) [312]). The most prominent of these zones can be found around Sgr B2 and Sgr C but also G0.11-0.11 associated with the radio continuum Arc. Even though molecular clouds emit spectral lines at millimetre wavelengths, diffuse emission has also been detected from them at the GC. Indeed, non-thermal radio continuum emission and X-ray from e^+/e^- is associated with *bremsstrahlung* produced inside molecular clouds. In addition, cosmic-ray protons would also emit γ-ray inside this environment [313].

Despite these challenges, strong bounds on DM annihilation may be established using the GC. In fact, the large magnetic field turns synchrotron emission into one of the most relevant mechanisms in the loss of energy for e^-/e^+ opening the possibility of significant constraints in the GC. For example, measurements of the total luminosity of Sgr A* black hole (BH) shows that its bolometric luminosity, $L = 100\, L_\odot$, is several orders of magnitude lower than the Eddington luminosity, revealing Sgr A* as an under-luminous supermassive BH [314]. This would leave open the possibility of detecting a significant radiative flux from DM with respect to the background at GC. Measurements of the emission from Sgr A* (for angular windows of $\sim 5'' \times 5''$) estimate a flux of $S_\nu \sim 0.05 - 1$ Jy within the radio frequencies range and up to ~ 20 Jy in near-infrared [315].

Both the Inner Galaxy and GC, have not been exempt from the controversy about possible DM signals, especially in the range of γ-ray. The intensive collection of data by many detectors, such as CANGAROO [316], VERITAS [317], HESS [318, 319], MAGIC [320] and Fermi-LAT [321] has attracted an increasing attention on certain regions of the Inner Galaxy. In this sense, Fermi-LAT reported a $\gamma-$ray excess within the first separation degrees around the GC, subsequently confirmed in numerous studies, some of them incorporating an explanation in terms of DM [321–325]. Depending on the kind of study, the intensity maps obtained by γ-ray telescopes are integrated over distinct solid angles of different particular regions of the sky. Even though larger solid angles imply also larger statistics in DM detection, it is strictly necessary to study the best integration region to ensure the reduction (and also an accurate description) of the background with respect to the potential DM signal. After modeling the background signal for those regions (considering mainly the contribution from $\pi^0\pi^0 \to \gamma\gamma$ already mentioned in Section 3.2), the excess is fitted with the DM contribution. In Ref. [324], the observed spectrum and morphology of the emission within $\sim 1.25^\mathrm{o}$ of the GC is in agreement with 7-10 GeV DM particle annihilating into $\tau^-\tau^+$ with a cross section between $4.6 \cdot 10^{-27}$ cm^3/s and $5.3 \cdot 10^{-26}$ cm^3/s. In Ref. [326] the γ-ray emission from a region of $15^\mathrm{o} \times 15^\mathrm{o}$ around the GC would be accommodated to a DM candidate with a mass of 50 to 190 GeV (10 to 90) GeV with an annihilation cross section from $1 \cdot 10^{-26}$ cm^3/s to $4 \cdot 10^{-25}$ cm^3/s ($6 \cdot 10^{-27}$ to $2 \cdot 10^{-25}$ cm^3/s). In addition, multi-TeV DM candidates have been also considered to explain the region excess HESS $J1745-290$ [327] centered on the GC within an angle of 0.11^o [328]. The interesting aspect from HESS $J1745-290$ source is that there is no significant evidence of variability and thus, in principle, it does not seem correlated with the super massive BH activity. However, unknown astrophysical contributions might also explain the γ-ray excess without DM. Some of them consist of a large population of unresolved pulsars that also would explain AMS [329–331], new cosmic-ray sources, proton or electron outbursts or the emission from a stellar over-density in the Galactic bulge.

Leaving aside the GC and the Inner Galaxy, some works focused on DM detection considering targets several degrees away from the Galactic Plane, a fact that minimises the effects of the unknown background at different frequencies [176, 332]. In the range of microwaves, an excess was identified by WMAP, the so-called WMAP Haze, i.e., a spherical microwave emission 20^o above and below the Galactic plane with a hard spectrum of $E^2 \mathrm{d}N/\mathrm{d}E \propto E^{0.1-0.2}$ [333]. Such an excess was in accordance with the synchrotron emission from e^+e^- from annihilating DM with a mass of 100 GeV and a thermally averaged cross section $\sim 3 \cdot 10^{-26}$ cm^3/s (and also TeV

TABLE 4.1: Magnetic field component and their observational signatures. This table was taken from [337].

Field component	**Observational signatures**
Total field	Total synchrotron intensity, corrected for inclination
Total field perpendicular to the l.o.s.	Total synchrotron intensity
Turbulent or tangled field	Total synchrotron emission, partly polarised, corrected for inclination
Isotropic turbulent or tangled field perpendicular to the l.o.s.	Unpolarised synchrotron intensity, Faraday depolarisation
Isotropic turbulent or tangled field along the l.o.s.	Faraday depolarisation
Ordered field perpendicular to the l.o.s.	Intensity and vectors of radio, optical, IR or submm polarisation
Anisotropic turbulent or tangled magnetic field perpendicular to the l.o.s.	Intensity and vectors of radio optical, IR or submm polarisation, and Faraday depolarisation
Regular field perpendicular to the l.o.s.	Intensity and vectors of radio, optical, IR or submm polarisation, Goldreich-Kylafis effect
Regular field along the l.o.s.	Faraday rotation and depolarisation, Goldreich-Kylafis effect

candidates) [334]. Even though such an emission, and its counterpart in γ-ray measured by Fermi-LAT, has been resolved through the Fermi Bubbles [335], current works still keep the possibility of some fraction of the Haze being explained in terms of DM [336].

4.2.2 Magnetic field in the Milky Way

As mentioned above, in this Chapter, we will focus on the radio signals produced by the synchrotron emission from e^-/e^+ injected by DM annihilations. This will allow us to determine how strong the restrictions imposed in the Milky Way are. In order to do so, an accurate description of the magnetic field is necessary. Indeed, the synchrotron emission could be significantly affected by the magnetic field spatial distribution in different regions of the Galaxy. In this regard, reconstructing galactic magnetic fields is possible by observing different signatures; the polarised optical-infrared starlight, the synchrotron emission, the Faraday rotation/depolarisation and Zeeman lines from, in general, HI, OH or CN. Each of these signatures unveils different field components, as seen in Table 5.1, (taken from Ref. [337]).

The first magnetic field observations were by studying the optical polarisation of starlight due to the dust alignment in the galactic magnetic fields, resulting in a large polarisation catalog. The main conclusion therein, still valid today, is the alignment of the magnetic field with the Galactic plane. Even though the polarisation method also revealed the symmetric properties of the magnetic field in the Milky Way, it was subjected to a small number of nearby star measurements, and thus, other tracers had to be considered. Sky surveys focused on the synchrotron emission in the range of $\sim 300\,\mathrm{MHz} - 10\,\mathrm{GHz}$ (to avoid absorption of synchrotron emission by gas and thermal gas emission), can be a suitable method to reveal more information.

Indeed, several analysis showed the Galactic emission with its maximum towards the GC. Also, the analysis of total synchrotron gives an equipartition strength for the magnetic field of 6 μG in the local neighbourhood and 10 μG at 3 kpc radius [337]. The main source of uncertainty comes from the fact that the synchrotron intensity has to be performed integrating from many emission areas over the l.o.s. and also from the limitation of the angular resolution in all-sky surveys, so the details of extended sources could not be fully understood. Following the abovementioned results, although different parametrisations of the magnetic field have been proposed [338], we consider the one chosen in Ref. [176] described by an exponential magnetic field with cylindrical symmetry and a dependence with the distance r to the galactic plane:

$$B(r,z) = B_0 \exp\left(-\frac{r-r_\odot}{\delta R} - \frac{|z|}{\delta L_z}\right). \tag{4.1}$$

In the previous expression, the diffusion dependence is given by the parameter δ which is usually adopted in numerical codes like GALPROP and DRAGON [198, 259].

4.2.3 Dark matter profile in the Milky Way

Furthermore, besides the magnetic field, it is necessary to know the role played by the DM density profile and the propagation in the products of annihilation. Therein, we will focus on the former since the latter was already studied in Section 3.2.

Even though N-body simulations provide a sophisticated method to describe the radial distribution of DM in the Galaxy, some discrepancies appear in inner locations of the halo. Simulations as Aquarius suggest that, in general, an NFW profile provides good fits except at inner regions, where Einasto profiles have smaller residuals and would better describe the density [224, 339]. On the contrary, Via Lactea II simulations lean more towards an NFW profile [340–342]. The main inconvenience is the finite resolution of the simulations at small radii. Moreover, these simulations do not consider the presence of baryons, whose role would not be negligible in regions around the centre [343–345]. Nevertheless, cored profiles, despite disfavoured by simulations, are observationally viable, i.e., observations of dwarf spirals and low-surface brightness galaxies [346] show that in some cases the Isothermal profile is preferred over the cuspy ones.

Finally, at the time of doing a study of the DM synchrotron emission in the Milky Way, we encountered two main difficulties that restrict our reasoning line.

- First, some limitations in our code to compute the emission in the whole galaxy. In fact, the analytical solution for the transport equation taken for the Milky Way requires the convergence of the Bessel-Fourier series in the whole galaxy, which may require around 10^7 coefficients C_{in}, while the number of coefficients we calculated was 10^5. Such a number of coefficients ensured the convergence of an Isothermal profile in a minimal diffusion model. The use of this model would imply an underestimation of the synchrotron signal in the whole galaxy. Even though the minimal diffusion has the effect of concentrating the emission at the centre, which would give an overestimation of the signal at low angles, the Isothermal profile causes a decreasing of at least one order of magnitude with respect to the NFW profile.

- The second difficulty, as commented at the beginning of this section, is the role played by the background coming from different directions in the sky for the whole range of radio frequencies. Thus, the main issue is not only determining the radio background for the Galaxy[†], that could

[†]In this work, the word background refers to all astrophysical signals added to the DM contribution. Many works use the word background as a synonym of extragalactic emission, while the galactic emission is called foreground.

be currently computed by GALPROP, but also the contribution of extragalactic radiation to compare with the experimental data. One of the first approaches to measure such an extragalactic component was made in the light of the balloon-borne experiment ARCADE 2 [347]. There, the isotropic background was estimated by subtracting the Galactic component by two methods that gave consistent results. The former was using a Galactic plane-parallel model with a cosec$(|b|)$ dependence on the galactic latitude while the latter consisted in correlating the ARCADE 2 data against a map of CII lines. Such estimations resulted in an isotropic signal ~ 5 larger than the total contribution expected from the radio emission of extragalactic sources. Such an excess does not have an immediate explanation in the current astrophysical scenario and a population of faint radio sources has to be introduced. Faint quasars, radio AGNs, star-forming galaxies and unresolved galactic sources have been considered to accommodate this excess, as well as DM. Although new data processing and techniques for the explanation of the radio background have improved (see for example [177] and references therein), the background treatment is beyond the scope of this work. Hence, in all the following sections, the radio signal emissions have been computed without considering the background, and therefore, constraints and prospects for DM remain conservative. Still, even in such scenarios without a background, the high sensitivity and resolution of radio frequency detectors, in particular, the SKA and precursors, may provide crucial information that can be extrapolated to more realistic scenarios.

4.3 Dark matter constraints with radio sky maps

Following the formalism in Section 2.5 c), we first discuss the spatial distribution of synchrotron emission along the Milky Way computing the brightness temperature $T_\nu(l,b)$, as in Fig. 4.2, that is related with the intensity I_ν Eq. (2.39) through the Rayleigh-Jeans approximation

$$T_\nu \approx \frac{I_\nu c^2}{2k_b \nu^2}. \tag{4.2}$$

For such a purpose, we follow the analysis in [176]. Fig. 4.2 was calculated in a grid (l,b) of 51×51 points that was subsequently interpolated. The chosen interval for (l,b) lies in $l \in [0^o, 360^o]$ and $b \in [-90^o, 90^o]$. The astrophysical framework is the model ISO-MIN. As mentioned before, such a model is not the most realistic one but it will allow us to study some generalities and set conservative constraints in the following sections.

Furthermore, Fig. 4.2 upper panel may serve as a reference point for the Milky Way study since it can be compared with Fig. 2 (upper right panel) of [176]. Indeed, in Fig. 4.2, a 45 MHz sky map has been calculated for a DM candidate annihilating into $\mu^+\mu^-$ with a mass of 10 GeV and a thermally averaged cross section $\langle \sigma v \rangle = 3 \cdot 10^{-26}$ cm^3/s. For this calculation, the chosen magnetic field is exponential, according to Eq. (4.1). The synchrotron emission from e^-/e^+ arises as to a diffusive signal that largely follows the DM concentration, dictated by the halo density profile (in our case Isothermal). The value for the temperature close to the GC is around $\sim 1.9 \cdot 10^4$ K, approximately an order of magnitude smaller than the NFW case in [176]. As a comparative data, a full sky map of the Galactic emission at 45 MHz was delineated in [307], observing a temperature of $\sim 5.4 \cdot 10^4$ K at GC. Furthermore, in our calculation, the signal seems to possess a central core situated around the regions $l \in [330^o, 30^o]$ and $b \in [-10^o, 10^o]$, and then extend on the l coordinate along the whole Galactic plane. Conversely, the temperature falls along the angle b abruptly, mainly as a consequence of the magnetic field.

Again, we repeated the calculation for a constant magnetic field, $B = 6\,\mu$G in Fig. 4.2 lower panel. The latter shows an oblate spheroidal core in contrast to the exponential case. Such a core extends around $l \in [336^o, 24^o]$ and $b \in [-14^o, 14^o]$, showing also the influence of the

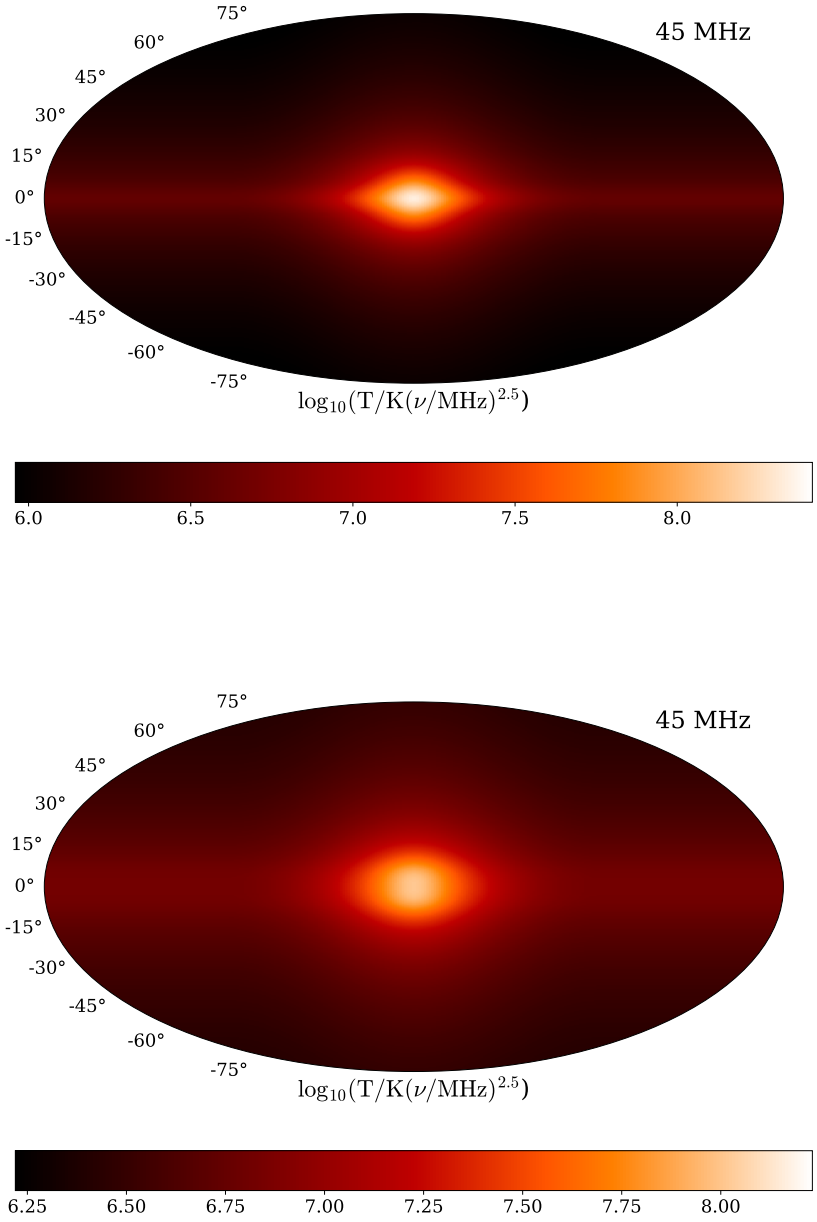

FIGURE 4.2: *Upper panel:* Radio emission sky map at 45 MHz from e^+ and e^- in the case of 10 GeV DM candidate annihilating into $\mu^+\mu^-$. The thermally averaged cross section is $3 \cdot 10^{-26}$ cm^3/s. Our numerical codes consider an exponential magnetic field depending on the galactic coordinates (l, b). The DM density profile is Isothermal while the diffusion is minimal. The former and the latter are not the more realistic models but allow to study generalities and set conservative constraints. The angular grid used for the sky map relies on 51x51 pixels of resolution calculating the value of $T_\nu(l, b)$ of each pixel. The calculations have been performed by our code based on *Python* with an improved version of the adaptive Monte Carlo *Vegas* algorithm method whose number of points is $3 \cdot 10^6$ per pixel. In addition, the number of terms in the Bessel-Fourier series is $(n, i) = (299, 299)$. The sky map projection used in the calculation is the Mollweide projection. *Lower panel:* Radio emission sky map at 45 MHz from e^+ and e^- in the case of 10 GeV DM candidate annihilating into $\mu^+\mu^-$. The thermally averaged cross section is $3 \cdot 10^{-26}$ cm^3/s. Numerical codes consider a constant magnetic field along the whole Galaxy. The angular grid used for the sky map relies on 51x51 pixels of resolution calculating the value of $T_\nu(l, b)$ of each pixel. The rest of parameters are equal to that in the upper panel.

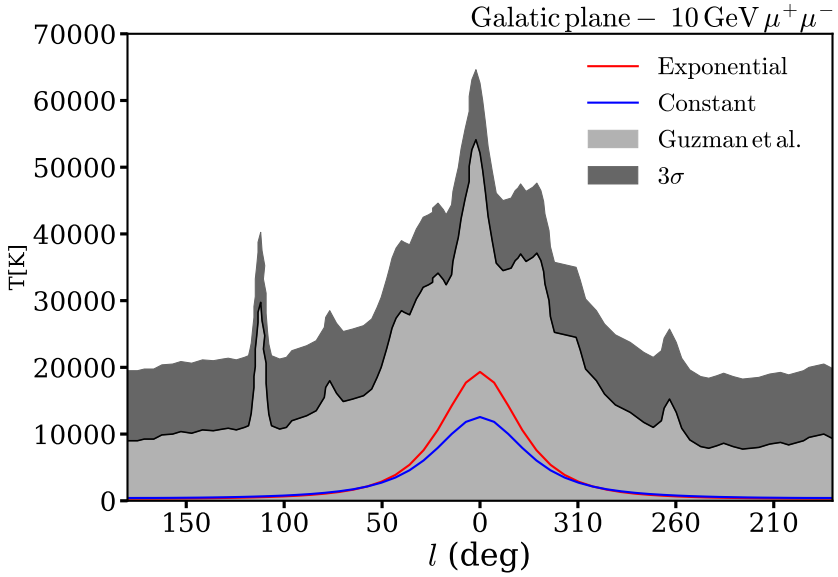

FIGURE 4.3: Synchrotron emission vs. measured total signal at 45 MHz [307]. This plot corresponds to the section $(l, b) = (l, 0^o)$ in the plots of Fig. 4.2. The red line corresponds to the exponential magnetic field case, presented in Eq. (4.1), while the blue line corresponds to a constant magnetic field case equal to 6 μG. In light grey, it is possible to observe the main features of our galaxy being the peaks: SNR Cas A (SNR at $l = 111.5^o$, $b = -2.3^o$), Vela SNR ($l = 263.9^o$, $b = -3.3^o$) and the GC while the extragalactic sources are radio galaxies such as Cen A ($l = 309.5^o$, $b = 19.4^o$) , Cyg A ($l = 76.2^o$, $b = 5.8^o$), Virgo A ($l = 285^o$, $b = 74.3^o$), Hydra A ($l = 243^o$, $b = 25^o$), Pictor A ($l = 252^o$, $b = -34^o$), and Fornax A ($l = 240^o$, $b = -56.3^o$). In dark grey, it has been plotted the rms total temperature plus 3 times the rms temperature noise, that set the limits of exclusion of our analysis.

cylindrical diffusion inserted in the Laplacian of the transport equation Eq. (2.28). Moreover, the red band emission that spreads along the Galactic plane, covers higher latitudes than the case of Fig. 4.2 upper panel. Indeed, for the exponential magnetic field, the synchrotron signal is more concentrated around 4º northern and southern latitude, while the band reaches 12º and -12º when $B = 6\,\mu$G. Thus, the constant magnetic field scenario may overestimate the DM constraints with the exception of the GC. Whereas the maximum of emission occurred at a temperature of $\sim 1.9 \cdot 10^4$ K in Fig. 4.2 upper panel, in 4.2 lower panel lies close to $\sim 1.2 \cdot 10^4$ K, a 35% of relative difference.

In Fig. 4.3, we represent the longitudinal section of both emission sky maps of Fig. 4.2 upper panel (in red) and Fig. 4.2 lower panel (in blue). In addition, in grey, it was plotted the results of the survey at 45 MHz from Ref. [307], that accounts for the Galactic large-scale synchrotron emission at $b \sim 0^o$ (the map was averaged within a resolution angle of 5º). According to the calculations for 10 GeV DM annihilating into $\mu^+\mu^-$, it seems that synchrotron emission from DM would contribute to a low percentage of the total emission along the whole Galactic plane, except at inner angles. For example, for an exponential magnetic field, DM emission accounts for a 37% of the total one at the GC, while at a longitude of either 50º or 310º the value falls to $\sim$ 15%. This may indicate that, again, the real problem at GC is not that detectors are not sensitive enough to measure annihilating DM with masses up to 100 TeV, but that disentangling such DM signals from the astrophysical background remains a major challenge. High resolution and sensitivity allow us for a better understanding of populations of faint sources and their contributions to the background. For outer longitudes, the DM emission seems to be negligible with respect to astrophysical signals. In addition, we should keep in mind that such amounts

have been calculated here for a 10 GeV DM particle. As mass increases, the synchrotron signal decreases according to $1/M^2$, as renders Eq. (2.6).

The dark grey region, in Fig. 4.3, is the temperature obtained in [307] plus three times the root mean square (rms) temperature noise σ taken in [176] as 3500 K. This limit would allow us to define the limit of exclusion for different DM candidates setting up in such a way that if the temperature from annihilating DM is greater than such a limit, the candidate is excluded. In Sections 4.3.1 and 4.3.2, we shall obtain the exclusion regions both for the case of model-independent DM and extradimensional DM by performing an analysis of the synchrotron temperature as presented in Fig. 4.3. The exclusion regions, as already mentioned, begin to be delimited when the theoretical predictions exceed the experimental data.

4.3.1 Model-Independent dark matter

In this analysis, we use the 3σ-level for the Galactic plane map at 45 MHz presented (Fig. 4.3) with the aim to set constraints on model-independent DM, annihilating 100% in one specific channel. For such a purpose we study the synchrotron signal by varying both the thermally averaged cross section $\langle\sigma v\rangle$ and the DM mass.

In Fig. 4.4, the grey band represents the region in which the thermally averaged cross section exceeds the thermal relic density cross section, while the bands in red, blue and light blue are the regions excluded by the study of the Galactic plane at 45 MHz. The red band corresponds to the case of DM annihilating into W^+W^-, while blue and light blue accounts for the channels $\tau^+\tau^-$ and $b\bar{b}$. As seen in Fig. 4.3, the region excluded for quarks is larger than bosons and leptons for all the range of masses at 45 MHz. In this sense, the $\tau^+\tau^-$ channel seems to present more difficulties than the W^+W^- channel to produce visible synchrotron emission at larger masses. In other words, as DM mass increases the slope of the curve delimiting the exclusion region is more pronounced for $\tau^+\tau^-$ than the rest of channels. Conversely, it is possible to observe that none of the annihilation channels lies under the thermal relic density curve. Indeed, the minimum thermally averaged cross section reached in this analysis is $1.5 \cdot 10^{-24}\text{cm}^3/\text{s}$ for DM annihilating into $b\bar{b}$ channel. For the W^+W^- such a limit is established at $\langle\sigma v\rangle = 1.9 \cdot 10^{-24}\text{cm}^3/\text{s}$ while for $\tau^+\tau^-$ is at $\langle\sigma v\rangle = 5.9 \cdot 10^{-24}\text{cm}^3/\text{s}$.

The study performed in this Section for model-independent DM has shown that the constraint limits, where $T_{\text{DM}} = T_{\text{sky}} + \Delta T_{3\sigma}$, usually takes place at around $l = 330^{\text{o}}$. Such a location corresponds to the emission between the GC and the Near 3 kpc Arm, at 3.3 kpc from the GC. Thus, this analysis suggests that the best region along the GC for DM detection corresponds to that area of the sky between the GC and the Near 3 kpc Arm. The first reason is that one can avoid the high background emission from the GC and the spiral arm. The second, we refer to Fig. 4.3 and [307], is the displacement of the GC with respect to $l = 0^{\text{o}}$ at this particular observation frequency. In fact, not all emission frequencies show such a shift. In Fig. 2 of [307] where the Galactic plane synchrotron at 408 MHz is represented, shows that the emission with respect to the centre of reference is aligned.

We should keep in mind that the constraints of Fig. 4.4 are conservative, meaning that other realistic scenarios would provide tightest constraints. In fact, as already mentioned, the NFW profile could produce temperatures at the GC beyond one order of magnitude. Moreover, we should keep in mind that no astrophysical background has been considered. Under this framework, our analysis would improve. Work in this direction may be raised in the future. In addition, also other frequencies can be explored. In fact, data from radio signals at 22 MHz, 408 MHz, 820 MHz and 1420 MHz are available and may present particular characteristics that would give some keys to elucidate DM signals in lower background.

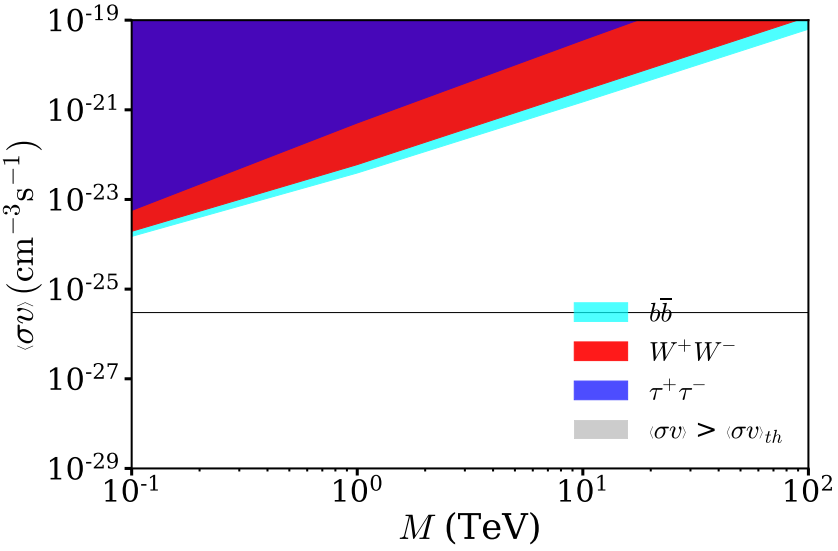

FIGURE 4.4: Constraints on the DM cross section (3σ of confidence level) for model-independent DM, annihilating into $b\bar{b}$, $\tau^+\tau^-$ and W^+W^- channels. The blue area includes also the red and purple areas and the red area includes also the purple one. In our analysis, we compare the expected emission from DM with the synchrotron temperature measured at the Galactic plane in Ref. [307]. The horizontal black line represents those DM candidates with $\langle\sigma v\rangle = 3 \cdot 10^{-26}$ cm^3/s. None of the candidates excluded with this method would be in agreement with the thermal relics.

4.3.2 Brane-World dark matter in the Galactic plane

In the this Section, we use the results of the Galactic plane map at 45 MHz presented above (Fig. 4.3) in order to constrain the parameter space $\{M, f\}$ of DM in Brane-World scenarios. In Fig. 4.5, exclusion regions are presented both in purple and red. The former is the exclusion we obtained in Fig. 3.8, while the latter represents the constraint we obtained for the Galactic plane ($l = 0^o$), in which the limit of exclusion lies on $T_{\rm DM} = T_{\rm sky} + \Delta T_{3\sigma}$. For better comparability, we have not plotted the tightest constraint obtained in AMS corresponding to NFW-MAX and whose maximum excluded mass and tensions were $\{M, f\} = \{32\,\mathrm{TeV}, 4.5\,\mathrm{TeV}\}$. Instead, we plotted the ISO-MIN case both for AMS and the exclusion at the Galactic plane ($b = 0^o$).

The black dashed line $f(M) = M/\sqrt{4\pi}$ separates the limit where the tree-level formalism for branons (considered in this work) is valid (weakly coupling region), as already explained in Section 3.4. Thus, the limits in which the maximum pair $\{M, f\}$ is excluded lie on the intersection between the colour area and the curve, $f(M) = M/\sqrt{4\pi}$, separating between the weakly and strong regions. For the AMS constraints, such a limit lied on $\{M, f\} = \{27.3\,\mathrm{TeV}, 3.8\,\mathrm{TeV}\}$, while for the constraints with the Galactic plane (Fig. 4.3) is at $\{M, f\} = \{15.5\,\mathrm{TeV}, 2.21\,\mathrm{TeV}\}$. This indicates that constraints from AMS results tighter than constraints using radio emission from the galactic plane. More precisely, a difference of 11.8 TeV in masses and 1.54 TeV in tensions. Such a small difference in tensions may result from the high dependence of the branon cross section with f. Indeed, none of the methods to constrain DM reach values close to the limit $\langle\sigma v\rangle = 3 \cdot 10^{-26}\mathrm{cm}^3/\mathrm{s}$. In fact, for the pair $\{M, f\} = \{15.5\,\mathrm{TeV}, 2.21\,\mathrm{TeV}\}$, such a thermally averaged cross section lies on $5.4 \cdot 10^{-21}\mathrm{cm}^3/\mathrm{s}$ while for the AMS constraints the limit $\{M, f\} = \{27.3\,\mathrm{TeV}, 3.8\,\mathrm{TeV}\}$ corresponds to $2.1 \cdot 10^{-21}\mathrm{cm}^3/\mathrm{s}$. Both results have been collected in Table 4.2 for better comparison. The fact that two observations separated 8.5 kpc provides similar constraints in f may suggest that branon constraint is very weakly dependent on the astrophysics when compared with its coupling given by a factor $\propto 1/f^8$ in the Lagrangian.

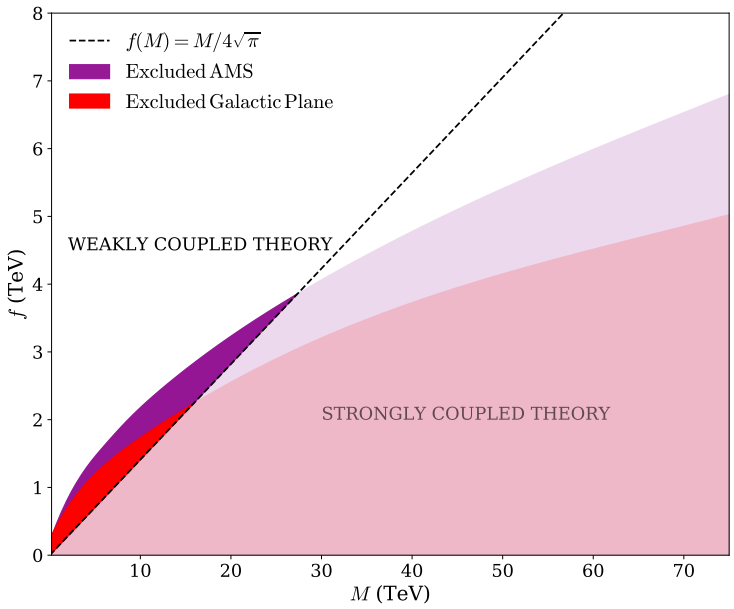

FIGURE 4.5: Exclusion diagrams for extra-dimensional branons. Bright coloured areas indicate the excluded region in the parameter space $\{M, f\}$ assuming the propagation model ISO-MIN. The lowest mass in this study is 200 GeV. Dashed black line sets the limit of the perturbative theory for branons and the validity of tree-level versus loop branon effects [302]. The exclusion is only valid in the weakly coupled region.

However, this conclusion only would be possible when a proper model of the background being regarded. Even though the extragalactic non-thermal background from non-resolved sources is removed from the 45 MHz map, knowing astrophysical emission remains in a difficult task. New developments point towards such a direction [177].

4.4 Sensitivity constraints with the SKA: prospects for the Galactic Centre and AntiCentre

In Section 4.3, we set constraints on the DM parameter space for both the model-independent DM and DM in Brane-World scenarios with radio signals in the Galactic Plane, measured by [307]. In the whole previous section, none of the constraints reached values lower than the thermally averaged cross section for thermal relics, $\langle \sigma v \rangle = 3 \cdot 10^{-26} \mathrm{cm}^3/\mathrm{s}$. In this section, we

TABLE 4.2: Intersection between the exclusion regions with the strongly coupled limit for branons. In this Table, we collect the results obtained in Section 3.4 and compare them with those obtained in this section. This study has been performed for an Isothermal MIN diffusion.

Quantity	Location	M(TeV)	f(TeV)	$\langle \sigma v \rangle (\mathrm{cm}^3/\mathrm{s})$
Positron Fraction (Sec. 3.4)	Earth ($\sim$ 8.5 kpc from GC)	27.3	3.8	$2.1 \cdot 10^{-21}$
Radio emission	Galactic Plane	15.5	2.21	$5.4 \cdot 10^{-21}$

will analyse the sensitivity constraints that SKA1 would impose on DM in the case that the latter could be disentangled from the background. At this point, we would like to remark that we already used the word *constraints* for regions excluded by experimental measurements and represented through an *exclusion plot*. However, from now we will use the term *sensitivity constraints* to refer to those regions that will be potentially excluded, taking into account the detector sensitivity. Sensitivity constraints will be represented through a *detectability plot*. In order to obtain sensitivity constraints, we shall perform an analysis for DM candidates by the use of the SKA1 sensitivity curves for 10, 100 and 1000 hours. The $S_{\rm min}$ measured by the detector has been obtained using Eq. 2.42, tabulating the System Equivalent Flux Density SEFD=$2k_b T_{\rm sys}/A_e$ from [348]. Consequently, in the following, we will focus on the same cases as above. First, we shall set sensitivity constraints on model-independent DM, annihilating 100% into one specific channel and, second, we shall study the case of Brane-World DM.

4.4.1 Model-independent dark matter

In the present study, two targets have been considered, namely the GC ($l = 0^{\rm o}, b = 0^{\rm o}$) and the GAC ($l = 180^{\rm o}, b = 0^{\rm o}$), in a region of $0.1^{\rm o} \times 0.1^{\rm o}$. The telescope may not be able to see both targets in the sky. However, both regions have been considered as hypothetical reachable targets with the aim of setting sensitivity constraints in the two most extreme cases. This will allow us to infer what happens in intermediate regions. The GC was selected with the aim to determine the maximum sensitivity constraints one can set by observing the Milky Way. By contrast, we also include the GAC to compare the emission in both regions of the galactic plane, thus setting detection limits. In order to do so, we prospect the DM parameter space, its thermally averaged cross section $\langle\sigma v\rangle$ and its mass, taking into account the SKA sensitivity. As a first step, we focus on model-independent DM, annihilating 100% into one specific channel.

In Fig. 4.6, solid lines represent the flux density from a 1 TeV DM candidate annihilating into different channels, both in the GC (left panel) and the GAC (right panel), without considering any astrophysical background. For a better understanding of the figure, note that the lines corresponding to the channels $q\bar{q}$ ($u\bar{u}$, $d\bar{d}$ and $s\bar{s}$) and $c\bar{c}$ overlap with the rest of the quarks ($b\bar{b}$ and $t\bar{t}$). Blue and orange bands correspond to the frequency coverage of SKA1-LOW and SKA1-MID, respectively, and dash-dotted lines are the SKA1 sensitivity limits for 10, 100 and 1000 hours of integration time.

The left panel of Fig. 4.6 shows the flux density S_ν at the GC. There, one can clearly distinguish between the lepton channels, and the boson and quark channels. The emission from leptons is more suppressed than that coming from bosons and quarks, and thus, boson and quark channels would be substantially better detected than leptons. The only point in which this tendency seems to change is around $\nu \sim 10^5$ MHz, out of the range of the SKA. Moreover, the slopes of the signal for boson and quark channels are larger than the leptonic channel, suggesting that bosons and quarks will be better detected by SKA1-LOW. In the case of leptons, given the fact that curves are less pronounced (the emission remains faint in the whole SKA frequency range), the reliability of detection would be mainly regulated by the characteristics of the detectors. In this sense, the highest sensitivity for SKA1 lies close to 1 GHz, region covered by SKA1-MID, suitable to detect lepton channels. Furthermore, the SKA sensitivity allows to distinguish between some channels within 10 hours of observation (Fig. 4.6): quarks and bosons could be differentiated from leptons in the range of frequencies of SKA due to the fact that the variation in the slope of the emission S_ν for the SKA frequency range is larger than the sensitivity of the detector.

Furthermore, Fig. 4.6 right panel presents the flux density in the GAC characterised by a reduction of S_ν in more than two orders of magnitude. However, for this specific 1 TeV DM candidate, its emission lies much higher than the SKA sensitivity curves. Although the spectrum

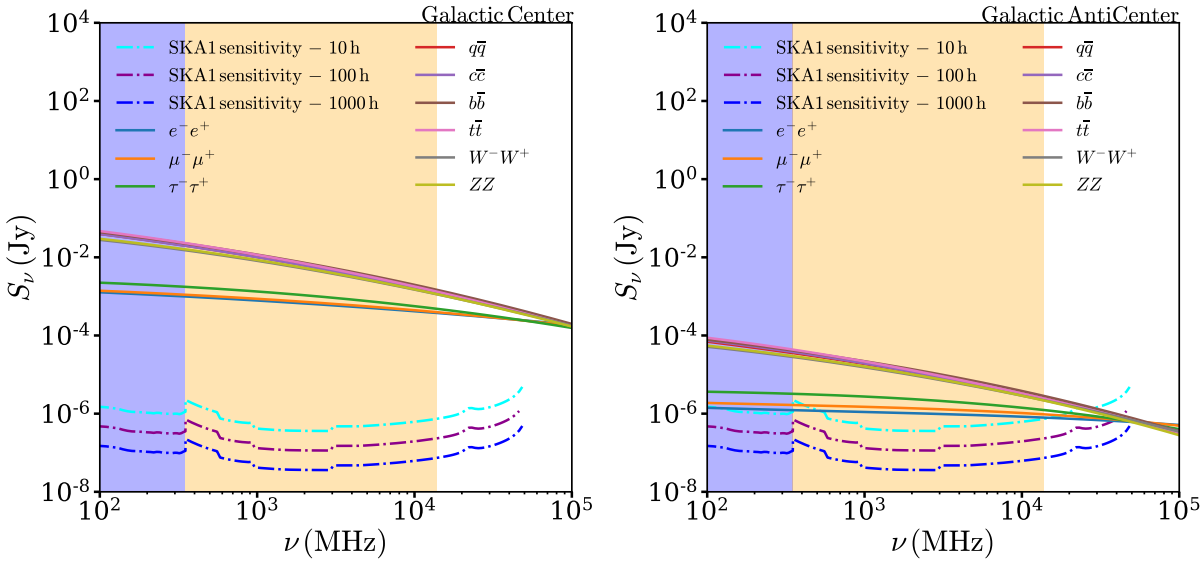

FIGURE 4.6: Flux density radio emission S_ν for 1 TeV DM candidate ($\beta_j = 1$) annihilating into different channels with a thermally averaged cross section of $3 \cdot 10^{-26}\text{cm}^3/\text{s}$. The angle window is $0.1^\text{o} \times 0.1^\text{o}$. Dash-dotted lines represent SKA1 1σ-sensitivity level after 10, 100 and 1000 hours of integration time, obtained from Ref. [348]. Colour bands correspond to the frequency range covered by SKA1-LOW (blue) and SKA1-MID (orange). *Left panel:* Flux density for TeV DM annihilating into leptons, quarks and bosons in the GC. *Right panel:* Flux density for TeV DM annihilating into leptons, quarks and bosons in the GAC.

seems to keep their dependence on the frequency, as in the case of the GC, small differences can be noticed. Specifically, the change of tendency in which the emission from leptonic channels is larger than that from boson and quark channels is situated at smaller frequencies compared with the GC case. Such a change reveals, although qualitatively imperceptible, the differences in the spectra between GC and GAC.

Considering the SKA1 sensitivity lines plotted in Fig. 4.6 for 10, 100 and 1000 hours, we prospect the detection of model-independent DM candidates through synchrotron emission. To that end, we chose three paradigmatic annihilation channels $\tau^+\tau^-$, $b\bar{b}$ and W^+W^- and compute their flux density for the masses, M, 100 GeV, 1 TeV, 10 TeV, 50 TeV and 100 TeV. On that basis, we observe in our study of Fig. 4.6, which thermally averaged cross section $\langle\sigma v\rangle$ lies on the limit of detectability of 10 hours, allowing us to plot $\langle\sigma v\rangle$ vs. M represented in Fig. 4.7. It is necessary to remark that Fig. 4.7 does not represent an exclusion diagram but a detectability plot, i. e., a plot that represents the capabilities of SKA1 to detect a DM candidate with specific $\langle\sigma v\rangle$ and M values. In the case in which SKA1 does not detect any signal then Fig.4.7 could be taken as an exclusion plot.

In Fig. 4.7, the grey area represents the region where $\langle\sigma v\rangle$ exceeds the thermal relic density cross section, and thus, the cosmological usual limits for WIMPs cross section are not respected. Conversely, the orange and blue lines, representing SKA1-LOW and SKA1-MID respectively, do not exhibit significant differences in the detection: SKA1-MID slightly reaches larger masses and lower thermally averaged cross sections. The detection limit for SKA1-MID is typically shaped by Band3 [1.65-3.05] GHz which is the most sensitive band. However, DM detection in SKA1-LOW highly depends on the shape of the flux density curve that usually handles more slope at low frequencies. Consequently, as we already discussed in Fig. 4.6 and is also observed on both panels of Fig. 4.7, boson and quark channels would be better detected than lepton channels for all the range of masses and in a range of frequencies, from 100 MHz to $1 \cdot 10^5$ MHz.

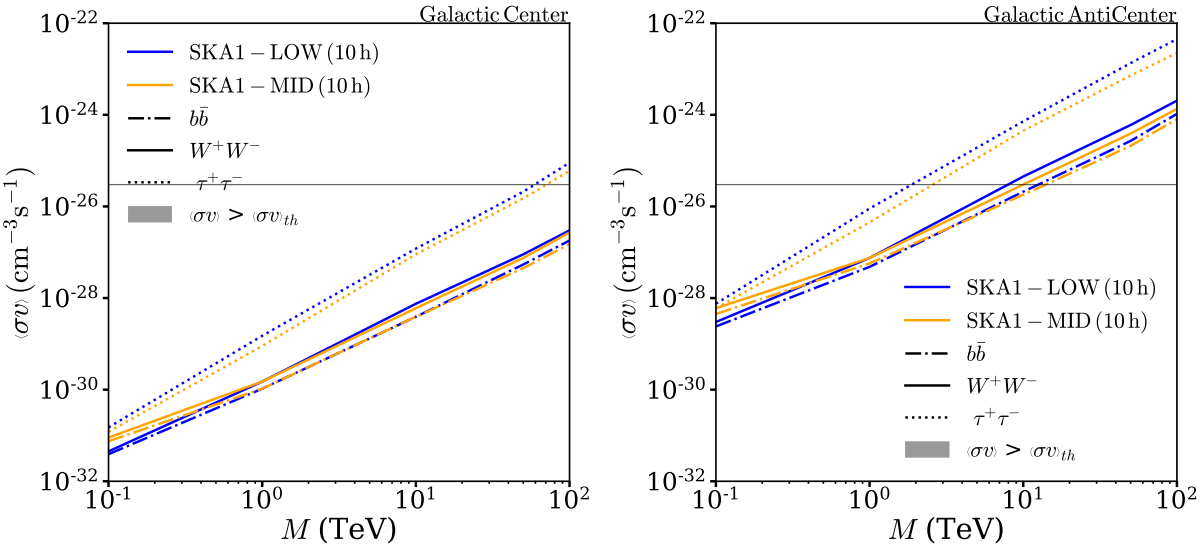

FIGURE 4.7: Sensitivity constraints on the DM cross section for model-independent DM annihilating into $b\bar{b}$, $\tau^+\tau^-$ and W^+W^- channels with SKA1 after 10 hours of integration time (1σ sensitivity curve of Fig. 4.6). The solid angle considered to set this map is $0.1^o \times 0.1^o$. The lines in blue would be detected within 1σ by SKA1-LOW while the lines in orange would be detected by SKA1-MID. The horizontal grey band represents those DM candidates with $\langle\sigma v\rangle = 3 \cdot 10^{-26}$ cm^3/s or greater. *Left panel:* Sensitivity constraints on the DM particle cross section at GC. *Right panel:* Sensitivity constraints on the DM particle cross section at GAC.

Indeed, the limit of detection of thermal relics annihilating into $\tau^+\tau^-$ in the GC (left panel) is $M \sim 59.6$ TeV for SKA1-LOW and $M \sim 70.6$ TeV for SKA1-MID while the channels W^+W^- and $b\bar{b}$ go over the limit of 100 TeV. For the GAC (right panel), thermal relics annihilating into $\tau^+\tau^-$ would be detected by SKA1-LOW at $M \sim 1.87$ TeV and by SKA1-MID at $M \sim 2.56$ TeV. Whereas, for W^+W^- the limit is $M \sim 7.87$ TeV and $M \sim 10.03$ TeV for SKA1-LOW and SKA1-MID respectively while it is $M \sim 12.55$ TeV and $M \sim 14.01$ TeV for the channel $b\bar{b}$. These values have been collected in Table 4.3. Comparing both plots, it is possible to observe that the GC is more restrictive than the GAC since the former reaches larger masses and lower thermally averaged cross sections. In fact, in the left panel, we observe the minimum thermally averaged cross section in the GC lying around $1 \cdot 10^{-31}$ cm^3/s for a $M = 100$ GeV. The right panel, however, shows a minimum in $\langle\sigma v\rangle$ equal to $\sim 5 \cdot 10^{-29}$ cm^3/s.

Finally, it should be reminded the importance of including the astrophysical background in the GC case if one requires a more realistic scenario. As commented before in the text, this case would be more complicated than the simpler scenario considered here.

4.4.2 Brane-World dark matter

In Section 3.4, constraints for DM in Brane-World scenarios were obtained in the light of AMS, PAMELA and Fermi-LAT measurements. In fact, an adequate explanation of data may require branons with a very large thermally averaged cross section, hence, the limits imposed on the branon parameter space exceed the value $\langle\sigma v\rangle = 3 \cdot 10^{-26}$ cm^3/s in several orders of magnitude. As observed in Fig. 3.8, those branons masses lying around tens TeV are only excluded by AMS for low tensions close to ~ 5 TeV. By using a similar strategy to that in 4.4.1, we perform a sensitivity analysis for DM in Brane-World theories.

TABLE 4.3: Sensitivity constraints for SKA1-LOW and SKA1-MID when $\langle\sigma v\rangle = 3 \cdot 10^{-26}\text{cm}^3/\text{s}$, assuming an exponential magnetic field. This table has been obtained by observing Fig. 4.7, where a sensitivity analysis has been performed for the channels W^+W^-, $b\bar{b}$ and $\tau^+\tau^-$. In fact, the depicted values for the mass correspond to the intersection between the limit of detectability of the SKA1-LOW and SKA1-MID and thermal cross section level in grey, Fig. 4.7.

Detector	Location	Channel	M (TeV)	Detector	Location	Channel	M (TeV)
SKA1-LOW	GC	$\tau^+\tau^-$	59.6	SKA1-MID	GC	$\tau^+\tau^-$	70.6
		W^+W^-	> 100			W^+W^-	>100
		$b\bar{b}$	> 100			$b\bar{b}$	>100
	GAC	$\tau^+\tau^-$	1.87		GAC	$\tau^+\tau^-$	2.56
		W^+W^-	7.87			W^+W^-	10.03
		$b\bar{b}$	12.55			$b\bar{b}$	14.01

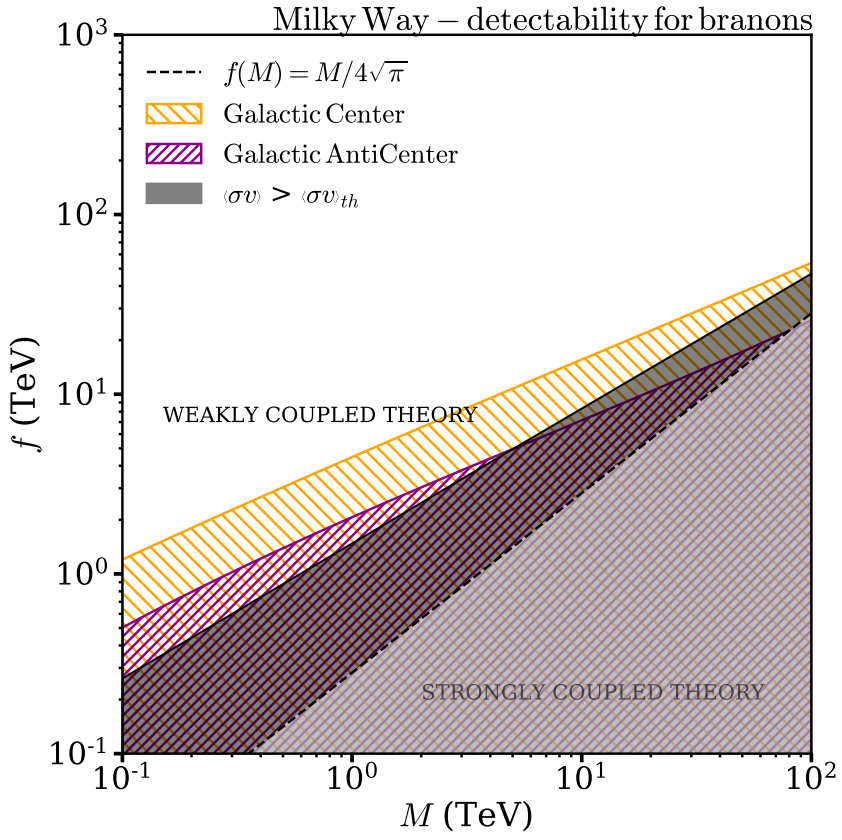

FIGURE 4.8: Detectability of branons both for GC and GAC with SKA1 on the $\{M, f\}$ parameter space after 10 hours of integration time (1σ of confidence level). The solid angle considered to set this map is $0.1^o \times 0.1^o$. The black line represents the curve $f(M)$ for a thermal relic with $\langle\sigma v\rangle = 3 \cdot 10^{-26}$ cm^3/s. The region in yellow would be detectable by SKA1 focused on the GC, while the region in purple is focused on the GAC. Dashed black line sets the limit of the perturbative theory for branons [302]. The sensitivity constraints are only applicable when the coloured area lies above the line (weakly coupled region).

In Fig. 4.8, we outline the diagram for detectability of branons (1σ of confidence level) in the Milky Way with SKA, both for the GC and the GAC. To do this, the SKA sensitivity curves, corresponding to an integration time of 10 h, delineate the detectable regions. The black solid line represents the limit of thermal relics in which $\langle\sigma v\rangle = 3 \cdot 10^{-26}\,\mathrm{cm}^3/\mathrm{s}$. Furthermore, masses larger than 5 TeV, with $\langle\sigma v\rangle = 3 \cdot 10^{-26}\,\mathrm{cm}^3/\mathrm{s}$, would be only detected at GC. Indeed, the purple region and the black line intersects at $\{M, f\} \sim \{5\,\mathrm{TeV}, 5\,\mathrm{TeV}\}$. Moving from that point towards either lower masses or lower tensions would require a different production mechanism for branons. Conversely, the SKA sensitivity would allow the detection of the whole range of masses of our study at the GC while the maximum detected tension would be 54.75 TeV for a branon mass of 100 TeV.

Moreover, observing the yellow and purple regions in Fig. 4.8, since their borders are qualitatively parallel, it seems that DM sensitivity constraints in the GC and GAC can be treated as a shift in tensions, f. In fact, the shift between regions can be represented by a multiplicative factor 2.39 at $M = 0.1$ TeV, while for $M = 100$ TeV turns into 2.22. This would not necessarily have to be like this, since the exponential magnetic field, with a spatial dependence along Galaxy, is mixed in the emissivity (Eq. 2.35) both with the mass and the frequency of emission. However, Fig. 4.6 already suggested that the flux density spectra in both regions of the sky do not change significantly except by a multiplicative factor.

The analysis of synchrotron signals could be much more restrictive than the AMS study, as observed comparing Fig. 4.8 with Fig. 3.8. The advantage of the latter is that the background could be approximately parametrised with local measurements. However, the range of detectable zones in the $\{M, f\}$ parameter space for branons is substantially bigger in the study of radio signals in the GC. Indeed, while in Fig. 3.8, the tension reached in the most optimistic case (NFW-MAX) is ~ 10 TeV, in the synchrotron emission analysis for the GC would be 54.75 TeV, mentioned above. Nevertheless, GAC would only reach 5 TeV in tensions. In Fig. 4.8, the white area represents the strong-coupled-theory region, in which the particle description in Brane-World theories requires loop corrections and the formalism considered in this work is not valid. Finally, we would like to mention that these conclusions remain valid in the case of considering an astrophysical background. Indeed, in our study considered that all the galactic emission comes the DM annihilation as an extreme case to put sensitivity constraints, however, for a more realistic case, the background signal should be added to the DM emission. This framework would provide tighter sensitivity constraints than those obtained in our work.

4.5 Detection maps in the Milky Way

Under the previous panorama described in Sections 4.3 and 4.4 two main results may be extracted.

• First, the new era of radio telescopes are sensitive enough to detect a signal from annihilating DM around a mass of 100 TeV (80 TeV for $\tau^+\tau^-$ channel and beyond 100 TeV for both W^+W^- and $b\bar{b}$ channels. For further information, see right panel Fig. 4.7).

• Second, there is a large background to be known that highly exceeds the DM signal, even for low GeV masses. On the basis of the study performed in the previous Section 4.4, in this section below, we analyse the SKA1 sensitivity in DM detections along the whole Milky Way. To that purpose, we compute the density flux from annihilating DM in a window of $0.1^o \times 0.1^o$ at different regions of the sky, comparing them with the flux sensitivity that SKA1 is expected to reach in the following years. Therefore, a similar method to that of Section 4.4 is used here by varying the coordinates (l, b). The goal of such an analysis is proposing new regions of the sky

that could be suitable for DM detection. In our study, we focus on the case of model-independent DM.

4.5.1 Detection maps for model-independent dark matter

For this analysis we compute the flux density for a model of DM annihilating into $\tau^-\tau^+$ for different masses ($M = 1$, 10, 50, 100 TeV) with $\langle\sigma v\rangle = 3 \cdot 10^{-26}$ cm^3/s. In Fig. 4.9 we show the sky regions where DM could be detected, at least, at one frequency within the SKA1 range. This means, that not all the SKA1 frequencies would be suitable to detect such a candidate. However, as explained above, two factors should be taken into account for SKA1 sensitivity curves. DM with low masses ($\sim$ GeV) is better detected with SKA1-LOW, mainly due to the spectral shape of the synchrotron radiation. In this regard, lighter DM candidates present a slope more pronounced than heavy DM (from around $\sim$ 1 TeV) in their expected synchrotron signal, S_ν. Conversely, we already mentioned that as DM mass increases the behaviour of S_ν with the frequency turns into an almost straight line. This fact makes that the detection of such heavy candidates depends more on the highest sensitivity band of the detector. In this regard, SKA1 encounters its maximum sensitivity at Band3 $[1.65 - 3.05]$ GHz.

Observing Fig. 4.9, we find that all the masses could be detected at inner regions of the galaxy, following higher densities determined by the DM density profile. As galactic coordinates (l, b) move away from the GC, the detection of DM candidates begins to be more problematic for heavy candidates. In general, those regions in Fig. 4.9 where DM may be detected, show a similar shape that those emission maps of Fig. 4.2. This can be an indicator of the importance of the magnetic field at the time to look for alternative sky locations for DM searches. This fact results in a lower probability as latitude increases out of the Galactic plane. At its best, after 10 hours of integration time, the maximum latitude of detection with the SKA would be $b_{\rm max} = 26^{\rm o}$ for 1 TeV candidate. Also in Fig. 4.9, the bands in yellow and orange (DM masses of 1 TeV and 10 TeV) are extended along the whole Galactic plane until high latitudes. Increasing the integration time for SKA1 between 100 h and 1000 h, those regions extend in b up to $35^{\rm o}$ and $50^{\rm o}$ for the 1 TeV candidate, while for the 10 TeV DM would reach $14^{\rm o}$ and $18^{\rm o}$. This allows us to predict those regions where DM candidates annihilating into light leptons would be better detected. Indeed, for a DM candidate annihilating into leptons in agreement with AMS, as spoken in Chapter 3, we should be able to disentangle the synchrotron signal with SKA1 in a region $b < 18^{\rm o}$ if the integration time is 1000 h. In the case of heavier DM candidates ($\sim$ 50 TeV), synchrotron would extend in a latitude up to $10^{\rm o}$ degrees, after 1000 h of integration time. This limit of detection in the latitude does not seem to change significantly with the DM mass, as observed in Fig. 4.9. In fact, purple and red regions show large differences along the Galactic plane, whereas the scope of detection out of the Galactic plane is similar for heavy DM, showing once more the influence of the magnetic field at the time of constraining DM candidates through synchrotron emission.

Details about angular limits of detection can be found in Table 4.4. There, only positive values of the angles were represented since the emission relies on axial symmetry. Again, such values should be taken as an underestimated idea of the best regions to detect DM candidates according to the ISO-MIN model used in this calculation. This map is open to changes to account for more realistic information about the SKA1 detection strategies. Such two changes would be, first, those regions of the sky are accessible to SKA1 detections. In this regard, we need to add a new mask to the figures we plotted covering those regions of the sky map where SKA does not reach. Second, the different baselines used in each detection would reveal the angular aperture used by the telescope leaving us to use a more realistic value for that $0.1 \times 0.1^{\rm o}$ we used.

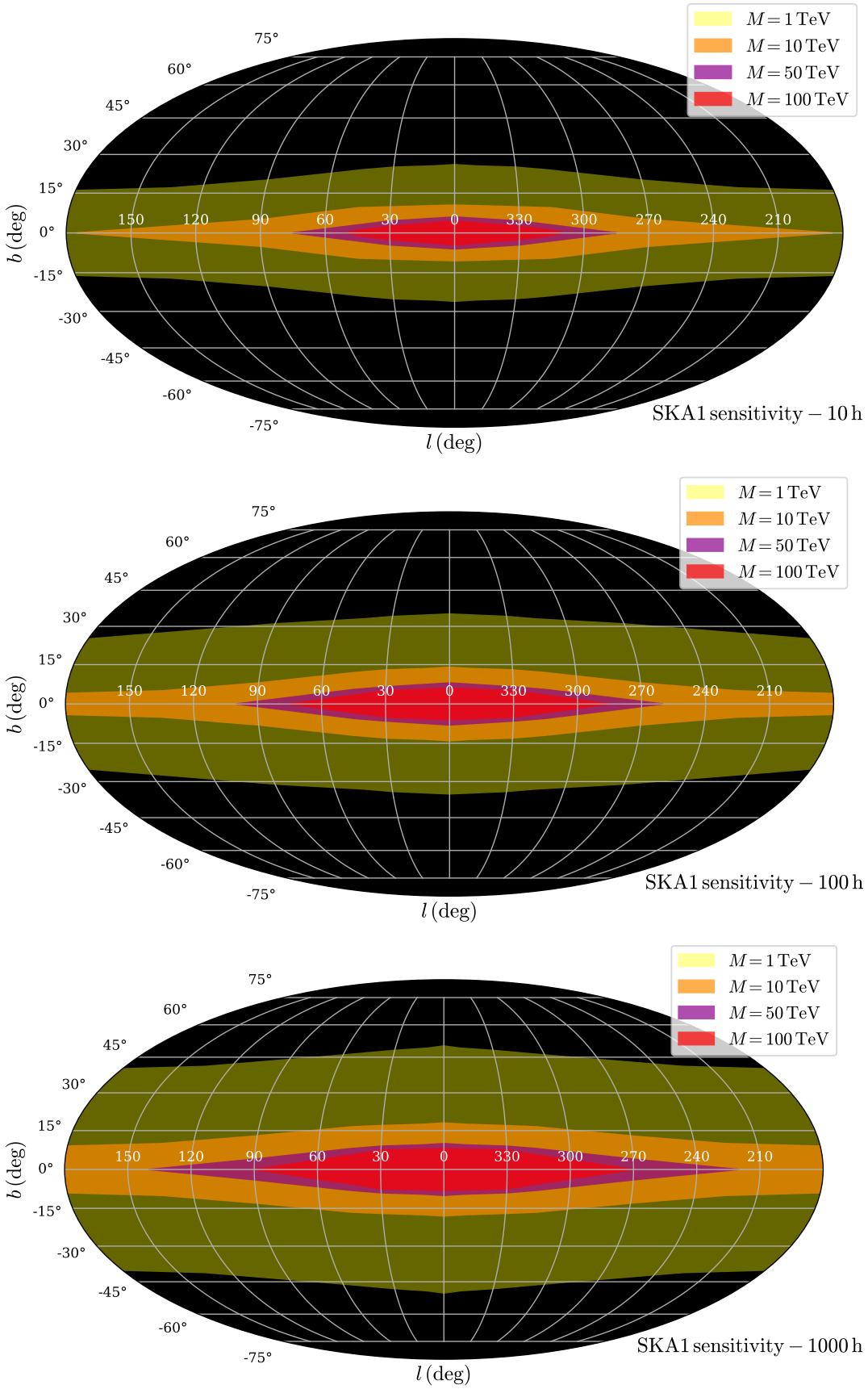

FIGURE 4.9: DM detectable regions in the Milky Way according to its mass without considering the astrophysical background. The bands in yellow, orange, violet and red are those areas in the sky in which DM candidates with masses 1 TeV, 10 TeV, 50 TeV and 100 TeV should be detected with SKA1 with an aperture of $0.1^o \times 0.1^o$.

TABLE 4.4: Angular limits for DM detection $\tau = 10$, 100, 1000 h with SKA1. This table corresponds to the limits obtained in Fig. 4.9.

M	$l_{max}(^{\circ})$	$b_{max}(^{\mathbf{o}})$	M	$l_{max}(^{\circ})$	$b_{max}(^{\mathbf{o}})$	M	$l_{max}(^{\circ})$	$b_{max}(^{\mathbf{o}})$	M	$l_{max}(^{\circ})$	$b_{max}(^{\mathbf{o}})$
$\tau = 10$ h											
1 TeV	0	26	10 TeV	0	10.5	50 TeV	0	6	100 TeV	0	4.5
	10	25.5		45	9.5		30	4.5		30	2.5
	30	25		90	5		45	3		45	1
	45	24		175	0		75	0		50	0
	90	20									
	135	17									
	179.9	16									
$\tau = 100$ h											
1 TeV	0	35	10 TeV	0	14	50 TeV	0	8	100 TeV	0	6
	10	25.5		30	13		30	6.5		30	5
	30	34		45	12		45	5.5		75	0
	45	33		90	8		100	0			
	90	31		135	5						
	135	28		180	4						
	179.9	25									
$\tau = 1000$ h											
1 TeV	0	50	10 TeV	0	18	50 TeV	0	10	100 TeV	0	8
	10	49		10	17.5		10	9.5		30	7.5
	30	48		30	17		30	9		45	5.5
	45	47		45	16.5		45	8		50	0
	90	44		90	13		90	4			
	135	41		135	10		140	0			
	179.9	40		179.9	9						

4.6 Chapter conclusions

In this Chapter, we have computed the synchrotron emission as the result of dark matter annihilation in the Milky Way. We have discussed the main reason to consider the Galactic Centre as one of the most suitable targets for dark matter searches; the reason being that dark matter density profiles show the highest dark matter concentration at central regions of the Milky Way. Even though one would expect significant radio signals from these latitudes, it has to be taken into account also the large background signal. Indeed, as shown in Fig. 4.3, the brightness temperature associated to a 10 GeV dark matter particle annihilating into $\mu^+\mu^-$, and a thermally averaged cross section $\langle\sigma v\rangle = 3\cdot 10^{-26}$ cm^3/s, would not be significant with respect to the total emission and practically negligible at higher longitudes l in the galactic plane. This indicates that it would be highly difficult to set constraints on thermal relic dark matter without a proper model of the background. Indeed, the flux density regarding the synchrotron emission from annihilating dark matter decreases with the factor $1/M^2$ and thus, provided a mass of 10 GeV generates a minor synchrotron signal, then heavier candidates would be even more difficult to detect. Therefore, the background would be essential to put constraints on WIMPs in the Galactic Centre. The next step for this analysis would be the use of codes like GALPROP to account for particle processes in the interstellar medium that would produce a significant contribution to the radio emission. Some works have already pointed towards that direction [177]. The strategy would consist of computing the radio background to observe how much space left there is for dark matter.

Regardless of the background challenge, we still have set constraints on non-thermal dark matter, i.e, $\langle\sigma v\rangle > 3\cdot 10^{-26}$ cm^3/s. Specifically, we focused, first, on the three channels we worked on Chapter 3, W^+W^-, $\tau^+\tau^-$, $b\bar{b}$ and, second, on branon dark matter. For the branon case, we observed that the cosmic-ray analysis set tighter constraints than that from synchrotron emission. However, we should keep in mind that this analysis is conservative since we do not consider the background and also due to the fact we assumed an Isothermal profile for the Milky Way. Such a profile has been taken due to a limitation of our code. Indeed, for an NFW profile, we would need a higher number of coefficients to ensure the convergence of Eq. (2.29) in the whole Galaxy. Work in that direction would be the next immediate step together with the background parametrisation with numerical codes.

Furthermore, in order to test the SKA capabilities in dark matter detection, we compute sensitivity constraints focusing on both the Galactic Centre and the Galactic AntiCentre as two extreme hypothetical situations in the detection. Our first approach consisted of a dark matter model-independent analysis, revealing that at the Galactic Centre SKA1 would be able to detect, at 1σ of confidence level, dark matter with masses up to ~ 70 TeV ($\tau^+\tau^-$ channel), while for the Galactic AntiCentre would reach masses of around 10 TeV (W^+W^- channel). A second approach was setting sensitivity constraints on branon dark matter also for both galactic locations. As for the case of model-independent dark matter, the Galactic Centre would allow us to detect masses greater than 100 TeV and tensions up to 60 TeV, which would imply to cover a very large region of the branon parameter space. The Galactic AntiCentre would allow reaching masses and tensions around 5 TeV. Even the latter case would improve the cosmic-ray constraints in Section 3.4 substantially.

Finally, and according to the background discussion we tested the SKA sensitivity in order to know the maximum latitude where synchrotron signals would be detected by SKA. This analysis would reveal whether the radio telescope would be able to measure synchrotron signals out of the galactic plane. In Fig. 4.9, attainable areas of the sky depending on the dark matter mass were represented. According to the maps presented in [307], these areas in which dark

matter could be detected would still have a large background. However, this analysis should be compared with sky maps at different frequencies.

Chapter 5

Radio signals from annihilating dark matter in dwarf spheroidals

5.1 Overview and leitmotiv

In Chapter 4, we studied the synchrotron radiation coming from annihilating DM in different regions of the Milky Way. The analysis in Section 4.3 revealed that the lack of knowledge on the astrophysical background highly limits the DM constraints. In this Chapter, we will study the synchrotron radiation in dSphs mainly through two quantities, the flux density S_ν and the specific intensity I_ν, described in Section 2.5 b). The main goal of this Chapter is to clarify whether the sensitivity of the new radio interferometer SKA will allow us to put tighter constraints on DM in the specific case of faint sources as dSphs. The main results of this Chapter have been collected in Ref. [199]. The work is organised as follows:

■ In Section 5.2, as well as in previous chapters, we shall provide a notion about the astrophysical framework, crucial to place the reader in the discussion. Herein, we shall mainly focus on those astrophysical aspects that could be significant for DM indirect detection: the galactic magnetic field, the diffusion and the DM density profile. Moreover, we shall focus on the particular case of Draco as a paradigmatic example. Indeed, the assumptions made on dSphs may drastically change the detection limits. We shall provide a general idea about how these changes would affect such limits.

■ Leaving aside the astrophysical framework, in Section 5.3, we shall evaluate S_ν and I_ν from a Particle Physics point of view. There, we shall try to disentangle if, having measured a DM signal, it is possible to reconstruct the responsible DM annihilation(s) channel(s). We shall also provide those frequencies in which the synchrotron signal from DM annihilation acquires its maximum. These values will intend to give a notion of which frequencies should be considered to detect different DM candidates according to their annihilation channels and mass.

■ In the next section, Section 5.4, we shall rely on the SKA characteristics to obtain sensitivity constraints for model-independent DM with the SKA. We shall try to establish our results within a more realistic framework than previous works, accounting here for an exponential magnetic field together with the largest angular scale of the SKA.

■ We will perform, in Section 5.5, a study analogous to the one presented in the previous section, this time for specific DM candidates. The study will be devoted to those candidates that are in agreement with HESS J1745.6 − 290 signal and also on Brane-World DM candidates. In addition, in the line of reasoning of some other authors, in this Section, we shall also consider the possibility of a dwarf hosting an intermediate-mass black hole (IMBH). The main idea herein will be to analyse how these objects may act as a boosting mechanism for DM annihilation signals. With this goal in mind, we shall use a modified DM profile $\rho_{\mathrm{DM+BH}}(r)$. After that, we

shall apply this particular case for Brane-World DM candidates in order to see how feasible it is to detect the branon parameter space with the SKA.

■ In Section 5.6, we shall calculate the emission for different dSphs in order to know the best targets for DM detection.

■ Section 5.7 shall be devoted to the main conclusions of this study.

5.2 Astrophysical considerations for dwarf spheroidals

In the previous chapter, the Milky Way was presented as one of the most promising targets for a multi-wavelength analysis of DM indirect searches. Because of its proximity to us ($\sim$ 8 kpc) as well as its large DM concentration, the Milky Way Galactic Centre would be the brightest DM source in the sky. In addition, this closeness ensures a large solid angle and provides angular information about the possible DM distribution. However, as discussed in Section 4.2 and Section 4.3, large backgrounds are expected at all energies so disentangling DM signals from astrophysical sources turns into a complicated task. In light of this situation, many studies focus on regions of the sky with a low percentage of astrophysical emission; such as areas away from the galactic plane and also extragalactic targets [179, 204, 349–351]. Among the latter, dSphs lie at the extreme of the lowest luminosity distribution [352, 353], and therefore they are one of the sources with the least baryonic content. As it has been shown by metallicity studies with colour-magnitude diagrams, most of the luminous fraction in dSphs often corresponds to stellar population systems that belong to the first generations of stars ($\sim$ 10 Gyr) (intermediate-age populations are found as well [354]) with no trace of recent star formation. In addition, immersed in an extremely low gas environment, some of the dSphs do not reach the gas mass value of $< 1\, M_\odot$ [355, 356]. Although both star populations and gas environment seem a minor detail in a system dominated by DM, their description remains fundamental in the case of dSphs: both of them carry the dynamic and the evolution information required to reconstruct the DM distribution, and also could be the foundation to grapple with existing controversies, such as the missing satellites problem [357] or the extremely large mass-to-light ratio observed in some specific systems [358].

The first dSphs, Sculptor and Fornax, were discovered in 1938 in the Harvard Observatory [359], however, it was not until 90's decade when Aaronson deduced the presence of a significant amount in DM in such galaxies studying the l.o.s. velocities of three carbon stars in Draco [360]. Since then, some detectors reported many of these roughly spherical objects in a series of studies including estimations through the virial theorem [360], spatial models of the mass-follows-light study [352] and mass-estimator studies based on the solution of the Jeans equation [361]. All of them confirmed the same main characteristic: the mass-to-light ratio M/L of dSphs seems to indicate an amount of mass that is higher than expected from the luminous matter. Indeed, comparing their dynamical mass-to-light ratios in the visual band ($M/L_{\rm V}$), we observe $M/L_V \gtrsim 10\,[M/L_V]_\odot$ [362]. This is the case of the Draco, Carina, Sextans dSphs whose mass-to-light ratios $M/L_{\rm V}$ lie close to 300, 67, 91 $[M/L_V]_\odot$ [363, 364] respectively. In the most extreme scenario, the ultra-faint dSphs Segue 1 deserves a special mention since its mass-to-light ratio determined by a Keck/DEIMOS survey confirms a mass-to-light ratio of $\sim 3400\,[M/L_V]_\odot$ [365]. However, considering that velocity estimators for dSphs are statistical and assume relaxed systems, one should consider possible effects that would inflate those values, the most common ones including: solid-body rotation about an axis misaligned with the line of sight, external tides and unresolved binary stars in the least massive galaxies. For Segue 1, the relevance of these mechanisms continues to be debated. In fact, Segue 1 presents a significant velocity variability indicating the possibility of binary systems together with its proximity to the Milky Way and

shape that would suggest the idea about the influence of tidal forces. Nevertheless, other studies claim that these effects are not significant and Segue 1 would still be the darkest galaxy [358].

Having these mass-to-light ratios in mind, dSphs have been widely considered with the aim of constraining particle DM through indirect searches [179, 204, 349–351]. However, these targets are not exempt from major uncertainties. With a view on the requirements for indirect searches, already explained in Section 2.5, we will briefly describe in this Section the tension between the characteristics of an ideal target (short distance and a large amount of DM) and the difficulty in modelling the astrophysical environment. As the reader will note, some of the results presented in this chapter are subjected to the determination of astrophysical parameters whose uncertainties are reflected in the analysis in radio frequencies. In many cases, such parameters are not directly extracted from dSphs but from irregular dwarf galaxies or other similar dwarf galaxies. Among the astrophysical quantities, the distance, the magnetic field, the DM density profile and the diffusion coefficients, are the most significant, as shown in Section 2.4.2:

- Firstly, RR Lyrae variables are usually the standard candles to determine distances to dSphs precisely. Most of dSphs are located within the virial radius of the Milky Way, established in $\sim$ 300 kpc, while the rest lies just beyond the border of the Milky Way or M31. Even though dSphs ensure to be close and brighter targets to be investigated they can also be difficult to study since they suffer from complicated dynamical processes as stripping, shocking and stirring due to tidal forces, having effects on their velocity dispersion, on the DM density profile at outer regions or even on the apparent core at inner regions. Often, these dynamical mechanisms also constitute an explanation to convert dwarf galaxies into dSphs.

- Regarding the diffusion governing the propagation of annihilating DM products, the parameters D_0 and δ, seen in Section 2.4.2 b), are not fully well determined in the case of dSphs. For the Milky Way, those coefficients are fixed by the ratio between primary and secondary cosmic rays, particularly by the B/C ratio. In the case of extragalactic sources this information often comes from diffuse γ-rays in $\pi^0\pi^0$ processes or ICS, whose emission is strictly related to the process of star formation [366]. However, such processes are not well understood for dSphs and propagation models are assumed in analogy with the Milky Way. Typically, the Kolmogorov description $D(E) = D_0 E^\delta$ with $\delta = 1/3$ that sometimes includes a degree of uniformity of the magnetic field, $D(E) = D_0 \frac{d_B^{2/3}}{B_{\rm avg}^{1/3}} E^\delta$, being d_B the minimum uniformity scale of the magnetic field and $B_{\rm avg}$ the averaged magnetic field, is assumed.

- Galactic magnetic fields interact with charged particles turning into the main cause for synchrotron signals from DM annihilation products. In general, reconstructing such magnetic fields is possible by observing different signatures, namely polarised optical-infrared starlight, synchrotron emission, Faraday rotation or Zeeman lines already mentioned in Section 4.2. Each of these signatures unveils different field components, as seen in Table 4.1 in Section 4.2.
A method usually used to measure magnetic fields in dwarf galaxies consists of searching for radiation from synchrotron emission and, after that, using the equipartition theorem to estimate the magnetic field strength. However, the lack of turbulent gas in dSphs turns this into a difficult task. Furthermore, an estimation of the l.o.s. integral of the magnetic fields and electron densities in dSphs can be measured through the Faraday rotation of the polarised emission from the background, as has been done for the Large Magellanic Cloud [367]. A sky map of the Galactic Faraday rotation has been presented in [368] with the reconstruction of the magnetic field, considering one source per square degree, with a resolution of $\sim 30'$. This resolution is not enough to resolve the magnetic field structure in dSphs.

Therefore, the usual method to estimate values on the strength of the magnetic field is by

reconstructing the magnetic field from dwarf galaxies similar to dSphs. Indeed, photometric properties and resolved stellar populations suggest that dwarf irregular galaxies and dSphs shared a similar evolutionary history until a few Gyrs ago [369]. Numerical simulations show that a combination of tidal and ram pressure stripping by the Milky Way would be an effective mechanism to transform irregular galaxies into dSphs. Assuming this scenario, dSphs would have had magnetic fields of $5-10\,\mu G$ in the past that had evolved in some way to the present values after the stellar evolution and gas stripping. The consideration of those similarities between dSphs and dwarf galaxies, put some limits on the magnetic field strength for the former and the general establishment is $\sim 1\,\mu$G. Furthermore, nearest dSphs to the Milky Way should be specially mentioned since some of them could be affected by the outer halo magnetic field of our galaxy. This fact could support a magnetic field strength of $2\,\mu$G in dSphs such as Segue 1 [178].

- Last, the third quantity to be determined is the DM density profile. In rotating spiral galaxies it is possible to directly relate the circular velocity $v_{circ}^2 = GM(r)/r$ with the enclosed mass considering young stars. However, in dSphs an ordered motion is negligible and statistical analysis through the dispersion of velocities over the l.o.s. σ_p^2 has to be done. In 1987, Aaronson predicted a velocity dispersion of 10 km/s over the l.o.s. for Draco. This velocity, estimated by considering 11 stars within Draco dSph, implied a mass-to-light ratio that revealed a large amount of non-luminous matter [370]. Even though other alternative mechanisms to explain the inflation of the velocity dispersion (such as unidentified binaries, stellar-atmospheric turbulences or tidal disruptions) were considered, all of them seemed to be unlikely. Since then, the number of stars with known l.o.s. velocities has grown in dSphs and thus, the improvement of the mass modeling. Some of the usual methods to determine characteristics of a halo is through mass estimators based on comparing the predicted stellar l.o.s. velocity dispersion profiles

$$\sigma_p^2(R) = \frac{2G}{\Sigma(R)} \int_R^\infty \mathrm{d}s\, s^{2\beta-2} \nu(s) M(s) \int_R^s \left(1-\beta\frac{R^2}{r^2}\right) \frac{r^{-2\beta+1}}{\sqrt{r^2-R^2}} \mathrm{d}r \tag{5.1}$$

with the observed ones, by solving the spherical Jeans equation (derived from the collisionless Boltzmann equation) and assuming that the anisotropy β is constant (as is generally assumed). The general idea (although there are some variations) is adopting a universal DM profile such as

$$\rho(r) = \frac{\rho_s}{(r/r_s)^\gamma (1+r/r_s)^{3-\gamma}}, \tag{5.2}$$

that includes both core and cusp halo models, and considering

$$M(s) = 4\pi \int_0^s r^2 \rho(\mathrm{r}) \mathrm{d}r, \tag{5.3}$$

to reproduce the experimental values for Eq. (5.1).

This method was useful to determine some common properties on DM density profiles in dSphs: all the systems that fit the velocity dispersion have the same value for the enclosed mass near the half-light radius. However, the observational data do not provide enough information to clearly determine the slope of the profile at inner regions, since it highly depends on the stellar density model, and more realistic stellar distribution functions should be considered. The Binney anisotropy parameter

$$\beta = 1 - v_t^2/v_r^2, \tag{5.4}$$

deserves a special mention since it is responsible for a degeneracy between the assumed profile density and the velocity distribution of the studied system, leading in some cases to an erroneous

mass estimation. Furthermore, the general statement of the stellar anisotropy, β, as a constant is not clear in dSphs. Both non-equilibrium stellar configurations for some dynamical models or the interaction of DM with baryons at the centre could generate significant anisotropies. In addition, it has been argued that there is no guarantee that some solutions of the Jeans equation correspond to a physical dynamical model, despite fitting the data.

From the numerical simulation point of view, the DM halo profiles for dSphs have some differences with respect to the dynamical description presented above. The first thing is DM profile in dSphs is not considered as a halo itself but a subhalo linked gravitationally to a hosting halo*. Structures in ΛCDM are produced hierarchically: small instabilities in the early Universe produce small bounded DM halos that either merge or accrete mass to other halos setting larger ones (see, e.g., [371]). Even after this process, some of those small subhalos would survive orbiting larger halos. The first approach was assuming that subhalos follow the same structural characteristics -through the parameter concentration $C(M)$- of large halos with the same mass, and in many cases, the same profile as we suggested with the expression (5.2). Dwarf galaxies, whose simulated DM density can be fitted by a universal NFW profile, have been well described through N-body codes under the ΛCDM statements, however, none of the simulations produced dSphs at the end. Different numerical studies show that subhalos are in general more concentrated than those halos with the same mass and with different structural characteristics. The closer they lie to their host halo centres, the larger their concentrations. In order to solve this, some authors proposed models that would be able to describe the evolution of a dwarf galaxy into a dSphs incorporating tidal forces between halos and subhalos [372]. The main difficulty is that adding tidal forces change the definitions of some quantities used for the halo description. In those models, tidal forces remove mass from the outer parts of subhalos truncating them at smaller radii than halos. This would imply subhalos more concentrated than halos. However, truncation implies that the virial radius of subhalos is not well defined, and thus the standard definition of halo concentration cannot be used. New structure definitions have been provided [373] in order to accurately describe subhalos as well as new profiles that incorporate those tidal effects, such as the cored and cusped Kasantzidis profile that will be studied in next sections.

5.2.1 Draco dSph

Once we have set the general characteristics for dSphs and presented the difficulties to constrain their astrophysical aspects, we study the particular case of Draco. Even though Segue 1, thanks to its apparently large amount of DM and the possibility of being influenced by the Milky Way magnetic field seems to be a suitable target, Draco has been usually studied given the fact that some of its parameters are better constrained than for the rest of dSphs. Its mass-to-light ratio, $\sim 300\,[M/L_V]_\odot$, still warrants a large amount of DM.

Observations of RR Lyrae place Draco at a distance of $\sim 80\,$kpc from the Sun and thus, within the Milky Way virial radius. This distance accounts for the gravitational interaction between Draco and the Milky Way by tidal forces. Considering this, some authors performed N-body simulations for a Draco-like object with the NFW density profile as an initial distribution, and study its evolution in the field of a Milky-Way like galaxy [374]. The resulting profile conserves the r^{-1} behaviour for inner regions but develops an exponential cut-off at large distances. In view of these circumstances, we took into account two profiles for the case of Draco. The

*However, throughout the whole Chapter (excepting this paragraph in which we use the term subhalo) we will refer to dSphs halo instead of subhalo

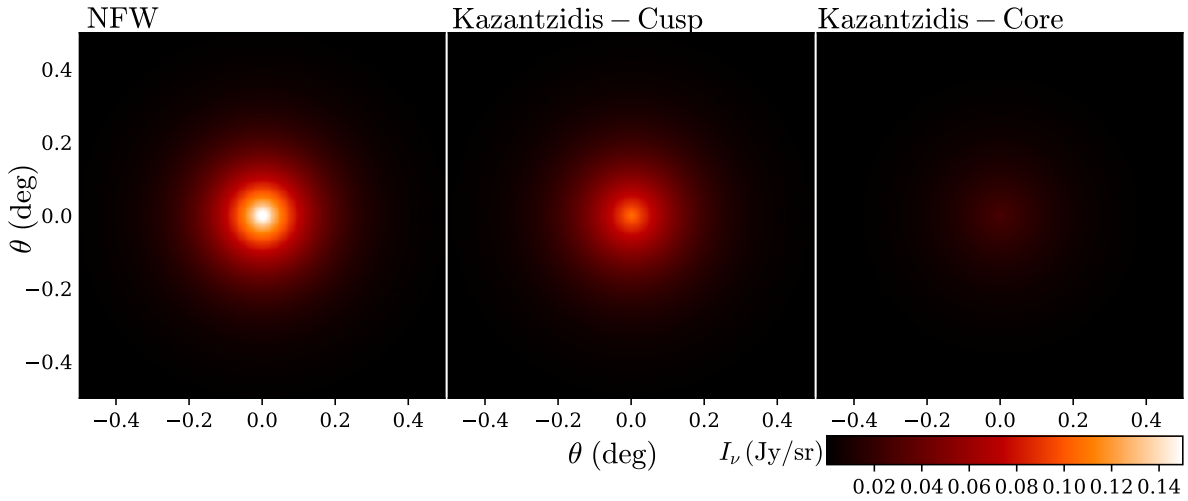

FIGURE 5.1: Intensity map I_ν as given by Eq. (2.39) at $\nu = 150$ MHz for different DM halos. The annihilation channel is $b\bar{b}$ for DM with mass $M = 1$ TeV and a thermally averaged cross section equal to $3 \cdot 10^{-26}\text{cm}^3/\text{s}$. The astrophysical parameters are set out in Table 5.1. In each panel a different DM profile has been considered: NFW (left panel), Kazantzidis-cusp (middle panel) and Kazantzidis-core (right panel).

well-known NFW distribution,

$$\rho_{\text{NFW}}(r) = \frac{\rho_s}{\frac{r}{r_s}\left(1+\frac{r}{r_s}\right)^2}, \tag{5.5}$$

with $\rho_s = 1.40\ \text{GeV}/\text{cm}^3$ and $r_s = 1$ kpc [179, 204], and also the Kazantzidis profile,

$$\rho_{\text{Kaz}}(r) = \frac{M_{\text{D}}}{4\pi r_{\text{b}}^2}\frac{1}{r^\alpha}\exp(-r/r_{\text{b}}). \tag{5.6}$$

The choice of parameters $\{r_{\text{b}},\ M_{\text{D}},\ \alpha\} = \{1.308\,\text{kpc}, 5.48 \cdot 10^8 M_\odot, 1\}$ indicates the Kazantzidis profile has a cusp at the centre (from now Kazantzidis-cusp). Nevertheless, it is claimed that tidal forces may be relevant in turning the cusp into a core profile. In such a case, the expression (5.6) would take the values $\{r_{\text{b}},\ M_{\text{D}},\ \alpha\} = \{0.24\,\text{kpc}, 1.22 \cdot 10^8 M_\odot, 0\}$ for the core Kazantzidis profile (from now Kazantzidis-core) [375].

The magnetic field $B(\mathbf{r})$, as already mentioned, is poorly determined. In this sense we introduce a spherical spatial distribution, according to [179] , yielding

$$B(r) = B_0 \exp(-r/r_c), \tag{5.7}$$

where B_0 is the magnetic field strength and $r_c = 0.22$ kpc is the core radius of Draco. Measurements in Ref. [376] indicate a magnetic field strength lying around $B \sim 1\ \mu$G.

In the following, we will analyse how the expected synchrotron signal from DM annihilation would change depending on the profile, magnetic field and diffusion.

TABLE 5.1: Astrophysical parameters for Fig. 5.1.

Target	$B(r)$	$B_0\,(\mu\mathrm{G})$	$r_c\,(\mathrm{kpc})$	$D_0\,(\mathrm{cm}^2/\mathrm{s})$	δ	$n_e\,(\mathrm{cm}^{-3})$
Draco dSph $d = 80\,\mathrm{kpc}$	Exponential, Eq. (5.7)	1	0.22	$3 \cdot 10^{28}$	1/3	$1 \cdot 10^{-6}$

a) Synchrotron and the dark matter density profile

In order to observe the astrophysical dependence of the synchrotron signal from DM annihilation, we calculate the intensity map I_ν according to the expression (2.39). In Fig. 5.1, we compute I_ν for a DM model annihilating into $b\bar{b}$ channel with a mass $M = 1$ TeV and a thermally averaged cross section equals to $3 \cdot 10^{-26}\mathrm{cm}^3/\mathrm{s}$. The value at 150 MHz belongs to the SKA1-LOW range of frequencies. The purpose of this plot is observing the spatial distribution of annihilating DM signals for the NFW profile but also the Kazantzidis-cusp and Kazantzidis-core described above. Those astrophysical parameters that remain fixed in the calculation are present in Table 5.1. For the three cases, n=500 terms for the series. In addition, the number of samples for each value $I_{150\,\mathrm{MHz}}(\theta)$ is $2 \cdot 10^7$ for the Adaptive Monte Carlo computation with the module Vegas for *Python*. For these figures, we compute the function $I_{150\,\mathrm{MHz}}(\theta)$. After that, since the problem has spherical symmetry [†], we extrapolate the function $I_\nu(\theta)$ to the function $I_\nu(\theta_x^2 + \theta_y^2)$ taking a number of pairs $\{\theta_x, \theta_y\}$ equal to 300×300. The preferred limit values for the specific intensity, $I_{150\,\mathrm{MHz}}(\theta)$, in the colour map are $I^{\mathrm{max}}_{150\,\mathrm{MHz}} = 0.5\,\mathrm{Jy}$ and $I^{\mathrm{min}}_{150\,\mathrm{MHz}} = 1\,\mu\mathrm{Jy}$.

On first thought, both Kazantzidis profiles (Fig. 5.1 middle and right panels) show a synchrotron signal spreading more diffusely than the NFW case, following the slope of their profiles. Indeed, the NFW shows a steeper distribution than the Kazantzidis-core and Kazantzidis-cusp profile at inner regions, as observed in Fig. 5.1. In addition, the extension of the emission for the NFW and the Kazantzidis-cusp is significantly similar and reach angles larger than that in the Kazantzidis-core. Furthermore, comparing left and centre panels of Fig. 5.1, even though in the Kazantzidis-cusp profile the cusp still remains after the e^+ and e^- diffusion, the intensity at the centre is clearly smaller than in the NFW profile. For the Kazantzidis-core, I_ν^{max} at $\theta \sim 0$ is estimated in $0.028\,\mathrm{Jy/sr}$ that differs from the NFW maximum in an 81 % with a value $I_\nu^{\mathrm{max}} = 0.15\,\mathrm{Jy/sr}$. Also, in the Kazantzidis-cusp case the maximum of the emission at the centre can be found at $0.1\,\mathrm{Jy/sr}$ differing a 33% with the NFW profile. Such differences can be better seen in Fig. 5.2, left panel in which we plot the angular profile for the specific intensity I_ν in the three cases. In such a figure (left panel), dark blue, blue and light blue represent the specific intensities I_ν for a DM model $b\bar{b}$(1 TeV) considering the NFW, the Kazantzidis - cusp and the Kazantzidis - core profiles respectively. In addition, we set a horizontal solid grey line at $I_\nu = 1\,\mu\mathrm{Jy}$ to artificially enclose Draco through the minimal value that a hypothetical detector could measure. At this value, the angular extension of the emission lies on $\theta_{1\mu\mathrm{Jy}} = 1.09^{\mathrm{o}}$ for the NFW profile and $\theta_{1\mu\mathrm{Jy}} = 1.08^{\mathrm{o}}$ and $\theta_{1\mu\mathrm{Jy}} = 0.97^{\mathrm{o}}$ for the Kazantzidis-cusp and core respectively. These angular values evidence that Draco would not be seen as a point-like source for detectors as SKA1-LOW since its resolution lies on 0.002^{o} at 150 MHz (with 500 km of baseline).

Integrating I_ν over the solid angle of Draco, Ω_{DRACO}, we obtain the flux density S_ν from the Eq. (2.41). In practice, integrating over the whole source means that when increasing the angle of

[†]Unlike the case of the Milky Way studied in Section 4.2, the spatial distribution of the emission is spherical. This fact has been determined by the kind of propagation in the Laplacian of the diffusion equation, Eq. (2.28), together with the spherical symmetry of the magnetic field, the DM density profile and the diffusion without spatial dependence.

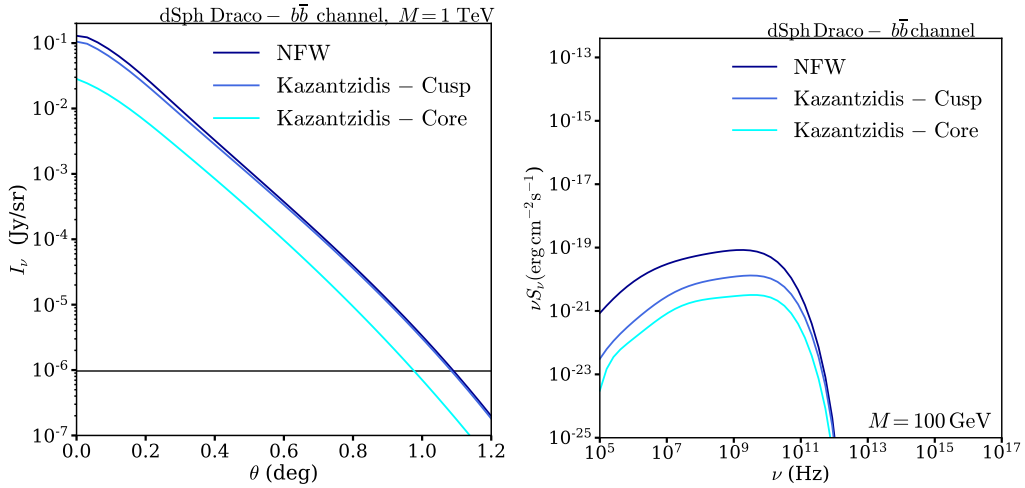

FIGURE 5.2: *Left panel:* Specific intensity I_ν as given by Eq. (2.39) with respect to the angle θ, delimited from the centre of Draco dSph. The annihilation channel is $b\bar{b}$ for DM with mass $M = 1$ TeV and a thermally averaged cross section equals to $3 \cdot 10^{-26}\text{cm}^3/\text{s}$. Dark blue line represent the emission considering an NFW profile, blue and light blue correspond to the Kazantzidis - cusp and the Kazantzidis - core profile. The grey line has been taken as an artificial limit for I_ν to discuss the detection limits of the synchrotron radiation. *Right panel:* Flux density S_ν as given by Eq. (2.41) times frequency ν for Ω_{DRACO} in the range of frequencies $10^5 - 10^{17}$ Hz. Again, dark blue line represent the emission considering an NFW profile, blue and light blue correspond to the Kazantzidis - cuspy and the Kazantzidis - core profile respectively. The major differences are between the NFW and the Kazantzidis core profile with a maximum νS_{min} which differs in more than one order of magnitude. The annihilation channel is $b\bar{b}$ for DM with mass $M = 100$ GeV and a thermally averaged cross section equals to $3 \cdot 10^{-26}\text{cm}^3/\text{s}$. The astrophysical parameters for this calculation are similar to Table 5.1.

integration θ no significant difference is noticed in the flux density, S_ν, when integrating from θ to $\theta + \Delta\theta$[‡].

In Fig. 5.2, right panel, we represent the flux density of $b\bar{b}\,(100\,\text{GeV})$ with $\langle\sigma v\rangle = 3 \cdot 10^{-26}\text{cm}^3/\text{s}$ for the three DM density profiles, in dark blue the NFW, in blue the Kazantzidis-cusp and in light blue the Kazantzidis-core. S_ν does not display qualitative changes in the dependence with the frequency for the mentioned DM distributions; all of them exhibit a similar shape. As will see in the following Section 5.2.1 and in Section 5.3, this dependence is fundamentally given by the galactic magnetic field and the channel of annihilation. However, the emission in Fig. 5.2 (right panel) seems slightly shifted in frequencies when different DM profiles are considered. In addition, the maximum of the emission S_ν^{max} is larger when the NFW one is taken into account, followed by the Kazantzidis - cusp and Kazantzidis core ones: the maxima can be found at $\left\{\nu[\text{Hz}], \nu S_\nu^{\text{max}}[\text{erg}\,\text{cm}^{-2}\,\text{s}^{-1}]\right\} = \left\{1.7 \cdot 10^9, 8.4 \cdot 10^{-20}\right\}$, $\left\{3.4 \cdot 10^9, 1.3 \cdot 10^{-20}\right\}$ and $\left\{3.8 \cdot 10^9, 3.2 \cdot 10^{-21}\right\}$ respectively. Furthermore, the emission is highly suppressed at higher frequencies constituting a cut-off imposed by the modified Bessel function, $K_{\frac{5}{3}}(\xi)$ in the expression (2.37). For a mass of 100 GeV, signals are limited by a critical frequency that lies on THz (IR) (Fig. 5.2).

With regard to the detection of these signals, if one considers roughly $S_{\text{min}} \sim 1\,\mu\text{Jy}$ for the

[‡]We are aware that a more realistic treatment could be done by imposing the largest angular scale as limits of integration. In next sections we will consider this situation.

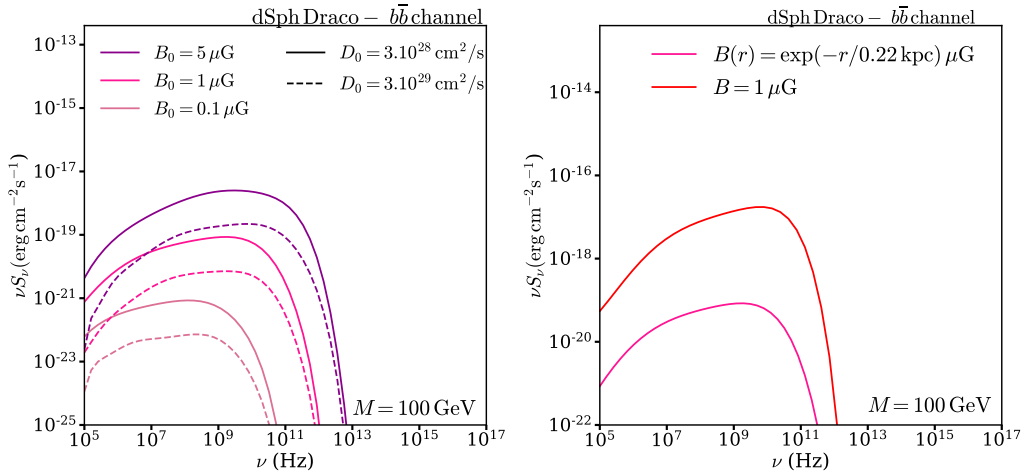

FIGURE 5.3: Flux density S_ν as given by Eq. (2.41) times frequency ν for Ω_{DRACO} in the range of frequencies $10^5 - 10^{17}$ Hz. The annihilation channel is $b\bar{b}$ for DM with mass $M = 100$ GeV and a thermally averaged cross section equals to $3 \cdot 10^{-26}\mathrm{cm}^3/\mathrm{s}$. *Left panel:* S_ν turns into very dependent with the chosen magnetic field [199]. In this panel, three values of B_0 have been depicted for illustrative purposes ($0.1\,\mu$G, $1\,\mu$G, $5\,\mu$G). The influence of the diffusion has been also illustrated, showing that for smaller values of D_0 the signal increases. *Right panel:* In the panel, the flux density for the case of an exponential magnetic field according to Eq. 5.7 and a constant magnetic field equal to $B = 1\,\mu$G have been compared. The difference between both signals becomes more than two orders of magnitude.

SKA (only for illustrative purposes), then $\nu S_{\mathrm{min}} \sim 10^{-20}\mathrm{erg} \cdot \mathrm{s}^{-1} \cdot \mathrm{cm}^{-2}$ at the frequency of the maximum of the signal. This means that $b\bar{b}\,(100\,\mathrm{GeV})$ would be detected in both cuspy profiles but not in the Kazantzidis-core one. As we observe, constraints on DM highly depend on a good characterisation of astrophysical components, such as the DM distribution. Therefore, for similar targets those which follows an NFW profile would provide tighter constraints on the DM parameter space than targets as the Kazantzidis profile, subjected to tidal forces. This has to be taken into account at the time of selecting the DM profile for an accurate study.

b) Synchrotron and magnetic field

With respect to the magnetic field, in Fig. 5.3 left panel, we represent the model $b\bar{b}\,(100\,\mathrm{GeV})$ with a thermally averaged cross section equals to $3 \cdot 10^{-26}\mathrm{cm}^3/\mathrm{s}$, whose e^+e^- after the annihilation are immersed in a magnetic field modelled by Eq. (5.7). The strength B_0 is the only parameter changed in Fig. 5.3 left panel, taking the values of $5\,\mu$G, $1\,\mu$G and $0.1\,\mu$G. In view of this analysis, i.e., comparing different signals for the three different values B_0, one can observe the crucial role that the magnetic field plays at the time of constraining DM through synchrotron emission, as showed in Fig. 5.3. For instance, in the left panel, the flux density times frequency for a 100 GeV DM candidate, annihilating into the $b\bar{b}$ channel, presents a value of $7.02 \cdot 10^{-20}$ erg cm^{-2} s^{-1} at $6 \cdot 10^9$ Hz when a magnetic field of 1 μG is considered while, at the same frequency, the value is $2.42 \cdot 10^{-18}$ erg cm^{-2} s^{-1} if $B = 5$ μG. This example shows how an increment of 4 μG for the magnetic field in Draco would enhance the radio signal around two orders of magnitude. In addition, according to Eqs. (2.36) and (2.37), the shape of the flux density can be affected by the strength values of the magnetic field. In this regard, we observe that the cut-off values lie on different frequencies depending on the strength. Whereas in the case of $B_0 = 0.1\,\mu$G, such a frequency lies in the range of microwave, $B_0 = 1\,\mu$G and $B_0 = 5\,\mu$G can find such a limit on IR.

TABLE 5.2: Astrophysical parameters for Fig. 5.4.

Target	Profile	$D_0\,(\mathrm{cm}^2/\mathrm{s})$	δ	$n_e\,(\mathrm{cm}^{-3})$
Draco dSph $d = 80\,\mathrm{kpc}$	NFW, $r_s = 1\mathrm{kpc}$ $\rho_s = 1.40\mathrm{GeV/c}$	$3 \cdot 10^{28}$	$1/3$	$1 \cdot 10^{-6}$

In Fig. 5.3 right panel, we represent the density flux S_ν times the frequency, in pink for the case of an exponential magnetic field and in red for B constant and equal to 1μG. The most noticeable effect is that both cases show a difference of more than two orders of magnitude in νS_ν. In this regard, the case with the constant magnetic field would impose tighter constraints to DM, however, it is necessary to determine how realistic this scenario would be. Constraints assuming a constant magnetic field may overestimate the synchrotron emission resulting in diagrams $\langle\sigma v\rangle/M$ with excluding regions that should not be excluded. In fact, it is sometimes assumed constant magnetic fields together with the point-like source approximation, which basically takes into consideration the emission as obtained from the whole source. Consequently, in this latter case, S_ν is obtained by integrating I_ν over the whole source together with a magnetic field that remains constant. Therefore, the contrast between constraints issued from either a constant or an exponential magnetic field is very significant. This fact may be better reflected in Fig. 5.4.

In Fig. 5.4, we study quantity I_ν for a constant magnetic field and compare it with the exponential magnetic field previously considered in Eq. (5.7). For the both cases, n=499 terms for the series in Eq. 2.33. In addition, the number of samples for each value $I_{150\,\mathrm{MHz}}(\theta)$ is $2 \cdot 10^7$ for the Adaptive Monte Carlo computation with the module Vegas for *Python*. For these figures, we compute the function $I_{150\,\mathrm{MHz}}(\theta)$. After that, since the problem has spherical symmetry, we extrapolate the function $I_\nu(\theta)$ to the function $I_\nu(\theta_x^2 + \theta_y^2)$ taking a number of pairs $\{\theta_x, \theta_y\}$ equal to 300×300. The range color has been fixed in with $I_{150\,\mathrm{MHz}}(\theta)$, in the color map are $I^{\mathrm{max}}_{150\,\mathrm{MHz}} = 0.6\,\mathrm{Jy}$ and $I^{\mathrm{min}}_{150\,\mathrm{MHz}} = 1\,\mu\mathrm{Jy}$.

Comparison between the right and left panels, immediate establish how both the specific intensity values and the spatial distribution of the signal change. Keeping in mind that magnetic field values at the centre ($\theta = 0$) are the same both for the constant and the exponential case, it is interesting to observe how the intensity I_ν shows discrepancies for both cases. The fact of considering a spatial dependency on magnetic field reduces the intensity value at the centre of Draco, fundamentally because the magnetic field also changes the e^+/e^- number density, $\psi(\mathbf{r}, E)$, through $g_n^{\pm}(r', E, E_s) = \frac{(r' \pm r_n r)^2}{\lambda_D^2(E, E_s)}$ in the Green function Eq. (2.33). Indeed, for a constant magnetic field $I_\nu^{\mathrm{max}} = 0.6\,\mathrm{Jy/sr}$ unlike the exponential case whose maximum, as already mentioned, is $I^{max} \sim 0.15\,\mu\mathrm{Jy/sr}$. With respect to the spatial extension of the emission, the constant magnetic field propagates the synchrotron signals to larger distances. The angle in which $I_\nu = 1\,\mu\mathrm{Jy/sr}$ becomes $\theta_{1\mu\mathrm{G}} = 2.44$ deg while, as already determined, for the exponential magnetic field, it becomes $\theta_{1\mu\mathrm{G}} = 1.09$ deg.

c) Synchrotron and diffusion

Regarding the diffusion, it was already mentioned that in analogy with the Milky Way, the Kolmogorov description is taken according to the expression $D(E) = D_0 E^\delta$ with $\delta = 1/3$. In Fig. 5.3 and Fig. 5.5, we observe the effects of the diffusion. In Fig. 5.5, for illustrative purposes and following [204], we plot the limit in which there is no spatial diffusion, i.e., It has been demonstrated that this case would not apply to the case of Draco, but it does in targets such as

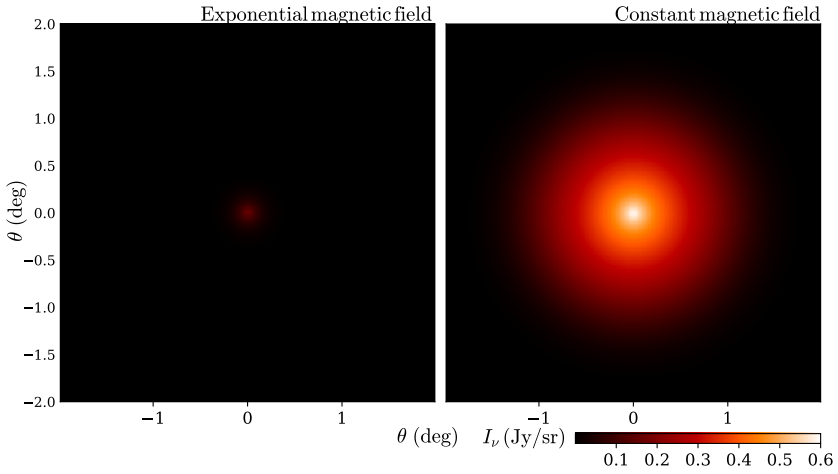

FIGURE 5.4: Intensity map I_ν as given by Eq. (2.39) at $\nu = 150$ MHz for different magnetic fields. The annihilation channel is $b\bar{b}$ for DM with mass $M = 1$ TeV and a thermally averaged cross section equals to $3 \cdot 10^{-26}\text{cm}^3/\text{s}$. The astrophysical parameters are set out in the Table 5.2. The left panel has been computed with a an exponential magnetic field according to 5.7 and the *Right* panel considering a constant magnetic field equal to $B = 1\,\mu$G.

the Coma Cluster [207]. However, in Fig. 5.5 we compute also this situation by using Eq. (5.8) as an extreme illustrative example.

$$\psi(\mathbf{r}, E) = \frac{1}{b(\mathbf{r}, E)} \int_E^M \mathrm{d}E_s \, q(\mathbf{r}, E_s). \tag{5.8}$$

In Fig. 5.5, we plot the specific intensity I_ν at 350 MHz (which lies on the limit among SKA1-LOW and SKA1-MID) after the annihilation, considering the cases with and without spatial diffusion. Therein, it is possible to observe that in the case without diffusion, results in a signal concentrated at the centre of Draco since the spatial distribution of annihilation follows the DM density profile strictly. In the case without diffusion, the inner window in Fig. 5.5 shows that the SKA1-LOW cannot resolve the peak of the signal and thus cannot resolve any structure in the emission either. Therefore, the target could be treated as a point-like source since most of the emission mainly occurs in the neighbourhood of the centre of Draco. On the contrary, the high sensitivity of the SKA1-MID allows us to resolve some part of the structure of the cusp, however, the emission still remains highly concentrated at $r \simeq 0$. Once the diffusion is considered, the radio emission extends spatially, decreases slightly with the angle θ, and the effect of the peak is less pronounced. In fact, as seen in Fig. 5.5 left panel, the peak still remains although, unlike what happens in the no-diffusion case, the steep cusp at the centre disappears. Consequently, whenever diffusion is considered, most of the signal does not come from the centre and hence the source cannot be thought of as being point-like. In this regard, we conclude that both SKA1-LOW and SKA1-MID can resolve part of the structure of the emission for Draco considering an angular resolution $\theta_{\text{res}} \sim 0.001$ deg for SKA1-LOW and $\sim 2.5 \cdot 10^{-4}$ deg for SKA1-MID at 350 MHz.

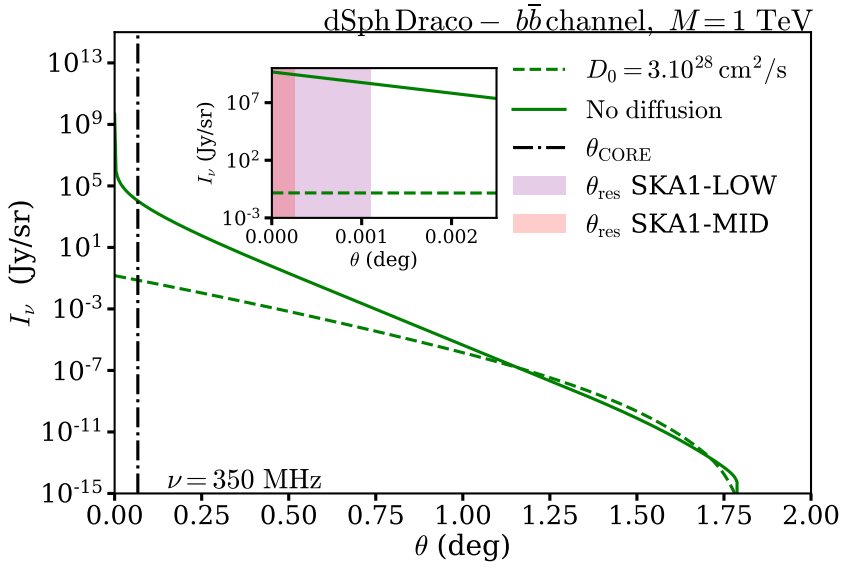

FIGURE 5.5: *Left panel:* specific intensity of the signal I_ν at $\nu = 350$ MHz for a $M = 1$ TeV DM model annihilating into $b\bar{b}$ channel. The vertical dash-dotted black line, represents the core radius of Draco ($\theta_{\rm DRACO} \sim 0.093$ kpc [204]) and the emission exceeds this limit. *Right panel:* the same specific intensity ($\nu = 350$ MHz, $M = 1$ TeV) for $b\bar{b}$ channel for small values of θ. Purple and red bands show the resolution, $\theta_{\rm res}$, of SKA1-LOW and SKA1-MID respectively for that frequency. In the case of SKA1-LOW, the no-diffusion emission model is unresolved in contrast to the SKA1-MID case. In addition, we observe that the angular distribution of the signal does not change significantly when diffusion is considered [199].

5.3 Particle physics considerations for dark matter synchrotron emission

5.3.1 Specific intensity study

Besides the astrophysical framework study performed in Section 5.3, the analysis of the synchrotron radiation from a Particle Physics point of view may be useful to reconstruct the DM annihilation(s) channel(s) once a synchrotron signal is detected. The synchrotron emission is sensitive to the annihilation channel but also to the mass of the DM candidate. The main objective of this section will be to study the effects that such quantities may have when they adopt different values.

When we work with Eq. (2.36), in order to calculate the synchrotron power, the factor $F_i(s)$ contains the critical frequency ν_c around which, approximately, all the synchrotron power is emitted. Both S_ν and I_ν also depend on both ν_c that is a function of the magnetic field and also the e^+e^- kinetic energy E. The role of the magnetic field was already discussed in the previous Section 5.2.1, together with the rest of the relevant astrophysical factors. Conversely, the fact that to calculate S_ν and I_ν is necessary to integrate over energies, see Eq. (2.35), produces the dependence of the resulting signal with the DM mass and also with the annihilation channel. Therefore, the synchrotron spectrum could indirectly provide information about the DM particle model. Indeed, one would expect M and $\frac{dN_e^j}{dE}$ to affect the synchrotron signal, not only S_ν, but also I_ν and its angular dependence through the critical frequency ν_c. In this regard, we should keep in mind that Draco is an extended source in radio frequencies. In this section we study if it is possible to extract some DM particle information, mass and channel of annihilation specifically, given the features of quantities I_ν and S_ν.

TABLE 5.3: Astrophysical parameters for Figs. 5.6 and 5.7

Target	Profile	$B(r)$	$B_0\,(\mu\mathrm{G})$	$r_c\,(\mathrm{kpc})$	$D_0\,(\mathrm{cm}^2/\mathrm{s})$	δ	$n_e\,(\mathrm{cm}^{-3})$
Draco dSph $d = 80\,(kpc)$	NFW, $r_s = 1\mathrm{kpc}$ $\rho_s = 1.40\mathrm{GeV/c}$	Exponential, Eq. (5.7)	1	0.22	$3 \cdot 10^{28}$	1/3	$1 \cdot 10^{-6}$

In order to do so, in Fig. 5.6, we represent the spatial distribution of I_ν for 1 TeV DM annihilating into different channels whose astrophysical parameters can be seen in Table 5.3. Comparing I_ν for different channels, the plot shows that major differences are established at inner regions of the galaxy. Although there are also differences in outer regions, they are accentuated by the logarithmic scale. Following the behaviour of astrophysical quantities studied in the previous section (mainly the magnetic field and the DM density profile), all the channels seem to be better detected at small angles where I_ν reaches its maximum. Boson and quark channels produce signals with a steeper slope in their spatial distribution than the leptonic channels whose emission spreads more diffusely.

Then, one method to disentangle lepton from boson or quark channel could be certainly studying the I_ν slope of the emission I_ν as Fig. 5.6. Even this strategy could be used to discriminate between different leptonic channels, such as e^+e^-, $\mu^+\mu^-$ and $\tau^+\tau^-$ thanks to their significant differences. Less optimistic is the picture for quark and boson channels. Even though their emission is higher than the lepton channels at the centre, their slope is only distinguishable at larger angles. In this sense, galactic edges would present a suitable location to distinguish channels thanks to the fact that I_ν falls with different curvatures depending on the channel. However, the reality is that no detector could reach the required sensitivity to measure I_ν at those distances. For this reason, we centred our attention on regions between 0.75^o and 1.25^o, inner window of Fig. 5.6, where the magnitude of the emission could be differentiated in different channels even though the slope is more straight (in logarithmic scale). Considering approximately an averaged sensitivity of $\sim 0.1\mu$Jy per beam (both green and blue bands) for SKA1-LOW at 350 MHz (limit between SKA1-LOW and SKA1-MID) after 1000 h of integration time, we observe that those bands are still narrower than the separation of I_ν between the group of boson channels and the group of quark channels, giving the idea that they may be distinguishable. However, this sensitivity would not be sufficient to disentangle particular channels in both groups of boson channels and lepton channels. In this regard, ZZ and W^+W^- channels present similar spatial distribution in I_ν as well as $c\bar{c}$ and $u\bar{u}$, $d\bar{d}$ and $s\bar{s}$ channels. Also, the $b\bar{b}$ channel presents a similar shape to the rest of the quarks at inner regions, however, its emission I_ν separates from the rest of quarks at $\theta \sim 1.2^\mathrm{o}$. The SKA would not be sensitive to detect it.

According to the above picture, the next step would be considering if there is any DM mass and any specific frequency in which this disentanglement becomes possible. Both quantities become mixed in Eq. (2.35). Thus the DM mass also affects the dependency of S_ν and I_ν with the frequency ν. In Fig. 5.7, we also represent the intensity I_ν against the angle θ in order to study how the spatial distribution changes both with the frequency (left panel) of the emission and the DM mass (right panel). First, in the left panel, we plot the specific intensity I_ν for 1 TeV DM particles annihilating into the $b\bar{b}$ channel. In this plot, we compare the extension of the diffuse emission at different frequencies that will be covered by SKA1-LOW (150 and 350 MHz) and SKA1-MID (350, 3050 and 14000 MHz). For high frequencies, the scope of the emission is confined in a small region while the signal at lower frequencies reaches larger angles. This indicates that low frequencies would be better detected than higher frequencies. The main

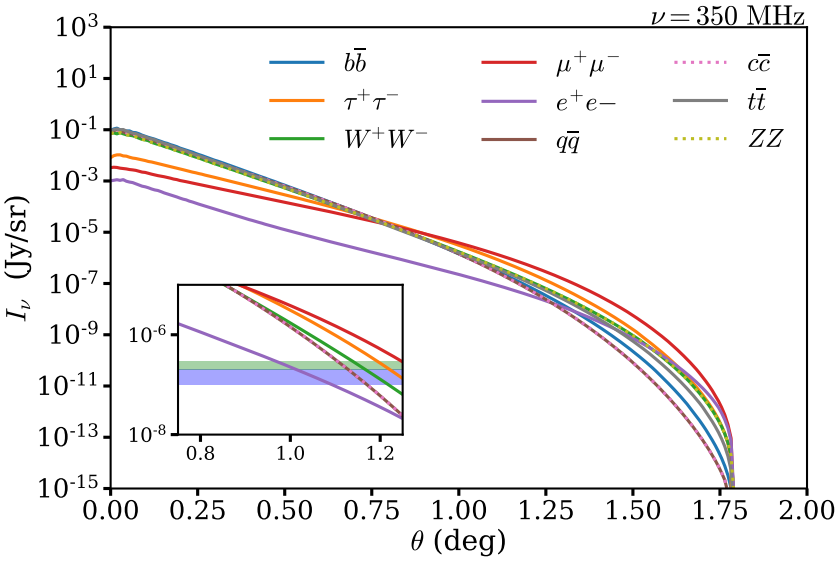

FIGURE 5.6: *Left panel:* specific intensity of the signal I_ν at 350 MHz for a $M = 1$ TeV DM model annihilating into SM particles. DM signals would present different slopes in their emission depending on the angle to the centre. Both bands in green and blue (inner panel) represent a hypothetical sensitivity per solid angle of around 0.1μJy/sr.

effects of increasing the frequency of detection are, first, a decrease of I_ν and, second, a slight change in the slope of the emission for outer regions. With respect to the former, the difference between $I_{150\,\mathrm{MHz}}$ and $I_{14\,\mathrm{GHz}}$ for the particular case of 1 TeV DM annihilating into $b\bar{b}$ reaches five orders of magnitude at the centre of Draco. Also, the fall of I_ν at high frequencies for outer regions shows that there is a certain number of e^+e^- that reach those angles with the sufficient energy to emit at those frequencies.

The role of the DM mass, as seen in Fig. 5.7 right panel, on the specific intensity I_ν is even more drastic. In a few words, higher DM masses have the effect of spreading the synchrotron signal along the galaxy. In the right panel, the dashed blue line corresponding to a DM with $M = 100$ TeV extends further than the mass $M = 100$ GeV, represented by the violet dashed line. If radio telescopes had extremely high sensitivities ($\sim$ 0.1 pJy), then constraining the DM mass until 100 TeV would be as simple as seen the extension of I_ν since it depends on the mass, as seen in Fig. 5.7, right panel. For larger DM masses, the synchrotron emission is less intense than for lighter candidates. However, this theoretical scenario is far from reality if one assumes that the sensitivity only would reach $\sim$ 0.1μJy. In order to show this, in Fig. 5.7 right panel, we plotted also a light blue line that corresponds to an estimated sensitivity for SKA1-LOW at 350 MHz of 0.1 μJy. For $M = 100\,\mathrm{GeV}$ and $M = 100\,\mathrm{TeV}$, violet and blue dashed lines reach the limit of sensitivity at smaller angles than $M = 1\,\mathrm{TeV}$ and $M = 10\,\mathrm{TeV}$.

In the study of the signal coming from different annihilation channels, we also represent the product νS_ν integrated over Ω_{DRACO}, with the purpose of identifying the best frequencies to detect DM.

5.3.2 Flux density study

In Fig. 5.8, we plot the quantity νS_ν coming from DM annihilating 100% into one specific channel. We replicated this plot for different channels grouping them in leptons (upper panel), quarks (middle panel) and bosons (lower panel).

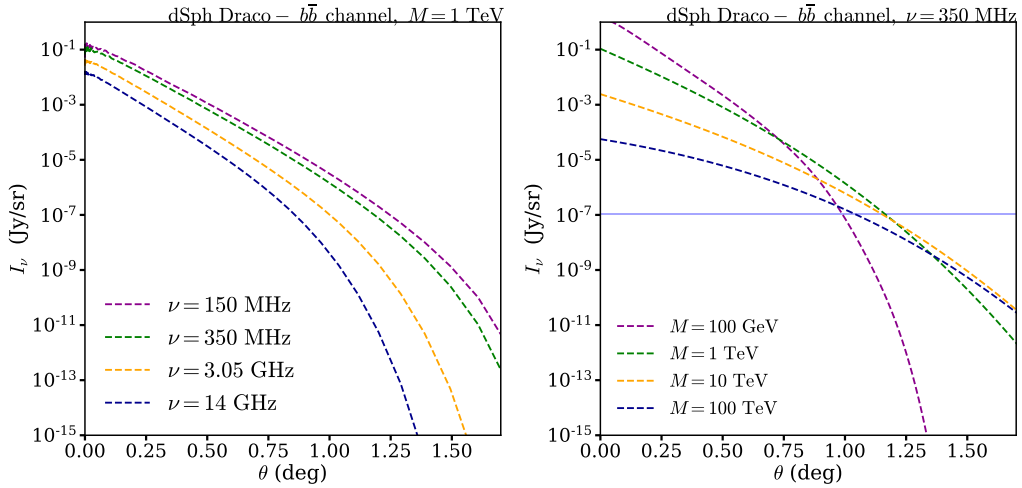

FIGURE 5.7: *Left panel:* specific intensity of the signal I_ν at different frequencies for a $M = 1$ TeV DM model annihilating into $b\bar{b}$ channel. The emission depends on the frequency showing that lower frequencies would be better detected than higher frequencies provided a DM signal. *Right panel:* the same specific intensity ($\nu = 350$ MHz) for $b\bar{b}$ channel and different DM masses. The emission for lighter candidates is more concentrated at the centre of the galaxy, while the emission for heavier candidates seem to be more spread. The bands in green and blue represents a hypothetical sensitivity per solid angle of around 0.1μJy/sr .

As a general behaviour for all the channels, the three panels show that the mass of the DM candidate clearly determines the maximum frequency of detection: different values of M shift the synchrotron signal to a different range of frequencies. According to this, lighter candidates would produce the emission at lower frequencies. On the contrary, heavier candidates would be able to reach up to seven orders of magnitude higher. For further details, in Table 5.4 we find the $\nu_{S_\nu^{\max}}$ for the emission of different channels at M equal to 100 GeV, 1 TeV, 10 TeV and 100 TeV. As explained in the previous section 5.2.1, $\nu_{S_\nu^{\max}}$ could vary with the strength of the magnetic field, however, a closer look of its tendency with the DM mass could be useful to determine the best strategy for detection. In this work, according to the discussion in Section 5.2, we fix the strength for the magnetic field in 1 μG.

To conclude, Fig. 5.8 and Table 5.4 show that sub-TeV DM, annihilating both in quark, lepton and boson channels, can be more easily detected at the range of radio and microwave frequencies, being quark channels situated on longer wavelength ($\sim$ MHz) than lepton and boson channels whose $\nu S_\nu^{\max}$ lies on the GHz range. In fact, after having fixed a DM mass, both lepton and boson channels are expected to have their maxima $\nu S_\nu^{\max}$ at larger frequencies than quark channels counterparts. Still, in radio and microwave frequencies, lighter TeV DM ($\sim$ 1 GeV) annihilating into quarks could be detected, although the $t\bar{t}$ channel has their peak of emission at 561 GHz reaching the far-infrared region, as well as lepton and boson channels. For DM particles ranging from 10 TeV to 100 TeV, the emission S_ν covers all the infrared spectrum until the soft-ultraviolet (and also until hard-ultraviolet only in the case of DM annihilating into e^+e^-).

Also, and according to detector sensitivities, as observed in Fig. 5.8, the DM mass affects the magnitude of the emission. That means that heavier candidates would present a weaker signal νS_ν than lighter candidates, demanding more sensitivity at higher frequencies to be detected. In Fig. 5.8, for lepton channels, the magnitude $\nu S_\nu^{\max}$ decreases about one and two orders of magnitude, between a DM candidate of 100 GeV and 100 TeV. In the case of DM annihilating into bosons, $\nu S_\nu^{\max}$ changes about one order of magnitude between a DM candidate

TABLE 5.4: Frequency at which S_ν is maximum. In this table, we suggest the best frequencies to detect DM candidates according to their masses. The $t\bar{t}$ channel is not opened when the dark matter mass is $M = 100\,\text{GeV}$ and, thus, the upper left table, does not have information. Moreover, for the $t\bar{t}$ at $M = 100\,\text{TeV}$, we have pointed out two maxima whose values are very similar but lie at different frequencies.

M	Annihilation	$\nu_{S_{\max}}$	M	Annihilation	$\nu_{S_{\max}}$
100 GeV	$q\bar{q}$	497.5 MHz	1 TeV	$q\bar{q}$	52.7 GHz
	$c\bar{c}$	746.1 MHz		$c\bar{c}$	52.7 GHz
	$b\bar{b}$	746.1 MHz		$b\bar{b}$	79.0 GHz
	$t\bar{t}$	-		$t\bar{t}$	561.1 GHz
	e^+e^-	52.7 GHz		e^+e^-	6 THz
	$\mu^+\mu^-$	19.1 GHz		$\mu^+\mu^-$	1.4 THz
	$\tau^+\tau^-$	7.9 GHz		$\tau^+\tau^-$	0.84 THz
	W^+W^-	131.0 GHz		W^+W^-	2.1 THz
	ZZ	121.2 GHz		ZZ	1.4 THz
M	Annihilation	$\nu_{S_{\max}}$	M	Annihilation	$\nu_{S_{\max}}$
10 TeV	$q\bar{q}$	2.4 THz	100 TeV	$q\bar{q}$	45 THz
	$c\bar{c}$	1.5 THz		$c\bar{c}$	45 THz
	$b\bar{b}$	1.4 THz		$b\bar{b}$	26 THz
	$t\bar{t}$	23.6 THz		$t\bar{t}$	14 THz, 1.32 PHz
	e^+e^-	711.7 THz		e^+e^-	71.1 PHz
	$\mu^+\mu^-$	129.6 THz		$\mu^+\mu^-$	13 PHz
	$\tau^+\tau^-$	67.7 THz		$\tau^+\tau^-$	4.2 PHz
	W^+W^-	123.2 THz		W^+W^-	7.34 PHz
	ZZ	124.6 THz		ZZ	7.34 PHz

with $M = 100\,\text{GeV}$ and $M = 100\,\text{TeV}$ while for quark channels variation turns out to be quite less than one order of magnitude.

In addition, the synchrotron signal produced by lepton, boson and quark channels could be identifiable since their dependence with the frequency is totally different, as seen in Fig. 5.8. Among them, the group more likely to be detected is the leptonic channel since the order of magnitude of $\nu_{S_\nu^{\max}}$ lies on larger values than the bosonic and quark channels. However, this signal is concentrated in a smaller range of frequencies unlike the other channels as it is possible to conclude by comparing the slope of νS_ν in the different panels of Fig. 5.8. For instance, for a DM mass of 100 GeV, that would produce the lowest frequency signal in our study, the emission in the leptonic channel would be centred at microwave - infrared, and a possible detection in low radio frequencies would be complicated due to the fall of emission. As we will see in the next section, the detection of the lepton channel is less suitable than the quark and bosons channels in the range of radio frequencies, even considering that $\nu S_\nu^{\max}$ for the lepton channel would be larger. Regarding the boson and quark channels, even though their emission is not so high as the lepton case, the signal νS_ν is more extended and thus, it could be detected in a larger range of frequencies. Similar to the study of I_ν performed in Fig. 5.6, S_ν would also allow us to disentangle between different lepton channels due to their distinct slopes, as seen in Fig. 5.8 upper panel. For boson channels, only if DM particles are not heavy ($\sim$ 100 GeV), the channel of annihilation is distinguishable. With the increase of the DM mass νS_ν becomes similar both in W^+W^- and ZZ channel. It should be kept in mind that the quantity S_ν is an indirect method to evaluate I_ν, the former is the integral of the latter over the solid angle. If two channels differ in the magnitude S_ν means that they must have different maps I_ν at some frequency.

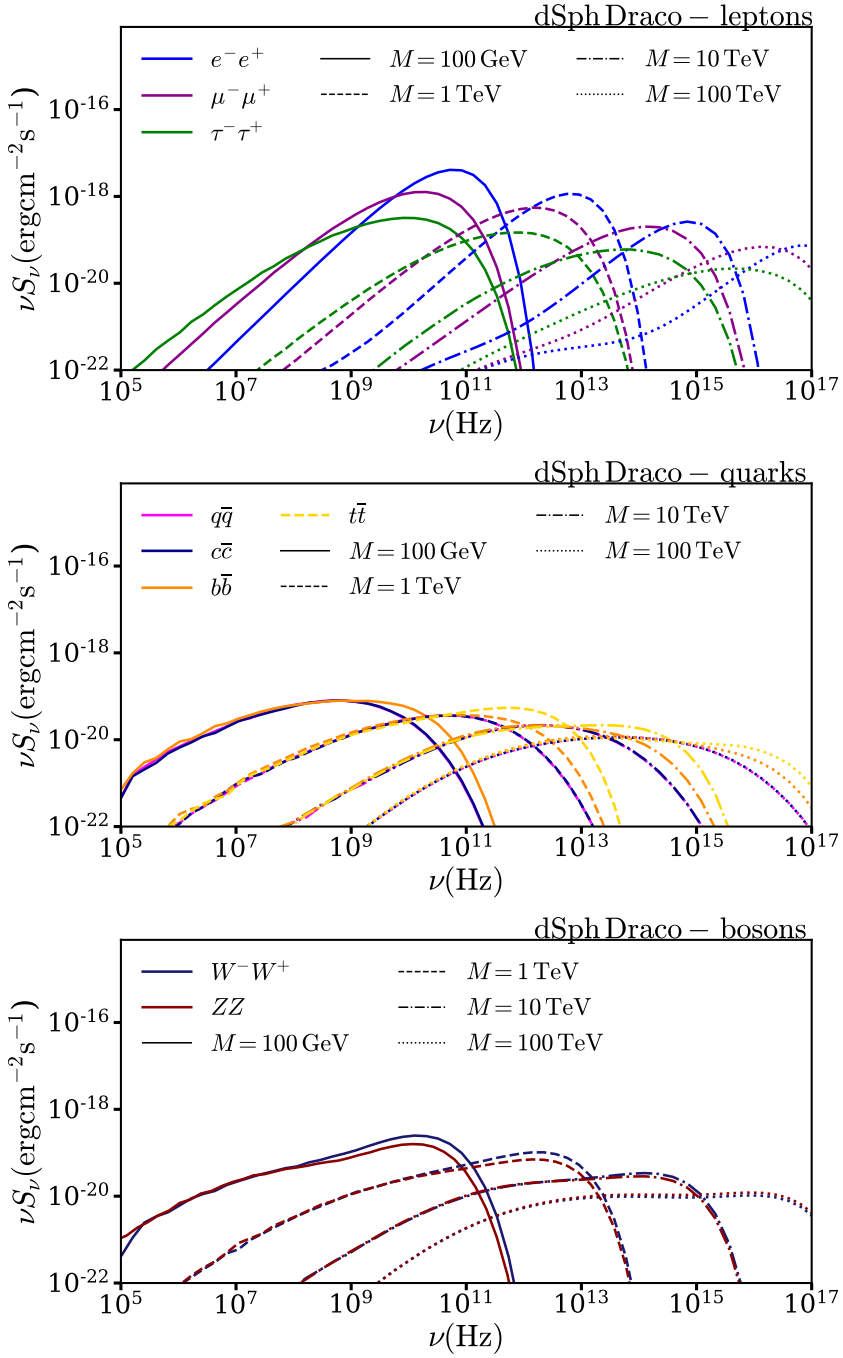

FIGURE 5.8: Flux density times frequency νS_ν for DM model annihilating into different channels and masses integrated over the angle Ω_{DRACO}. Synchrotron signals between groups of particles (boson, leptons and quarks) seem to present similarities. The most significant differences can be found in leptons. In Table 5.4, it has been represented the maxima νS_{max} for the different annihilation channels represented in this figure.

5.4 Sensitivity constraints on model-independent dark matter

Once we have set the fundamental pillars for synchrotron DM searches in dSphs, in this section, we present an analysis to put sensitivity constraints with the SKA on the DM parameters space, as to be provided by maps $\langle\sigma v\rangle$ vs. M. The section focuses on model-independent DM which means, as already mentioned, DM annihilating 100 % into one specific channel ($\beta = 1$).

5.4.1 Multi-TeV dark matter with the SKA

First of all, we will obtain the flux density S_ν for DM integrating over the solid angle Ω according to Eq. (2.41), as depicted in Fig. 5.9. Whereas the specific intensity I_ν focuses on the spatial distribution of the signal, the advantage of analysing the flux density S_ν is that such a quantity enables us to establish the best frequency range - and hence appropriate detectors - to measure signals from specific DM candidates. Thus, it allows the comparison of theoretical predictions with the data. For S_ν estimations, we shall also take into account angular limitations for the SKA largest angular scale, $\Omega_{\rm SKA}(\lambda)$ determined by Eq. (2.45) with the minimal baseline, $D_{\rm min}$.

In Fig. 5.9 upper-left panel, we calculate S_ν for two sub-TeV DM candidates (60 GeV and 500 GeV) annihilating into $b\bar{b}$ channel, once again using the thermally averaged cross section value $\langle\sigma v\rangle = 3 \cdot 10^{-26}{\rm cm}^3/{\rm s}$. Dashed lines correspond to S_ν integrated over the whole solid angle of Draco, $\Omega_{\rm DRACO}$, as in previous sections. There, solid lines correspond to the emission over the SKA largest angular scale, $\Omega_{\rm SKA}(\lambda)$. Dashed lines are represented with the aim of analysing the synchrotron emission relying only on the DM model and astrophysical features, while solid lines also take into account the sensitivity limitations of the radio detector, due to the fact that its largest angular scale depends on the frequency. At this stage, let us emphasise that the flux density shows a steepness at lower frequencies, implying that SKA1-LOW presents more competitive features to detect these kinds of candidates. As the DM mass increases, (see the dashed lines referred to the candidates $M = 60$ GeV and $M = 500$ GeV in the upper-left panel) the slope is less pronounced and SKA1-MID might detect the signal, although signatures start to be undetectable at high frequencies ≈ 1 GHz when $\Omega_{\rm SKA}(\lambda)$ is considered (solid lines).

Regarding the upper-right, lower-right and lower-left panels in Fig. 5.9, we present the SKA sensitivity to detect TeV-DM annihilating into $t\bar{t}$, $\tau^+\tau^-$ and W^+W^- channels, respectively. In those panels, it is possible to observe that higher masses seem to be more easily detected by the SKA1-MID. Also there, for higher DM masses, the slope becomes smoother at low frequencies and the signal S_ν turns into an almost straight line. Basically, this occurs because heavier DM allows e^+/e^- to achieve higher energies and thus the frequency of the peak, proportional to the kinetic energy E (see Eq. 2.38), would be displaced to higher frequencies. The lower-right panel corresponding to $\tau^+\tau^-$ is the most unfavourable case for detection to occur due to the fact that among 10 and 100 hours would be necessary to detect that channel for a DM candidate with a mass of 1 TeV. Taking into consideration the $S_{\rm min}$ limit as obtained by Eq. (2.42), lower-right panel shows that the mass of 10 TeV remains unreachable even if the integration time τ increases in one order of magnitude (around 5000 hours would be needed). The $t\bar{t}$ and W^+W^- channels, as presented on the upper-right and lower-left panels respectively, display that such channels seem to be better detected by SKA1. In fact, for those two channels, within a time integration of 10 hours, 1 TeV DM particles would be detected. Nevertheless, for DM masses close to 10 TeV, 1000 hours would be needed.

One result that can be seen by observing the four panels in Fig. 5.9 is that integrating over $\Omega(\lambda)_{\rm SKA}$ instead of integrating over $\Omega_{\rm DRACO}$ would provide the same DM sensitivity constraints. Indeed, the most sensitive SKA band, SKA Band3 [1.65-3.05] GHz, lies at frequencies lower than

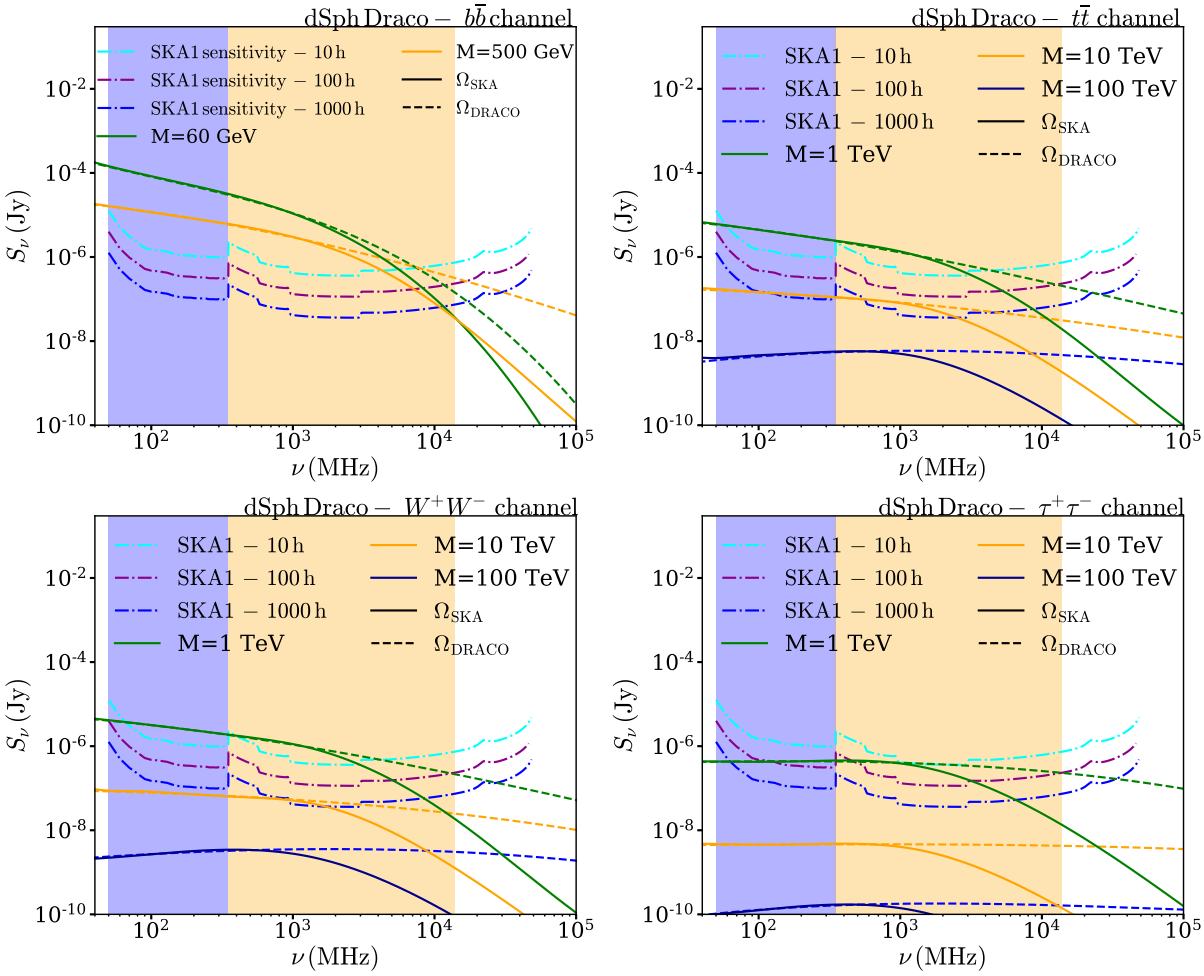

FIGURE 5.9: Flux density radio emission S_ν for several annihilation channels with the canonical thermally averaged cross section of $3 \cdot 10^{-26}\text{cm}^3/\text{s}$ and $\beta_j = 1$ [199]. Colour bands correspond to the energy (frequency) range covered by SKA1-LOW (blue) and SKA1-MID (orange), respectively. Dash-dotted lines represent SKA1 sensitivity for different integration times τ, 10, 100 and 1000 hours, and have been obtained following Ref. [348]. Solid lines represent the flux density of radiation integrated over a solid angle $\Omega_{\text{SKA}}(\lambda)$ while dashed lines correspond to the solid angle Ω_{DRACO}. *Upper-left panel:* Sub-TeV DM annihilating into $b\bar{b}$ channel with masses of 60 GeV and 500 GeV according to Ref. [351]. *Upper-right and lower-right/left panels:* Flux density of radiation for DM annihilating into $t\bar{t}$, $\tau^+\tau^-$ and W^+W^- channels. The first two scenarios would be detectable for masses beyond 10 TeV, while the $\tau^+\tau^-$ channel is less favoured to be detected and smaller DM masses would be required. Also, for these three panels lighter DM candidates seem to be detected better with SKA1-LOW, given the fact the flux density is higher at low frequencies. For heavier masses candidates, the flux density turns into an almost-flat straight line provided an integration performed over Ω_{DRACO}.

that one in which the SKA limitations start. In order words, solid lines begin to be suppressed at frequencies greater than Band3 (Fig. 5.9).

Lastly, Fig. 5.9 suggests that provided $M = 100$ TeV or heavier masses, SKA1 would be inadequate to measure radio signals from $t\bar{t}$, W^+W^- and $\tau^+\tau^-$ channels, since the necessary integration time τ would have to extend in several orders of magnitude.

5.4.2 Sensitivity constraints

In Fig. 5.10, we have considered a detectability diagram $\langle\sigma v\rangle$ vs. M. Therefore, we analyse the SKA1-LOW and SK1-MID sensitivities in the detection of model-independent DM candidates, annihilating into $b\bar{b}$, $\tau^+\tau^-$ and W^+W^- channels. The magnetic field we use for this study is exponential, according to Eq. (5.7), and the DM density profile selected is an NFW according to Eq. (5.5). The lines in orange suggest that SKA1-MID will cover a larger parameter space than SKA1-LOW if an integration time of 1000 hours is considered. As has already been mentioned, SKA1-MID appears to be more appropriate to find heavier candidates while SKA1-LOW becomes suitable for lighter ones. Indeed, as already mentioned, although SKA1-MID results more sensitive than SKA1-LOW, light DM ($\sim 100\,$GeV) presents a slope more pronounced in S_ν at low frequencies in comparison with heavier candidates ($\sim 1\,$TeV), and thus, better detected in that frequency range. It is possible to see this fact in Fig. 5.10 for masses around 0.1 TeV in the channels W^+W^- and $b\bar{b}$. Indeed, for the $b\bar{b}$ channel (dash-dotted line), SKA1-LOW reaches smaller cross sections $\langle\sigma v\rangle$ (around $1\cdot10^{-28}$ cm^3/s) than SKA1-MID whose scope becomes $9\cdot10^{-27}$ cm^3/s. In the case of W^+W^- channel the difference is smaller (less than $0.5\cdot10^{-27}$ cm^3/s). In the case of the $\tau^+\tau^-$ channel, we do not observe differences between measuring S_ν with SKA1-LOW and SKA1-MID at masses around 0.1 TeV. However, as in the cases for W^+W^- and $b\bar{b}$ channels, the separation of the blue and orange dotted lines (Fig. 5.10) would start at lower masses, being SKA1-LOW more sensitive than SKA1-MID at low masses.

Conversely, by observing the intersection between the lines in blue and orange with the black dashed, it is possible to determine the maximum mass detected by SKA1 in the limit of thermal relic DM. Indeed, the analysis in Fig. 5.10 suggests that SKA1-LOW would be able to detect thermal relic candidates with a mass up to around 2 TeV for the $\tau^+\tau^-$ channel, that would extend until 3 TeV for SKA1-MID. In the case of the W^+W^- channel, SKA1-LOW could measure a mass up to 7 TeV, while SKA1-MID would achieve $M = 11\,$TeV. Finally, the channel that presents the best circumstances to be detected in the limit of thermal relic density becomes $b\bar{b}$, reaching a mass up to 9 TeV with SKA1-LOW and a mass equal limit up to 14 TeV. For comparative purposes, in green, we present the limits obtained in [377] for antiprotons. In this regard, SKA1 will be able to improve such limits in more than two orders of magnitude in $\langle\sigma v\rangle$.

In addition, in Fig. 5.11, we also compute a detectability plot $\langle\sigma v\rangle$ vs. M for SKA1 after 1000 hours. This time with the same NFW density profile but with a constant magnetic field, $B(r) = B = 1\mu$G. The channels analysed as part of the study are W^+W^- and $b\bar{b}$ for comparative purposes. This figure reveals a quite different picture than the previous one.

- In the first place, the lowest thermally averaged cross section that both SKA1-LOW and SKA1-MID would measure considering a constant magnetic field lies on $2\cdot10^{-30}$ cm^3/s and $3\cdot10^{-30}$ cm^3/s for a 0.1 TeV DM candidate annihilating into W^+W^- (solid line).

- In contrast, in the case of the channel $b\bar{b}$ (dash-dotted line), the limit in the thermally averaged cross section for 0.1 TeV wouold be $7\cdot10^{-31}$ cm^3/s and $1\cdot10^{-30}$ cm^3/s for SKA1-LOW and SKA1-MID respectively. These values in $\langle\sigma v\rangle$ for a constant magnetic field, show a difference of around two orders of magnitude with respect to the previous exponential study, in which $\langle\sigma v\rangle \sim 10^{-28}$ cm^3/s.

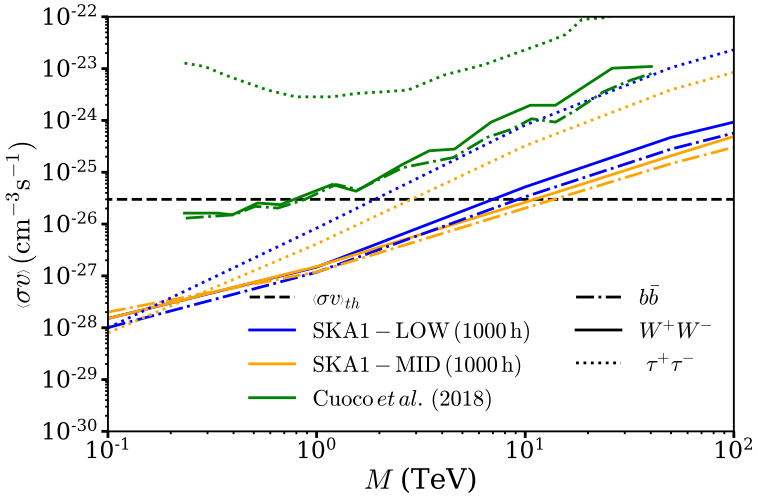

FIGURE 5.10: Sensitivity constraints on the DM particle cross section for model-independent DM annihilating into $b\bar{b}$, $\tau^+\tau^-$ and W^+W^- channels with SKA1 [199] as a paradigmatic example of leptonic, quark and boson channels. For this detectability diagram, it has been considered the exponential magnetic field described in Eq. (5.7). The solid angle considered to set this map is $\Omega_{\mathrm{SKA}}(\lambda)$ with a minimal baseline of 30 m. The lines in blue would be detected within 1σ of confidence level by SKA1-LOW while the lines in orange would be detected by SKA1-MID, after 1000 hours of integration time. For comparison purposes, we plot green lines according to the upper limits from cosmic-ray antiproton data [377]. The horizontal dashed black line represents those DM candidates with $\langle\sigma v\rangle_{th} \equiv \langle\sigma v\rangle = 3\cdot10^{-26}$ cm^3/s according to the limit for thermal relics. For example, the sensitivity constraint for the W^+W^- channel lies close to $M = 7$ TeV for SKA1-LOW and $M = 12$ TeV for SKA1-MID.

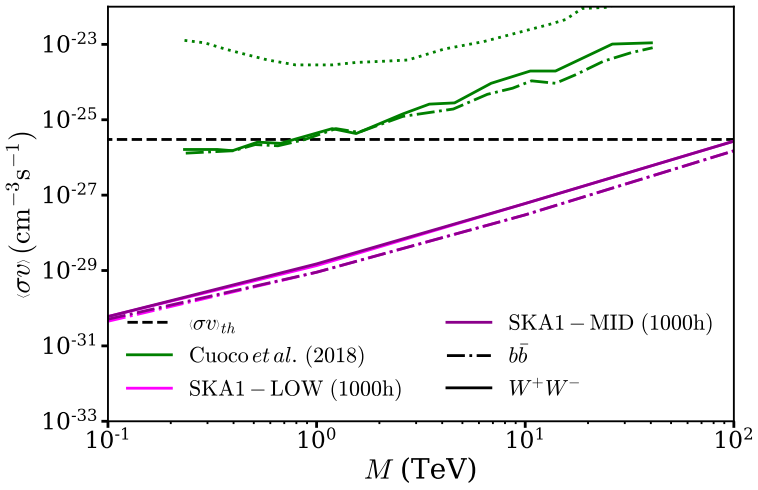

FIGURE 5.11: Sensitivity constraints on the DM particle cross section for model-independent DM annihilating into $b\bar{b}$ and W^+W^- channels with SKA1. For this detectability plot, it has been considered a constant magnetic field equal to 6 μG. The solid angle considered to set this map is $\Omega_{\mathrm{SKA}}(\lambda)$ with a minimal baseline of 30 m. The lines in pink would be detected within 1σ of confidence level by SKA1-LOW while the lines in purple would be detected by SKA1-MID, after 1000 hours of integration time. For comparison purposes, we plot green lines according to the upper limits from cosmic-ray antiproton data [377]. The horizontal dashed black line represents those DM candidates with $\langle\sigma v\rangle = 3\cdot10^{-26}$ cm^3/s according to the limit for thermal relics.

TABLE 5.5: Sensitivity constraints for SKA1-LOW and SKA1-MID when $\langle\sigma v\rangle = 3\cdot 10^{-26}\text{cm}^3/\text{s}$, assuming an exponential (Eq. 5.7) and a constant magnetic field ($B = 1\,\mu G$). This table has been obtained by observing Fig. 5.11, where a sensitivity analysis has been performed for the channels W^+W^-, $b\bar{b}$ and $\tau^+\tau^-$.

Detector	Magnetic field	Channel	M (TeV)
SKA1-LOW	Constant	W^+W^-	>100
		$b\bar{b}$	>100
	Exponential	$\tau^+\tau^-$	1.90
		W^+W^-	7.09
		$b\bar{b}$	9.36
SKA1-MID	Constant	W^+W^-	>100
		$b\bar{b}$	>100
	Exponential	$\tau^+\tau^-$	2.87
		W^+W^-	11.07
		$b\bar{b}$	13.83

• In addition, the intersection between the black dashed line and the pink and violet lines occurs for masses close to 100 TeV, a much higher limit than in the exponential case lied close $\sim$ 10 TeV. This difference reflects the uncertainty produced in the sensitivity constraints due to the lack of information about the magnetic field structure. Considering such an intersection in Fig. 5.11, a DM candidate annihilating into either W^+W^- or $b\bar{b}$ channels with a thermally averaged cross section $\langle\sigma v\rangle = 3\cdot 10^{-26}$ cm^3/s could be detected by SKA1-LOW and SKA1-MID even if such a candidate would have a mass greater than 100 TeV.

5.5 Synchrotron emission from dark matter candidates in Draco dSph

One of the most remarkable potentialities in DM indirect searches lies in determining the compatibility of different observations. Indeed, the variety of studies at different regions of the sky or with different DM annihilation products allows to determine whether a DM candidate able to explain some of the excesses, e.g. in the Milky Way, may be excluded in other targets. Following this reasoning, one question would be if studying dSphs would confirm the validity of some specific DM candidates in agreement with the signatures in Milky Way, or on the contrary, if such target would rule them out. According to this, we focus on very-high-energy γ-rays ($E \geq$ 100GeV) coming from the GC. In particular, from the γ-ray fluxes measured by the High Energy Stereoscopic System (HESS) from the source J1745-290 in the GC region [378] (Section 5.5.1). In section 5.5.2, we set some sensitivity constraints on Brane-World theories together with the branon parameter space.

In this section, we provide some prospects for the synchrotron emission both for HESS J1745.6-290 candidates and also for branons from Brane-World scenarios. Moreover, we study the role of the SKA1 in terms of sensitivity for futures searches in order to shed light on the question: Is the SKA sensitive enough to put constraints on 'Milky Way DM candidates' in dSphs?

5.5.1 HESS J1745.6-290 dark matter candidates

From 2004, measurements of the GC have been reported from CANGAROO, VERITAS, HESS, and MAGIC finding very-high-energy γ-rays. The increment of statistics in the measurements, allowed to report significant deviations from the usual power-law spectrum and the

TABLE 5.6: DM candidates in agreement with HESS J1745 − 290 according to [378]. Both the masses and their uncertainties are taken from [378]. All the models annihilate 100% in the channel presented below. The thermally averaged cross section is $\langle \sigma v \rangle = 3 \cdot 10^{-26} \mathrm{cm}^3/\mathrm{s}$

Annihilation channel	M (TeV)
e^+e^-	7.51 ± 0.11
$\mu^+\mu^-$	7.89 ± 0.21
$\tau^+\tau^-$	12.4 ± 1.3
$u\bar{u}$	27.9 ± 1.8
$d\bar{d}$	42.0 ± 4.4
$s\bar{s}$	53.9 ± 6.2
$c\bar{c}$	31.4 ± 6.0
$b\bar{b}$	82.0 ± 12.8
$t\bar{t}$	87.7 ± 8.2
W^+W^-	48.8 ± 4.3
ZZ	54.5 ± 4.9

presence of a curvature in the energy spectrum of photons [300, 319, 321, 328, 379–386]. The energy spectrum detected over 2004, 2005 and 2006 seems to show a cut-off as a distinctive feature. The cut-off seems to be likely from a photon source, and not from interstellar absorption. This cut-off has been usually described by a power law with an exponential cut-off:

$$\frac{d\Phi_\gamma}{dE} = \Phi_0 \left(\frac{E}{\mathrm{GeV}}\right)^{-\Gamma} \exp\left(-E/E_{\mathrm{cut}}\right) \tag{5.9}$$

or a broken power-law spectrum

$$\frac{d\Phi_\gamma}{dE} = \Phi_0 \left(\frac{E}{\mathrm{GeV}}\right)^{-\Gamma_1} \left[1 + \left(\frac{E}{E_{\mathrm{break}}}\right)^{\Gamma_2 - \Gamma_1}\right]^{-1} \tag{5.10}$$

The nature of the aforementioned photons source remains not clear. The usual astrophysical proposal is that such a γ-ray signal comes from either the propagation of cosmic rays in the shell of Sgr A East SNR or from thee acceleration of protons to TeV energies by turbulent magnetic fields in the surroundings of Sgr A*. Such models proved to be capable of fitting γ-ray signals from the J1745 − 290 GC source as measured by HESS, prevailing over more exotic proposals concluding that the spectral features of these γ-rays disfavoured a DM origin [383, 384]. However, more recently combined analyses of Fermi-LAT and HESS data have opened new interpretations [328, 378, 385], through a power law background and γ-rays coming from DM annihilation:

$$\frac{d\Phi_\gamma}{dE} = B_{\mathrm{bkg}}^2 \left(\frac{E}{\mathrm{GeV}}\right)^{-\Gamma} + \frac{d\Phi_\gamma^{\mathrm{DM}}}{dE} \tag{5.11}$$

Since the energy cut-off lies on the order of TeV, all the DM candidates fitting HESS J1745 − 290 would have masses in that range of energies according to the cut-off imposed by the energy-momentum conservation in the DM annihilation. In the following, we shall study the radio emission counterpart of those multi-TeV DM candidates fitting the HESS data and evaluate the sensitivity of SKA1 in their possible detection (Table 5.6).

In Fig. 5.12, we calculate S_ν for the multi-TeV DM candidates presented in Table 5.6. In the right panel, leptonic and bosonic channels have been plotted with solid lines, while in the left panel quark channels were represented also with solid lines. The sharp fall of S_ν in all channels corresponds to $\Omega_{\rm SKA}(\lambda)$ limited by the minimal baseline of 30 m. According to Fig. 5.12, all the solid lines lie below the sensitivity curve after 1000 hours of integration time. This indicates that none of the HESS candidates would be detected by the SKA1 after 1000 hours of integration time τ. Even the apparent detection of the candidate with the highest S_ν, $u\overline{u}(M = 27.9\,\text{TeV})$, would not be possible after $\tau = 5000$ hours, time that is not considered for SKA1 and thus, these mass would be inaccessible. This result could be anticipated for the case of the candidates $W^+W^-(M = 48.8\,\text{TeV})$, $b\overline{b}(M = 82.6\,\text{TeV})$ and , $\tau^+\tau^-(M = 12.4\,\text{TeV})$ since those masses clearly exceeds the limits we obtained in Fig. 5.10.

In addition, at this stage it should be interesting to remark the case of the candidates $e^+e^-(M = 7.51\,\text{TeV})$, $\mu^+\mu^-(M = 7.89\,\text{TeV})$ and $\tau^+\tau^-(M = 12.4\,\text{TeV})$. According to Fig. 5.8, Section 5.3, we showed that leptons show higher S_ν in their maximum of emission than the rest of the channels. However, SKA1 shows more difficulties to detect leptons (for example, $\tau^+\tau^-$) than other channels, as was suggested in the diagram $\langle\sigma v\rangle$ vs. M in Fig. 5.10. Indeed, Fig. 5.12 left panel shows that quarks seem to be more easily detected than leptons, even if the former are heavier ($e^+e^-(M = 7.51\,\text{TeV})$ and $u\overline{u}(M = 27.9\,\text{TeV})$, for example). This is an example of the detector limitations at the time of searching for a DM signal; the synchrotron radiation S_ν is larger for leptons (Fig. 5.8) but the detector range of frequencies, together with the $\Omega_{\rm SKA}(\lambda)$ limits, does not seem the best option for these channels. Considering that SKA would not be able to detect the DM candidates in agreement with HESS J1745 − 290, we will introduce an astrophysical justified boost factor for Draco and study the detectability of those candidates once again. In the following, we will consider two cases. First a boost factor due to DM substructures in halos, and second, a boost due to the presence of an IMBH at the centre of the dwarf spheroidal.

a) The role of the boost factor I: substructures in dark matter halos

According to the analysis just above, none of the HESS J1745 − 290 GC candidates can be constrained by SKA1. Thus our second line of reasoning will consist of including a justified boost factor due to DM subclumps in order to know if such candidates could be detected in a reasonable time. Indeed, DM boosters have been extensively considered in several works of to DM indirect searches, including subclumps [387] in DM halos, Sommerfeld enhancement [388] and BH-spikes [389]. The introduction of such a boost factor is accompanied by uncertainties related to the brief discussion we raised in Section 5.2.

As a first approximation, some works have calculated the substructure boost assuming that structural properties, as the concentration parameter $C(M)$, are the same both for the halos and subhalos with the same mass [390]. Even assuming this, some works have differed considerably in the boost factor value. For instance, the description in [387] following [391], implies a moderate multiplicative boost factor of 3.43 for Draco-like dShps for DM. However large boost factors have been proposed in [392] or [393] (the latter with a boost ~ 20 for dwarf galaxies with similar masses to the Draco DM halo). The main discrepancies lie on the low resolution and the lack of simulations for low mass halos (below $\sim 10^9 - 10^{10}\,h^{-1}M_\odot$). Thus, in this regime the concentration parameter $C(M)$ is sometimes extrapolated by a power law along many orders of magnitude enlarging the boost factor. To this it should be added that boost factors are extremely sensitive to the concentration mass.

In this work, as a first approximation, we choose the value 3.43 taken explicitly in [387] following [391], as a multiplicative factor of the quantity S_ν. In this case, the concentration mass is not

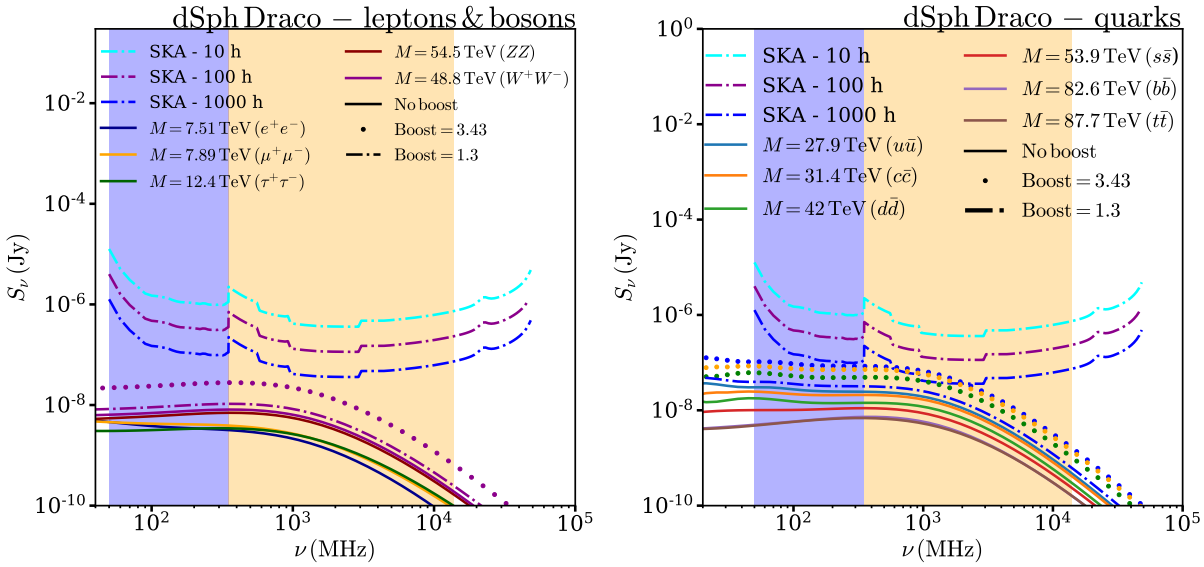

FIGURE 5.12: Flux density radio emission over $\Omega_{\mathrm{SKA}}(\lambda)$ for DM candidates that would be in agreement with γ-ray signals from J1745 − 290 GC as detected by HESS [378]. In all cases the canonical thermally averaged cross section $3 \cdot 10^{-26}\mathrm{cm}^3/\mathrm{s}$ is considered. As in Fig. 5.9 colour bands correspond to the energy (frequency) range covered by SKA1-LOW (blue) and SKA1-MID (orange) respectively. Dash-dotted lines represent SKA1 sensitivity (1σ confidence level) for different integration times τ of 10, 100 and 1000 hours. *Left panel:* leptonic and bosonic channels without boost factor (solid lines), with a boost factor of 1.3 (dash-dotted line) and with a boost factor of 3.43 (dashed line) for W^+W^- channel ($M = 48.8$ TeV) only. Results show that SKA1 would not detect any of the candidates, even if a boost factor is included. *Right panel:* quark channels without boost factor (solid lines), with a boost factor of 1.3 (dash-dotted line) and with a boost factor of 3.43 (dashed line) for channels $u\bar{u}$ ($M = 27.9$ TeV), $d\bar{d}$ ($M = 42$ TeV) and $s\bar{s}$ ($M = 53.9$ TeV) only. Results show that $u\bar{u}$ ($M = 27.9$ TeV), $d\bar{d}$ ($M = 42$ TeV) and $c\bar{c}$ ($M = 31.4$ TeV) channels would be eventually detected after an integration time of 1000 hours (or longer).

TABLE 5.7: Detectability of dark matter candidates (1σ confidence level) for HESS J1745-290 from Ref. [378] after 1000 hours with SKA-Phase 1. In this table, we present which candidates could be detected with a Boost of 3.43 and a Boost of 1.3. In the case in which a particular channel is potentially measured, we indicate the SKA1 module able to detect it, otherwise, we use a hyphen.

Annihilation channel	M (TeV)	Boost = 3.43	Boost = 1.3	Detector
e^+e^-	7.51 ± 0.11	No	No	-
$\mu^+\mu^-$	7.89 ± 0.21	No	No	-
$\tau^+\tau^-$	12.4 ± 1.3	No	No	-
$u\bar{u}$	27.9 ± 1.8	Yes	No	SKA1-MID
$d\bar{d}$	42.0 ± 4.4	Yes	No	SKA1-MID
$s\bar{s}$	53.9 ± 6.2	No	No	-
$c\bar{c}$	31.4 ± 6.0	Yes	No	SKA1-MID
$b\bar{b}$	82.0 ± 12.8	No	No	-
$t\bar{t}$	87.7 ± 8.2	No	No	-
W^+W^-	48.8 ± 4.3	No	No	-
ZZ	54.5 ± 4.9	No	No	-

extrapolated but fitted following a combination of the $c(M)$ parametrisation from [391] and comparing with simulations at low masses (Ishiyama+13, Moore+01, Colin+04, Via Lactea II, Anderhalden & Diemand 13, Diemand+05). In addition, we also compute S_ν with a smaller multiplicative factor $\sim$ 1.3 (if one assumes $M_{\rm vir} = 7 \cdot 10^7 M_\odot$ [387]) times the smooth halo contribution. This boost factor is estimated from recent considerations of tidal stripping effects on the subhalo population [373].

In Fig. 5.12, we plot S_ν for DM candidates which would be in agreement with the emission J1745 $-$ 290 GC γ-ray signal detected by HESS, as mentioned in this section. There, quarks channels are represented in the left panel, while bosonic and leptonic channels appear in the right panel. As a matter of fact, DM substructures in the DM galactic halo have been considered to plot 5.12. A boost of 1.3, that includes tidal stripping effects, would not render some candidates detectable. However, the value of 3.43 would be enough to shift the signal to sensitive regions. Fig. 5.12 shows that model-independent DM candidates annihilating in either bosonic or leptonic channels would not be in the sensitive region of SKA1 after 1000 hours of integration, assuming an optimistic boost factor of 3.43 due to halo substructures. Moreover, provided a boost of 3.43, DM candidates annihilating into quark channels $u\overline{u}$ ($M = 27.9$ TeV), $d\overline{d}$ ($M = 42$ TeV) and $c\overline{c}$ ($M = 31.4$ TeV) would be potentially detected after1000 hours of integration time. In this case, as the figure shows, the astrophysical boost due to clumps in the dSph halo is unable of boosting the signals to SKA1-sensitive regions. Even if the integration time increases to tens of thousands of hours, the SKA1 sensitivity able to detect eventual signals from such candidates would not be reached. Finally, let us conclude this analysis by highlighting again that the detection of candidates described in this section lies near the limit of the SKA1 sensitivity curves $\sim 0.1\mu$Jy in SKA1-MID Band3, and thus, an accurate description of the halos and its substructures would make an important difference in this study.

b) The role of the boost factor II: Intermediate-mass black hole

In the present section, we analyse how the presence of a BH in the centre of Draco would result in an enhancement of the radio emission (both S_ν and I_ν) by some orders of magnitude. Indeed, several authors have claimed that the presence of a BH at the Milky Way GC may cause an enhancement in the multi-messenger signals [394–397]. This fact has been extrapolated to the case of dSphs. Even though there are no strict experimental measurements about the presence of BH at the centre of Draco dSph, some works have discussed this possibility and evaluated the expected signals from DM annihilating in this novel scenario [204, 389]. The main support of this reasoning lies in certain observational evidence, mostly based on AGN tracers, which suggest the existence of an IMBH in dwarf galaxies [398–400]. Dwarf galaxies should not be confused with dSphs, the latter being a particular case inside that group. However, AGN tracers have been also found when dwarf galaxies lie in the low-mass and low-luminosity limits [398–400]. For the specific case of Draco, since its environment is not a gas-rich one, it would be reasonable to assume that such a BH would not be in an accreting luminous phase [204].

Consequently, although being aware that this scenario has not been strictly proved, in the following we shall assume the existence of BH in dSphs and analyse the possibility of Draco hosting a BH at its centre with a mass $M_\bullet$ of $10^3 M_\odot$ or $10^5 M_\odot$, according to [398–400]. The purpose of this study is to evaluate how the presence of a BH would change the synchrotron signals. In addition, this would allow us also to provide the rudiments, to be further discussed in Section 5.5.2, on how the BH inclusion can enlarge the parameter space of both model-independent and Brane-World DM candidates to be detected at radio frequencies.

The methodology to incorporate the BH effect in DM indirect detection studies relies on the study of how the DM density profile changes when the BH is located at the centre of the DM

halo [401]. Usually, a piecewise function for the DM density profile delineates an inner region where the BH may expose its gravitational influence, characteristically, for radius smaller than $r_{\rm cut}$. At this radius, in which the total mass of the density profile results in $2M_\bullet$, being $M_\bullet$ the BH mass. For higher distances, a conventional DM density distribution is expected. With the aim to approach to that, authors in [401] studied the case where a BH grows adiabatically and thus, the inner part of the DM profile $\rho(r) \sim r^{-\gamma}$ is adiabatically contracted into a final profile $\rho(r) \sim r^{-\gamma_{\rm sp}}$, with $\gamma_{\rm sp} > \gamma$. Consequently, the modified DM density profile $\rho_{\rm DM+BH}(r)$ in a presence of a BH becomes

$$\rho_{\rm DM+BH}(r) = \begin{cases} \frac{M}{\langle\sigma v\rangle(t-t_f)} & \text{if } r < r_{\rm cut} \\ \rho_{\rm DM}(r_{\rm sp}) \left(\frac{r}{r_{\rm sp}}\right)^{-\gamma_{\rm sp}} & \text{if } r_{\rm cut} \leq r < r_{\rm sp} \\ \rho_{\rm DM}(r) & \text{if } r \geq r_{\rm sp}\,, \end{cases} \tag{5.12}$$

with $\rho_{\rm DM}(r)$ being the standard DM distribution, i.e., without considering a BH. In this analysis, we shall consider an NFW profile and therefore $\rho_{\rm DM}(r) = \rho_{\rm NFW}(r)$. In the region $r < r_{\rm cut}$, Eq. (5.12) presents an upper limit, $\frac{M}{\langle\sigma v\rangle(t-t_f)}$, in the DM density profile $\rho_{\rm DM+BH}(r)$ on account of an effective DM annihilation ratio. In such formula, M is the mass of DM and $(t - t_f)$ holds for the BH age, taken as 10^{10} yr for Draco. Moreover, the boundary among the aforementioned upper limit $\frac{M}{\langle\sigma v\rangle(t-t_f)}$, and the DM density in the region in which the BH has no influence ($r \geq r_{\rm sp}$) is progressively connected by a power law with exponent $\gamma_{\rm sp} = (9 - 2\gamma)/(4 - \gamma)$. A wide discussion on how the presence of a BH in Draco would influence the multi-wavelength study can be found in [204]. As observed in Eq. (5.12), the BH effects become a spike in the DM profile.

Considering that masses for a BH bigger than $10^7 M_\odot$ are dynamically excluded (see the discussion in Section V of Ref. [204]), in the following we shall evaluate a BH with masses of either $10^3 M_\odot$ or $10^5 M_\odot$ following [398–400]. In Fig. 5.13 left panel, we study the specific intensity I_ν for a 1 TeV model-independent DM candidate annihilating into $b\bar{b}$ channel. This plot shows an enhancement of I_ν near the centre of Draco on account of the BH presence $10^3 M_\odot$. For outer regions, the specific intensity I_ν tends to the same limit for both the cases with and without BH. Moreover, considering the SKA1-LOW and SKA1-MID resolutions at 350 MHz, $\theta_{\rm res} = 0.001^{\rm o}$ and $\theta_{\rm res} = 2.5 \cdot 10^{-4\rm o}$ respectively (given by their maximum baselines), Fig. 5.13 left panel shows that both detectors may resolve part of the structure of the spike of the emission due to the BH.

With respect to the flux density S_ν, in Fig. 5.13 right panel, we analyse the synchrotron radiation for a model-independent DM candidate annihilating into W^+W^- channel with $M = 100$ TeV. As can be observed there, even assuming 1000 h of integration time τ, SKA1 would not be able to measure any signal from such a DM mass. Nevertheless, considering the smallest BH mass of our study ($M_\bullet = 10^3 M_\odot$), a DM mass of $M = 100$ TeV would be reachable in less than 10 hours for both SKA1-LOW and SKA1-MID. For a BH mass of $10^5 M_\odot$, the integration time τ would become shorter. Accordingly, DM indirect studies around a central BH would be a suitable region to be considered by SKA1 focusing on TeV DM and heavier candidates. Moreover, as observed in Fig. 5.13 right panel, no qualitative differences can be seen in the shape of the emission among the cases with and without a BH.

5.5.2 Branons and extra-dimensional theories

In this section, we study the SKA1 sensitivity to detect branons DM in Draco dSph. To that end, we have focused on the flux density S_ν from TeV branon annihilation. The probabilities of

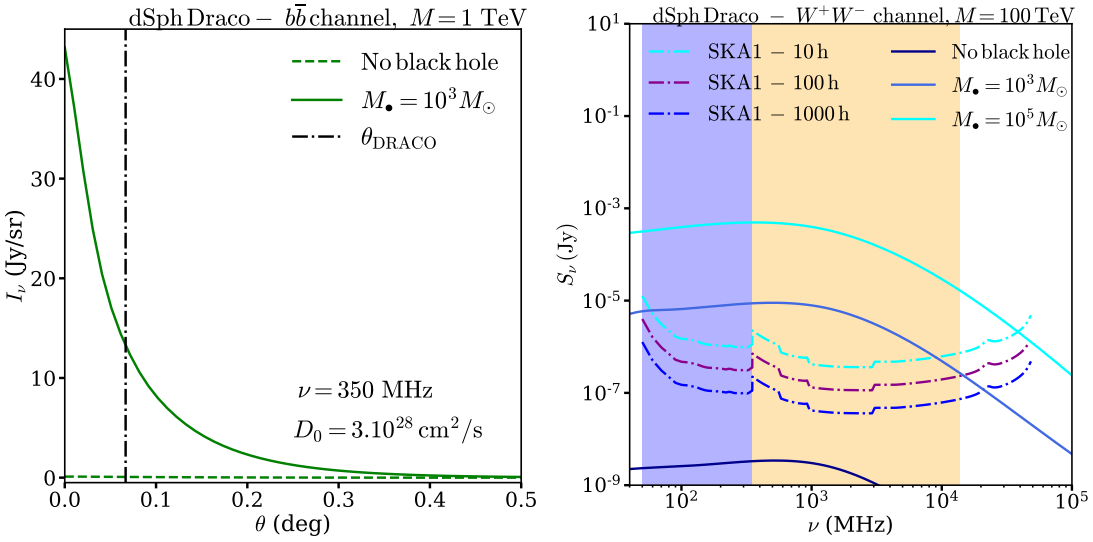

FIGURE 5.13: *Left panel:* Specific intensity at $\nu = 350$ MHz for a $M = 1$ TeV DM candidate, both without and with a BH of $M_\bullet = 10^3 M_\odot$. The canonical thermally averaged cross section $3 \cdot 10^{-26}$cm^3/s is considered. As can be seen the emission including a BH exceeds the core of Draco ($\theta_{\rm DRACO} \sim 0.093$ kpc [204]). *Right panel:* Effect in the flux density when a BH in the centre of Draco is included. DM mass $M = 100$ TeV and annihilation happens 100% in the W^+W^- channel. Two paradigmatic black-hole masses have been considered. As observed there, the signal from TeV DM candidates which, in principle could not be detected by SKA1, would be boosted to SKA1-detectable regions by the inclusion of such a BH, rendering the detection of TeV DM feasible, even for short SKA1 integration times.

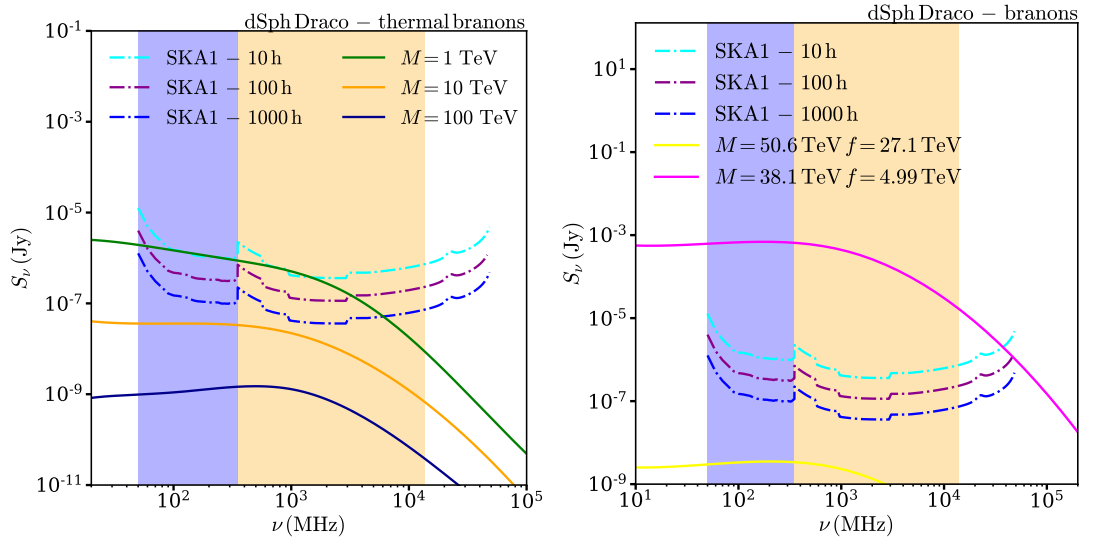

FIGURE 5.14: *Left panel*: Flux density of radiation S_ν over $\Omega_{\rm SKA}(\lambda)$ for freeze-out thermal branons [99, 402]. For illustrative purposes we considered one extra-dimension ($D = 5$). Colour bands and dash-dotted lines have the same meaning as in previous figures. *Right panel*: Flux density over $\Omega_{\rm SKA}(\lambda)$ for two branons of interest as explained in Refs. [403] and [229] and commented in Section 5.5.2. Colour bands and dash-dotted lines have the same meaning as in previous figures. The non-thermal branon with $M = 38.1$ TeV and $f = 4.99$ TeV (magenta lines) could be detected for a SKA1 integration time of 10 hours, while SKA1 could detect the thermal branon with $M = 50.6$ TeV and $f = 27.1$ TeV (yellow lines) after 10^5 hours of integration time provided a boost factor 3.43 is taken.

annihilation for TeV branons, as for the previous sections, show that e^+/e^- are mainly produced via W^+W^- and ZZ bosonic channels [404].

In Fig. 5.14, the flux density S_ν for thermal branons with $3 \cdot 10^{-26}\text{cm}^3/\text{s}$ is evaluated for the SKA1 frequency range. Without considering any boost factor, the SKA1 detection of thermal branons for 1000 hours of integration time τ turns into manageable for masses up to 6 TeV in some specific frequencies of SKA1.

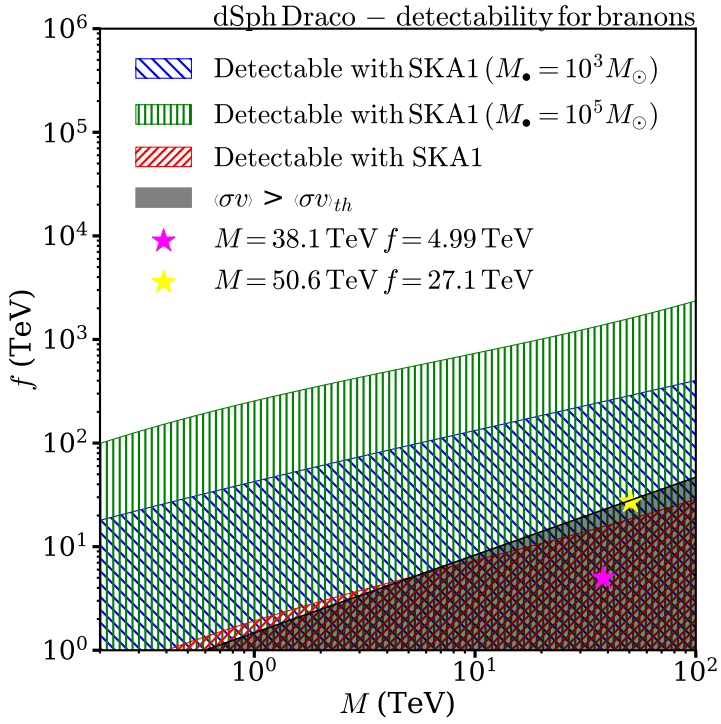

FIGURE 5.15: Detectability of branons from Draco with SKA1 on the (M, f) parameter space after 1000 hours of integration time. The solid angle considered to set this map is $\Omega_{\text{SKA}}(\lambda)$ with a minimal baseline of 30 m. The black line represents the curve $f(M)$ for a thermal relic with $\langle\sigma v\rangle = 3 \cdot 10^{-26}$ cm^3/s. Within the black region $\langle\sigma v\rangle$ is greater than $\langle\sigma v\rangle_{th}$. The region in red would be detectable by SKA1 without a boost while blue and green regions represent the detectable parameter space considering a BH mass of $10^3 M_\odot$ and $10^5 M_\odot$ respectively. In addition, we show as a yellow star the branon DM candidate $M = 50.6$ TeV and tension $f = 27.1$ TeV, and as magenta star the candidate $M = 38.1$ TeV and tension $f = 4.99$ TeV.

Moreover, let us focus on two specific cases for branons that would fit the data of other detectors. The first candidate is a branon with $f = 4.99$ TeV and $M = 38.1$ TeV, that would be in agreement with the AMS positron fraction excess [§]. The second candidate is a branon with $f = 27.5$ TeV and $M = 50.6$ TeV that would fit the γ-ray data detected by HESS from [403]. The candidate with $f = 4.99$ TeV and $M = 38.1$ TeV holds for a thermally averaged cross section equal to $1.76 \cdot 10^{-21}$ cm^3/s, that highly exceeds the thermal relic cross section $3 \cdot 10^{-26}$ cm^3/s. Although there are works that have justified such high boost factors [405], it is unlikely to think that the branon model with such parameters can achieve the correct relic density within the standard freeze-out mechanism. Therefore, additional production mechanism will be needed in this case. The second with candidate $f = 27.5$ TeV and $M = 50.6$ TeV has a thermally averaged cross

[§]After the update of Section 3.8 with the new AMS data this candidate seems to be ruled out.

section $\langle\sigma v\rangle = 1.14 \cdot 10^{-26}$ cm^3/s, slightly below the canonical thermally averaged cross section $3 \cdot 10^{-26}$ cm^3/s Fig. 5.14 right panel, indicates that SKA1 would detect the branon with $f = 4.99$ TeV and $M = 38.1$ TeV without considering any boost factor. However, for the second case ($f = 27.5$ TeV, $M = 50.6$ TeV), SKA1 only could detect it when an integration time of around 10^5 h is considered if a boost factor is added or 10^4 hours in the case a boost factor of 3.43.

Finally, we set sensitivity constraints on the parameter space $\{M, f\}$ in extra-dimensional Brane-World theories. As seen in Eq. (1.37), if the thermally averaged cross section is not fixed, both the DM mass M and the tension of the brane f can be fully considered as free parameters. In Fig. 5.15, we plot the sensitivity constraints on the $\{M, f\}$ parameter space that would be provided by the SKA1 telescope. In addition, there, the black line represents the curve $f(M)$ associated to the thermal relic with $\langle\sigma v\rangle = 3 \cdot 10^{-26}$ cm^3/s. Below such black line we represent the part of the parameter space in which $\langle\sigma v\rangle > \langle\sigma v\rangle_{th}$. Indeed, the thermally averaged cross section in branons increases with the mass and it is inversely proportional to the tension. The red region would be possible to detect by SKA1 with no boost. This fact indicates that SKA1 would detect thermal branons with masses below 6 TeV and tensions $f < 10$ TeV. Regions in blue and green shows the detectable parameter region, (f, M), assuming a BH with a mass of either $10^3 M_\odot$ or $10^5 M_\odot$ respectively.For comparative purposes, on the one hand, we show as a yellow star the DM candidate with $M = 50.6$ TeV and tension $f = 27.1$ TeV branon, that is thermal with $\langle\sigma v\rangle = 1.1 \cdot 10^{-26}$cm^3/s. Conversely, the magenta star represents the DM candidate $M = 38.1$ TeV and tension $f = 4.99$ TeV branon fitting the AMS positron data. Nevertheless, this candidate would require some non-conventional mechanism of DM production in the Early Universe to be considered.

5.6 Particle dark matter searches in dwarf spheroidals

At the beginning of this chapter, in Section 5.2.1, we motivated our study of Draco dSph based on the fact that such a target has been widely studied and that some of its parameters are better constrained than the rest of dSphs. However, as both the resolution/sensitivity in detectors and the N-body simulations improve, additional important features from other dSphs can be known. In particular, as discussed in Section 5.2.1, the DM density profile, the magnetic field and the propagation parameters seem to be crucial to ensure an accurate study through synchrotron emission. In this section, we will compute the flux density S_ν in other targets within the dSphs group, namely Ursa Minor, Segue 1 and Willman 1. To that end, we focus our study by taking into account the impact of dSphs features such as the DM density profile, the distance of the dSphs from the Earth, the mass-to-light ratio and the magnetic field as well.

For this study we follow the γ-ray counterpart of Ref. [406] in which the most suitable targets for γ-ray DM searches with Cherenkov telescopes are presented. Our main objective is selecting some of those targets and performing the expected synchrotron emission and the subsequent detectability with SKA1. Table 5.8 provides some of the most suitable candidates obtained from [406], that we consider for our study: Draco, Ursa Minor, Segue 1 and Willman 1.

Fig. 5.16 shows the flux density S_ν for a DM particle with a mass of 10 TeV, annihilating into W^+W^- with a thermally averaged cross section equal to $3 \cdot 10^{-26}$cm^3/s. For this analysis we chose $M = 10$ TeV because this was the approximate limit in masses that SKA1 could be measure (see Table 5.5). Indeed, a larger S_ν is expected from Ursa Minor and Willman 1, and consequently, tighter constraints could be obtained directing SKA1 to these two targets. For example, a value of $S_{1\,\mathrm{GHz}} = 2.38 \cdot 10^{-7}$ Jy is expected in Willman 1 and $S_{1\,\mathrm{GHz}} = 1.032 \cdot 10^{-7}$ Jy in Ursa Minor for $\nu = 1$ GHz, while in Draco is $S_{1\,\mathrm{GHz}} = 5.23 \cdot 10^{-8}$ Jy. The last two lie on the window close to 100

TABLE 5.8: Astrophysical parameters for targets depicted in Fig. 5.16. Parameter values of the DM profiles have been taken from [406].

Target	Distance (kpc)	M/L	DM profile	B_0 (μG)
Draco	80	320	NFW	1
Ursa Minor	66	580	NFW	1
Segue 1	23	>1000	Einasto	2
Willman 1	38	700	NFW	1

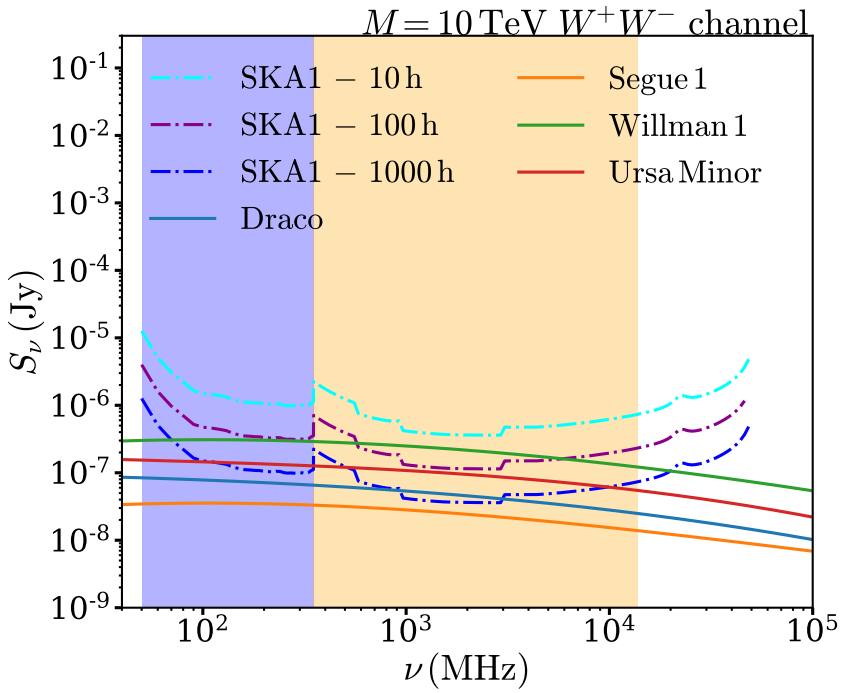

FIGURE 5.16: Flux density radio emission S_ν for 10 TeV DM candidate annihilating into W^+W^- for different dSphs: Draco, Segue 1, Willman 1 and Ursa Minor. The angle taken for this calculation is the whole galaxy and the thermally averaged cross section is $\langle\sigma v\rangle = 3 \cdot 10^{-26}$ cm^3/s. Colour bands and dash-dotted lines have the same meaning as in previous figures.

hours of integration time, while in the case of Draco around 1000 h is necessary for the detection of the candidate W^+W^-(10 TeV).

Conversely, Segue 1 seemed to be one of the best targets for DM detection. Its proportion of DM (a mass-to-light ratio of $\sim 3400\,[M/L_V]_\odot$ according to [365]) with respect to the luminous matter allows to refer to it as the darkest galaxy [358]. Furthermore, the proximity of Segue 1 to us (23 kpc), led to consider that Segue 1 may be influenced by the Milky Way magnetic field allowing us to reach a value of 2 μG for such dSphs [178]. However, this scenario is the less pessimistic among the considered targets for DM detection. In fact, the DM candidate annihilating into W^+W^- with $M = 10$ TeV lies out of the detectability zone of SKA1 after 1000 h.

5.7 Chapter conclusions

In Chapter 5, we studied annihilating dark matter signals in dwarf spheroidal galaxies from synchrotron emission. Indeed, dwarf spheroidal galaxies are considered one of the most suitable targets for dark matter detection, not only due to the high proportion of dark matter with respect to baryonic matter, but also due to the expected low background. The main challenge for such searches lies in determining their astrophysical parameters, such as magnetic field, diffusion and also dark matter density profile. Throughout the Chapter, we studied the specific intensity I_ν and the flux density S_ν. The former gave us information about the angular dependence of the signal, while the latter provided us a spectral analysis to disentangle which frequencies would be better for dark matter detection.

In Section 5.2, we addressed the variability of synchrotron signals with respect to these astrophysical parameters. In general, the flux density times the frequency νS_ν could variate, around two or three orders of magnitude when the magnetic field strength changes in a few νG. In this regard, we have chosen a conservative value of $\sim 1\,\mu$G for the magnetic field. Furthermore, both the diffusion and the dark matter halos also may affect in one or two order of magnitudes (for more details, please refer to Figs. 5.2, 5.3 and 5.8). Thus, the synchrotron signals would be highly dependent on the astrophysical parameters.

In Section 5.3, we analysed potential dark matter signatures from a Particle Physics point of view. First, through a spatial analysis I_ν, trying to understand whether it is possible to reconstruct the dark matter annihilation channels provided it was measured a synchrotron signature from dark matter. Essentially, it would be only possible to disentangle leptonic channels from the rest by observing the angular dependence of the emission. Second, through a flux density study S_ν, we provided the best frequencies of detection depending on the channel and dark matter mass (Table 5.4). A dark matter candidate of 100 GeV presents its emission maximum at radio frequencies of $\sim 10^{11}$ Hz, while 100 TeV DM particles emit synchrotron emission up to X-rays ($\sim 10^{17}$ Hz), opening novel prospectives of detectability with other experiments. Indeed, the SKA frequency range would not coincide with the maximum peak of the emission of S_ν for TeV dark matter, as seen in Fig. 5.17, and another range of frequencies would be needed to be studied. In other words, even though SKA1 becomes one of the most sensitive telescopes to detect dark matter, its frequency range would be only suitable to detect GeV dark matter. However, in Fig. 5.17, we observe that SKA1 still remains as one of the most competitive detectors to search for dark matter not due to its range of frequencies but due to such a high sensitivity. In fact, concerning radio frequencies, let us mention GBT, whose frequency band (67-115 GHz) lies on the most convenient region to detect synchrotron emission as produced by TeV DM, as seen in Fig. 5.17.

In Section 5.4, we set sensitivity constraints both for SKA-1 LOW and SKA-1 MID in a dark-matter independent analysis. The most fundamental conclusion is displayed in Fig. 5.10, where we estimate an upper limit for the dark matter mass detection of around 10 TeV both for the W^+W^- and $b\bar{b}$ channels, while for the $\tau^+\tau^-$ channel would be around 3 TeV (to see the specific values consult Table 5.5) when the thermally averaged cross section is $3 \cdot 10^{-26}\text{cm}^3/\text{s}$. Even though this study is performed for three specific channels, according to the similarities observed in Fig. 5.8, we could extend similar limits for the rest of the channels. It is necessary to have in mind that this result applies for an exponential magnetic field. In the case of a constant magnetic field, the channels W^+W^- and $b\bar{b}$ could be detected in the whole TeV range of masses (Fig.5.11).

In the light of the results of our model-independent analysis, in Section 5.5, we concluded that multi-TeV dark matter candidates able to explain the HESS J1745 $-$ 290 excess in Table (5.6) will not be detected by SKA1 within 1000 hours of integration time. Indeed, the lightest candidates

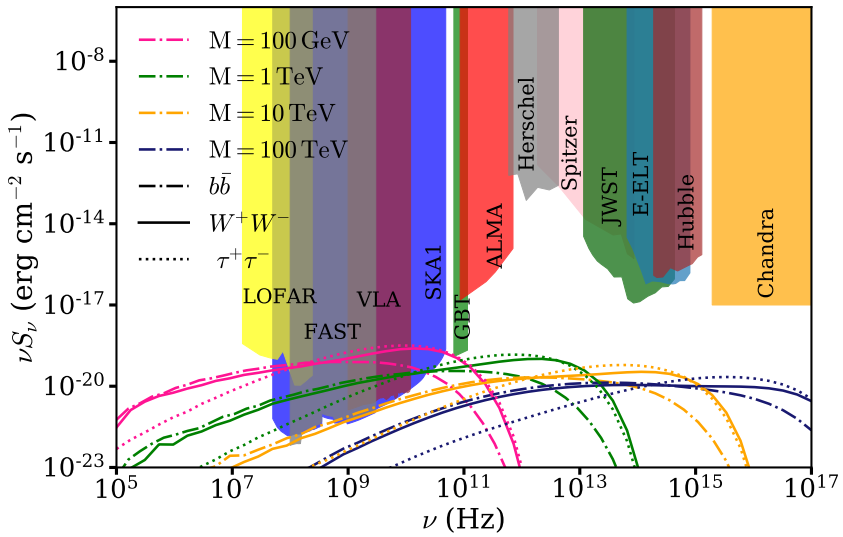

FIGURE 5.17: Flux density S_ν over Ω_{DRACO} as given in Eq. (2.41) times frequency ν for a Draco-like dSph in the range of frequencies $10^5 - 10^{17}$ Hz as produced by e^+e^- synchrotron emission for different dark matter masses and annihilation channels [199]. Colour bands represent regions of detectability for different detectors: SKA1 [348], FAST [139], VLA [139], LOFAR [408], GBT [139], ALMA [409], Herschel [409], Spitzer [409], JWST [410], E-ELT [411], Hubble [409] and Chandra [412] on a large range of frequencies. Whereas GeV dark matter seems suitable to be detected in radio frequencies, TeV dark matter would be better detected at higher frequencies. Even though SKA1 exhibits a competitive sensitivity to measure dark matter indirect signals up to 10 TeV (yellow lines), for heavier TeV dark matter, the maximum of emission shifts to frequencies higher than the SKA1 range. Targets with a radio signal boost mechanism could improve the competitiveness of these detectors.

would correspond to the channels with dark matter masses e^+e^- ($M = 7.51$ TeV), $u\bar{u}$ ($M = 27.9$ TeV) and W^+W^-($M = 48.8$ TeV), for the different families of particles (bosons, leptons or quarks). Therefore, we speculate about the possibility of adding a justified boost factor to test whether those candidates are detectable under these circumstances. In our analysis two boost factors were considered: either a boost due to dark matter substructures or due to a hypothetical intermediate-mass black hole at the centre of Draco. For the former three dark matter candidates, $u\bar{u}$ ($M = 27.9$ TeV), $d\bar{d}$ ($M = 42$ TeV) and $s\bar{s}$ ($M = 53.9$ TeV), could be detected only if the Draco dark matter halo is not subjected to tidal disruptions. For the latter, intermediate-mass black holes could enhance the synchrotron signals several orders of magnitude. Indeed, for a black-hole mass of $M_\bullet = 10^3 M_\odot$ the signal could be enhanced in more than three orders of magnitude. This fact turns dark matter searches around black holes into an attractive target to take into account. Some works have already considered such a possibility [407]. In our study we set sensitivity constraints for Brane-World dark matter under the assumption of the intermediate-mass black hole, observing that the whole TeV range of masses could be accessible with the SKA (Fig. 5.15).

Finally, in Section 5.6, performing the flux density S_ν for other dwarf spheroidal galaxies, we observe that better constraints could be obtained, in particular, in galaxies as Ursa Minor or Willman 1.

Chapter 6

Conclusions

The missing mass problem, developed from the end of the eighteenth century and enunciated at the end of the nineteenth century, conducted inevitably to the concept of dark matter: not all the matter in the Universe is luminous. Astrophysical studies on galaxies and galaxy clusters (dynamics, X-ray or lensing) necessarily invoke to dark matter, but also such a concept emerges from a cosmological point of view. Indeed, according to the cosmological ΛCDM Concordance Model, 26.8% of the energy content of the Universe is composed of dark matter. Even though dark matter in Astrophysics and Cosmology is formulated differently (in the former dark matter is usually presented from a kinematic point of view, while in the latter it appears as a density in the Friedmann Equations), both formulations are connected in the formalism of growth of structures in the Early Universe. On the other hand, the incorporation of dark matter from a particle point of view is addressed from two approaches: the first one is the proposal of WIMPs, as particles able to reproduce the cosmological dark matter density of the Universe today. While the second approach emerges as the need to explain some open questions in Particle Physics such as the strong CP violation or the hierarchy problem. Within some of the extensions of the Standard Model of particles, some particles emerge as natural candidates for dark matter. Although astrophysical and cosmological dark matter can be strictly linked and the dark matter problem appears naturally at those scales, dark matter as a particle can be only classified as a proposal. N-body simulations, which do introduce particles, consider particles with masses typically around $10^9 M_\odot$ but without any physical meaning. Alternatives to explain the dark matter effects have been proposed, such as Modified Gravity.

Within the particle description for dark matter, there are different possibilities for its detection, usually classified in collider, direct and indirect searches that we revised in Chapter 2. The price to be paid in the use of these searches is the loss of generality. Indeed, collider, direct and indirect searches require to take a position in the kind of dark matter to be searched. In the case of colliders, in which dark matter would appear as an invisible particle, the most general searches are EFT and Simplified Models whose difficulty lies in extracting relevant information forcing us to perform more specific searches (e.g., SUSY). In the case of direct searches, the own fact of electing the material of the detector also restricts the range of masses to be detected. Meanwhile, indirect searches require to choose the annihilation channel. Thus, the key lies in combining all these detection strategies to extract more general information. However, making use of these searches together needs for the specification of the underlying particle model. In other words, the particle dark matter candidate is first specified and then searched and not the other way around. Considering this fact, the possibilities about the nature of dark matter grow with the number of particle candidates and their range of interaction. In this regard, throughout this research, it has been noticed that some researchers point out that the idea of dark matter as a particle may not be a falsifiable hypothesis, not only due to the number of candidates but also the extension of their parameter space, for instance, in the case of indirect searches the diagram $\langle \sigma v \rangle / M$. The candidate mass could be taken arbitrarily large and the thermally cross section arbitrarily small. In other words, the main question to pose in the context of dark matter

searches can be summarised as follows: *when do we stop to search particle dark matter candidates?* This question can only be answered within each specific particle theory proposed. For example, cold relics cannot be larger than 340 TeV in order to conserve the unitarity of the dispersion matrix.

Considering the discussion above, in our study devoted to indirect searches, we intended to be as general as possible. Essentially, we worked on model-independent dark matter, although we also implemented the study to particular cases. In our analysis, we work with dark matter annihilating mainly into three different channels W^+W^-, $b\bar{b}$ and $\tau^+\tau^-$. However, the similarities we found in their energy spectrum throughout the study of the positron fraction and also the synchrotron emission allow us to find general features shared by each family of particles (leptons, bosons and quarks). For more refined studies, it would be necessary to analyse each channel in particular. In the general case, with the current sensitivity in radio, from the study of Chapter 5, we concluded that model-independent dark matter with masses of few TeV (and $\langle\sigma v\rangle = 3 \cdot 10^{-26}\mathrm{cm}^3/\mathrm{s}$) can be detected at radio frequencies in dwarf spheroidals which would imply one of the most ideal targets thanks to their low content of luminous matter with respect to dark matter. Our research also showed that one candidate with a mass around 0.1-3 TeV would be suitable to explain the AMS positron excess (Chapter 3) provided that such a candidate annihilates into leptons in a non-negligible proportion with respect to other channels. Otherwise, an astrophysical explanation would be favoured for the AMS data, although there is still the possibility that AMS measured a two or more-than-two dark matter species, as discussed in the conclusions of Chapter 3. In addition, the AMS candidate would be potentially detectable by SKA in Draco dwarf spheroidal galaxy, according to the study performed in Chapter 5.

Assuming a dark matter candidate with a mass greater than $\sim$ 10 TeV, then the study of indirect searches with radio signals would be possible in a cluster of galaxies [351] or a galaxy as the Milky Way, in a region approximately close to the Galactic Plane (see Fig. 3.12). To address this latter scenario competitively it would be fundamental having a model about the propagation of cosmic rays and their radiative losses. Otherwise, dark matter constraints will be limited to non-thermal dark matter as seen in Fig. 4.4. Aside from galaxies like the Milky Way or Galaxy clusters, other alternative ideas to detect heavy dark matter (masses greater than 10 TeV) lies in setting constraints on astrophysical targets in which the dark matter signal may be boosted. In our work, we observed the effects of considering either halo substructures or the presence of a black hole (Section 5.5.1). In the case of substructures, the enhancement of signals is not significant for dwarf spheroidals assuming that some dwarfs experience tidal effects in the interaction with the Milky Way. However, the contraction of the halo due to the presence of an intermediate-massive black hole could be relevant and change the emission in several orders of magnitude. Indeed, the fact that in inner regions the dark matter density profile is inversely proportional to the thermally averaged cross section and directly proportional to the dark matter mass, Eq. (5.12), is a subtlety that should be explored in more detail in future investigations. The main reason is that the dark matter halo contraction around this astrophysical massive object changes (with respect to the usual behaviour $\langle\sigma v\rangle / M^2$) the dependence of the signal with both the thermally averaged cross section and the dark matter mass, increasing the achievable dark matter parameter space to constrain.

Furthermore, it is necessary to keep in mind that the value of $\sim$ 10 TeV we mentioned above is solely a maximum limit in masses obtained at Draco with the SKA1, which at the present is one of the most sensitive detectors in radio frequencies. In the first place, we remark that according to the study showed in Fig. 5.16 for dwarf spheroidals, this limit could be extended a few TeV more by focusing on other dwarf spheroidals. Also, considering the high SKA1 sensitivity, it would be interesting to extend these studies to possible nearby missing satellites or galactic subclumps that would be affected by the Milky Way magnetic field, similar to the case of Segue

I discussed in Section 5.6. A possible rough preliminary calculation would consist of treating a particular dark matter substructure with the same formalism we used for dwarf spheroidals. This may serve to constrain dark matter and also to extract some information about the possible dark matter substructures. Second, as we mentioned in Fig. 5.17 and Table 5.4, the range of frequencies covered by the SKA would not be the most suitable to measure TeV dark matter signatures. But yet, as the most sensitive one, SKA is also one of the most competitive in the detection of dark matter with radio signals. In this regard, constraining dark matter at higher frequencies with other detectors could improve the parameter restrictions for TeV dark matter. For this reason, we have in mind to expand the study to different frequencies focusing on other e^+/e^- energy losses, as Inverse Compton Scattering, whose range lies from X-ray to γ-ray. This last study seems feasible in the shorter term since it would consist of changing the synchrotron power of Eq. (2.36) by a, for instance, an Inverse Compton Scattering power. Preliminary checks and updates have been already performed in our code to include other energy losses.

Besides model-independent dark matter studies, we also paid special attention to Brane-World dark matter in the context of extra-dimensional theories. Obviously, the conclusions in the studies both for branons and model-independent coincide. However, in the former, we constrained the branon parameter space $\{M, f\}$. In the first place, we proposed a set of χ^2 minima in the cosmic-ray analysis that would correspond to different branon candidates. Suitable masses to fit the positron fraction with branons range from ~ 30 to ~ 70 TeV according to the studies in Fig. 3.9 but also Fig. 3.11 considering the annihilation channels. Indeed, in Section 3.5, we propose a specific candidate. However, taking into account the latest AMS data, such a candidate would be highly disfavoured. Furthermore, concerning the $\{M, f\}$ constraints, we observe the difficulty of excluding tensions f values (Fig. 4.5), essentially due to the high suppression of the coupling with such a tension. For such branon candidates, we have in mind improving the constraints studying the behaviour of the dark matter halo around black holes, but also studying the Milky Way. For the former, according to Eq. (5.12), the dark matter halo spike around a black hole would increase with the inverse of the thermally averaged cross section, and thus would be proportional to the tension of the brane. The suppression of the tension in the emission (see, for example, the dependence of the different signatures with the thermally averaged cross section in Section 2.5.1 and the branon cross section in Eq. 1.39) would be compensated by the contraction of the halo around the black hole. Second, the SKA1 sensitivity would allow us to constrain TeV DM candidates around the Galactic plane (see Fig.4.9 for model-independent DM).

Getting back to the question of whether dark matter is a falsifiable hypothesis, maybe one possibility would be combining particle dark matter searches with alternative experiments in which only the gravitational information is involved. This would allow us to determine the dark matter features in a more unambiguous way. In this regard, throughout this research, some interesting lines of reasoning emerged to be followed in the future, essentially, based on finding distinct astrophysical environments to those usually considered in dark matter indirect searches. Fundamentally, according to the discussion above in this section, we would suggest studies focusing on the dark matter halo around massive objects, such as pulsars or black holes. For example, in order to perform such a study, the maps obtained in Fig. 4.2 could be computed again changing the dark matter halo by a contracted dark matter halo, as in Section 5.5.1 b). Moreover, it would be possible to perform a study about the gravitational lensing effects by analysing the synchrotron specific intensity in a curved space-time. In order to do this, the ray tracing and the radiative transfer schemes used in Ref. [407] could be included in our maps of Fig. 4.2. This study could be relevant in view of the latest results of the Event Horizon Telescope [413] that measured the radio emission of M87 and would also release information about Sgr A* at the centre of the Milky Way in the following years. Furthermore, considering that the geometry of the emission slightly changes with the annihilation channel, according to our study

(see Fig. 5.6), it would be interesting to understand whether some of this spatial dependence is accentuated in the surrounding of a black hole.

Furthermore, there also exists the possibility of combining indirect dark matter searches around massive objects with a detailed study of gravitational-wave signals in their merging. Indeed, the gravitational wave could be distorted by the presence of dark matter halos leaving, for example, dephasing effects in the gravitational wave (for other signals see, for example, [414]). This analysis together with the indirect detection counterpart could be crucial in the determination of dark matter features. In addition, in this astrophysical framework other possibilities can be also considered. Indeed, the merging of a neutron star and a black hole has been investigated to constrain axion dark matter [415] (as seen in Section 1.4.1 c)). The pulsar magnetosphere would convert axion dark matter into photons in the dark matter halo surrounding the black hole. This specific case could be also generalised for annihilating dark matter whose synchrotron emission would be enhanced by the pulsar high magnetic field and the black hole spike. In Sections 5.3 and 5.13, we delineated the high dependence of the radio emission both with the magnetic field and the presence of a black hole, respectively.

In addition, supplementary studies to dark matter indirect searches are also possible in Cosmology. The line of reasoning we have begun to investigate is the study of cosmological caustics. The latter are hypersurfaces defined by points in which the Jacobian between the Euler space and the Lagrangian space of dark matter, treated as a fluid, is zero. These hypersurfaces would indicate those regions in which the density of dark matter is high (infinity for dark matter with nearly zero velocity), and thus, annihilating dark matter signals would be expected [416]. With this purpose, the Zeldovich approximation is being considered. This study would allow us to cross-correlate annihilating dark matter signals with all-sky surveys. Preliminary results for simple models have been obtained.

In conclusion, dark matter indirect detection proves to be a powerful tool that would allow us to search for dark matter with masses at the GeV scale but also a few TeV. Indeed, according to our study, the explanation of the positron fraction could be in terms of a 1-2 TeV dark matter candidate whose existence may be tested by the SKA1. Furthermore, heavy dark matter candidates of around tens TeV could be studied in some specific targets as either black holes or centres of galaxies as the Milky Way. Also, with the addition of new technology, the progression to SKA2 will start gradually, allowing us to study such heavy candidates. Finally, dark matter indirect searches in radio frequencies could be extended to other frequencies and be combined with studies of lensing and gravitational waves in massive compact objects merging, providing more specific information about the nature of dark matter.

Bibliography

[1] G. Bertone and D. Hooper. *History of dark matter*. Reviews of Modern Physics, vol. 90, no. 4, (**2018**).

[2] R. H. Sanders. *The dark matter problem: a historical perspective*. Cambridge University Press, (**2010**).

[3] G. Bothun. *Modern cosmological observations and problems*. CRC Press, (**1998**).

[4] S. Ettori. *The physics inside the X-ray/SZ scaling relations for galaxy clusters*. Building the Euclid Cluster Survey-Scientific Program, proceedings of a conference held July 6-11 2014 at the Sexten Center for Astrophysic, (**2014**).

[5] B. W. Carroll and D. A. Ostlie. *An introduction to modern astrophysics*. Cambridge University Press, (**2017**).

[6] R. Massey, T. Kitching, and J. Richard. *The dark matter of gravitational lensing*. Reports on Progress in Physics, vol. 73, no. 8, (**2010**).

[7] S. Pires, J. L. Starck, A. Leonard, and A. Réfrégier. *Weak Gravitational Lensing*. Taylor & Francis, (**2012**).

[8] M. Meneghetti. *Introduction to gravitational lensing*. Lecture Notes organized in a course on web, `http://www.ita.uni-heidelberg.de/~massimo/sub/glensing.html`, (**2006**).

[9] P. Peter and J. P. Uzan. *Primordial cosmology*. Oxford University Press, (**2013**).

[10] A. Liddle. *An introduction to modern cosmology*. John Wiley & Sons, (**2015**).

[11] J. Garcia-Bellido. *Astrophysics and cosmology*. arXiv preprint hep-ph/0004188, (**2000**).

[12] O. Piattella. *Lecture Notes in Cosmology*. Springer, (**2018**).

[13] M. Bucher. *Physics of the cosmic microwave background anisotropy*. International Journal of Modern Physics D, vol. 24, no. 02, (**2015**).

[14] D. Scott and G. Smoot. *Cosmic background radiation mini-review*. arXiv preprint astro-ph/0406567, (**2004**).

[15] E. Kolb. *The early universe*. CRC Press, (**2018**).

[16] P. S. Dev, A. Mazumdar, and S. Qutub. *Constraining non-thermal and thermal properties of dark matter*. Frontiers in Physics, vol. 2, (**2014**).

[17] S. Profumo. *TASI 2012 Lectures on astrophysical probes of dark matter*. arXiv preprint arXiv:1301.0952, (**2013**).

[18] G. Bertone, D. Hooper, and J. Silk. *Particle dark matter: Evidence, candidates and constraints*. Physics reports, vol. 405, no. 5-6, (**2005**).

[19] P. Gondolo. *Introduction to non-baryonic dark matter*. arXiv preprint astro-ph/0403064, (**2004**).

[20] F. Zwicky. *Die rotverschiebung von extragalaktischen nebeln*. Helvetica Physica Acta, vol. 6, (**1933**).

[21] F. Zwicky. *On the Masses of Nebulae and of Clusters of Nebulae*. The Astrophysical Journal, vol. 86, (**1937**).

[22] V. C. Rubin, W. K. Ford Jr, and N. Thonnard. *Extended rotation curves of high-luminosity spiral galaxies. IV-Systematic dynamical properties, SA through SC*. The Astrophysical Journal, vol. 225, (**1978**).

[23] W. T. B. Kelvin. *Baltimore lectures on molecular dynamics and the wave theory of light*. CJ Clay and Sons, (**1904**).

[24] H. Poincare. *The milky way and the theory of gases*. Popular Astronomy, vol. 14, (**1906**).

[25] J. C. Kapteyn. *First Attempt at a Theory of the Arrangement and Motion of the Sidereal System*. The Astrophysical Journal, vol. 55, (**1922**).

[26] E. Opik. *Selective absorption of light in space, and the dynamics of the Universe*. Bull. de la Soc. Astr. de Russie, vol. 21, no. 150, (**1915**).

[27] J. H. Oort et al. *The force exerted by the stellar system in the direction perpendicular to the galactic plane and some related problems*. Bulletin of the Astronomical Institutes of the Netherlands, vol. 6, (**1932**).

[28] E. Hubble and M. L. Humason. *The velocity-distance relation among extra-galactic nebulae*. The Astrophysical Journal, vol. 74, (**1931**).

[29] H. Andernach and F. Zwicky. *English and Spanish Translation of Zwicky's (1933) The Redshift of Extragalactic Nebulae*. arXiv preprint arXiv:1711.01693, (**2017**).

[30] S. Smith. *The mass of the Virgo cluster*. The Astrophysical Journal, vol. 83, (**1936**).

[31] E. Hubble. *The distribution of extra-galactic nebulae*. The Astrophysical Journal, vol. 79, (**1934**).

[32] J. Neyman, T. Page, and E. Scott. *Conference on the Instability of Systems of Galaxies*. Astronom. J, vol. 66, (**1961**).

[33] H. J. Rood. *The Dynamics of the Coma Cluster of Galaxies.* (**1965**).

[34] S. D. White. *Mass segregation and missing mass in the Coma cluster*. Monthly Notices of the Royal Astronomical Society, vol. 179, no. 2, (**1977**).

[35] J. F. Meekins et al. *Physical sciences: X-rays from the coma cluster of galaxies*. Nature, vol. 231, no. 5298, (**1971**).

[36] V. C Rubin and W. K. Ford Jr. *Rotation of the Andromeda nebula from a spectroscopic survey of emission regions*. The Astrophysical Journal, vol. 159, (**1970**).

[37] R. N. Whitehurst and M. S. Roberts. *High-Velocity Neutral Hydrogen in the Central Region of the Andromeda Galaxy*. The Astrophysical Journal, vol. 175, (**1972**).

[38] C. Carignan, L. Chemin, W. K. Huchtmeier, and F. J. Lockman. *The extended HI rotation curve and mass distribution of M31*. The Astrophysical Journal Letters, vol. 641, no. 2, (**2006**).

[39] E. P. Hubble. *Extragalactic nebulae.* The Astrophysical Journal, vol. 64, (**1926**).

[40] K. Lundmark. *Über eine Periodenamplitudenbeziehung und eine Helligkeitsamplitudenbeziehung für anagalaktische und galaktische Cepheiden (Meddelande från Lunds Astronomiska Observatorium Ser. I, Nr. 128.) Mit 5 Abbildungen (Eingegangen am 29. August 1931)*. Zeitschrift fur Astrophysik, vol. 3, (**1931**).

[41] H. W. Babcock. *The rotation of the Andromeda Nebula*. Lick Observatory Bulletin, vol. 19, (**1939**).

[42] F. D. Kahn and L. Woltjer. *Intergalactic Matter and the Galaxy.* The Astrophysical Journal, vol. 130, (**1959**).

[43] M. S. Roberts and A. Rots. *Comparison of rotation curves of different galaxy types*. Astronomy and Astrophysics, vol. 26, (**1973**).

[44] A. Bosma. *The distribution and kinematics of neutral hydrogen in spiral galaxies of various morphological types*. PhD thesis. Rijksuniversiteit te Groningen., (**1978**).

[45] A. Burkert. *The structure of dark matter halos in dwarf galaxies*. The Astrophysical Journal Letters, vol. 447, no. 1, (**1995**).

[46] J. F. Navarro. *The structure of cold dark matter halos*. Symposium-international astronomical union, vol. 171. Cambridge University Press. (**1996**).

[47] J. Einasto. *Kinematics and dynamics of stellar systems, Trudy Inst*. Astrofiz. Alma-Ata, vol. 5, (**1965**).

[48] H. Böhringer et al. *The structure of the Virgo cluster of galaxies from Rosat X-ray images*. Nature, vol. 368, no. 6474, (**1994**).

[49] N. J. Woolf. *On the stabilization of clusters of galaxies by ionized gas*. The Astrophysical Journal, vol. 148, (**1967**).

[50] D. Fabricant, M. Lecar, and P. Gorenstein. *X-ray measurements of the mass of M87*. The Astrophysical Journal, vol. 241, (**1980**).

[51] P. E. J. Nulsen and H. Böhringer. *A ROSAT determination of the mass of the central Virgo Cluster*. Monthly notices of the royal astronomical society, vol. 274, no. 4, (**1995**).

[52] D. E. McLaughlin. *Evidence in Virgo for the universal dark matter halo*. The Astrophysical Journal Letters, vol. 512, no. 1, (**1999**).

[53] A. D. Lewis, D. A Buote, and J. T. Stocke. *Chandra Observations of Abell 2029: The Dark Matter Profile Down to< 0.01 R_vir in an Unusually Relaxed Cluster*. arXiv preprint astro-ph/0209205, (**2002**).

[54] M. Bradač et al. *Revealing the properties of dark matter in the merging cluster macs j0025. 4–1222*. The Astrophysical Journal, vol. 687, no. 2, (**2008**).

[55] J. N. Bahcall and C. L. Sarazin. *Parameters and predictions for the X-ray emitting gas of Coma, Perseus, and Virgo*. The Astrophysical Journal, 213, L99-L103, (**1977**).

[56] O. Urban et al. *X-ray spectroscopy of the Virgo Cluster out to the virial radius*. Monthly Notices of the Royal Astronomical Society, vol. 414, no. 3, (**2011**).

[57] B. Binggeli. *The virgo cluster-home of M 87*. The Radio Galaxy Messier 87, Springer, (**1999**).

[58] C. Balland and A. Blanchard. *On the Uncertainty in X-Ray Cluster Mass Estimates from the Equation of Hydrostatic Equilibrium*. The Astrophysical Journal, vol. 487, no. 1, (**1997**).

[59] T. Theuns. *Institute for Computational Cosmology - Lectures*. 2019. URL: `icc.dur.ac.uk/~tt/Lectures/Galaxies/GravitationalLensing/GalaxyClusters/index.html`.

[60] D. Clowe et al. *A direct empirical proof of the existence of dark matter*. The Astrophysical Journal Letters, vol. 648, no. 2, (**2006**).

[61] D. Clowe, A. Gonzalez, and M. Markevitch. *Weak-lensing mass reconstruction of the interacting cluster 1E0657–558: Direct evidence for the existence of dark matter*. The Astrophysical Journal, vol. 604, no. 2, (**2004**).

[62] A. G. Riess et al. *Observational evidence from supernovae for an accelerating universe and a cosmological constant*. The Astronomical Journal, vol. 116, no. 3, (**1998**).

[63] S. Perlmutter et al. *Measurements of Ω and Λ from 42 high-redshift supernovae*. The Astrophysical Journal, vol. 517, no. 2, (**1999**).

[64] C. A. P. Bengaly, R. Maartens, N. Randriamiarinarivo, and A. Baloyi. *Testing the Cosmological Principle in the radio sky*. arXiv preprint arXiv:1905.12378, (**2019**).

[65] G. Hinshaw et al. *Nine-year Wilkinson Microwave Anisotropy Probe (WMAP) observations: cosmological parameter results*. The Astrophysical Journal Supplement Series, vol. 208, no. 2, (**2013**).

[66] P. A. R. Ade et al. *Planck 2015 results-xiii. cosmological parameters*. Astronomy & Astrophysics, vol. 594, (**2016**).

[67] R. H. Cyburt, B. D. Fields, and K. A. Olive. *A bitter pill: the primordial Lithium problem worsens*. arXiv preprint arXiv:0808.2818, (**2008**).

[68] J. Dunkley et al. *Five-Year Wilkinson Microwave Anisotropy Probe* Observations: Likelihoods and Parameters from The Wmap Data*. The Astrophysical Journal Supplement Series, vol. 180, no. 2, (**2009**).

[69] N. Aghanim et al. *Planck 2018 results. VI. Cosmological parameters*. arXiv preprint arXiv:1807.06209, (**2018**).

[70] D. N. Spergel. *The dark side of cosmology: Dark matter and dark energy*. Science, vol. 347, no. 6226, (**2015**).

[71] G. F. Smoot et al. *Structure in the COBE differential microwave radiometer first-year maps*. The Astrophysical Journal, vol. 396, (**1992**).

[72] C. Bennett et al. *Preliminary maps and basic results,"* arXiv preprint astro-ph/0302207, (**2003**).

[73] P. A. Ade et al. *Planck 2013 results. I. Overview of products and scientific results*. Astronomy & Astrophysics, vol. 571, (**2014**).

[74] A. Boyarsky, J. Lesgourgues, O. Ruchayskiy, and M. Viel. *Lyman-α constraints on warm and on warm-plus-cold dark matter models*. Journal of Cosmology and Astroparticle Physics, vol. 2009, no. 05, (**2009**).

[75] M. Viel, G. D. Becker, J. S. Bolton, and M. G. Haehnelt. *Warm dark matter as a solution to the small scale crisis: New constraints from high redshift Lyman-α forest data*. Physical Review D, vol. 88, no. 4, (**2013**).

[76] L. Bergström. *Non-baryonic dark matter: observational evidence and detection methods*. Reports on Progress in Physics, vol. 63, no. 5, (**2000**).

[77] S. T. Petcov. *The nature of massive neutrinos*. Advances in High Energy Physics, vol. 2013, (**2013**).

[78] R. D. Peccei and H. R. Quinn. *CP Conservation in the Presence of Instantons*. Phys. Rev. Lett., vol. 38, no. ITP-568-STANFORD, (**1977**).

[79] R. D. Peccei and H. R. Quinn. *Constraints imposed by CP conservation in the presence of pseudoparticles*. Physical Review D, vol. 16, no. 6, (**1977**).

[80] L. D. Duffy and K. Van Bibber. *Axions as dark matter particles*. New Journal of Physics, vol. 11, no. 10, (**2009**).

[81] K. Saikawa et al. *Production and Evolution of Dark Matter Axions in the Early Universe*. Proceedings, 10th Patras Workshop on Axions, WIMPs and WISPs (AXION-WIMP 2014): Geneva, Switzerland, June 29-July 4, (**2014**).

[82] D. Cadamuro, S. Hannestad, G. Raffelt, and J. Redondo. *Cosmological bounds on sub-MeV mass axions*. Journal of Cosmology and Astroparticle Physics, vol. 2011, no. 02, (**2011**).

[83] D. J. Marsh. *Axion cosmology*. Physics Reports, vol. 643, (**2016**).

[84] C Hagmann, S. Chang, and P Sikivie. *Axions from string decay*. Nuclear Physics B-Proceedings Supplements, vol. 72, (**1999**).

[85] S. Chang, C Hagmann, and P Sikivie. *Axions from wall decay*. Nuclear Physics B-Proceedings Supplements, vol. 72, (**1999**).

[86] T. W. Donnelly et al. *Do axions exist?* Physical Review D, vol. 18, no. 5, (**1978**).

[87] R. Frezzotti, M. Garofalo, and G. C. Rossi. *Nonsupersymmetric model with unification of electroweak and strong interactions*. Physical Review D, vol. 93, no. 10, (**2016**).

[88] M. Bertolini. *Lectures on supersymmetry*. Lecture notes given at SISSA, (**2015**).

[89] L. Bergstrom. *Dark matter candidates*. New Journal of Physics, vol. 11, no. 10, (**2009**).

[90] N. Arkani-Hamed, S. Dimopoulos, and G. R. Dvali. *The Hierarchy problem and new dimensions at a millimeter*. Phys. Lett., vol. B429, (**1998**).

[91] N. Arkani-Hamed, S. Dimopoulos, and G. R. Dvali. *Phenomenology, astrophysics and cosmology of theories with submillimeter dimensions and TeV scale quantum gravity*. Phys. Rev., vol. D59, (**1999**).

[92] I. Antoniadis, N. Arkani-Hamed, S. Dimopoulos, and G. R. Dvali. *New dimensions at a millimeter to a Fermi and superstrings at a TeV*. Phys. Lett., vol. B436, (**1998**).

[93] S. S. Gubser and J. D. Lykken. *Strings, branes and extra dimensions: TASI 2001, Boulder, Colorado, USA, 4-29 June 2001*. World Scientific, (**2004**).

[94] A. Datta, B. Mukhopadhyaya, and A. Raychaudhuri. *Physics at the large hadron collider*. Springer Science & Business Media, (**2010**).

[95] T. Appelquist, H.-C. Cheng, and B. A. Dobrescu. *Bounds on universal extra dimensions*. Physical Review D, vol. 64, no. 3, (**2001**).

[96] L. Randall and R. Sundrum. *Large mass hierarchy from a small extra dimension*. Physical review letters, vol. 83, no. 17, (**1999**).

[97] L. Randall and R. Sundrum. *An alternative to compactification*. Physical Review Letters, vol. 83, no. 23, (**1999**).

[98] J. A. R. Cembranos. *Lagrangianos efectivos en teorias con dimensiones extras*. PhD thesis. Universidad Complutense de Madrid, (**2004**).

[99] J. A. R. Cembranos, A Dobado, and A. L. Maroto. *Brane-world dark matter*. Physical review letters, vol. 90, no. 24, (**2003**).

[100] M. Bando, T. Kugo, T. Noguchi, and K. Yoshioka. *Brane fluctuations and suppression of Kaluza-Klein mode couplings*. Physical Review Letters, vol. 83, no. 18, (**1999**).

[101] R. Sundrum. *Effective field theory for a three-brane universe*. Phys. Rev., vol. D59, (**1999**).

[102] M. Bando, T. Kugo, T. Noguchi, and K. Yoshioka. *Brane fluctuation and suppression of Kaluza-Klein mode couplings*. Phys. Rev. Lett., vol. 83, (**1999**).

[103] A. Dobado and A. L. Maroto. *The Dynamics of the Goldstone bosons on the brane*. Nucl. Phys., vol. B592, (**2001**).

[104] J. Cembranos, A. Dobado, and A. L. Maroto. *Brane Skyrmions and wrapped states*. Physical Review D, vol. 65, no. 2, (**2001**).

[105] J. A. R. Cembranos, A. Dobado, and A. L. Maroto. *Goldstone bosons and solitons on the brane*. Lepton and photon interactions at high energies. Proceedings, 20th International Symposium, LP 2001, Rome, Italy, July 23-28, 2001, (**2001**).

[106] J. Alcaraz, J. A. R. Cembranos, A. Dobado, and A. L. Maroto. *Limits on the brane fluctuations mass and on the brane tension scale from electron positron colliders*. Phys. Rev., vol. D67, (**2003**).

[107] T. Kugo and K. Yoshioka. *Probing extra dimensions using Nambu–Goldstone bosons*. Nuclear physics B, vol. 594, no. 1-2, (**2001**).

[108] J. A. R. Cembranos, A. Dobado, and A. L. Maroto. *Dark geometry*. Int. J. Mod. Phys., vol. D13, (**2004**).

[109] A. L. Maroto. *The Nature of branon dark matter*. Phys. Rev., vol. D69, (**2004**).

[110] A. L. Maroto. *Brane oscillations and the cosmic coincidence problem*. Phys. Rev., vol. D69, (**2004**).

[111] J. A. R. Cembranos and A. L. Maroto. *Disformal scalars as dark matter candidates Branon phenomenology*. International journal of modern physics A, vol. 31, no. 14n15, (**2016**).

[112] J. A. R. Cembranos, A. Dobado, and A. L. Maroto. *Cosmological and astrophysical limits on brane fluctuations*. Phys. Rev. D, vol. 68, (**2003**).

[113] M. Milgrom. *A modification of the Newtonian dynamics as a possible alternative to the hidden mass hypothesis*. The Astrophysical Journal, vol. 270, (**1983**).

[114] J. P. Bruneton and G. Esposito-Farese. *Field-theoretical formulations of MOND-like gravity*. Physical Review D, vol. 76, no. 12, (**2007**).

[115] G. W. Horndeski. *Second-order scalar-tensor field equations in a four-dimensional space*. International Journal of Theoretical Physics, vol. 10, no. 6, (**1974**).

[116] J. Gleyzes, D. Langlois, F. Piazza, and F. Vernizzi. *Healthy theories beyond Horndeski*. arXiv preprint arXiv:1404.6495, (**2014**).

[117] M. Blagojević, F. W. Hehl, and T. Kibble. *Gauge theories of gravitation: a reader with commentaries*. World Scientific, (**2013**).

[118] F. W. Hehl, J. D. McCrea, E. W. Mielke, and Y. Ne'eman. *Metric-affine gauge theory of gravity: field equations, Noether identities, world spinors, and breaking of dilation invariance*. Physics Reports, vol. 258, no. 1-2, (**1995**).

[119] T. Biswas, E. Gerwick, T. Koivisto, and A. Mazumdar. *Towards singularity-and ghost-free theories of gravity*. Physical review letters, vol. 108, no. 3, (**2012**).

[120] Á. de la Cruz-Dombriz, F. J. M. Torralba, and A. Mazumdar. *Nonsingular and ghost-free infinite derivative gravity with torsion*. Physical Review D, vol. 99, no. 10, (**2019**).

[121] T. Clifton, P. G Ferreira, A. Padilla, and C. Skordis. *Modified gravity and cosmology*. Physics reports, vol. 513, no. 1-3, (**2012**).

[122] E. W. Kolb. *Particle physics in the early universe*. Techniques and Concepts of High Energy Physics X, Springer, (**1999**).

[123] S. Tremaine and J. E. Gunn. *Dynamical role of light neutral leptons in cosmology*. Physical Review Letters, vol. 42, no. 6, (**1979**).

[124] B. Audren et al. *Strongest model-independent bound on the lifetime of Dark Matter*. Journal of Cosmology and Astroparticle Physics, vol. 2014, no. 12, (**2014**).

[125] R. J. Wilkinson, J. Lesgourgues, et al. *Using the CMB angular power spectrum to study Dark Matter-photon interactions*. Journal of Cosmology and Astroparticle Physics, vol. 2014, no. 04, (**2014**).

[126] J. Miralda-Escude. *A test of the collisional dark matter hypothesis from cluster lensing*. The Astrophysical Journal, vol. 564, no. 1, (**2002**).

[127] S. W. Randall et al. *Constraints on the self-interaction cross section of dark matter from numerical simulations of the merging galaxy cluster 1E 0657–56*. The Astrophysical Journal, vol. 679, no. 2, (**2008**).

[128] M. R. Buckley and P. J. Fox. *Dark matter self-interactions and light force carriers*. Physical Review D, vol. 81, no. 8, (**2010**).

[129] M. Kaplinghat, S. Tulin, and H. B. Yu. *Dark matter halos as particle colliders: unified solution to small-scale structure puzzles from dwarfs to clusters*. Physical Review Letters, vol. 116, no. 4, (**2016**).

[130] C. G. Lacey and J. P. Ostriker. *Massive black holes in galactic halos?* Astrophysical journal., vol. 299, (**1985**).

[131] B. Moore. *An upper limit to the mass of black holes in the halo of the galaxy*. The Astrophysical Journal, vol. 413, (**1993**).

[132] H. W. Rix and G. Lake. *Can the Dark Matter be* 10^6*Solar Mass Objects?* arXiv preprint astro-ph/9308022, (**1993**).

[133] A. Boveia and C. Doglioni. *Dark matter searches at colliders*. Annual Review of Nuclear and Particle Science, vol. 68, (**2018**).

[134] K. Freese, M. Lisanti, and C. Savage. *Annual modulation of dark matter: a review*. arXiv preprint arXiv:1209.3339, (**2012**).

[135] G. B. Gelmini. *Direct dark matter searches: Fits to WIMP candidates*. arXiv preprint arXiv:1106.6278, (**2011**).

[136] J. M. Gaskins. *A review of indirect searches for particle dark matter*. Contemporary Physics, vol. 57, no. 4, (**2016**).

[137] O. Adriani et al. *Ten years of PAMELA in space*. arXiv preprint arXiv:1801.10310, (**2018**).

[138] M. Tinivella. *A review of Cosmic-ray electrons and fermi-LAT*. arXiv preprint arXiv:1610.03672, (**2016**).

[139] P. Dewdney et al. *SKA1 system baseline design*. Document number SKA-TEL-SKO-DD-001 Revision, vol. 1, no. 1, (**2013**).

[140] M. Escudero, A. Berlin, D. Hooper, and M. X. Lin. *Toward (finally) ruling out Z and Higgs mediated dark matter models*. arXiv preprint arXiv:1609.09079, (**2016**).

[141] G. Busoni, A. De Simone, E. Morgante, and A. Riotto. *On the Validity of the Effective Field Theory for Dark Matter Searches at the LHC*. Phys. Lett., vol. B728, (**2014**).

[142] B. Penning. *The pursuit of dark matter at colliders—an overview*. Journal of Physics G: Nuclear and Particle Physics, vol. 45, no. 6, (**2018**).

[143] M. Aaboud et al. *Search for squarks and gluinos in events with an isolated lepton, jets, and missing transverse momentum at s= 13 TeV with the ATLAS detector*. Physical Review D, vol. 96, no. 11, (**2017**).

[144] M. Bravin et al. *The CRESST dark matter search*. Astroparticle Physics, vol. 12, no. 1-2, (**1999**).

[145] S. Baum, K. Freese, and C. Kelso. *Dark Matter implications of DAMA/LIBRA phase2 results*. Physics Letters B, vol. 789, (**2019**).

[146] J. Amaré et al. *First results on dark matter annual modulation from ANAIS-112 experiment*. arXiv preprint arXiv:1903.03973, (**2019**).

[147] G. Adhikari et al. *An experiment to search for dark matter interactions using sodium iodide detectors*. arXiv preprint arXiv:1906.01791, (**2019**).

[148] E. Shields, J. Xu, and F. Calaprice. *SABRE: A new NaI (T1) dark matter direct detection experiment*. Physics Procedia, vol. 61, (**2015**).

[149] K. I. M. S. collaboration et al. *Limits on WIMP-nucleon cross section with CsI (Tl) crystal detectors*. Phys. Rev. Lett, vol. 99, (**2007**).

[150] P. Gorel. *Search for Dark Matter with Liquid Argon and Pulse Shape Discrimination: Results from DEAP-1 and Status of DEAP-3600*. arXiv preprint arXiv:1406.0462, (**2014**).

[151] K. Abe et al. *Direct dark matter search by annual modulation in XMASS-I*. Physics Letters B, vol. 759, (**2016**).

[152] C. E. Aalseth et al. *CoGeNT: A search for low-mass dark matter using p-type point contact germanium detectors*. Physical Review D, vol. 88, no. 1, (**2013**).

[153] A. Aguilar-Arevalo et al. *First Direct-Detection Constraints on eV-Scale Hidden-Photon Dark Matter with DAMIC at SNOLAB*. Physical review letters, vol. 118, no. 14, (**2017**).

[154] Q. Arnaud et al. *First results from the NEWS-G direct dark matter search experiment at the LSM*. Astroparticle Physics, vol. 97, (**2018**).

[155] S. J. Plank. *The DRIFT Dark Matter Project: Directionality, Sensitivity, and Environmental Backgrounds*. The University of Edinburgh, (**2008**).

[156] N. Polukhina and N. Starkov. *New experiment for WIMP direct search (NEWSdm)*. EPJ Web of Conferences, vol. 191. EDP Sciences. (**2018**).

[157] C. Amole et al. *Dark Matter Search Results from the PICO- 60 C 3 F 8 Bubble Chamber*. Physical review letters, vol. 118, no. 25, (**2017**).

[158] L. Stodolsky et al. *The CRESST II dark matter search*. Journal of Physics: Conference Series, vol. 384. 1. IOP Publishing. (**2012**).

[159] A. H. Abdelhameed et al. *First results from the CRESST-III low-mass dark matter program*. arXiv preprint arXiv:1904.00498, (**2019**).

[160] G. Angloher et al. *The COSINUS project: perspectives of a NaI scintillating calorimeter for dark matter search*. The European Physical Journal C, vol. 76, no. 8, (**2016**).

[161] P. Brink et al. *The Cryogenic Dark Matter Search (CDMS) experiment: Results and prospects*. Journal of Physics: Conference Series, vol. 150. 1. IOP Publishing. (**2009**).

[162] V. Sanglard et al. *Final results of the EDELWEISS-I dark matter search with cryogenic heat-and-ionization Ge detectors*. Physical Review D, vol. 71, no. 12, (**2005**).

[163] E. Aprile et al. *The XENON dark matter search experiment*. New Astronomy Reviews, vol. 49, no. 2-6, (**2005**).

[164] D. S. Akerib et al. *First results from the LUX dark matter experiment at the Sanford Underground Research Facility*. Physical review letters, vol. 112, no. 9, (**2014**).

[165] M. Xiao et al. *First dark matter search results from the PandaX-I experiment*. Science China Physics, Mechanics & Astronomy, vol. 57, no. 11, (**2014**).

[166] D. McKinsey et al. *The LUX dark matter search*. Journal of Physics: Conference Series, vol. 203. 1. (**2010**).

[167] A. Rubbia. *ArDM: a ton-scale liquid Argon experiment for direct detection of Dark Matter in the Universe*. Journal of Physics: Conference Series, vol. 39. 1. (**2006**).

[168] R Brunetti et al. *WARP liquid argon detector for dark matter survey*. New Astronomy Reviews, vol. 49, no. 2-6, (**2005**).

[169] P. Agnes et al. *First results from the DarkSide-50 dark matter experiment at Laboratori Nazionali del Gran Sasso*. Physics Letters B, vol. 743, (**2015**).

[170] R. Catena and P. Ullio. *A novel determination of the local dark matter density*. Journal of Cosmology and Astroparticle Physics, vol. 2010, no. 08, (**2010**).

[171] M. Weber and W. de Boer. *Determination of the local dark matter density in our galaxy*. Astronomy & Astrophysics, vol. 509, (**2010**).

[172] A. K. Drukier, K. Freese, and D. N. Spergel. *Detecting cold dark-matter candidates*. Physical Review D, vol. 33, no. 12, (**1986**).

[173] E. Aprile et al. *Search for electronic recoil event rate modulation with 4 years of XENON100 data*. Physical review letters, vol. 118, no. 10, (**2017**).

[174] X. Collaboration et al. *Direct dark matter search by annual modulation with 2.7 years of XMASS-I data*. Physical Review D, vol. 97, no. 10, (**2018**).

[175] M. Cirelli et al. *PPPC 4 DM ID: A Poor Particle Physicist Cookbook for Dark Matter Indirect Detection*. JCAP, vol. 1103, (**2011**).

[176] N. Fornengo, R. A. Lineros, M. Regis, and M. Taoso. *Galactic synchrotron emission from WIMPs at radio frequencies*. Journal of Cosmology and Astroparticle Physics, vol. 2012, no. 01, (**2012**).

[177] N. Fornengo, R. A. Lineros, M. Regis, and M. Taoso. *The isotropic radio background revisited*. JCAP, vol. 1404, (**2014**).

[178] A. Natarajan, J. E. Aguirre, K. Spekkens, and B. S. Mason. *Green Bank Telescope Constraints on Dark Matter Annihilation in Segue I* (**2015**).

[179] A. McDaniel, T. Jeltema, S. Profumo, and E. Storm. *Multiwavelength Analysis of Dark Matter Annihilation and RX-DMFIT*. JCAP, vol. 1709, no. 09, (**2017**).

[180] P. Bull et al. *Fundamental Physics with the Square Kilometer Array* (**2018**). arXiv: `1810.02680 [astro-ph.CO]`.

[181] A. W. Strong, I. V. Moskalenko, and V. S. Ptuskin. *Cosmic-ray propagation and interactions in the Galaxy*. Ann. Rev. Nucl. Part. Sci., vol. 57, (**2007**).

[182] J. Giacalone and J. R. Jokipii. *The transport of cosmic rays across a turbulent magnetic field*. The Astrophysical Journal, vol. 520, no. 1, (**1999**).

[183] R. Schlickeiser. *Cosmic-ray transport and acceleration. I-Derivation of the kinetic equation and application to cosmic rays in static cold media. II-Cosmic rays in moving cold media with application to diffusive shock wave acceleration*. The Astrophysical Journal, vol. 336, (**1989**).

[184] F. Casse, M. Lemoine, and G. Pelletier. *Transport of cosmic rays in chaotic magnetic fields*. Physical Review D, vol. 65, no. 2, (**2001**).

[185] A. P. Snodin et al. *Global diffusion of cosmic rays in random magnetic fields*. Monthly Notices of the Royal Astronomical Society, vol. 457, no. 4, (**2016**).

[186] F. Aharonian et al. *Cosmic Rays in Galactic and Extragalactic Magnetic Fields*. Vol. 166, no. 1-4, (**2012**).

[187] A. N. Kolmogorov. *The local structure of turbulence in incompressible viscous fluid for very large Reynolds numbers*. Proceedings of the Royal Society of London. Series A: Mathematical and Physical Sciences, vol. 434, no. 1890, (**1991**).

[188] R. H. Kraichnan. *Inertial-range spectrum of hydromagnetic turbulence*. The Physics of Fluids, vol. 8, no. 7, (**1965**).

[189] E. Fermi. *On the origin of the cosmic radiation*. Physical Review, vol. 75, no. 8, (**1949**).

[190] A. Thornbury and L. O. Drury. *Power requirements for cosmic ray propagation models involving re-acceleration and a comment on second-order Fermi acceleration theory*. Monthly Notices of the Royal Astronomical Society, vol. 442, no. 4, (**2014**).

[191] L. O. Drury and A. W. Strong. *Cosmic-ray diffusive reacceleration: a critical look*. PoS, vol. ICRC2015, (**2016**). arXiv: `1508.02675 [astro-ph.HE]`.

[192] R. Genzel et al. *The Sins survey of z 2 galaxy kinematics: properties of the giant star-forming clumps*. The Astrophysical Journal, vol. 733, no. 2, (**2011**).

[193] S. F. Newman et al. *The SINS/zC-SINF survey of z 2 galaxy kinematics: outflow properties*. The Astrophysical Journal, vol. 761, no. 1, (**2012**).

[194] S. F. Newman et al. *Shocked Superwinds from the z 2 Clumpy Star-forming Galaxy, ZC406690*. The Astrophysical Journal, vol. 752, no. 2, (**2012**).

[195] J. E Everett et al. *The Milky Way's kiloparsec-scale wind: a hybrid cosmic-ray and thermally driven outflow*. The Astrophysical Journal, vol. 674, no. 1, (**2008**).

[196] J. S. Mathis, P. G. Mezger, and N. Panagia. *Interstellar radiation field and dust temperatures in the diffuse interstellar matter and in giant molecular clouds*. Astronomy and Astrophysics, vol. 128, (**1983**).

[197] X. Chi and A. W. Wolfendale. *The interstellar radiation field: a datum for cosmic ray physics*. Journal of Physics G: Nuclear and Particle Physics, vol. 17, no. 6, (**1991**).

[198] I. V. Moskalenko and A. Strong. *Production and propagation of cosmic-ray positrons and electrons*. The Astrophysical Journal, vol. 493, no. 2, (**1998**).

[199] J. A. R. Cembranos, A. de la Cruz-Dombriz, V. Gammaldi, and M. Mendez-Isla. *SKA-Phase 1 sensitivity for synchrotron radio emission from multi-TeV Dark Matter candidates*. (**2019**). arXiv: `1905.11154 [hep-ph]`.

[200] C. L. Sarazin. *The Energy spectrum of primary cosmic ray electrons in clusters of galaxies and inverse Compton emission*. Astrophys. J., vol. 520, (**1999**).

[201] G. B. Rybicki and A. P. Lightman. *Radiative processes in astrophysics*. John Wiley & Sons, (**2008**).

[202] T. Delahaye et al. *Galactic electrons and positrons at the Earth: new estimate of the primary and secondary fluxes*. Astronomy & Astrophysics, vol. 524, (**2010**).

[203] K. Ferriere, W. Gillard, and P. Jean. *Spatial distribution of interstellar gas in the innermost 3 kpc of our Galaxy*. Astron. Astrophys., vol. 467, (**2007**).

[204] S. Colafrancesco, S. Profumo, and P. Ullio. *Detecting dark matter WIMPs in the Draco dwarf: A multi-wavelength perspective*. Phys. Rev., vol. D75, (**2007**).

[205] T. Delahaye et al. *Galactic secondary positron flux at the Earth*. Astron. Astrophys., vol. 501, (**2009**).

[206] T. Delahaye et al. *Positrons from dark matter annihilation in the galactic halo: theoretical uncertainties*. Physical Review D, vol. 77, no. 6, (**2008**).

[207] S. Colafrancesco, S. Profumo, and P. Ullio. *Multi-frequency analysis of neutralino dark matter annihilations in the Coma cluster*. Astron. Astrophys., vol. 455, (**2006**).

[208] E. A. Baltz and J. Edsjö. *Positron propagation and fluxes from neutralino annihilation in the halo*. Physical Review D, vol. 59, no. 2, (**1998**).

[209] V. Gammaldi, E. Karukes, and P. Salucci. *Theoretical predictions for dark matter detection in dwarf irregular galaxies with gamma rays*. Phys. Rev., vol. D98, no. 8, (**2018**). arXiv: `1706.01843 [astro-ph.CO]`.

[210] M. Aguilar et al. *First result from the Alpha Magnetic Spectrometer on the International Space Station: precision measurement of the positron fraction in primary cosmic rays of 0.5–350 GeV*. Physical Review Letters, vol. 110, no. 14, (**2013**).

[211] M. Aguilar et al. *Cosmic-ray positron fraction measurement from 1 to 30 GeV with AMS-01*. Physics Letters B, vol. 646, no. 4, (**2007**).

[212] M. Aguilar et al. *Electron and positron fluxes in primary cosmic rays measured with the Alpha Magnetic Spectrometer on the International Space Station*. Physical review letters, vol. 113, no. 12, (**2014**).

[213] W. Atwood et al. *The large area telescope on the Fermi gamma-ray space telescope mission*. The Astrophysical Journal, vol. 697, no. 2, (**2009**).

[214] S. Abdollahi et al. *Cosmic-ray electron-positron spectrum from 7 GeV to 2 TeV with the Fermi Large Area Telescope*. Physical Review D, vol. 95, no. 8, (**2017**).

[215] W Atwood et al. *Pass 8: toward the full realization of the Fermi-LAT scientific potential*. arXiv preprint arXiv:1303.3514, (**2013**).

[216] P. Dewdney et al. *SKA1 system baseline V2 description*. SKA Organisation (November 2015), (**2015**).

[217] S. Johnston and J. Wall. *Science with ASKAP - the Australian Square Kilometre Array Pathfinder*. Exper. Astron., vol. 22, (**2008**).

[218] A. Foley et al. *Engineering and science highlights of the KAT-7 radio telescope*. Monthly Notices of the Royal Astronomical Society, vol. 460, no. 2, (**2016**).

[219] R. Booth, W. De Blok, J. Jonas, and B Fanaroff. *MeerKAT key project science, specifications, and proposals*. arXiv preprint arXiv:0910.2935, (**2009**).

[220] G. P. Lepage. *A new algorithm for adaptive multidimensional integration*. Journal of Computational Physics, vol. 27, no. 2, (**1978**).

[221] G. P. Lepage. *VEGAS-An adaptive multi-dimensional integration program*. Tech. rep. (**1980)**.

[222] J. Diemand, M. Kuhlen, and P. Madau. *Dark matter substructure and gamma-ray annihilation in the Milky Way halo*. The Astrophysical Journal, vol. 657, no. 1, (**2007**).

[223] J. Diemand et al. *Clumps and streams in the local dark matter distribution*. Nature, vol. 454, (**2008**).

[224] V. Springel et al. *The Aquarius Project: the subhalos of galactic halos*. Mon. Not. Roy. Astron. Soc., vol. 391, (**2008**).

[225] S. Garrison-Kimmel, M. Boylan-Kolchin, J. S. Bullock, and K. Lee. *ELVIS: Exploring the local volume in simulations*. Monthly Notices of the Royal Astronomical Society, vol. 438, no. 3, (**2014**).

[226] B. F. Griffen et al. *The Caterpillar project: a large suite of milky way sized halos*. The Astrophysical Journal, vol. 818, no. 1, (**2016**).

[227] T. Sawala et al. *The APOSTLE simulations: solutions to the Local Group's cosmic puzzles*. Monthly Notices of the Royal Astronomical Society, vol. 457, no. 2, (**2016**).

[228] M. H. Hani et al. *The diversity of the circumgalactic medium around z= 0 Milky Way-mass galaxies from the Auriga simulations*. Monthly Notices of the Royal Astronomical Society, vol. 488, no. 1, (**2019**).

[229] J. A. Cembranos, A. de la Cruz-Dombriz, P. K. Dunsby, and M. Méndez-Isla. *Analysis of branon dark matter and extra-dimensional models with AMS-02*. Physics Letters B, vol. 790, (**2019**).

[230] M. Glasmacher et al. *The cosmic ray energy spectrum between* 10^{14} *and* 10^{16} *eV*. Astroparticle Physics, vol. 10, no. 4, (**1999**).

[231] T. Antoni et al. *KASCADE measurements of energy spectra for elemental groups of cosmic rays: Results and open problems*. Astroparticle physics, vol. 24, no. 1-2, (**2005**).

[232] F. Arqueros and T. H. Collaboration. *Energy spectrum and chemical composition of cosmic rays between 0.3 and 10 PeV determined from the Cherenkov-light and charged-particle distributions in air showers*. arXiv preprint astro-ph/9908202, (**1999**).

[233] M. Takeda et al. *Energy determination in the Akeno giant air shower array experiment*. Astroparticle Physics, vol. 19, no. 4, (**2003**).

[234] R. Abbasi et al. *Measurement of the flux of ultra high energy cosmic rays by the stereo technique*. Astroparticle Physics, vol. 32, no. 1, (**2009**).

[235] Pierre Auger Observatory Collaboration and others. *The Pierre Auger Observatory I: The Cosmic Ray Energy Spectrum and Related Measurements, proc 32rd ICRC (2011) Beij // ijing, China, August 2011. (* **2011***)*.

[236] A. López Oramas and E. Férnandez Sánchez. *Multi-year campaign of the gamma-ray binary LS I+ 61º 303 and search for VHE emission from gamma-ray binary candidates with the MAGIC telescopes* (**2014**).

[237] S. Barwick et al. *Measurements of the cosmic-ray positron fraction from 1 to 50 GeV*. The Astrophysical Journal Letters, vol. 482, no. 2, (**1997**).

[238] N. Lund. *Cosmic-ray elemental abundances*. Advances in Space Research, vol. 4, no. 2-3, (**1984**).

[239] J. George et al. *Elemental composition and energy spectra of galactic cosmic rays during solar cycle 23*. The Astrophysical Journal, vol. 698, no. 2, (**2009**).

[240] H. Palme, K. Lodders, and A. Jones. *Solar system abundances of the elements*. Planets, Asteriods, Comets and The Solar System, Volume 2 of Treatise on Geochemistry (Second Edition). Edited by Andrew M. Davis. Elsevier, 2014., vol. 2, (**2014**).

[241] E.-S. Seo and V. S. Ptuskin. *Stochastic reacceleration of cosmic rays in the interstellar medium*. The Astrophysical Journal, vol. 431, (**1994**).

[242] A. Strong and J. Mattox. *Gradient model analysis of EGRET diffuse Galactic gamma-ray emission.* Astronomy and Astrophysics, vol. 308, (**1996**).

[243] W. Baade and F. Zwicky. *Cosmic rays from super-novae*. Proceedings of the National Academy of Sciences, vol. 20, no. 5, (**1934**).

[244] M Kachelriess. *Lecture notes on high energy cosmic rays*. arXiv preprint arXiv:0801.4376, (**2008**).

[245] V. Ginzburg. *On the origin of cosmic rays*. Il Nuovo Cimento (1955-1965), vol. 8, (**1958**).

[246] A. W. Strong and I. V. Moskalenko. *Modelling cosmic rays and gamma rays in the Galaxy*. AIP Conference Proceedings, vol. 410. 1. (**1997**).

[247] A. Strong, I. Moskalenko, and V Schönfelder. *Numerical models for cosmic ray propagation and gamma ray production*. arXiv preprint astro-ph/9706010, (**1997**).

[248] S. H. Lee. *Study of Non-thermal Emission from Supernova Remnants and Cosmic Ray Injection in the Milky Way Using the Fermi Large Area Telescope*. Stanford University, (**2011**).

[249] D. C. Ellison et al. *Particle acceleration in supernova remnants and the production of thermal and nonthermal radiation*. The Astrophysical Journal, vol. 661, no. 2, (**2007**).

[250] L. O. Drury, F. Aharonian, and H. Völk. *The gamma-ray visibility of supernova remnants: a test of cosmic ray origin*. arXiv preprint astro-ph/9305037, (**1993**).

[251] C. Stephane. *Viewpoint: The first result from the space-borne alpha magnetic spectrometer confirm an unexplained excess of high-energy positrons in Earth-bound cosmic rays*. Physics, vol. 6, (**2013**).

[252] O. Adriani et al. *Cosmic-ray positron energy spectrum measured by PAMELA*. Physical review letters, vol. 111, no. 8, (**2013**).

[253] M. Ackermann et al. *Measurement of separate cosmic-ray electron and positron spectra with the Fermi Large Area Telescope*. Physical Review Letters, vol. 108, no. 1, (**2012**).

[254] E. Orlando et al. *GALPROP cosmic-ray propagation code: recent results and updates*. Nuclear and Particle Physics Proceedings, vol. 297, (**2018**).

[255] M. Di Mauro et al. *Interpretation of AMS-02 electrons and positrons data*. JCAP, vol. 1404, (**2014**).

[256] A. Kounine. *Latest results from the alpha magnetic spectrometer: positron fraction and antiproton/proton ratio, presentation at AMS Days at CERN—The future of Cosmic Ray Physics and latest results*. CERN, Geneva, Switzerland, (**2015**).

[257] M. Aguilar et al. *Antiproton flux, antiproton-to-proton flux ratio, and properties of elementary particle fluxes in primary cosmic rays measured with the alpha magnetic spectrometer on the international space station*. Physical Review Letters, vol. 117, no. 9, (**2016**).

[258] M.-Y. Cui et al. *Revisit of cosmic ray antiprotons from dark matter annihilation with updated constraints on the background model from AMS-02 and collider data*. Journal of Cosmology and Astroparticle Physics, vol. 2018, no. 06, (**2018**).

[259] C. Evoli, D. Gaggero, D. Grasso, and L. Maccione. *Cosmic ray nuclei, antiprotons and gamma rays in the galaxy: a new diffusion model*. Journal of Cosmology and Astroparticle Physics, vol. 2008, no. 10, (**2008**).

[260] C. Evoli et al. *Cosmic-ray propagation with DRAGON2: I. numerical solver and astrophysical ingredients*. Journal of Cosmology and Astroparticle Physics, vol. 2017, no. 02, (**2017**).

[261] R. Kappl and A. Reinert. *Secondary cosmic positrons in an inhomogeneous diffusion model*. Physics of the dark universe, vol. 16, (**2017**).

[262] I. Gebauer and W. de Boer. *An Anisotropic Propagation Model for Galactic Cosmic Rays*. arXiv preprint arXiv:0910.2027, (**2009**).

[263] R. Cowsik and L. W. Wilson. *The nested leaky-box model for Galactic cosmic rays*. International Cosmic Ray Conference, vol. 2. (**1975**).

[264] R. Cowsik and B. Burch. *On the positron fraction and the spectrum of the electronic component in cosmic rays*. arXiv preprint arXiv:0905.2136, (**2009**).

[265] R. Cowsik, B. Burch, and T. Madziwa-Nussinov. *The origin of the spectral intensities of cosmic-ray positrons*. The Astrophysical Journal, vol. 786, no. 2, (**2014**).

[266] T. K. Gaisser, R. Engel, and E. Resconi. *Cosmic rays and particle physics*. Cambridge University Press, (**2016**).

[267] M. Aguilar et al. *Precision measurement of the boron to carbon flux ratio in cosmic rays from 1.9 GV to 2.6 TV with the alpha magnetic spectrometer on the international space station*. Physical Review Letters, vol. 117, no. 23, (**2016**).

[268] K. Blum, B. Katz, and E. Waxman. *AMS-02 results support the secondary origin of cosmic ray positrons*. Physical review letters, vol. 111, no. 21, (**2013**).

[269] S. Ahlen et al. *Measurement of the isotopic composition of cosmic-ray helium, lithium, beryllium, and boron up to 1700 MeV per atomic mass unit*. The Astrophysical Journal, vol. 534, no. 2, (**2000**).

[270] P.-F. Yin, Z.-H. Yu, Q. Yuan, and X.-J. Bi. *Pulsar interpretation for the AMS-02 result*. Physical Review D, vol. 88, no. 2, (**2013**).

[271] A. Erlykin and A. W. Wolfendale. *Cosmic ray positrons from a local, middle-aged supernova remnant*. Astroparticle Physics, vol. 49, (**2013**).

[272] H. Yuksel, M. D. Kistler, and T. Stanev. *TeV gamma rays from Geminga and the origin of the GeV positron excess*. Physical review letters, vol. 103, no. 5, (**2009**).

[273] D. A. Green. *A revised Galactic supernova remnant catalogue*. arXiv preprint arXiv:0905.3699, (**2009**).

[274] J. Taylor, R. Manchester, and A. Lyne. *Catalog of 558 pulsars*. The Astrophysical journal supplement series, vol. 88, (**1993**).

[275] E. Berezhko et al. *Cosmic ray production in supernova remnants including reacceleration: The secondary to primary ratio*. Astronomy & Astrophysics, vol. 410, no. 1, (**2003**).

[276] P. Blasi. *Origin of the positron excess in cosmic rays*. Physical Review Letters, vol. 103, no. 5, (**2009**).

[277] P. Mertsch and S. Sarkar. *AMS-02 data confront acceleration of cosmic ray secondaries in nearby sources*. Physical Review D, vol. 90, no. 6, (**2014**).

[278] I. Cholis and D. Hooper. *Constraining the origin of the rising cosmic ray positron fraction with the boron-to-carbon ratio*. Physical Review D, vol. 89, no. 4, (**2014**).

[279] N. Tomassetti and F. Donato. *The connection between the positron fraction anomaly and the spectral features in galactic cosmic-ray hadrons*. The Astrophysical Journal Letters, vol. 803, no. 2, (**2015**).

[280] P. Sturrock. *A model of pulsars*. The Astrophysical Journal, vol. 164, (**1971**).

[281] P. Slane. *Pulsar wind nebulae*. arXiv preprint arXiv:1703.09311, (**2017**).

[282] M. Di Mauro, F. Donato, N. Fornengo, and A. Vittino. *Dark matter vs. astrophysics in the interpretation of AMS-02 electron and positron data*. Journal of Cosmology and Astroparticle Physics, vol. 2016, no. 05, (**2016**).

[283] J. Feng and H.-H. Zhang. *Dark Matter Search in Space: Combined Analysis of Cosmic-Ray Antiproton-to-proton Flux Ratio and Positron Flux Measured by AMS-02*. The Astrophysical Journal, vol. 858, no. 2, (**2018**).

[284] M. Laletin. *Can dark matter annihilations explain the AMS-02 positron data?* arXiv preprint arXiv:1705.05687, (**2017**).

[285] H.-C. Cheng et al. *AMS-02 positron excess and indirect detection of three-body decaying dark matter*. Journal of Cosmology and Astroparticle Physics, vol. 2017, no. 03, (**2017**).

[286] E. Carquin et al. *Confronting recent AMS-02 positron fraction and Fermi-LAT extragalactic γ-ray background measurements with gravitino dark matter*. Physics of the Dark Universe, vol. 11, (**2016**).

[287] J. Conrad and O. Reimer. *Indirect dark matter searches in gamma and cosmic rays*. Nature Physics, vol. 13, no. 3, (**2017**).

[288] E. A. Baltz. *Dark matter candidates*. arXiv preprint astro-ph/0412170, (**2004**).

[289] P. Ciafaloni et al. *Weak corrections are relevant for dark matter indirect detection*. Journal of Cosmology and Astroparticle Physics, vol. 2011, no. 03, (**2011**).

[290] A. Ibarra, A. S. Lamperstorfer, and J. Silk. *Dark matter annihilations and decays after the AMS-02 positron measurements*. Phys. Rev., vol. D89, no. 6, (**2014**).

[291] M. Grefe. *Indirect searches for gravitino dark matter*. J. Phys. Conf. Ser., vol. 375, (**2012**).

[292] L. Feng et al. *AMS-02 positron excess: new bounds on dark matter models and hint for primary electron spectrum hardening*. Phys. Lett., vol. B728, (**2014**).

[293] S.-J. Lin, Q. Yuan, and X.-J. Bi. *Quantitative study of the AMS 02 electron positron spectra: Implications for pulsars and dark matter properties*. Physical Review D, vol. 91, no. 6, (**2015**).

[294] B.-Q. Lu and H.-S. Zong. *Constraints on dark matter from AMS-02 electron data*. Physical Review D, vol. 92, no. 10, (**2015**).

[295] L. Gleeson and W. Axford. *Cosmic rays in the interplanetary medium*. The Astrophysical Journal, vol. 149, (**1967**).

[296] L. Gleeson and W. Axford. *Solar modulation of galactic cosmic rays*. The Astrophysical Journal, vol. 154, (**1968**).

[297] D. Hooper, A. Stebbins, and K. M. Zurek. *The PAMELA and ATIC excesses from a nearby clump of neutralino Dark Matter*. arXiv preprint arXiv:0812.3202, (**2008**).

[298] D. Cumberbatch and J. Silk. *Local dark matter clumps and the positron excess*. Monthly Notices of the Royal Astronomical Society, vol. 374, no. 2, (**2007**).

[299] M. Lattanzi and J. Silk. *Can the WIMP annihilation boost factor be boosted by the Sommerfeld enhancement?* Physical Review D, vol. 79, no. 8, (**2009**).

[300] S. Profumo. *TeV γ-rays and the largest masses and annihilation cross sections of neutralino dark matter*. Physical Review D, vol. 72, no. 10, (**2005**).

[301] M Boudaud et al. *The pinching method for Galactic cosmic ray positrons: implications in the light of precision measurements*. Astronomy & Astrophysics, vol. 605, (**2017**).

[302] J. A. R. Cembranos, A. Dobado, and A. L. Maroto. *Branon radiative corrections to collider physics and precision observables*. Phys. Rev., vol. D73, (**2006**). arXiv: `hep-ph/0510399 [hep-ph]`.

[303] J. Cembranos et al. *Photon spectra from WIMP annihilation*. Physical Review D, vol. 83, no. 8, (**2011**).

[304] J. Kopp. *Constraints on dark matter annihilation from AMS-02 results*. Physical Review D, vol. 88, no. 7, (**2013**).

[305] M. Aguilar et al. *Towards understanding the origin of cosmic-ray positrons*. Physical review letters, vol. 122, no. 4, (**2019**).

[306] S. Profumo, F. Queiroz, and C. Siqueira. *Has AMS-02 Observed Two-Component Dark Matter?* arXiv preprint arXiv:1903.07638, (**2019**).

[307] A. E. Guzmán, J. May, H. Alvarez, and K. Maeda. *All-sky Galactic radiation at 45 MHz and spectral index between 45 and 408 MHz*. Astronomy & Astrophysics, vol. 525, (**2011**).

[308] T. LaRosa, N. E. Kassim, T. J. W. Lazio, and S. Hyman. *A wide-field 90 centimeter VLA image of the galactic center region*. The Astronomical Journal, vol. 119, no. 1, (**2000**).

[309] F. Yusef-Zadeh et al. *Interacting cosmic rays with molecular clouds: a bremsstrahlung origin of diffuse high-energy emission from the inner $2^o \times 1^o$ of the Galactic center*. The Astrophysical Journal, vol. 762, no. 1, (**2012**).

[310] R Güsten and C Henkel. *H2 densities and masses of the molecular clouds close to the galactic center*. Astronomy and Astrophysics, vol. 125, (**1983**).

[311] J. Bally, A. A. Stark, R. W. Wilson, and C. Henkel. *Galactic center molecular clouds. I-Spatial and spatial-velocity maps*. The Astrophysical Journal Supplement Series, vol. 65, (**1987**).

[312] M Morris, N Polish, B Zuckerman, and N Kaifu. *The temperature of molecular gas in the galactic center region*. The Astronomical Journal, vol. 88, (**1983**).

[313] M Chernyakova et al. *The high-energy, Arcminute-scale galactic center gamma-ray source*. The Astrophysical Journal, vol. 726, no. 2, (**2010**).

[314] F. Yusef-Zadeh and M Wardle. *The underluminous nature of Sgr A*. AIP Conference Proceedings, vol. 1248. 1. (**2010**).

[315] R. Narayan et al. *Advection-dominated accretion model of Sagittarius A*: evidence for a black hole at the Galactic center*. The Astrophysical Journal, vol. 492, no. 2, (**1998**).

[316] K. Tsuchiya et al. *Detection of sub-TeV gamma rays from the Galactic center direction by CANGAROO-II*. The Astrophysical Journal Letters, vol. 606, no. 2, (**2004**).

[317] K. Kosack et al. *TeV gamma-ray observations of the galactic center*. The Astrophysical Journal Letters, vol. 608, no. 2, (**2004**).

[318] F. Aharonian et al. *Very high energy gamma rays from the composite SNR G 0.9+ 0.1*. Astronomy & astrophysics, vol. 432, no. 2, (**2005**).

[319] A Abramowski et al. *Detection of very-high-energy γ-ray emission from the vicinity of PSR B1706–44 and G 343.1–2.3 with HESS*. Astronomy & Astrophysics, vol. 528, (**2011**).

[320] C. Fruck et al. *The Galactic Center region imaged with MAGIC and variability searches during the G2 pericenter passage*. The 34th International Cosmic Ray Conference, vol. 236. SISSA Medialab. (**2016**), p. 859.

[321] V. Vitale, A. Morselli, et al. *Indirect search for dark matter from the center of the milky way with the Fermi-Large Area Telescope*. arXiv preprint arXiv:0912.3828, (**2009**).

[322] T. Daylan et al. *The characterization of the gamma-ray signal from the central Milky Way: a compelling case for annihilating dark matter*. arXiv preprint arXiv:1402.6703, (**2014**).

[323] L. Goodenough and D. Hooper. *Possible evidence for dark matter annihilation in the inner milky way from the Fermi gamma ray space telescope*. arXiv preprint arXiv:0910.2998, (**2009**).

[324] D. Hooper and L. Goodenough. *Dark matter annihilation in the galactic center as seen by the Fermi gamma ray space telescope*. Physics Letters B, vol. 697, no. 5, (**2011**).

[325] D. Hooper and T. Linden. *Origin of the gamma rays from the Galactic Center*. Physical Review D, vol. 84, no. 12, (**2011**).

[326] C. Karwin et al. *Dark matter interpretation of the Fermi-LAT observation toward the galactic center*. Physical Review D, vol. 95, no. 10, (**2017**).

[327] M. Vivier, C. van Eldik, J.-F. Glicenstein, and W. Hofmann. *Spectrum and variability of the Galactic Center VHE γ-ray source HESS J1745-290*. Energy (TeV), vol. 1, (**2009**).

[328] J. A. R. Cembranos, V. Gammaldi, and A. L. Maroto. *Possible dark matter origin of the gamma ray emission from the galactic center observed by HESS*. Phys. Rev., vol. D86, (**2012**).

[329] M Ajello et al. *Characterizing the population of pulsars in the inner galaxy with the FERMI Large Area Telescope* (**2019**).

[330] R Bartels, S Krishnamurthy, and C Weniger. *Strong support for the millisecond pulsar origin of the Galactic center GeV excess (2015)*. arXiv preprint arXiv:1506.05104, (**2015**).

[331] S. K. Lee et al. *Evidence for Unresolved gamma-Ray Point Sources in the Inner Galaxy*. Phys. Rev. Lett., vol. 116, no. 5, (**2016**).

[332] M. Cirelli, P. Panci, and P. D. Serpico. *Diffuse gamma ray constraints on annihilating or decaying Dark Matter after Fermi*. Nuclear Physics B, vol. 840, no. 1-2, (**2010**).

[333] D. Finkbeiner. *Microwave ISM emission observed by WMAP Astrophys*. J, vol. 614, (**2004**).

[334] D. Hooper, D. P. Finkbeiner, and G. Dobler. *Possible evidence for dark matter annihilations from the excess microwave emission around the center of the Galaxy seen by the Wilkinson Microwave Anisotropy Probe*. Physical Review D, vol. 76, no. 8, (**2007**).

[335] M. Su, T. R. Slatyer, and D. P. Finkbeiner. *Giant gamma-ray bubbles from Fermi-LAT: active galactic nucleus activity or bipolar galactic wind?* The Astrophysical Journal, vol. 724, no. 2, (**2010**).

[336] G Rubtsov and Y Zhezher. *Spatial structure of the WMAP-Planck haze*. arXiv preprint arXiv:1812.05228, (**2018**).

[337] R. Beck and R. Wielebinski. *Magnetic Fields in the Milky Way and in Galaxies*. arXiv preprint arXiv:1302.5663, (**2013**).

[338] M. Pshirkov, P. Tinyakov, P. Kronberg, and K. Newton-McGee. *Deriving the global structure of the galactic magnetic field from Faraday rotation measures of extragalactic sources*. The Astrophysical Journal, vol. 738, no. 2, (**2011**).

[339] V. Springel et al. *Prospects for detecting supersymmetric dark matter in the Galactic halo*. Nature, vol. 456, no. 7218, (**2008**).

[340] J. Diemand et al. *Clumps and streams in the local dark matter distribution*. Nature, vol. 454, no. 7205, (**2008**).

[341] J. F. Navarro, C. S. Frenk, and S. D. White. *A universal density profile from hierarchical clustering*. The Astrophysical Journal, vol. 490, no. 2, (**1997**).

[342] L. Pieri, J. Lavalle, G. Bertone, and E. Branchini. *Implications of high-resolution simulations on indirect dark matter searches*. Physical Review D, vol. 83, no. 2, (**2011**).

[343] G. R. Blumenthal, S. Faber, R. Flores, and J. R. Primack. *Contraction of dark matter galactic halos due to baryonic infall*. The Astrophysical Journal, vol. 301, (**1986**).

[344] B. S. Ryden and J. E. Gunn. *Galaxy formation by gravitational collapse*. The Astrophysical Journal, vol. 318, (**1987**).

[345] O. Y. Gnedin et al. *Halo contraction effect in hydrodynamic simulations of galaxy formation*. arXiv preprint arXiv:1108.5736, (**2011**).

[346] G. Gentile et al. *The cored distribution of dark matter in spiral galaxies*. Monthly Notices of the Royal Astronomical Society, vol. 351, no. 3, (**2004**).

[347] D. Fixsen et al. *ARCADE 2 measurement of the absolute sky brightness at 3-90 GHz*. The Astrophysical Journal, vol. 734, no. 1, (**2011**).

[348] R. Braun et al. *Anticipated SKA1 Science Performance*. SKA-TEL-SKO-0000818, (**2017**).

[349] L. E. Strigari. *Dark matter in dwarf spheroidal galaxies and indirect detection: a review*. Reports on Progress in Physics, vol. 81, no. 5, (**2018**).

[350] M. Ackermann et al. *Searching for dark matter annihilation from Milky Way dwarf spheroidal galaxies with six years of Fermi Large Area Telescope data*. Physical Review Letters, vol. 115, no. 23, (**2015**).

[351] S. Colafrancesco et al. *Probing the nature of Dark Matter with the SKA*. PoS, vol. AASKA14, (**2015**).

[352] M. Mateo. *Dwarf galaxies of the Local Group*. Annual Review of Astronomy and Astrophysics, vol. 36, no. 1, (**1998**).

[353] A. W. McConnachie. *The observed properties of dwarf galaxies in and around the Local Group*. The Astronomical Journal, vol. 144, no. 1, (**2012**).

[354] E. K. Grebel. *Near-field cosmology with Local Group dwarf spheroidals*. Proceedings of the International Astronomical Union, vol. 1, no. C198, (**2005**).

[355] J. Grcevich and M. E. Putman. *H I in local group dwarf galaxies and stripping by the galactic halo*. The Astrophysical Journal, vol. 696, no. 1, (**2009**).

[356] K. Spekkens et al. *The dearth of neutral hydrogen in galactic dwarf spheroidal galaxies*. The Astrophysical Journal Letters, vol. 795, no. 1, (**2014**).

[357] J. Bullock. *Notes on the missing satellites problem*. Local Group Cosmology, vol. 20, (**2013**).

[358] J. D. Simon et al. *A complete spectroscopic survey of the milky way satellite Segue 1: the darkest galaxy*. The Astrophysical Journal, vol. 733, no. 1, (**2011**).

[359] H. Shapley. *Two stellar systems of a new kind*. Nature, vol. 142, no. 3598, (**1938**).

[360] M. Aaronson. *Accurate radial velocities for carbon stars in Draco and Ursa Minor-The first hint of a dwarf spheroidal mass-to-light ratio*. The Astrophysical Journal, vol. 266, (**1983**).

[361] M. G. Walker et al. *A universal mass profile for dwarf spheroidal galaxies?* The Astrophysical Journal, vol. 704, no. 2, (**2009**).

[362] S. Faber and D. Lin. *Is there nonluminous matter in dwarf spheroidal galaxies*. The Astrophysical Journal, vol. 266, (**1983**).

[363] E. L. Lokas, G. A. Mamon, and F. Prada. *Dark matter distribution in the Draco dwarf from velocity moments*. Mon. Not. Roy. Astron. Soc., vol. 363, (**2005**).

[364] E. L. Łokas. *The mass and velocity anisotropy of the Carina, Fornax, Sculptor and Sextans dwarf spheroidal galaxies*. Monthly Notices of the Royal Astronomical Society: Letters, vol. 394, no. 1, (**2009**).

[365] J. D. Simon et al. *High-resolution measurements of the halos of four dark matter-dominated galaxies: deviations from a universal density profile*. The Astrophysical Journal, vol. 621, no. 2, (**2005**).

[366] I. V. Moskalenko. *Cosmic rays in the milky way and beyond*. Nuclear Physics B-Proceedings Supplements, vol. 243, (**2013**).

[367] B. M. Gaensler et al. *The magnetic field of the Large Magellanic Cloud revealed through Faraday rotation*. Science, vol. 307, no. 5715, (**2005**).

[368] N. Oppermann et al. *An improved map of the Galactic Faraday sky*. Astronomy & Astrophysics, vol. 542, (**2012**).

[369] F. Calura, G. A. Lanfranchi, and F. Matteucci. *The evolution of the photometric properties of Local Group dwarf spheroidal galaxies*. Astronomy & Astrophysics, vol. 484, no. 1, (**2008**).

[370] M. Aaronson and E. Olszewski. *The search for dark matter in Draco and Ursa Minor: a three year progress report*. Symposium-International Astronomical Union, vol. 117. Cambridge University Press. (**1987**).

[371] S. D. White and M. J. Rees. *Core condensation in heavy halos: a two-stage theory for galaxy formation and clustering*. Monthly Notices of the Royal Astronomical Society, vol. 183, no. 3, (**1978**).

[372] J. Klimentowski et al. *Tidal evolution of discy dwarf galaxies in the Milky Way potential: the formation of dwarf spheroidals*. Monthly Notices of the Royal Astronomical Society, vol. 397, no. 4, (**2009**).

[373] Á. Moliné, M. A. Sánchez-Conde, S. Palomares-Ruiz, and F. Prada. *Characterization of subhalo structural properties and implications for dark matter annihilation signals*. Monthly Notices of the Royal Astronomical Society, vol. 466, no. 4, (**2017**).

[374] S. Kazantzidis et al. *Density profiles of cold dark matter substructure: implications for the missing-satellites problem*. The Astrophysical Journal, vol. 608, no. 2, (**2004**).

[375] M. A. Sánchez-Conde, F. Prada, and E. L. Łokas. *Dark Matter in Draco: new considerations of the expected gamma flux in IACTs*. AIP Conference Proceedings, vol. 878. 1. American Institute of Physics. (**2006**), pp. 125–131.

[376] K. T. Chyży, M. Weżgowiec, R. Beck, and D. J. Bomans. *Magnetic fields in Local Group dwarf irregulars*. Astronomy & Astrophysics, vol. 529, (**2011**).

[377] A. Cuoco, J. Heisig, M. Korsmeier, and M. Krämer. *Constraining heavy dark matter with cosmic-ray antiprotons*. Journal of Cosmology and Astroparticle Physics, vol. 2018, no. 04, (**2018**).

[378] J. A. R. Cembranos, V. Gammaldi, and A. L. Maroto. *Spectral Study of the HESS J1745-290 Gamma-Ray Source as Dark Matter Signal*. JCAP, vol. 1304, (**2013**).

[379] J. Albert et al. *Observation of gamma rays from the galactic center with the MAGIC telescope*. The Astrophysical Journal Letters, vol. 638, no. 2, (**2006**).

[380] T. Linden, E. Lovegrove, and S. Profumo. *The morphology of hadronic emission models for the gamma-ray source at the galactic center*. The Astrophysical Journal, vol. 753, no. 1, (**2012**).

[381] D. Horns. *Erratum to: TeV-radiation from Dark Matter annihilation in the Galactic center [Phys. Lett. B 607 (2005) 225]*. Physics letters B, vol. 611, (**2005**).

[382] L. Bergström, T. Bringmann, M. Eriksson, and M. Gustafsson. *Gamma rays from heavy neutralino dark matter*. Physical review letters, vol. 95, no. 24, (**2005**).

[383] F. Aharonian et al. *HESS observations of the Galactic Center region and their Possible dark matter interpretation*. Physical Review Letters, vol. 97, no. 22, (**2006**).

[384] F. Aharonian and A. Neronov. *High-energy gamma rays from the massive black hole in the Galactic center*. The Astrophysical Journal, vol. 619, no. 1, (**2005**).

[385] A. V. Belikov, G. Zaharijas, and J. Silk. *Study of the gamma-ray spectrum from the Galactic Center in view of multi-TeV dark matter candidates*. Physical Review D, vol. 86, no. 8, (**2012**).

[386] R. M. Crocker et al. *The AGASA and SUGAR anisotropies and TeV gamma rays from the Galactic Center: A possible signature of extremely high energy neutrons*. The Astrophysical Journal, vol. 622, no. 2, (**2005**).

[387] G. Beck and S. Colafrancesco. *A Multi-frequency analysis of dark matter annihilation interpretations of recent anti-particle and γ-ray excesses in cosmic structures*. JCAP, vol. 1605, (**2016**).

[388] B.-Q. Lu, Y.-L. Wu, W.-H. Zhang, and Y.-F. Zhou. *Constraints on the Sommerfeld-enhanced dark matter annihilation from the gamma rays of subhalos and dwarf galaxies*. JCAP, vol. 1804, no. 04, (**2018**).

[389] A. X. Gonzalez-Morales, S. Profumo, and F. S. Queiroz. *Effect of Black Holes in Local Dwarf Spheroidal Galaxies on Gamma-Ray Constraints on Dark Matter Annihilation*. Phys. Rev., vol. D90, no. 10, (**2014**).

[390] M. A. Sánchez-Conde and F. Prada. *The flattening of the concentration–mass relation towards low halo masses and its implications for the annihilation signal boost*. Mon. Not. Roy. Astron. Soc., vol. 442, no. 3, (**2014**).

[391] F. Prada et al. *Halo concentrations in the standard Λ cold dark matter cosmology, MNRAS 423 (July, 2012) 3018–3030*. arXiv preprint arXiv:1104.5130, (**2012**).

[392] L. Gao et al. *Where will supersymmetric dark matter first be seen?* Monthly Notices of the Royal Astronomical Society, vol. 419, no. 2, (**2011**).

[393] A. Pinzke, C. Pfrommer, and L. Bergström. *Prospects of detecting gamma-ray emission from galaxy clusters: cosmic rays and dark matter annihilations*. Physical Review D, vol. 84, no. 12, (**2011**).

[394] P. Gondolo and J. Silk. *Dark matter annihilation at the galactic center*. Phys. Rev. Lett., vol. 83, (**1999**).

[395] P. Ullio, H. Zhao, and M. Kamionkowski. *A Dark matter spike at the galactic center?* Phys. Rev., vol. D64, (**2001**).

[396] D. Merritt, M. Milosavljevic, L. Verde, and R. Jimenez. *Dark matter spikes and annihilation radiation from the galactic center*. Phys. Rev. Lett., vol. 88, (**2002**).

[397] B. D. Fields, S. L. Shapiro, and J. Shelton. *Galactic Center Gamma-Ray Excess from Dark Matter Annihilation: Is There A Black Hole Spike?* Phys. Rev. Lett., vol. 113, (**2014**).

[398] A. E. Reines, J. E. Greene, and M. Geha. *Dwarf Galaxies with Optical Signatures of Active Massive Black Holes*. Astrophys. J., vol. 775, (**2013**).

[399] F. R. Marleau, D. Clancy, R. Habas, and M. Bianconi. *Infrared signature of active massive black holes in nearby dwarf galaxies*. Astronomy & Astrophysics, vol. 602, (**2017**).

[400] E. C. Moran et al. *Black Holes at the Centers of Nearby Dwarf Galaxies*. Astron. J., vol. 148, (**2014**).

[401] M. Wanders. *Dark matter self-annihilation signals from Galactic dwarf spheroidals; intermediate mass black holes and mini-spikes*. PhD thesis. (**2014**).

[402] J. A. R. Cembranos, A. Dobado, and A. L. Maroto. *Cosmological and astrophysical limits on brane fluctuations*. Phys. Rev., vol. D68, (**2003**).

[403] J. A. R. Cembranos, V. Gammaldi, and A. L. Maroto. *Cosmic Rays from Heavy Dark Matter from the Galactic Center*. arXiv preprint arXiv:1310.8230, (**2013**).

[404] V. Gammaldi, J. A. R. Cembranos, A. de la Cruz-Dombriz, and A. L. Maroto. *Indirect constraints to branon dark matter*. AIP Conf. Proc., vol. 1458, (**2011**).

[405] J. Bovy. *Substructure Boosts to Dark Matter Annihilation from Sommerfeld Enhancement*. Phys. Rev., vol. D79, (**2009**).

[406] M. A. Sánchez-Conde et al. *Dark matter searches with Cherenkov telescopes: nearby dwarf galaxies or local galaxy clusters?* JCAP, vol. 12, no. 11, (**2011**).

[407] T. Lacroix et al. *Unique probe of dark matter in the core of M87 with the Event Horizon Telescope*. Physical Review D, vol. 96, no. 6, (**2017**).

[408] A. Krankowski et al. *POLFAR-Polish incarnation of the LOFAR. Scientific objectives and system realization*. 2014 20th International Conference on Microwaves, Radar and Wireless Communications (MIKON), (**2014**).

[409] S. T. S. Institute. *Historical Sensitivity Estimates*. URL: `http://www.stsci.edu/jwst/about-jwst/history/historical-sensitivity-estimates`.

[410] NASA. *Technical FAQ On A Variety Of Mission Issues, Aspects And Capabilities. Targeted At The Science/Technical Community*. URL: `https://jwst.nasa.gov/faq_scientists.html`.

[411] J. Dalcanton et al. *From Cosmic Birth to Living Earths: The Future of UVOIR Space Astronomy* (**2015**).

[412] NASA. *About Chandra*. URL: `http://cxc.harvard.edu/cdo/about_chandra/`.

[413] K. Akiyama et al. *First M87 Event Horizon Telescope Results. IV. Imaging the Central Supermassive Black Hole*. The Astrophysical Journal Letters, vol. 875, no. 1, (**2019**).

[414] G. Bertone et al. *Gravitational wave probes of dark matter: challenges and opportunities*. arXiv preprint arXiv:1907.10610, (**2019**).

[415] T. D. Edwards et al. *A Unique Multi-Messenger Signal of QCD Axion Dark Matter*. arXiv preprint arXiv:1905.04686, (**2019**).

[416] A. Natarajan and P. Sikivie. *Inner caustics of cold dark matter halos*. Physical Review D, vol. 73, no. 2, (**2006**).